DEVELOPMENT OF SELECTIVELY INTERACTING SOFT MATERIALS FOR GAS SENSOR APPLICATIONS

by

John Nicholas Hodul

A Dissertation

Submitted to the Faculty of Purdue University

In Partial Fulfillment of the Requirements for the degree of

Doctor of Philosophy

Department of Chemistry

West Lafayette, Indiana

May 2022

THE PURDUE UNIVERSITY GRADUATE SCHOOL

STATEMENT OF COMMITTEE APPROVAL

Dr. Bryan W. Boudouris, Chair

Davidson School of Chemical Engineering

Dr. Shelley A. Claridge

Department of Chemistry

Dr. Jianguo Mei

Department of Chemistry

Dr. Jeffrey F. Rhoads

School of Mechanical Engineering

Approved by:

Dr. Christine Hrycyna

This thesis is dedicated to my parents:

Gloria A. Hodul and Paul J. Hodul

ACKNOWLEDGMENTS

I would like to first thank my advisor, Professor Bryan W. Boudouris for his mentorship during my graduate studies. I was truly impressed and inspired by his professionalism, fairness, patience, and focus on my personal growth while being a member in the POWER lab. Additionally, I truly appreciated his work ethic and his proactiveness when completing any task. These qualities made graduate school an excellent learning environment. This healthy learning experience fostered growth in myself as well as in my peers. Moreover, I noticed his ability to put his student's growth first. This, in my opinion, struck me as an amazing leadership quality. Given this incredible quality, I believe he will enjoy success as this quality continues to grow and reflect in his students every day. I will remember this quality as in the future I hope to become as great a leader as Professor Boudouris.

I would like to also thank my former advisor Professor John C. Parker (Lewis University) for his mentorship during my undergraduate research and preparing me for my graduate studies. I think it took an amazing deal of patience and persistence to mentor me while I had a limited experience in chemistry at the time. Additionally, teaching me basic knowledge and important considerations as I was starting to perform research for the first time. Your teachings proved to be extremely helpful in graduate school and I feel like I could not have got this far without them. Finally, it was an honor to follow in your footsteps at Purdue University as you achieved your Ph.D. in Physics in 1988 from Purdue University and had an exciting and successful career in industry afterwards.

Next, I would like to thank Professor Jason Keleher (Lewis University) and Professor Charles Crowder (Lewis University) for their teachings and for their letters of recommendation when applying to graduate schools. Professor Keleher, you were a passionate and experienced organic chemistry professor and you prepared me extremely well for organic chemistry at the graduate level. I will never forget the heated discussion on aromatic electron withdrawing versus donating groups during our organic chemistry course. I enjoyed seeing that east coast honest, straightforward, and blunt responses as my father would likely give me similar feedback in my life. I am grateful to have you for all my organic courses at Lewis University. Professor Crowder, our paths only crossed in my general physics level courses at Lewis University, however you were an excellent professor, and I learned some fascinating physics concepts.

Next, I would like to thank our collaborating sensors team in Mechanical Engineering at Purdue University, Professor Jeffrey F. Rhoads, Dr. Allison K. Murray, Nikhil F. Carneiro, Zachary A. Siefker, and Joseph R. Meseke. You were all extremely helpful when trying to understand basic mechanical engineering principles and trying to incorporate chemistries onto the sensor devices. This experience we shared has taught me that it takes interdisciplinary teamwork when trying to produce a final working product. I will never forget the term "super awk" as it is an engineering principle not expressed predominantly in previous literature, however it describes many different situations in engineering research ranging from in-lab to manuscript writing experiences. I wish you all the best in your future endeavors.

Next, I would like to thank the Notre Dame WATER team, Professor William A. Phillip, Michael Dugus, and Jialing Xu for being a great team and assisting me with my membrane questions and experiments. I wish you the best in your future endeavors. Additionally, I would like to thank Dr. Xinping He who was a visiting scholar at Purdue University who assisted me on the uranium uptake membranes project. Xinping, you were a tremendous help and provided a fresh mind to the project which allowed the research to more forward.

Next, I would like to thank the POWER Lab group members over the years: Sid, Roy, Sheng-Ning, Ying, Connie, OO (the great), Carsten, AA-ron, Hamas, Brennen, Hyunki, Ara, Kuluni, Teng, Jaeyub, Daniel, Zihao, Varad, Stephen, and Noelia. Additionally, my undergraduate researchers Katie, Wilson, Arsh, and Kelly. You all were a tremendous help and a pleasure to work with as we maintained a professional and friendly work environment. We shared some great laughs and insightful conversations which helped me grow as a scientist. I hope we can all go on another canoe trip again as a group. Sid, Roy, Teng, and Kuluni bootcamp survivors summer of 2018!

Next, I would like to thank Dan Friend and the Lewis Men's volleyball program. Being a part of the Lewis Men's volleyball team during my undergraduate studies taught me many life lessons. One specific example was our focus on controlling chaos and not letting the chaos of the moment become too big to handle. I thought in graduate school there were many chaotic moments where I remained stoic in times of adversity, and this led me to having success. Being a part of this volleyball program was one of the hardest physical and mental times in my life and it prompted much growth in myself. Being a member of the team and experiencing first-hand the culture of the program, I believe the team can and will achieve a national championship in future seasons!

Finally, I would like to thank my parents, Gloria A. Hodul and Paul J. Hodul. You both were my first mentors in my life and provided me with the resources to be successful. I could not have achieved this much without your patience, advice, support, and unconditional love. Also, thank you for not always shielding me from the difficulties in life as it was necessary to face my challenges and learn to embrace a struggle versus running away from it.

TABLE OF CONTENTS

LIST OF TABLES 11
LIST OF FIGURES 12
ABSTRACT 20
CHAPTER 1. INTRODUCTION 21
1.1 Thesis Overview 23
1.2 References 26
CHAPTER 2. IMPORTANCE OF INDOOR AIR QUALITY, MEMS GAS SENSORS, BACKGROUND ON TARGET ANALYTES AND SELECTIVE SURFACE CHEMISTRIES 28
2.1 Overview 28
2.2 Microelectromechanical Systems (MEMS) Gas Sensors 30
2.3 Background on Indoor Target Gas Analytes 36
2.4 Designing Selective Surface Chemistries for MEMS Devices 38
2.5 References 42
CHAPTER 3. MODIFYING THE SURFACE CHEMISTRY OF CARBON NANOTUBES FACILITATES THE DETECTION OF AROMATIC HYDROCARBON GASES 48
3.1 Overview 48
3.2 Introduction 49
3.3 Experimental Information 53
3.3.1 Materials 53
3.3.2 General Methods 53
3.3.3 Device Instrumentation 54
3.3.4 Device Functionalization 56
3.3.5 Device Testing 56
3.4 Results and Discussion 57
3.5 Conclusions 70
3.6 Acknowledgments 71
3.7 Supporting Information Figures 72
3.8 References 76

CHAPTER 4. MANIPULATING POLYMER COMPOSITION TO CREATE LOW-COST, HIGH-FIDELITY SENSORS FOR INDOOR CO_2 MONITORING 82
4.1 Overview 82
4.2 Introduction 82
4.3 Experimental Information 85
4.3.1 Materials 85
4.3.2 General Methods 86
4.3.3 Device Testing 87
4.3.4 Device Instrumentation 88
4.3.5 Device Functionalization 90
4.4 Results and Discussion 90
4.4.1 Sensor Response and Dynamic Range 90
4.4.2 Performance in Indoor Environments 93
4.4.3 Sensor Selectivity 96
4.4.4 Polymer Film Properties Impact CO_2 Detection 97
4.4.5 The Hydrophilic Properties of PEO Further Enhance CO_2 detection 100
4.4.6 Conclusions 102
4.4.7 Acknowledgments 103
4.5 Supporting Information Figures 103
4.6 References 105
CHAPTER 5. SORPTION KINETICS OF POLY(ETHYLENEIMINE)-POLY(ETHYLENE OXIDE) BLENDS AND THE IMPLICATION FOR LOW-COST, SMALL-SCALE CO_2 SENSORS 110
5.1 Overview 110
5.2 Introduction 111
5.3 Experimental Information 113
5.3.1 Materials 113
5.3.2 General Methods 113
5.3.3 Experimental Adsorption Apparatus and Procedure 114
5.3.4 Device Fabrication 115
5.3.5 Adsorbed Mass and Resonance Frequency Correlation 115

5.4 Results and Discussion 116
5.4.1 Characterization of Polymer Blend 116
5.4.2 CO_2 Adsorption-Desorption Profiles 119
5.4.3 Analysis of CO_2 Sorption Kinetics 122
5.5 Conclusions 125
5.6 Acknowledgements 126
5.7 Supporting Information Figures 127
5.8 References 128
CHAPTER 6. INVESTIGATING POLY (5-CARBOXYINDOLE) BETA-CYCLODEXTRIN NANOCOMPOSITE FOR THE ENHANCED INDOOR DETECTION OF FORMALDEHYDE GAS 134
6.1 Overview 134
6.2 Introduction 135
6.3 Experimental Information 139
6.3.1 Materials 139
6.3.2 General Methods 139
6.3.3 Device Functionalization 140
6.3.4 Device Instrumentation 141
6.3.5 Device Testing 142
6.4 Results and Discussion 143
6.4.1 Material Characterization 143
6.4.2 Sensor Performance 151
6.5 Conclusions 159
6.6 Acknowledgments 160
6.7 Supporting Information Figures 161
6.8 References 162
CHAPTER 7. FUTURE WORK 168
7.1 Overview 168
7.2 Introduction of Gas Sensor Pre-concentrators and Pre-concentrator Integration 169
7.3 Optimizing The Processing of Materials onto Sensor Devices 175
7.3.1 Electro-Spinning 176

7.3.2 Spin Coating 177
7.3.3 Chemical Vapor Deposition 178
7.3.4 Additional Processing Step Consideration 182
7.4 Pre-Selective Recognition Layers for Resonant Mass Sensor Devices 182
7.5 References 188
LIST OF PUBLICATIONS 193
VITA 194

LIST OF TABLES

Table 1. Summary of Gas Sensing Materials Advantages and Limitations. 40

Table 2. A comparison of device performance using PEI and PEO 103

Table 3. The average frequency shift of resonators functionalized with 1 μL of P5C solution, 1 μL of P5C-BCD solution, or left unfunctionalized (i.e., reference). Resonators were exposed to 20 min pulse of xylene, acetone, and methanol. The resonators were then run again in similar conditions, except that the resonators were tested in the presence of formaldehyde at 1000 ppm in each 20 min pulse at the same time as the other analytes. 156

LIST OF FIGURES

Figure 1. Pie chart of the percentage of time spent in indoor and outdoor environments. Data were collected from the United States Environmental Protection Agency (US EPA) sponsored National Human Activity Pattern Database (NHAPS). The total number of participants was 9196, and approximately 87% of the time spent in indoor environments was in residential buildings, office buildings, restaurants, and other indoor places, such as malls, stores, schools, churches, public buildings, salons, health clubs, parking garages, auto-repair shops, and laundromats. This figure was reproduced from Figure 1 in Reference 1. 29

Figure 2. Example schematic of an Electrochemical Sensor. As the analyte interacts with the selective chemistry there is a change in the current flow direction of the circuit and thus yields a response which can be monitored in real-time. 32

Figure 3. Example schematic of an Electromechanical gravimetric sensor. As the analyte interacts with the selective chemistry there is a change in applied mass which alters the resonator frequency and thus yields a response which can be transduced into a real-time. This figure was reproduced from Figure 2 in Reference 17. 34

Figure 4. Example schematic of an NDIR Sensor. As the analyte absorbs the infrared light this then transduces a response which can be monitored in real-time. 35

Figure 5. Schematic of the device chemical functionalization protocol. 53

Figure 6. (a) Schematic representation of the Pierce oscillator circuit with the oscillator (outlined by red dashed lines) and a series of inverters (outlined by blue dashed lines). C_1 and C_2 are load capacitors. R_1 is a feedback resistor, and R_2 is an isolation resistor. V_{cc} is the supply voltage, and V_{out} is the output voltage that enters the FPGA frequency counter. (b) Experimental setup utilized to test the sensors exposed to the target gases. The functionalized oscillators were evaluated in a chamber filled with analyte gas from bubblers connected to mass flow controllers and diluted with a stream of nitrogen. 55

Figure 7. (a) The average shift in oscillation frequency of devices functionalized with SWCNTs and 1 mg mL-1 of HHCl exposed to either benzene, toluene, or xylene, as a function of increasing concentration (500 ppm ≤ C ≤ 2,000 ppm). The error bars represent the maximum and minimum observed shifts across 4 trials. (b) The change in oscillation frequency of a device functionalized with SWCNTs and 1 mg mL^{-1} of HHCl exposed to 2,000 ppm of BTX analytes as a function of time. The response of an unfunctionalized device (reference) exposed to 2,000 ppm of benzene is shown in green for comparison. The yellow bars indicate the concentration of the analyte present and the white bars indicate a nitrogen-only environment. 58

Figure 8. (a) Raman spectra comparison of SWCNTs alone (blue), after 1 mg mL^{-1} HHCl treatment (red), and after 100 mg mL^{-1} HHCl treatment (black). (b) Zoomed overlap view of Raman spectra of the G-band (λ = 1591.4 cm^{-1}) and D-band (λ = 1308.5 cm^{-1}) after the different treatments had been performed. 61

Figure 9. XPS spectra of the C1s level of SWCNTs with increasing concentration of HHCl treatments. 62

Figure 10. Proposed mechanism for the production of NO_2 functional groups upon treatment with HHCl. 64

Figure 11. The oscillation frequency of an oscillator functionalized with different combinations of 0.1 mg mL^{-1} SWCNTs and 0.2 mg mL^{-1} HHCl exposed to 2,000 ppm xylene. Impure SWCNTs were not treated with any HCl prior to testing. These combinations consisted of no chemistry added on the device (reference), impure SWCNTs without the HHCl treatment, impure SWCNTs with the HHCl treatment, pure SWCNTs without the HHCl treatment, and pure SWCNTs with the HHCl treatment. The yellow bars indicate the corresponding concentration of xylene in the testing chamber and the white bars indicate a nitrogen-only environment. 65

Figure 12. The shift in oscillation frequency of (a) an unfunctionalized oscillator and (b) an oscillator functionalized with 1 mg mL^{-1} HHCl and SWCNTs as referenced from the initial oscillation frequency of devices exposed to 750 ppm of xylene, anisole, aniline, and trimethylbenzene with respect to time. The yellow bars indicate the concentration of the analyte with a background of nitrogen. 66

Figure 13. The change in oscillation frequency of a device functionalized with SWCNTs and 1 mg mL^{-1} of HHCl exposed to 2,000 ppm of xylene as a function of time in the presence of increasing relative humidity (RH) levels indicated by the blue line. (a) 0% RH (b) 20% RH (c) 40% RH (d) 60% RH I 80% RH. The response of an unfunctionalized device (reference) under same conditions at same time indicated by the black line. The yellow bars indicate the concentration of the xylene analyte present and the white bars indicate a nitrogen-only environment. 67

Figure 14. The change in oscillation frequency of a device functionalized with SWCNTs and 1 mg mL^{-1} of HHCl exposed to (a) ethanol and propane pulses as a function of time indicated by the blue line. The response of an unfunctionalized device (reference) under same conditions at same time is indicated by the black line. (b) Ethanol and propane with 2,000 ppm of xylene pulses as a function of time indicated by the blue line. 68

Figure 15. The oscillation frequency of an oscillator functionalized with 0.2 mg mL^{-1} of HHCl and 0.1 mg mL^{-1} SWCNTs exposed to 100 ppm of xylene in nitrogen. The black lines and red lines represent the oscillation frequency of the functionalized and unfunctionalized device (reference) in response to xylene, respectively. The yellow bars indicate the concentration of the analyte present and the white bars indicate a nitrogen-only environment. 70

Figure 16. SEM images of SWCNTs after being drop cast onto a glass slide and dried for 12 h under vacuum. The two panels show the same film at two different magnification levels. 72

Figure 17. SEM images of SWCNT films after being cast from a 0.1 mg mL-1 SWCNTs in tetrahydrofuran solution, being treated with 1.0 mg mL-1 of HHCl in methanol, being drop cast onto a glass slide, and dried for 24 h under vacuum. The three panels show the same film at three different magnification levels. 73

Figure 18. SEM images of SWCNT films after being cast from a 0.1 mg mL-1 SWCNTs in tetrahydrofuran solution, being treated with 100 mg mL-1 of HHCl in methanol, being drop cast onto a glass slide, and dried for 24 h under vacuum. The three panels show the same film at three different magnification levels. 74

Figure 19. To demonstrate the stability of the sensor, resonators functionalized with SWCNTs and HHCl were tested with five 30-minute pulses of xylene at 2,000 ppm. The average frequency shift of the resonators for their respective pulse number was recorded. As shown in the above plot, the measured frequency shift from resonators functionalized with SWCNTs and HHCl varies only approximately 10% from the initial pulse. The response time of the sensor can be characterized by a time constant of 31 s while the recovery time was 49 s. 75

Figure 20. Experimental Testing Set-up with Resonant mass sensor board in testing chamber. . 76

Figure 21. (a) Schematic of the gas distribution system used for sensor testing. Mass flow controllers (MFCs) modulated supply gases to the test chamber containing functionalized oscillators. Bubblers connected to a MFC were used to moderate distractant analytes and humidity levels inside the testing chamber. A frequency counter, executed on a MyRIO FPGA monitored the frequency of each oscillator in parallel. (b) A schematic of the Pierce oscillator used. The resonant element, outlined by the red box, is shown on the left of the circuit diagram. The remainder of the oscillator circuit, which is contained on the instrumentation board, is outlined by the blue box. This portion of the diagram contains two load capacitors (C_1 and C_2), a feedback resistor (R_1), and an isolation resistor (R_2). A series of inverters between the supply voltage (V_{cc}) and the output voltage (Vout) are used to square-off the oscillator output signal to facilitate frequency counting. (c) A single packaged resonant element shown on a US quarter for scale. (d) An exposed quartz crystal resonant element. (e) A resonant mass sensing system with 16 Pierce oscillators. A resonator board (left) containing 16 resonant elements is shown offset from the instrumentation board (right) which completes the Pierce oscillator circuit. 89

Figure 22. Sensor response to CO_2 shown as a frequency shift of the resonant element. (a) Sensor response to CO_2 over time with a background of nitrogen. The resonant frequency shift response is indicated by the blue line (left vertical axis), and the red bars indicate when CO_2 is present (right vertical axis). (b) Sensor response to CO_2 over time with a background of air. The resonant frequency shift response is indicated by the blue line (left vertical axis), and the red bars indicate when CO_2 is present (right vertical axis). The use of air brought the baseline CO_2 concentration to 1,200 ppm. (c) Total frequency shift of the device after 1 h of CO_2 at specified concentrations. The average of 8 responses is shown with error bars representing one standard deviation. Regardless of the baseline conditions, a similar linear response is obtained by the sensor, as demonstrated by the linear regression fit. (d) The dynamic range of the sensor is shown by plotting the resonant frequency shift in response to 1 h of CO_2 in a background of nitrogen. For comparison, outdoor air CO_2 concentrations[35] are indicated by the solid blue line, healthy indoor air CO_2 levels[32] are indicated by the dashed green line, poor indoor air CO_2 levels[32,36] are indicated by the dashed orange line, and toxic CO_2 levels[37] are indicated by the dashed red line. Additionally, the sensitivity (indicated by the change in frequency per change in CO_2 concentration, $\partial f \partial c$ is shown at both low and high concentrations. 92

Figure 23. (a) Psychrometric chart defining the 'Comfort Zone' air temperature and humidity range, as defined by the engineering association, ASHRAE. Testing was performed across this region to simulate environmental conditions expected in high performance buildings. (b) Frequency response of devices functionalized with PEI only, and a 3:1 PEO:PEI blend ranging from 0 to 80% relative humidity (RH). Tests were performed holding temperature at 24 °C. The average of 8 responses is shown with error bars representing one standard deviation. (c) Sensor response to CO_2 while varying temperature from 22-26 °C and relative humidity from 10-80% to cover the indoor

air comfort zones.[39] The average of 8 responses is shown with error bars representing one standard deviation. A baseline condition of 400 ppm CO_2 in nitrogen was used to simulate outdoor air conditions and a linear response is obtained at each condition, as demonstrated by the linear regression fits. (d) The rate of change in frequency shift after each increase in CO_2 concentration from a background of 400 ppm. The average of 8 responses is shown with error bars representing one standard deviation. A similar linear response is obtained at each condition, as demonstrated by the linear regression fits. 95

Figure 24. Sensor response to 1,000 ppm pulses of CO_2 and various distractants. (a) Frequency shift responses of a sensor in the presence of various interfering gas analytes. (b) Zoomed frequency shift response of a sensor in response to CO_2 in the presence of acetone. The time series data shows 30 min pulses of CO_2 with a background of nitrogen, followed by pulses of acetone, pulses of CO_2 and acetone together, and finally pulses of CO_2 with a constant background of acetone. 97

Figure 25. (a) SEM images of a 3:1 PEO:PEI blend film. Both images shown are of the same film but in different sections and locations. (b) AFM images of a 3:1 PEO:PEI blend films. (c) XRD patterns of PEO, 3:1 PEO:PEI blend, 2.5:1.5 PEO:PEI blend, 1:1 PEO:PEI blend, 1:3 PEO:PEI blend, and PEI only films. (d) DMA of a 2.5:1.5 PEO:PEI blend, 3:1 PEO:PEI blend, and PEO-only films. 99

Figure 26. Proposed mechanisms of CO_2 capture by PEI with and without the presence of water. The intermediate step indicated in red is the key step in this reaction process. Without the presence of water the reaction does not proceed and the amine does not become accessible. With the presence of water the reaction can proceed forward due to a free amine which can capture more CO_2..... 102

Figure 27. (a) and (b) SEM images of a PEI film after being drop cast onto a silicon wafer and dried for 12 h under vacuum. The two panels show the same film at two different magnification levels. (c) and (d) SEM images of a 1:1 PEO:PEI (by weight) blend film after being drop cast onto a silicon wafer and dried for 12 h under vacuum. The two panels show the same film at two different magnification levels. 104

Figure 28. (a) FTIR spectra of a 1:1 PEO:PEI polymer blend film after being annealed and dried under vacuum to remove any excess solvent and exposed to 40% relative humidity at room temperature for up to 5 hours. (b) FTIR spectra of a 3:1 PEO:PEI polymer blend film after being annealed and dried under vacuum to remove any excess solvent and exposed to 40% relative humidity at room temperature for up to 5 hours. The broad OH stretch is observed at 3300 cm^{-1}. 105

Figure 29. SEM images of a 3:1 PEO:PEI blend film. (a) Room temperature image of the polymer film. These images are highlighting the micron-sized pores formed in the polymer matrix. All of the images shown are of the same film but in different sections and locations. (b) A polymer film exposed to a > 343.15 K (max 423.15 K), isotherm for 15 min, and then imaged. These images are highlighting the melting of the polymer film and the loss of porous structure. All of the images shown are of the same film but in different sections and locations. 117

Figure 30. (a) FTIR spectra of PEI, PEO, and 3:1 PEO:PEI polymer films. Dashed lines highlight the spectrum peaks at 3270 cm^{-1}, 2880 cm^{-1}, 1580 cm^{-1}, 1475 cm^{-1}, 1380 cm^{-1}, 1310 cm^{-1}, and 1090

cm^{-1} which occur in the 3:1 PEO:PEI polymer sample corresponding to the peaks in PEO and PEI. (b) XRD patterns of PEI, PEO, 3:1 PEO:PEI blend films. Highlighting the crystal structure of PEO expressed in the 3:1 PEO:PEI polymer film. (c) DSC heating and cooling traces of PEO and 3:1 PEO:PEI polymer films. Highlighting that PEO has a T_m of 338.15 K and T_c of 317.15 K while a 3:1 PEO:PEI film has a T_m of 331.15 K and a T_c of 310.15 K. Upon integration, 3:1 PEO:PEI heating and cooling peaks were 70% of the PEO peaks area, respectively. 119

Figure 31. Representative time-series data showing the response of 3:1 PEO:PEI functionalized resonator to concentrations of CO2 between 0% and 0.8 % in a 325 K environment..... 120

Figure 32. (a) CO_2 adsorption-desorption cycles at various temperatures for a 3:1 PEO:PEI functionalized resonator in response to 1-hr on/off pulses of CO_2 at a concentration of 0.84 %. (b) The mean resonance frequency shift after 1-hr of CO_2 exposure at various concentrations for a 3:1 PEO:PEI functionalized resonator. The error bars represent one standard deviation of the data. 121

Figure 33. (a) A fit of the Langmuir adsorption isotherm (Equation 6) to frequency data of a 3:1 PEO:PEI functionalized resonator at a concentration of 0.84 % CO_2 and in a 300 K environment. (b) Fit to calculated k_{obs} for a 3:1 PEO:PEI functionalized resonator in a 300 K environment. (c) Fitted relationship between k_{obs} and CO_2 concentration for pristine PEI and a 3:1 PEO:PEI blend for temperatures ranging from 300 K to 325 K. (d) Calculated Gibbs free energy at each temperature condition for pristine PEI and a 3:1 PEO:PEI blend. 124

Figure 34. Arrhenius plot showing (a) k_a and (b) k_d for PEI alone and a 3:1 PEO:PEI functionalized resonator. Notably, k_a is relatively constant while k_d increases with increasing temperature. Thus, the decrease in response can partly be attributed to a faster desorption rate at higher temperatures. 125

Figure 35. Schematic of the experimental setup used for sensor characterization. The mass flow controllers (MFCs) modulated supply gases to the test chamber containing functionalized quartz crystal resonators. A recirculating heater/chiller and a thermal wrap were used to regulate the temperature of the test chamber at the reported conditions. 127

Figure 36. (a) CO_2 adsorption-desorption cycles at various temperatures for a PEI functionalized resonator in response to 1-hr on/off pulses of CO_2 at a concentration of 0.84 %. (b) The mean resonance frequency shift after 1-hr of CO_2 exposure at various concentrations for a PEI functionalized resonator. The error bars represent one standard deviation of the data. 128

Figure 37. (a) A schematic representation of the Pierce oscillator circuit with the oscillator (outlined by orange dashed lines) and a series of inverters (outlined by blue dashed lines). C1 and C2 are load capacitors. R1 is a feedback resistor, and R2 is an isolation resistor. V_{cc} is the supply voltage, and V_{out} is the output voltage that enters the FPGA frequency counter. (b) The experimental setup utilized to test target analyte gases. The functionalized oscillators were evaluated in a chamber filled with analyte gas from bubblers connected to mass flow controllers and diluted with a stream of pure nitrogen or dry air. 142

Figure 38. SEM images of (a) the P5C polymer and (b) P5C-BCD polymer after being dissolved in ethanol (1 mg mL^{-1}), drop cast onto a silicon wafer, dried for 12 h under vacuum, and coated with carbon. The three panels show the same film at three different magnification levels..... 144

Figure 39. Attenuated total internal reflectance-Fourier transform infrared (ATR-FTIR) spectrum of the P5C, P5C-BCD, and BCD samples. This spectrum highlights the sharp P5C peaks at 1690 cm^{-1}, 1534 cm^{-1}, 1450 cm^{-1}, 1220 cm^{-1}, and 760 cm^{-1} and broad (3250 cm^{-1}) and sharp (1077 cm^{-1}) BCD peaks, which appeared in the P5C-BCD nanocomposite..... 145

Figure 40. (a) DSC heating trace of P5C and P5C-BCD highlighting that P5C has approximately a T_g of 156 °C and a T_m of 199 °C while P5C has approximately a T_g of 155 °C and a T_m of 211 °C. Note, P5C-BCD showed a 12 °C increase in melting point. (b) Thermogravimetric analysis (TGA) of P5C, P5C-BCD, and BCD under ambient air conditions. This TGA study highlights P5C degradation (i.e., passing 10% weight loss) after 225 °C, P5C-BCD degradation (i.e., passing 10% weight loss) after 300 °C, and BCD degradation (i.e., passing 14% weight loss) at 310 °C. 147

Figure 41. X-ray photoelectron spectroscopy analysis of P5C and P5C samples. (a) XPS survey spectra highlighting C 1s, N 1s, and O 1s in both the P5C and P5C-BCD samples. (b) P5C and P5C-BCD C 1s region of the XPS spectra. Dashed lines in this region are highlighting carbon sp2, C-N, C-O, C=O, and O=C-O regions in the XPS spectra. (c) P5C and P5C-BCD N 1s region of the XPS spectra. This region is highlighting the different protonation states of the nitrogen in the P5C polymer. (d) P5C and P5C-BCD O 1s region of the XPS spectra. This region is highlighting the carboxylic acid groups in P5C as well as the C-OH character increase in P5C-BCD..... 149

Figure 42. Structure of P5C highlighting the proton exchange mechanism of P5C. Nitrogen protonation and carboxylic acid deprotonation showing the existence of NH and NH_2^+ states. 151

Figure 43. The average oscillation frequency shifts after 20 min plotted against different formaldehyde concentrations as recovered in a (a) background of nitrogen and (b) background of air. The blue triangles, red circles, and black squares represent the average oscillation frequency shifts of P5C-BCD, P5C, and unfunctionalized (i.e., reference) chemistries, respectively. Error bars represent one standard deviation from the average. 152

Figure 44. (a) Resonators exposed to 20 min pulses of formaldehyde, methanol, acetone, and xylene separately at concentrations of 500 ppm and 1,000 ppm with a background of nitrogen. (b) Resonators exposed to 20 min pulses of methanol, acetone, and xylene at concentrations of 500 and 1,000 ppm in the presence of 1,000 ppm formaldehyde with a background of nitrogen. The red and blue lines refer to the oscillation frequency shift of resonators functionalized with 1 μL of P5C solution and 1 μL of P5C-BCD solution, respectively, with respect to time. The black line represents the oscillation frequency shift of a reference resonator. Yellow, blue, green, and orange bars indicate the concentration of methanol, acetone, xylene, and formaldehyde, respectively. 155

Figure 45. Resonators were exposed to 30 min pulse of formaldehyde at concentrations of 1,000 ppm with a background of nitrogen and different relative levels of humidity: (a) 0% relative humidity, (b) 20% relative humidity, (c) 40% relative humidity, (d) 60% relative humidity, and (e) 80% relative humidity. Relative humidity values were measured at a dry bulb temperature of 22.5 °C. The red and blue lines refer to the oscillation frequency shift with respect to time of resonators functionalized with 1 μL of P5C solution and 1 μL of P5C-BCD solution, respectively. The black lines represent the oscillation frequency shift of an unfunctionalized resonator (i.e., reference). Yellow bars indicate the presence of formaldehyde. 157

Figure 46. The red circles and blue triangles refer to the average oscillation frequency shift of resonators functionalized with 1 μL of P5C solution and 1 μL of P5C-BCD solution, respectively,

with respect to each relative humidity level. The black squares represent the average oscillation frequency shift of an unfunctionalized resonator (i.e., reference). Resonators were exposed to 30 min pulses of formaldehyde at 1000 ppm at different levels of relative humidity. Error bars represent one standard deviation from the average. 159

Figure 47. Real-time data of resonator frequency when exposed to 20 min pulses of formaldehyde at a concentration of 25 ppm with a background of (a) nitrogen and (b) air. The red and blue lines refer to the oscillation frequency shift with respect to time of resonators functionalized with 1 μL of P5C solution and 1 μL of P5C-BCD solution, respectively. The black line represents the oscillation frequency shift of an unfunctionalized resonator (i.e., reference). Yellow bars indicate when the formaldehyde analyte was injected into the testing chamber. 161

Figure 48. The average oscillation frequency shift of resonators functionalized with 1 μg of P5C and 1 μg of P5C-BCD with respect to 20-min pulses of formaldehyde at a concentration of 1,000 ppm. Error bars represent one standard deviation from the average value that is plotted. 162

Figure 49. Proposed configuration of current sensing testing setup with added micro pre-concentrator component. This component shown in purple will be added at the interface of the manifold tubing (inlet) from manifold and the chamber entrance (outlet) to resonators. 172

Figure 50. Proposed pre-concentrator schematic. Blue boxes indicating the micro heaters underneath the material. Red boxes indicating the absorbent material on top of the micro heaters. (a) Indicating the top view of the proposed pre-concentrator. (b) Indicating the side view of the proposed pre-concentrator. The thickness of the absorbent material recommends being in the range of 1-500 μm thickness with a surface area ranging from 1-1000 mm^2 to maintain low dead volume and high breakthrough capacity depending on the absorbent material. The length of the pre-concentrator and amount of absorbent material can be altered to optimize pressure and thermal desorption conditions. 174

Figure 51. (a) Schematic of an electrospinning set-up consisting of a syringe pump, syringe, and a power supply. (b) SEM image of electrospun polymer fibers consisting on the nano scale in diameter. This image was reproduced from Figure 1 in Reference 27. 177

Figure 52. (a) A spin coater instrument from Elve Flow. (b) An adaptable chuck substrate from Elve Flow. These images were reproduced from the Elve Flow manufacture's website. 178

Figure 53. Schematic of the oCVD process outlining the location and operating temperatures of each component. This Figure has been reproduced from Figure 3 in Reference 38. 180

Figure 54. Proposed schematic of the CCVD process outlining the growth of CNTs on the catalytic particles on the resonators. 181

Figure 55. Schematic of MIP fabrication process. A mixture of monomer, template, cross-linker, initiator, and solvent (if necessary) is activated using heat or UV light which creates a cross-linked polymer network. The template in the cross-linked polymer matrix can then be removed by washing with solvent to generate a MIP. 185

Figure 56. MIP incorporation process onto the chemically functionalized resonators. 186

Figure 57. Fabrication process of MIMs. A prefabricated membrane is soaked in template monomer solution. The membrane is then removed and heated to activate the radical initiator and

cross-link the polymer around the template on the membrane surface. The membrane is then soaked in a solvent to remove the template in the cross-linked polymer matrix. After soaking the membrane is dried and ready for processing onto resonators. 187

Figure 58. Addition process of the MIM onto the mass resonator devices. The MIM will be added above the chemical recognition layer to act as a barrier to minimize the diffusion of interfering analytes and only allowing the target analyte to actively diffuse onto the surface chemistry.... 188

ABSTRACT

Interior air quality (IAQ) continues to gain attention as humans spend more of their routine time in interior locations. In fact, humans spend 80 – 90% of their routine time indoors. This creates concerns as gas compounds which can be deleterious to human health can accumulate in interior locations in poorly ventilated areas. This created the term "sick building syndrome", which describes a situation in which the occupants of a building experience acute health- or comfort-related effects that seem to be linked directly to the time spent exposed to harmful compounds in a building. Thus, it is important to monitor the air quality of these interior spaces to maintain proper ventilation and limit human exposure to potentially harmful gas compounds.

Monitoring these gas compounds will require gas sensors. Moreover, these gas sensors will need to be incorporated into these interior spaces to monitor these gas compounds in real time. In this case, the gas sensors must be low-power, low-cost, small-scale, selective, and sensitive to be seamlessly incorporated into existing building infrastructures. Given these parameters, there is a limited variety of sensor options available on the current market. Additionally, most of the sensors available require surface material chemistries to act as chemical recognition layers to meet these performance metrics.

In this thesis, we detail the efforts on the incorporation of different surface chemistries onto microelectromechanical systems (MEMS) resonant mass gas sensors to monitor a variety of gas analytes. These analytes span from benzene, toluene, xylene (BTX), carbon dioxide (CO_2), and formaldehyde. These soft surface chemistries, ranging from graphene to polymer to nanocomposite materials, when incorporated onto mass sensors allow for selective and sensitive real time monitoring while remaining processable, low-cost, low-power, and small-scale.

CHAPTER 1. INTRODUCTION

Gas leak and air quality monitoring has a long history that dates to the 19th and 20th centuries as miners would use canaries as a method of detecting carbon dioxide, carbon monoxide, and methane in mining tunnels.[1] This would effectively allow miners enough time to escape death as high exposure concentrations to these gases would kill the canary and be an indication to evacuate the tunnel. Over time, humans have evolved and improved their gas sensor technologies to increase safety and limit harmful exposure to deleterious gas analytes. This evolution of gas monitoring has carried over into current indoor air sensors to monitor air quality. As people spend most of their lives in indoor environments, this has a significant influence on human health and productivity.[2-4] Given the fact that humans now spend more time indoors than they ever have previously, indoor air quality (IAQ) monitoring and ventilation is a crucial necessity. Therefore, a gas sensor capable of interior monitoring of deleterious gas analytes is in increasing demand.

Previous improvements in gas monitoring have transpired in the last century as the age of electronics has progressed and could be implemented into targeting the chemistry of these deleterious analytes. Gas sensors made from existing characterization platforms, such as mass spectrometers and gas chromatographs, have all been explored in this era.[5] However, each of these sensing platforms comes with drawbacks and limitations for practical use. These drawbacks are related to the size (footprint), performance (i.e., sensitivity and selectivity), real-time processing, and the cost of the sensor when applying it to its targeted indoor application space. Thus, further work was pursued for gas sensors that could be small-scale, selective, reliable, real-time, and ideally low-cost to be seamlessly incorporated into existing infrastructures.

Over the course of the last few decades, alternative gas sensor platforms called microelectromechanical systems (MEMS) sensors have been pursued and as a result have greatly

expanded the gas sensor field. Moreover, this pursuit has created a variety of small-scale and low-cost gas sensors for the indoor air monitoring application space. MEMS sensors have 3 main categories of sensors which are electrochemical, acoustic/electromechanical, and optical.[6,7] The performance of the electrochemical and electromechanical sensor devices rely heavily on their surface chemistry which drives the interaction between the device surface and the target analyte. This surface chemistry is referred to as the chemical recognition layer. In principle, as the target analyte interacts with the chemical recognition layer there is a change in physical property (i.e., change in conductivity or mechanical oscillation) which can be transduced into a response on the device. These sensors offer promising selectively and perform well in practical indoor conditions while remaining lost-cost and consuming low-power. On the other hand, optical sensors rely on light which can be absorbed by the gas molecule. This absorption can be monitored by a detector and act as the method of transducing a response on the device to the target analyte. Optical sensors are reliable, low-cost, and fast responding (i.e., < 1 s response time are possible) and can detect a wide range of gas analytes. However, there is an added challenge with the light absorption process as different gas molecules can absorb light in similar wavelength regions. Thus, optical sensors can lack selectively to the target analytes which reduces the practicality of this sensor class. Therefore, electrochemical and electromechanical gas sensors have become dominant on the current interior gas sensor market due to their robust performance in their sensitivity and selectivity. The widespread use of these devices has created a continuously increasing demand for next generation gas sensor chemistries to utilize as chemical recognition layers on these existing sensor platforms to produce robust and low-cost gas sensors for interior monitoring.

1.1 Thesis Overview

The motivation for this work focuses on creating new chemical recognition surface chemistries for processing on top of current electromechanical gravimetric type sensors for IAQ monitoring of gas analytes. This work will focus on the synthesis, characterization, and determination of structure-property relationships of the surface chemistries for chemically selective gas sensor applications. More specifically, the chemistry of single walled carbon nanotubes (SWCNTs), a graphene-based material, with an in-situ surface treatment allows for robust selective detection of benzene, toluene, and xylene (BTX) gas analytes. The surface segregation and structure property temperature dependent relationships of poly (ethylene imine) and poly (ethylene oxide) polymer blends, when optimizing the blend ratio, allows for reliable detection of carbon dioxide gas. The cylindrical morphology and carboxylic acid functionality in poly (5-carboxyindole) and beta-cyclodextrin nanocomposites allow for reliable detection of formaldehyde gas. Overall, the incorporation of these soft materials ranging from graphene to polymer to nanocomposite onto gravimetric devices allows for robust, real-time, and practical gas sensor platforms due to the high sensitivity to target gas analytes while remaining relatively low-cost and maintaining the facile processability of chemistry.

Chapter 2 provides background on the importance of indoor air quality (IAQ) and the primary MEMS gas sensor devices being utilized to monitor IAQ. Moreover, this chapter will address the target analytes in this report (benzene, toluene, xylene, carbon dioxide, formaldehyde) and share background on the soft surface chemistries previously investigated for gas sensor recognition layers.

Chapter 3 has been published as “Modifying the Surface Chemistry of Carbon Nanotubes Facilitates the Detection of Aromatic Hydrocarbon Gases”, by John N. Hodul, Allison K. Murray, Nikhil F. Carneiro, Joseph R. Meseke, Jacob Morris, Xinping He, Dmitry Zemlyanov, George T.-

C. Chiu, James E. Braun, Jeffrey F. Rhoads, and Bryan W. Boudouris, *ACS Applied Nanomaterials*. **2020**, *3*, 10389 – 10398. Here, a study of the in-situ surface treatment of single walled-carbon nanotubes (SWCNTs) was performed to elucidate the mechanism necessary to selectively detect aromatic hydrocarbon gases. The residual iron impurities in the carbon nanotubes provided a necessary ingredient to promote surface nitration when treating the SWCNTs with hydroxylamine hydrochloride on the devices. The hydroxylamine hydrochloride reduces the iron impurities and as a result nitrates the carbon nanotube surface which changes the electronic properties on the SWCNTs and thus drives a different non-covalent and selective interaction towards electron rich aromatic compounds.

Chapter 4 has been published as "Manipulating Polymer Composition to Create Low-Cost, High-Fidelity Sensors for Indoor CO_2 Monitoring", by Zachary A. Siefker, John N. Hodul, Xikang Zhao, Nikhil Bajaj, Kelly M. Brayton, Carsten Flores-Hansen, Wenchao Zhao, George T.-C. Chiu, James E. Braun, Jeffrey F. Rhoads & Bryan W. Boudouris, *Scientific Reports* **2021**, *11*, 13237. Here, a study on a poly(ethylene oxide) (PEO) and poly(ethyleneimine) (PEI) polymer blend was conducted to elucidate the mechanism for the chemical detection of carbon dioxide gas. The incorporation of PEO into a PEI matrix allows for a two-fold improvement in the adsorption process of carbon dioxide. First, the PEO semi-crystalline features separate interchain and intrachain amines in the PEI polymer matrix which induced surface segregation and a macromolecular rearrangement to create more accessible amines. As a result, this created pores in the polymer matrix to assist in CO_2 gas diffusion and enhanced the interaction between carbon dioxide and PEI. Second, the PEO allows for improved moisture uptake which sequentially allows more carbon dioxide uptake due to more available amine groups. Overall, this polymer blend allowed for robust detection of CO_2 when coated onto a resonant mass sensor device.

Chapter 5 discusses the role of temperature on the sorption kinetics of CO_2 onto the PEO and PEI blend. This work provides deeper insight into the temperature dependent working limits of PEO and PEI that might be encountered in an interior location. At room temperature, the PEO:PEI blended material adsorbed more CO_2, at a faster rate, than PEI alone. This high adsorption is due to the crystalline features of PEO disrupting strong interchain and intrachain PEI amine entanglements, causing surface segregation and pore formation in the polymer film, and thus increasing the diffusion of CO_2 gas and the accessible amine moieties that CO_2 can interact with. Upon heating, when the temperature approaches 325 K (52 °C) there is a decrease in the adsorption of CO_2 onto the PEO and PEI blend. As temperature increases in the system, the polymers begin to melt with an onset melting point as low as 322 K (49 °C). This melting causes the porous structure in the polymer film to disappear. Moreover, the PEO semi-crystalline features that once separated the entangled amines in the PEI polymer matrix and induced surface segregation to create more accessible amines are no longer apparent. Overall, this PEO:PEI blended polymer system provides higher sensitivity and faster response times for indoor sensing applications over PEI alone and will perform well until the PEO moiety melts. The work discussed in this chapter has been submitted for publication and is currently under review. Once published, the rights to this work will be held by the respected publisher.

Chapter 6 discusses the use of poly(5-carboxyindole), a conductive polymer, for the detection of formaldehyde gas on a resonant mass sensor. Here, a study is conducted to investigate the adsorption process of formaldehyde gas onto a poly(5-carboxyindole) (P5C) polymer film. The incorporation β-cyclodextrin (BCD) into a P5C polymer matrix, to create a nanocomposite material, allowed for enhanced detection of formaldehyde gas and improved sensor response at low concentration levels (25 ppm). BCD adds features into the P5C such as its ability to form

strong host-guest interactions with formaldehyde, its ability to buffer P5C protonation states to allow for more protonated carboxylic acid moieties on P5C which can hydrogen bond more effectively with formaldehyde, as well as creating a cylindrical morphology with the polymer film to assist the diffusion of formaldehyde into the polymer matrix. The work discussed in this chapter has been submitted for publication and is currently under review. Once published, the rights to this work will be held by the respected publisher.

Chapter 7 discusses potential future methods of improving the MEMS resonant mass sensor platform through engineering and materials chemistry improvements. First, this section will discuss the use of pre-concentrators to enhance the sensitivity of the surface chemistry and lower the detection limits currently stated in this report. Second, the improvement of processability methods of the surface chemistry onto the devices will be discussed to further the surface area of the chemistry to enhance the interaction with the target analytes and therefore increase the sensitivity on the resonant mass sensor devices. Third, the possibility of gaining selectivity will be discussed by utilizing a molecularly imprinted technology (MIT) pre-selective layer over the chemical recognition layer. MIT incorporation seeks to ensure selectivity and accurate concentration readings on sensor devices by limiting the diffusion of interfering analytes to the chemical recognition layer.

1.2 References

(1) Pollock, C. The Canary in the Coal Mine. *J. Avian Med. Surg.* **2016**, *30*, 386–391.

(2) Saini, J.; Dutta, M.; Marques, G. A Comprehensive Review on Indoor Air Quality Monitoring Systems for Enhanced Public Health. *Sustain. Environ. Res.* **2020**, *30*, 6.

(3) Joshi, S. M. The Sick Building Syndrome. *Indian J. Occup. Environ. Med.* **2008**, *12*, 61–64.

(4) Mannan, M.; Al-Ghamdi, S. G. Indoor Air Quality in Buildings: A Comprehensive Review on the Factors Influencing Air Pollution in Residential and Commercial Structure. *Int. J. Environ. Res. Public Health* **2021**, *18*, 3276.

(5) Feng, S.; Farha, F.; Li, Q.; Wan, Y.; Xu, Y.; Zhang, T.; Ning, H. Review on Smart Gas Sensing Technology. *Sensors (Switzerland)* **2019**, *19*, 1–22.

(6) Spinelle, L.; Gerboles, M.; Kok, G.; Persijn, S.; Sauerwald, T. Review of Portable and Low-Cost Sensors for the Ambient Air Monitoring of Benzene and Other Volatile Organic Compounds. *Sensors (Switzerland)* **2017**, *17*. 1520.

(7) Aleixandre, M.; Gerboles, M. Review of Small Commercial Sensors for Indicative Monitoring of Ambient Gas. *Chem. Eng. Trans.* **2012**, *30*, 169–174.

CHAPTER 2. IMPORTANCE OF INDOOR AIR QUALITY, MEMS GAS SENSORS, BACKGROUND ON TARGET ANALYTES AND SELECTIVE SURFACE CHEMISTRIES

2.1 Overview

In modern society, humans spend most of their time in interior locations. Even more time is now spent indoors as the pandemic has minimized in-person interaction and work from home protocols have been implemented. As reported in Figure 1, humans spend their time mainly in their respective residential buildings (i.e., 69%). However, humans also spend a large amount of their time in office buildings, restaurants, and other indoor places, such as malls, stores, schools, churches, public buildings, salons, health clubs, parking garages, auto-repair shops, and laundromats.[1]

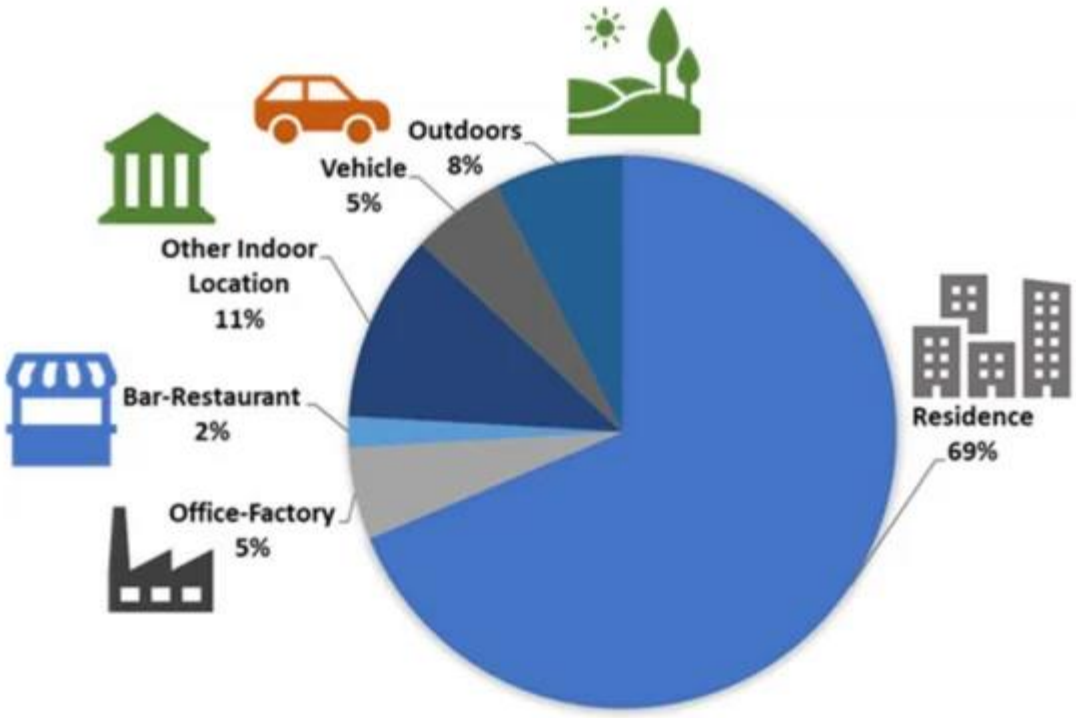

Figure 1. Pie chart of the percentage of time spent in indoor and outdoor environments. Data were collected from the United States Environmental Protection Agency (US EPA) sponsored National Human Activity Pattern Database (NHAPS). The total number of participants was 9196, and approximately 87% of the time spent in indoor environments was in residential buildings, office buildings, restaurants, and other indoor places, such as malls, stores, schools, churches, public buildings, salons, health clubs, parking garages, auto-repair shops, and laundromats. This figure was reproduced from Figure 1 in Reference 1.

In these interior locations, however, the indoor air quality (IAQ) can diminish over time due to poor ventilation. The general purpose of ventilation in buildings is to provide healthy air for breathing by diluting the concentration of pollutants originating in the building.[2] However, poor ventilation can occur when there is a lack of air flow through the building from a natural and mechanical ventilation force which brings outside air into the interior space.[3] The root cause of indoor air pollutants is mainly from degrading building materials containing polishes, furniture, cooking systems, paints, HVAC systems, refrigeration systems, cleaning agents, and excess building occupants that can release volatile organic compounds (VOCs) or other deleterious gases

over time.[4] As these gas analytes increase in concentration, they can cause a variety of health or comfort related effects that decrease the human quality of life.[5] The main diseases caused by indoor air pollution are acute lower respiratory disease (ALRI), chronic obstructive pulmonary disease (COPD), ischaemic heart disease (IHD), and lung cancer.[6] According to the World Health Organization, over 1.5 million deaths reportedly were caused by indoor air pollution in the year 2000.[7] As a result, indoor air pollution has been recognized as the third main cause for disability-adjusted life years globally.[8] Thus, it is important to have a system implemented into existing building architectures to monitor for these gas pollutants to create awareness to the building occupants to increase ventilation or to evacuate the building to decrease the associated health risks with these compounds. Therefore, there is a need for gas sensors to monitor the IAQ and to have sensors that can be easily integrated into existing buildings to work synergistically with existing ventilation systems to alert building occupants of the air quality to minimize human exposure to deleterious gas analytes.

To incorporate gas sensors seamlessly into existing buildings, the sensors need to be small-scale, selective, reliable, perform real-time, and ideally low-cost. In addition to these requirements, there is not a single sensing class or technology that can effectively detect every target analyte of interest in every possible environment. Rather, selecting the optimum sensing approach from a group of technologies may be the best method to address a sensing need.[9] As a result, this has created an ongoing need for more gas sensing technologies to be incorporated into the common place to monitor for specific deleterious analytes and address the IAQ health crisis.

2.2 Microelectromechanical Systems (MEMS) Gas Sensors

The ongoing demand to monitor IAQ has prompted the development of a variety of small-scale and low-cost gas sensor device platforms called MEMS.[10] As mentioned previously, MEMS

sensors cover a broad range of sensor devices from electrochemical to acoustic/electromechanical to optical sensors. MEMS devices are small-scale, low-cost, user-friendly devices that rely on physical changes in stimulus which can be transduced into a real-time sensor response for the user.[11,12] These compact gas sensors each have their own method of operation that can offer benefits or limitations given the indoor environment where the MEMS sensor would be installed. Thus, it is important to understand the method of function for each of the categories of MEMS devices and how to better optimize these devices for applications in interior monitoring.

Electrochemical gas sensors are devices that utilize a semi-conductive or conductive chemically selective layer as a recognition element that is placed between electrodes. As a target analyte interacts with the chemical recognition layer there is a change in the electronic properties of the chemical selective layer through a series of oxidation or reduction reactions that occur between the target analyte and chemical recognition layer.[13] These reactions generate a positive or negative current flow through said external circuit which can be transduced into a sensor response.[13-15] In this way, the higher the concentration of analyte the more oxidation or reduction reactions occur in the electronic chemical recognition layer causing more change in the direction of the current flow in the circuit. Thus, the change in electronic properties of the circuit can then be directly transduced into an analytically useful signal to determine the concentration of gas analyte present. An example schematic of this process can be viewed in Figure 2 below.

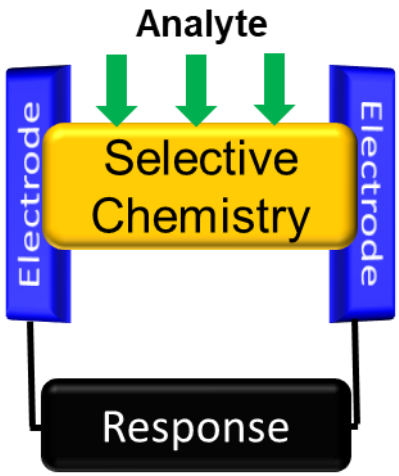

Figure 2. Example schematic of an Electrochemical Sensor. As the analyte interacts with the selective chemistry there is a change in the current flow direction of the circuit and thus yields a response which can be monitored in real-time.

Different sub-categories of electrochemical sensors exist based on the way the sensor is monitored such as: potentiometric (monitoring the change of potential); conductometric (monitoring the change of conductance); chemiresistive or impedimetric (monitoring the change of resistance/impedance); and voltametric or amperometric (monitoring the change of current). The main challenge with electrochemical sensors is choosing a selective recognition layer that is sensitive and selective to the target gas analyte while also maintaining performance under environmental conditions such as temperature and humidity fluctuations. Additionally, electrochemical sensors require a semiconductive or conductive surface chemistry coating to perform optimally which can create design limitations when targeting different target analytes. For example, metal oxide sensors are a type of electrochemical sensor which uses a semi-conductive metal oxide material as the active sensing layer.[16] Overall, electrochemical sensors offer a relatively low-cost and reliable gas sensor option granted there is a surface chemistry that can interact with the target analyte selectively and is compatible with the electrochemical device.

Acoustic or electromechanical gas sensors are devices that utilize a mechanical or acoustic wave in a piezoelectric material to monitor the presence of target gas analytes. When a gas analyte is present, the force of the applied mass of the gas analyte alters the mechanical or acoustic wave (i.e., change in oscillation frequency). This alteration is transduced into a signal on the sensor and produces a real-time response. There are many types of acoustic devices such as bulk acoustic wave, film-bulk acoustic resonators (FBARs), and surface acoustic wave (SAW) devices. However, a type of bulk acoustic electromechanical gas sensor called a gravimetric sensor has shown robust IAQ gas sensing properties. Gravimetric sensors are essentially electromechanical oscillators that use a solid material (i.e., quartz) that is oscillated at a constant frequency.[17-19] These gravimetric oscillators function based on the principal derived from the Sauerbrey equation where mass is inversely related to frequency in piezoelectric materials.[20] This equation can be further derived and manipulated based on the sensing device utilized. As shown in Figure 3, as a target analyte contacts the surface of the oscillator this alters the resonant frequency, causing a change (also known as a shift) in the resonant frequency, and this is transduced into a response. The frequency shift can then be related to the concentration of the target analyte since the mass of the target analyte is proportional to its concentration. The mass loading of the target gas analyte is caused by the gas adsorption onto a chemically selective recognition layer deposited on the mechanical resonator. Thus, knowing the chemical affinity of the chemical recognition layer with the gas molecules (target analyte) is critical to the performance of the sensor. Overall, gravimetric sensors offer a relatively low-cost and reliable gas sensor option granted there is a surface chemistry that can interact with the target analyte selectively and perform in interior location conditions.

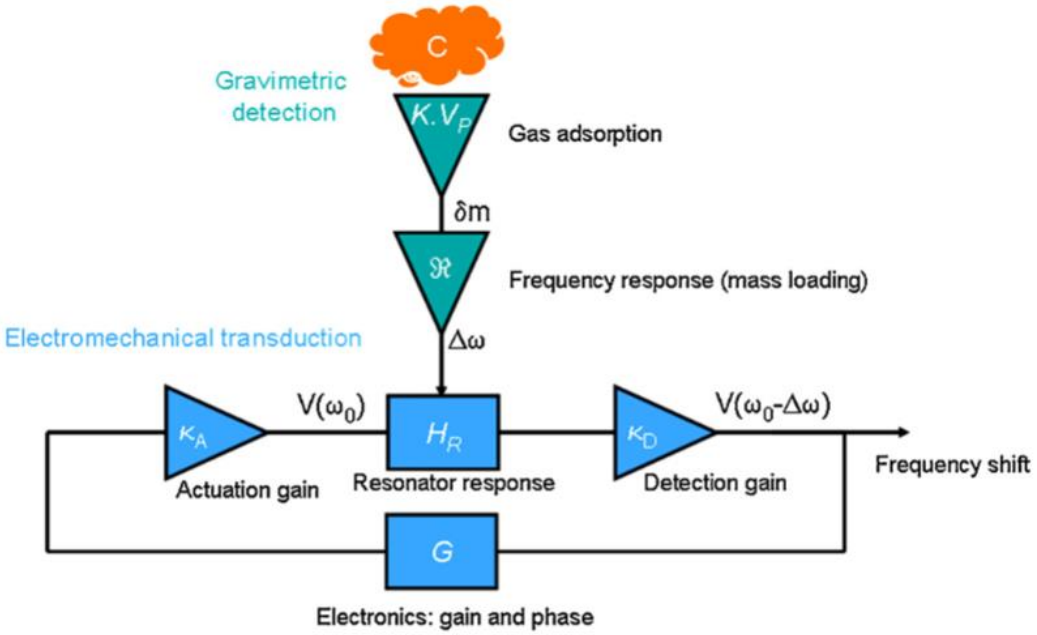

Figure 3. Example schematic of an Electromechanical gravimetric sensor. As the analyte interacts with the selective chemistry there is a change in applied mass which alters the resonator frequency and thus yields a response which can be transduced into a real-time. This figure was reproduced from Figure 2 in Reference 17.

Optical gas sensors are devices that utilize a light-based sensing mechanism to monitor for the presence of gas analytes. Many chemical species exhibit strong absorption in the ultraviolet, visible, near infrared, or mid infrared regions of the electromagnetic spectrum, allowing for gas molecules to be detected as they absorb light, altering the light proceeding to the sensor detector.[21] This absorption of light by the molecules transduces a sensor response. Because the transduction method makes a direct measurement of a molecule's absorption at a specific wavelength, measurements are self-referenced, making them inherently reliable and instant.[21,22] Additionally, this allows for optical sensors to operate at ambient conditions and remain small-scale. For IAQ monitoring, non-dispersive infrared (NDIR) optical gas sensors have shown the most promise in providing real-time detection of gas analytes.[22] The "non-dispersive" term referring to the lack of

a dispersive element (i.e., a prism or a diffraction grating). As shown in Figure 4, in NDIR sensors, infrared light is applied to gas molecules and as a result the molecules absorb the light and vibrate.[23] This is based on the principle of the Beer-Lambert law which related the concentration of a molecule to its absorbance.[24] Thus, the absorbance of light can then be transduced into a response in real-time on the sensor device to determine the concentration of gas analyte present. However, NDIR sensors require an infrared light source which can experience drift issues in the signal as the device ages over time. Additionally, NDIR light will absorb to a variety of molecules which may overlap in wavelength of light. This can cause selectively issues when distinguishing between analytes and when moisture or carbon dioxide is present in the air.

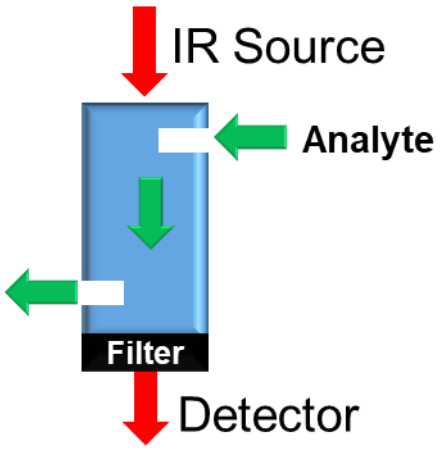

Figure 4. Example schematic of an NDIR Sensor. As the analyte absorbs the infrared light this then transduces a response which can be monitored in real-time.

Overall, MEMS gas sensors have shown promise in meeting small-scale, low-cost, real-time and reliability performance metrics for IAQ monitoring. However, improvements in device performance could be made to widen the capability of these sensor devices and expand upon the target analytes of interest. Improvements to MEMS sensor devices rely either on pushing the boundaries of the device components or the boundaries of the chemistry that is used to enhance

the device function (i.e., improving the chemical selective recognition layer). It is important to note, to remain low-cost, it is easier to enhance the selective recognition chemistry on the devices. Soft materials, discussed in Section 2.4 below, offer many unexplored cheap and processable options which can allow for sensitivity and selectively on electrochemical and acoustic/electromechanical sensor devices. Therefore, this report looks to ameliorate the MEMS sensor devices by investigating chemical recognition layers that are soft materials due to these unique processable properties.

2.3 Background on Indoor Target Gas Analytes

There are multiple target gas analytes that can affect IAQ. However, the main target analytes focused on in this report are benzene, toluene, xylene (BTX), carbon dioxide, and formaldehyde. These gas compounds are primary sources of indoor air pollution, and each have their own exposure limits and health risks. These gases will be described throughout the report as well as the importance to monitor these gases in indoor air.

The permissible exposure limit (PEL), recommended by US National Institute for Occupational Safety and Health, for benzene, toluene, and xylene (BTX) as the 8 h time-weighted average (TWA) is 1.0, 100, and 100 ppm, respectively.[25] BTX are aromatic volatile compounds that are created during the processing of petroleum products. BTX are some of most abundantly produced chemicals in the world due to their unique properties that tie them to a diverse number of applications. BTX has applications in consumer goods such as paints and lacquers, thinners, rubber products, adhesives, inks, cosmetics and more. Unfortunately, human exposure to these compounds even at levels lower than the exposure limits can cause deleterious health effects such as causing headaches, nausea, weakness, lack of concentration, loss of appetite and fatigue.[26,27] At higher concentrations, they can even cause cancer.[28] Due to their volatile nature, BTX compounds

can easily diffuse into the surrounding environment which creates issues in poorly ventilated interior locations. When interior locations are poorly ventilated, there can be a buildup of BTX compounds and thus expose humans to unhealthy concentration levels.

The permissible exposure limit (PEL), recommended by the US National Institute for Occupational Safety and Health, for carbon dioxide (CO_2) as the 8 h time-weighted average (TWA) is 5000 ppm.[29] CO_2 is mainly regarded as a greenhouse gas and is widely known for its impact on earth's atmosphere as increasing CO_2 concentration can lead to changes in the climate.[30] In an exterior setting, CO_2 is mainly produced by combustion of fossil fuels by humans such as burning coal for electric power or burning petrol fuels in internal combustion engines in vehicles.[30] However, CO_2 in an exterior setting remains at safe concentrations for human intake as it exists below 450 ppm.[31] On the other hand, CO_2 can also exist in an interior setting and can reach much higher concentrations in poorly ventilated areas. In an interior setting, CO_2 is mainly produced as a bio effluent due to a buildup in the number of building occupants which can produce CO_2 over time. Even below the 5000-ppm exposure limit, at 1000-3000 ppm concentration levels, CO_2 can cause cognitive decline affecting decision making performance.[32,33] When interior locations are poorly ventilated there can be a buildup of CO_2 and thus impact human performance.

The permissible exposure limit (PEL), recommended by the US National Institute for Occupational Safety and Health, for formaldehyde as the 8 h time-weighted average (TWA) is 0.016 ppm.[34] Formaldehyde, a volatile organic compound, is produced through the catalytic oxidation of methanol and is used in many indoor application products. These products can range from plywood, and fiberboard; glues and adhesives; permanent-press fabrics; paper product coatings; and certain insulation materials.[35-37] However, over time as these materials degrade can release formaldehyde into the ambient air. This can be an issue in poorly ventilated indoor areas

as the exposure limit is so low. Some of the health risks of formaldehyde exposure include irritation of the eyes, skin, and the respiratory and nervous systems in the short term.[38-40] Additionally, long-term exposure to formaldehyde has been linked to acute myeloid leukemia and Hodgkin's disease.[41-43] When interior locations are poorly ventilated there can be a buildup of formaldehyde which could be lethal.

Overall, the target gas compounds discussed in this report are deleterious to human health and must be monitored to limit human exposure. Utilizing sensor devices that could be seamlessly incorporated into existing buildings to monitor for these target analytes is of great importance. Additionally, designing surface chemistries on the devices that can interact well with the target analytes are important to maintain high device performance while keeping the costs of the device low.

2.4 Designing Selective Surface Chemistries for MEMS Devices

As discussed previously, due to the high performance, miniaturization, and low costs of MEMS gas sensors, these sensors have become the benchmark for monitoring IAQ. However, to further this benchmark and to progress the output of these devices more chemical research needs to be investigated as selective chemical recognition layers. Minus optical sensors which are typically not reliant on surface chemistry for their recognition layers, electrochemical and electromechanical sensors rely on a selective recognition chemistry layer that is applied to their surface. Moreover, this surface chemistry impacts how the sensor detects the target gas analyte and how the sensor performs under different environmental factors. Thus, research has been completed on using "soft" materials as gas sensor surface chemistries. These materials fall mainly under the categories of metal oxides, polymers, and graphene-based materials. Soft materials are mainly utilized due to their high-performance, processability, tunability, and low-cost that can

make them excellent candidates to be used in MEMS sensor devices. Additionally, these materials offer the capability to tune their dimensionality, introduce dopants, control their morphology, exploit their hierarchical structures, and develop tailored interfaces using additives and composite materials to expand a wide range of interesting opportunities in gas sensors. As shown in Table 1, each of these categories of materials offer specific advantages; however, each category of material has limiting factors that can impact sensor performance. This means there is no one perfect material for each type of target analyte and more research needs to be performed to account for potential drawbacks which can impact sensor performance and fabrication.

Table 1. Summary of Gas Sensing Materials Advantages and Limitations.

Gas Sensing Material	Advantages	Drawbacks
Metal Oxide Materials (*ref 44 - 49*)	1) High Surface Area 2) Low-Cost 3) Short Response Time 4) Long-Life Span 5) Conductive	1) Requires High Operating Temperatures 2) Sensitive to Humidity 3) Low Selectivity 4) Can Agglomerate, Impacting Sensing Properties
Polymers (*ref 50* - 54)	1) High Sensitivity 2) Low-Cost 3) Perform at Room Temperature 4) Processable 5) Facile Synthetic Modifications 6) Many Preparation Methods Available	1) Can Be Affected by Humidity 2) Polymer Morphology Impacts Sensing Properties 3) Long Response Times 4) Low Selectivity 5) Not all Polymers are Conductive
Graphene-Based Materials (*ref 55-60)*	1) High Sensitivity 2) Can be Chemically Modified 3) Processable 4) Conductive 5) High Surface Area (> 1300 m^2 g^{-1})	1) Can Agglomerate, Impacting Sensing Properties 2) High Energy Input During Production 3) Difficult to Purify 4) Sp2 defects on Surface Impact Sensing Properties

To overcome the drawbacks in the main categories of sensor materials discussed above, it was determined that the material expressed will have to either be further modified within its material category or combined with another material category to get more optimal performance in sensing properties. Modifications of materials, such as adding functional chemistry groups, creating blends of different materials in the same category, or doping with different additives are prime examples. For example, the surface of graphene-based carbon nanotubes can be modified with functional chemistry groups to increase the sensitivity and selectivity of the sensor device.[61] Additionally, polymers can be combined to create polymer blends which create unique physical properties (i.e., enhanced diffusion) to enhance sensitivity of target analytes.[62] Combining of materials, such as mixing one material category with another has shown great promise in creating better performing materials and better sensors. The drawbacks of one material category can be accounted for by the advantages of another material category. For example, polymers can be combined with graphene materials, in this case carbon nanotubes, to create nanocomposites to allow for better sensitivity and have better conductivity properties.[63] These nanocomposites also remain processable and reduce the drawback of agglomeration of the carbon nanotubes. Graphene can also be mixed with metal oxides which has allowed for better electron doping or de-doping redox (adding or removing electrons) properties which can result in increased sensitivity to target analytes and improved performance of the metal oxide by operating at room temperature.[64] Conducting polymer and metal oxide can also be combined to form nanocomposites. These nanocomposites typically work by forming a p-n junction between the p-type polymer and n-type metal oxide which form a depletion layer which can be expanded or reduced by a target analyte.[65] As a result, this alters the conductivity of the material which can be transduced into a sensor signal.

In addition, these materials have high surface area and are easily processable making them suitable for various sensor devices.[65]

Overall, there are many methods of designing selective chemical recognition layers on the surface of gas sensors. In this work, we detail the efforts for surface chemistries for BTX, carbon dioxide, and formaldehyde gas analytes utilizing either a modification or combination of the materials categories addressed above. This work serves to expand the surface chemistries and methods currently available for the detection of these target gas analytes.

2.5 References

(1) Mannan, M.; Al-Ghamdi, S. G. Indoor Air Quality in Buildings: A Comprehensive Review on the Factors Influencing Air Pollution in Residential and Commercial Structure. *MDPI Int. J. Environ. Res. Public Health* **2021**, *18*, 3276.

(2) Etheridge D, Sandberg M. Building Ventilation — Theory and Measurement. Chichester, UK: John Wiley & Sons; **1996**.

(3) Atkinson J, Chartier Y, Pessoa-Silva CL, et al., editors. Natural Ventilation for Infection Control in Health-Care Settings. Geneva: World Health Organization; **2009**. 2, Concepts and Types of Ventilation.

(4) Tran, V. Van; Park, D.; Lee, Y.-C. Indoor Air Pollution, Related Human Diseases, and Recent Trends in the Control and Improvement of Indoor Air Quality. *Int. J. Environ. Res. Public Health* **2020**, *17*, 2927.

(5) Dales, R.; Liu, L.; Wheeler, A. J.; Gilbert, N. L. Quality of Indoor Residential Air and Health. *Can. Med. Assoc. J.* **2008**, *179*, 147–152.

(6) World Health Organization: Burden of Disease from Household Air Pollution for 2012. (accessed on 12th Jan 2022)

(7) World Health Organization. Indoor Air Pollution: National Burden of Disease Estimates; WHO: Geneva, Switzerland, **2007**. Available online: (accessed on 12 Jan 2022).

(8) Apte, K.; Salvi, S. Household Air Pollution and Its Effects on Health [Version 1; Peer Review: 2 Approved]. *F1000Research* **2016**, *5*, 2593.

(9) Liu, C. C.; Hesketh, P. J.; Hunter, G. W. Chemical Microsensors. *Electrochem. Soc. Interface* **2004**, *13*, 22–27.

(10) Asri, M. I. A.; Hasan, M. N.; Fuaad, M. R. A.; Yunos, Y. M.; Ali, M. S. M. MEMS Gas Sensors: A Review. *IEEE Sens. J.* **2021**, *21*, 18381–18397.

(11) Nazemi, H.; Joseph, A.; Park, J.; Emadi, A. Advanced Micro- and Nano-Gas Sensor Technology: A Review. *Sensors* **2019**, *19*, 1285.

(12) Wang, J.; Yang, J.; Chen, D.; Jin, L.; Li, Y.; Zhang, Y.; Xu, L.; Guo, Y.; Lin, F.; Wu, F. Gas Detection Microsystem With MEMS Gas Sensor and Integrated Circuit. *IEEE Sens. J.* **2018**, *18*, 6765–6773.

(13) Antuña-Jiménez, D.; Díaz-Díaz, G.; Blanco-López, M. C.; Lobo-Castañón, M. J.; Miranda-Ordieres, A. J.; Tuñón-Blanco, P. Chapter 1 – Molecularly Imprinted Electrochemical Sensors: Past, Present, and Future; Li, S., Ge, Y., Piletsky, S. A., Lunec, J. B. T.-M. I. S., Eds.; Elsevier: Amsterdam, **2012**; 1–34.

(14) Mead, M. I.; Popoola, O. A. M.; Stewart, G. B.; Landshoff, P.; Calleja, M.; Hayes, M.; Baldovi, J. J.; McLeod, M. W.; Hodgson, T. F.; Dicks, J.; et al. The Use of Electrochemical Sensors for Monitoring Urban Air Quality in Low-Cost, High-Density Networks. *Atmos. Environ.* **2013**, *70*, 186–203.

(15) Arroyo, P.; Meléndez, F.; Suárez, J. I.; Herrero, J. L.; Rodríguez, S.; Lozano, J. Electronic Nose with Digital Gas Sensors Connected via Bluetooth to a Smartphone for Air Quality Measurements. *Sensors (Basel).* **2020**, *20*, 786.

(16) Dey, A. Semiconductor Metal Oxide Gas Sensors: A Review. *Mater. Sci. Eng. B* **2018**, *229*, 206–217.

(17) Fanget, S.; Hentz, S.; Puget, P.; Arcamone, J.; Matheron, M.; Colinet, E.; Andreucci, P.; Duraffourg, L.; Myers, E.; Roukes, M. L. Gas Sensors Based on Gravimetric Detection—A Review. *Sensors Actuators B Chem.* **2011**, *160*, 804–821.

(18) Hodul, J. N.; Murray, A. K.; Carneiro, N. F.; Meseke, J. R.; Morris, J.; He, X.; Zemlyanov, D.; Chiu, G. T.-C.; Braun, J. E.; Rhoads, J. F.; et al. Modifying the Surface Chemistry and Nanostructure of Carbon Nanotubes Facilitates the Detection of Aromatic Hydrocarbon Gases. *ACS Appl. Nano Mater.* **2020**, *3*, 10389–10398.

(19) Siefker, Z. A.; Hodul, J. N.; Zhao, X.; Bajaj, N.; Brayton, K. M.; Flores-Hansen, C.; Zhao, W.; Chiu, G. T.-C.; Braun, J. E.; Rhoads, J. F.; et al. Manipulating Polymer Composition to Create Low-Cost, High-Fidelity Sensors for Indoor CO2 Monitoring. *Sci. Rep.* **2021**, *11*, 13237.

(20) Vogt, B. D.; Lin, E. K.; Wu, W.; White, C. C. Effect of Film Thickness on the Validity of the Sauerbrey Equation for Hydrated Polyelectrolyte Films. *J. Phys. Chem. B* **2004**, *108*, 12685–12690.

(21) Hodgkinson, J.; Tatam, R. P. Optical Gas Sensing: A Review. *Meas. Sci. Technol.* **2012**, *24*, 12004.

(22) Dinh, T.-V.; Choi, I.-Y.; Son, Y.-S.; Kim, J.-C. A Review on Non-Dispersive Infrared Gas Sensors: Improvement of Sensor Detection Limit and Interference Correction. *Sensors Actuators B Chem.* **2016**, *231*, 529–538.

(23) B. Stuart. Infrared Spectroscopy: Fundamentals and Applications John Wiley & Sons, Ltd.; **2004**.

(24) Wypych, G. B. T.-H. of U. V. D. and S. Second E., Ed.; ChemTec Publishing; **2015**. ISBN: 978-1-895198-86-7.

(25) Barsan, M. E. NIOSH Pocket Guide to Chemical Hazards; National Institute for Occupational Safety and Health: USA, **2007**.

(26) Cometto-Muñiz, J. E.; Cain, W. S.; Abraham, M. H. Detection of Single and Mixed VOCs by Smell and by Sensory Irritation. *Indoor Air* **2004**, *14 Suppl 8*, 108–117.

(27) Bernstein, J. A.; Alexis, N.; Bacchus, H.; Bernstein, I. L.; Fritz, P.; Horner, E.; Li, N.; Mason, S.; Nel, A.; Oullette, J.; et al. The Health Effects of Non-Industrial Indoor Air Pollution. *J. Allergy Clin. Immunol.* **2008**, *121*, 585–591.

(28) Masih, A.; Lall, A. S.; Taneja, A.; Singhvi, R. Exposure Levels and Health Risk Assessment of Ambient BTX at Urban and Rural Environments of a Terai Region of Northern India. *Environ. Pollut.* **2018**, *242*, 1678–1683.

(29) The Occupational Safety and Health Administration. Occupational Health Guideline for Carbon Dioxide. **2020**.

(30) Cassia, R.; Nocioni, M.; Correa-Aragunde, N.; Lamattina, L. Climate Change and the Impact of Greenhouse Gasses: CO2 and NO, Friends and Foes of Plant Oxidative Stress. *Frontiers in Plant Science* 2018. Article # 273

(31) Wang, X.; Song, C. Carbon Capture From Flue Gas and the Atmosphere: A Perspective. *Frontiers in Energy Research* . **2020**. Article #560849.

(32) Satish, U.; Mendell, M. J.; Shekhar, K.; Hotchi, T.; Sullivan, D.; Streufert, S.; Fisk, W. J. Is CO_2 an Indoor Pollutant? Direct Effects of Low-to-Moderate CO_2 Concentrations on Human Decision-Making Performance. *Environ. Health Perspect.* **2012**, *120*, 1671–1677.

(33) Azuma, K.; Kagi, N.; Yanagi, U.; Osawa, H. Effects of Low-Level Inhalation Exposure to Carbon Dioxide in Indoor Environments: A Short Review on Human Health and Psychomotor Performance. *Environ. Int.* **2018**, *121*, 51–56.

(34) Occupational Safety and Health Guideline for Formaldehyde Potential Human Carcinogen; U.S. Department of Health and Human Services: Washington, DC, USA, **1988**. 16.

(35) Que, Z.; Furuno, T.; Katoh, S.; Nishino, Y. Evaluation of Three Test Methods in Determination of Formaldehyde Emission from Particleboard Bonded with Different Mole Ratio in the Urea–Formaldehyde Resin. *Build. Environ.* **2007**, *42*, 1242–1249.

(36) An, J.-Y.; Kim, S.; Kim, H.-J.; Seo, J. Emission Behavior of Formaldehyde and TVOC from Engineered Flooring in under Heating and Air Circulation Systems. *Build. Environ.* **2010**, *45*, 1826–1833.

(37) Liu, J.; Wang, W.; Li, S.; Liu, M.; He, S. Advances in SAW Gas Sensors Based on the Condensate-Adsorption Effect. *Sensors* **2011**, *11*, 11871–11884.

(38) Gupta, K. C.; Ulsamer, A. G.; Preuss, P. W. Formaldehyde in Indoor Air: Sources and Toxicity. *Environ. Int.* **1982**, *8*, 349–358.

(39) Hu, J.; Wu, X.; Zeng, W. Formaldehyde Sensor Based on Polypyrrole/β-Cyclodextrin. *J. Control. Release* **2011**, *152*, 211–213.

(40) Kim, W. J.; Terada, N.; Nomura, T.; Takahashi, R.; Lee, S. D.; Park, J. H.; Konno, A. Effect of Formaldehyde on the Expression of Adhesion Molecules in Nasal Microvascular Endothelial Cells: The Role of Formaldehyde in the Pathogenesis of Sick Building Syndrome. *Clin. Exp. Allergy* **2002**, *32*, 287–295.

(41) Hauptmann, M.; Lubin, J. H.; Stewart, P. A.; Hayes, R. B.; Blair, A. Mortality From Lymphohematopoietic Malignancies Among Workers in Formaldehyde Industries. *JNCI J. Natl. Cancer Inst.* **2003**, *95*, 1615–1623.

(42) Pinkerton, L. E.; Hein, M. J.; Stayner, L. T. Mortality among a Cohort of Garment Workers Exposed to Formaldehyde: An Update. *Occup. Environ. Med.* **2004**, *61*, 193 – 200.

(43) Zhang, L.; Steinmaus, C.; Eastmond, D. A.; Xin, X. K.; Smith, M. T. Formaldehyde Exposure and Leukemia: A New Meta-Analysis and Potential Mechanisms. *Mutat. Res. Mutat. Res.* **2009**, *681*, 150–168.

(44) Korotcenkov, G. Current Trends in Nanomaterials for Metal Oxide-Based Conductometric Gas Sensors: Advantages and Limitations. Part 1: 1D and 2D Nanostructures. *Nanomater. (Basel, Switzerland)* **2020**, *10*, 1392.

(45) Barsan, N.; Schierbaum, K. *Gas Sensors Based on Conducting Metal Oxides: Basic Understanding, Technology and Applications*; Elsevier, **2018**.

(46) Ihokura, K.; Watson, J. *The Stannic Oxide Gas Sensor Principles and Applications*; CRC Press, **2017**.

(47) Lu, S.; Hu, X.; Zheng, H.; Qiu, J.; Tian, R.; Quan, W.; Min, X.; Ji, P.; Hu, Y.; Cheng, S.; et al. Highly Selective, Ppb-Level Xylene Gas Detection by Sn_2^+-Doped NiO Flower-Like Microspheres Prepared by a One-Step Hydrothermal Method. *Sensors* **2019**, *19*, 2958.

(48) Zhang, H.-J.; Meng, F.-N.; Liu, L.-Z.; Chen, Y.-J. Convenient Route for Synthesis of Alpha-Fe_2O_3 and Sensors for H_2S Gas. *J. Alloys Compd.* **2019**, *774*, 1181–1188.

(49) Carpenter, M. A.; Mathur, S.; Kolmakov, A. *Metal Oxide Nanomaterials for Chemical Sensors*; Springer Science & Business Media, **2012**.

(50) Bai, H.; Shi, G. Gas Sensors Based on Conducting Polymers. *Sensors (Basel).* **2007**, *7*, 267–307.

(51) Persaud, K. C. Polymers for Chemical Sensing. *Mater. Today* **2005**, *8*, 38–44.

(52) Fratoddi, I.; Venditti, I.; Cametti, C.; Russo, M. V. Chemiresistive Polyaniline-Based Gas Sensors: A Mini Review. *Sensors Actuators B Chem.* **2015**, *220*, 534–548.

(53) Gao, N.; Yu, J.; Tian, Q.; Shi, J.; Zhang, M.; Chen, S.; Zang, L. Application of PEDOT:PSS and Its Composites in Electrochemical and Electronic Chemosensors. *Chemosensors* **2021**, *9*, 79.

(54) Slater, J. M.; Watt, E. J.; Freeman, N. J.; May, I. P.; Weir, D. J. Gas and Vapour Detection with Poly(Pyrrole) Gas Sensors. *Analyst* **1992**, *117*, 1265–1270.

(55) Schedin, F.; Geim, A. K.; Morozov, S. V.; Hill, E. W.; Blake, P.; Katsnelson, M. I.; Novoselov, K. S. Detection of Individual Gas Molecules Adsorbed on Graphene. *Nat. Mater.* **2007**, *6*, 652–655.

(56) Yuan, W.; Shi, G. Graphene-Based Gas Sensors. *J. Mater. Chem. A* **2013**, *1* , 10078–10091.

(57) Kumar, B.; Min, K.; Bashirzadeh, M.; Farimani, A. B.; Bae, M.-H.; Estrada, D.; Kim, Y. D.; Yasaei, P.; Park, Y. D.; Pop, E. The Role of External Defects in Chemical Sensing of Graphene Field-Effect Transistors. *Nano Lett.* **2013**, *13*, 1962–1968.

(58) Kang, I.-S.; So, H.-M.; Bang, G.-S.; Kwak, J.-H.; Lee, J.-O.; Won Ahn, C. Recovery Improvement of Graphene-Based Gas Sensors Functionalized with Nanoscale Heterojunctions. *Appl. Phys. Lett.* **2012**, *101*, 123504.

(59) Hafiz, S. M.; Ritikos, R.; Whitcher, T. J.; Razib, N. M.; Bien, D. C. S.; Chanlek, N.; Nakajima, H.; Saisopa, T.; Songsiriritthigul, P.; Huang, N. M. A Practical Carbon Dioxide Gas Sensor Using Room-Temperature Hydrogen Plasma Reduced Graphene Oxide. *Sensors Actuators B Chem.* **2014**, *193*, 692–700.

(60) Han, T.; Nag, A.; Chandra Mukhopadhyay, S.; Xu, Y. Carbon Nanotubes and Its Gas-Sensing Applications: A Review. *Sensors Actuators A Phys.* **2019**, *291*, 107–143.

(61) Schroeder, V.; Savagatrup, S.; He, M.; Lin, S.; Swager, T. M. Carbon Nanotube Chemical Sensors. *Chem. Rev.* **2019**, *119*, 599–663.

(62) Hosseini, S. H.; Entezami, A. A. Conducting Polymer Blends of Polypyrrole with Polyvinyl Acetate, Polystyrene, and Polyvinyl Chloride Based Toxic Gas Sensors. *J. Appl. Polym. Sci.* **2003**, *90*, 49–62.

(63) Pandis, C.; Peoglos, V.; Kyritsis, A.; Pissis, P. Gas Sensing Properties of Conductive Polymer Nanocomposites. *Procedia Eng.* **2011**, *25*, 243–246.

(64) Sun, D.; Luo, Y.; Debliquy, M.; Zhang, C. Graphene-Enhanced Metal Oxide Gas Sensors at Room Temperature: A Review. *Beilstein J. Nanotechnol.* **2018**, *9*, 2832–2844.

(65) Ansari, M. O.; Ansari, S. A.; Cho, M. H.; Ansari, S. P.; Abdel-wahab, M. S.; Alshahrie, A. Conducting Polymer Nanocomposites as Gas Sensors. **2019**, 911–940.

CHAPTER 3. MODIFYING THE SURFACE CHEMISTRY OF CARBON NANOTUBES FACILITATES THE DETECTION OF AROMATIC HYDROCARBON GASES

Content from this chapter has been reprinted with permission from:
Hodul, J. N.; Murray, A. K.; Carneiro, N. F.; Meseke, J. R.; Morris, J.; He, X.; Zemlyanov, D.; Chiu, G. T.-C.; Braun, J. E.; Rhoads, J. F.; Bryan W. Boudouris,
ACS Appl. Nano Mater. 2020, 3, 10389 – 10398.

3.1 Overview

The benzene, toluene, and xylene (BTX) compounds currently utilized in many building materials and paints have been linked to deleterious health effects, and thus, monitoring the presence of these compounds is of increasing importance with respect to public health. As such, there is a critical need for next-generation low-cost, selective, and sensitive indoor BTX sensors. Current BTX detection systems require multi-component, complex devices or require high power input to achieve BTX detection at meaningful concentrations, but this long-standing paradigm can be altered through the introduction of tailored nanomaterials. Specifically, we demonstrate a selective BTX resonant mass sensor platform that leverages the unique properties of single-walled carbon nanotubes (SWCNTs) treated with hydrochloric acid (HCl) and hydroxylamine hydrochloride (HHCl), as the resultant surface chemistry and nanostructure provides specific BTX response. That is, SWCNTs are used in this case due to their high surface area that provides a robust interaction with the target gas analyte. After the SWCNTs are treated with HCl, impurities residual from the commercial synthesis of the SWCNTs are removed, which includes reducing the amount of surface iron oxide (i.e., a residual component of the catalysis used to synthesize the SWCNTs) present into iron chlorides. There is then a following HHCl treatment that leads to the reduction of iron (III) chloride to iron (II). This produces nitrous oxide gas, which provides a

means to generate in place surface functionalization of the SWCNTs; in turn, this allows for the selective adsorption of electron-dense aromatic analytes. Accordingly, these materials have selective interactions and unique responses towards each of the BTX analytes, and when these tailored nanomaterials are drop cast onto mass resonator devices, they provide for a chemically-selective mass uptake response. In turn, this provides a clear pathway towards a practical, low-cost, efficient, and reusable sensor for BTX detection based on SWCNTs.

3.2 Introduction

Aromatic hydrocarbons, a subgroup of volatile organic compounds (VOCs), are frequently contained within consumer materials used in building interiors (e.g., paints, lacquers, adhesives, and dyes) among other settings.[1] While aromatic hydrocarbons, including benzene, toluene, and xylene (BTX), have been widely used in these various settings, these compounds have been linked to long-term deleterious health effects.[2–5] Due to their organic nature, BTX components are absorbed and are widely distributed throughout the body. For instance, acute exposure to lower concentrations of BTX compounds in air (i.e., < 100 ppm) can affect the central nervous system.[6] High concentrations of BTX in air (i.e., > 700 ppm) can even lead to human fatalities.[7] Additionally, BTX compounds are linked to acute myeloid leukemia and other hematological malignancies that can have long-term deleterious effects on the health and wellbeing of humans.[8,9] As a result, these chemicals are strictly regulated and monitored in many countries.[10] Given this situation, there is a pressing need for a low-cost, energy-efficient, and high-fidelity sensing platform that is tailored to have high selectivity and sensitivity for BTX compounds.

To date, various techniques have been implemented for the detection of gas-phase BTX molecules. Metal oxide-based resistive sensors, specifically, are effective in sensing BTX species.[11–14] Though effective in the detection of aromatic hydrocarbons, metal oxide resistive

sensing requires high operating temperatures (i.e., > 200 °C), making them impractical for many common applications.[1] As such, some groups have turned their attention to nanomaterials-based platforms. For instance, recent work focused on utilizing cobalt porphyrin-functionalized TiO_2 nanoparticles as a sensing material for BTX compounds on a suspended microheater, which allowed for lowered operating temperatures.[15] These sensors, though intriguing in the metal oxide area of BTX sensing, are limited by extensive device fabrication protocols that limit the possibility of high-throughput, low-cost fabrication processes. In addition to the metal oxide approach, there has also been work completed on BTX detection utilizing polymer and metal-organic framework (MOF) materials on photonic crystal sensors, which also offer low operating temperatures, but also suffer from arduous device fabrication techniques.[16,17] Conversely, the detection of aromatic hydrocarbons at low operating temperatures and using devices fabricated in methods that are consistent with solution-processing protocols has occurred with polymer-functionalized quartz crystal microbalances (QCMs).[18–21] Additionally, QCMs have shown promise with frequency counting algorithms for the selective detection of xylene at 2,500 ppm.[22] However, these QCMs tend to be expensive or rely on humidity-sensitive detection methods, and these factors limit their potential to be incorporated into existing buildings and interior spaces. Moreover, photoionization detectors (PIDs), amperometric detectors, semiconductors (i.e., chemiresistive sensors), flame ionization detectors (FIDs), and portable gas chromatographs/mass spectrometers (GC/MS) have been implemented for the detection of aromatic hydrocarbons.[23–29] These sensors, though sensitive to BTX, lack selectivity and durability, and have high power consumption and cost.[30] Therefore, there exists a critical need for a sensor platform that can provide high chemical sensitivity and selectivity among BTX analytes without compromising reusability, cost, and power metrics.

In order to satisfy these demands, sensor platforms utilizing single-walled carbon nanotubes (SWCNTs) are used extensively in gas sensing applications due to their ability to provide a robust interaction with the target gas analyte and high chemical stability.[31] This strong interaction is attributed to the high surface area of the SWCNTs (> 1500 $m^2 g^{-1}$) and high surface area-to-volume ratio.[32] However, when incorporating these SWCNTs into a sensing platform to target specific analytes, such as BTX, these sensors must meet certain criteria. A practical and efficient BTX gas sensor should offer: (i) high sensitivity and selectivity; (ii) a fast response time to BTX exposure and recovery time when BTX is removed (i.e., ~1 s); (iii) a low operating temperature (i.e., near-room temperature) and temperature-independent operation; and (iv) chemical and device stability upon cycling.[33,34] To meet these sensor metrics, these nanomaterials are typically chemically-modified with various functional groups, polymers, and metal oxide nanoparticles to improve their selectivity and sensitivity to target analyte gases.[35–38] These chemical modifications allow certain SWCNT-based devices to meet the sensor criteria and provide the ability to sense target analytes selectively; however, these modifications can be costly due to the expensive functional chemistries utilized. Thus, creating a sensor platform that leverages the nanoscale advantages of SWCNTs and that satisfies the necessary sensing criteria with little to no additional cost of added materials has great value in the sensing field.

Here, a resonant mass sensor is coated with SWCNTs and then chemically treated with an inexpensive and commonly-used hydroxylamine hydrochloride (HHCl) reagent to dope the SWCNTs in a single step (Figure 5). This doping allows for the selective detection of BTX compounds. This never-before-reported chemical functionalization protocol, in combination with the resonant mass sensor platform, allows for low-cost and practical BTX detection. In comparison to other SWCNT sensing counterparts, this sensor offers high sensitivity, low operating

temperature, small size, and long-term cyclability. Using Pierce oscillators implemented with a frequency counting algorithm, the simultaneous monitoring of 16 sensors, each with a temporal resolution of 1 s and frequency resolution of ~1 Hz, is achieved. This Pierce oscillator system with this functional chemistry allows for selective detection of BTX compounds. These functional materials require low-energy input, and they do not require humidity to perform unlike other functional materials on QCMs. Moreover, this resonant mass sensor platform offers lower cost materials to manufacture and is smaller in size, requires less cumbersome electronics and controls to perform tests, and is more portable than a standard QCM. Additionally, the chemistry and nanoscale structure of the SWCNTs allows for detection of aromatic hydrocarbon analytes selectively due to an electron-withdrawing character that is associated with the SWCNTs after their treatment with HHCl. Thus, the apparent selective adsorption of BTX analytes is related to the electron density in each of the aromatic structures of each target analyte. The surface treatment creates minor surface alterations in the SWCNTs without any additional device manipulations to achieve BTX detection. Thus, this nanomaterials platform offers an easily functionalized, low-cost, low-power, multi-channel sensing array capable of quick and reliable detection. The resonant mass sensor platform with this functional chemistry offers advantages by creating a low-cost and selective alternative to BTX detection without the need for a high-power input, extensive chemical treatment, or device manipulation protocols. Thus, this work provides a feasible and reliable surface treatment method that, when paired with pre-existing sensor platforms, can offer robust BTX selective detection. The ease of surface treatment allows for high responses to aromatic analytes and provides a novel chemical functionalization protocol for an important class of functional nanomaterials.

Figure 5. Schematic of the device chemical functionalization protocol.

3.3 Experimental Information

3.3.1 Materials

All chemicals were purchased from Sigma-Aldrich, and they were used as received unless otherwise noted. High-pressure carbon monoxide (HiPco) synthesized SWCNTs were purchased from ChemElectronics Inc., and they were treated by exposing them to air at 300 °C. Then, the SWCNTs were washed with concentrated (i.e., 38%, by weight) hydrochloric acid (HCl) in water to remove some of the remaining metal catalysts prior to use.[39,40] After acid treatment the SWCNTs were then isolated via centrifugation. SWCNT inks were prepared by dispersing the SWCNTs in a tetrahydrofuran (THF) solution at a loading of 0.1 mg mL^{-1} using a probe tip sonicator (Qsonica, LLC) producing a murky dark yellow solution. Hydroxylamine hydrochloride (HHCl) was stored under nitrogen conditions in a glove box upon receipt and all the solutions containing HHCl were prepared in the glove box.

3.3.2 General Methods

Raman spectra were obtained using a Horiba/Jobin-Yvon LabRAMHR800 confocal microscope Raman spectrometer equipped with a 633 nm He:Ne laser. For these spectra, the SWCNT samples were fabricated by depositing 0.5 mL of a 0.1 mg mL^{-1} SWCNT suspension onto a glass microscope slide and drying the slide under vacuum ($P \leq 0.4$ Torr) for 30 min to remove

solvent. Then, the spectra were acquired before and after treatment with HHCl. For samples analyzed after the HHCl treatment, after the vacuum drying step, the SWCNT-coated substrates underwent a 1 μL treatment of either 1 mg mL^{-1} or 100 mg mL^{-1} HHCl solution. These samples were then dried under vacuum again prior to testing. Optical microscopy images were acquired using a 2× telecentric lens with a color USB camera (Edmund Optics, EO-1312). The same sample preparation protocol that was utilized in obtaining the Raman spectra was utilized for this imaging as well. A Hitachi S-4800 Field Emission scanning electron microscope (SEM) was utilized to image the SWCNTs. For these images, 0.5 mL of the 0.1 mg mL^{-1} SWCNT solution were printed on silicon dioxide substrates and dried under vacuum for 24 h. For samples that were treated with HHCl, the HHCl was pipetted on top of the dried SWCNTs, and then these films were dried under vacuum for another 24 h. All the films were then coated with 20 nm of carbon prior to imaging using a SPI carbon sputter coater. A Kratos Axis Ultra DLD imaging X-ray photoelectron spectrometer with a monochromatic Al Kα (E = 1486.6 eV) was utilized for X-ray photoelectron spectroscopy (XPS) measurements, and these data were acquired while the sample was under high vacuum (P ~10^{-9} Torr). Casa XPS software was utilized for all the XPS data analyses.

3.3.3 Device Instrumentation

The sensor array in this work consisted of 16 Pierce oscillators (Figure 6a). Each oscillator consisted of an inverter, two load capacitors (C_1 = 22 pF and C_2 = 22 pF), one feedback resistor (R_1 = 2 MΩ), one isolation resistor (R_2 = 510 Ω), and a quartz crystal resonator (Kyocera Corp., CX3225) with the cap removed, where the capacitance of the resonator was C_L = 12 pF. The crystal oscillator driver (Texas Instruments, SN74LVC1GX04) provided the circuit with the Pierce oscillator inverter, as well as three additional inverters, which converted the oscillator output signal to a square wave. A Field Programmable Gate Array (FPGA) was implemented as a frequency

counter to track the oscillation frequency of each oscillator in parallel. This resulted in 16 parallel frequency measurements every second with a frequency resolution of 1 Hz. To improve experimental efficiency, the 16 resonators were isolated on a disposable resonator board. This was mechanically-coupled to an instrumentation board that contained the remaining elements of the oscillator circuitry. Additionally, a labeled picture of the testing instrumentation is provided in Supporting Information Figure 20.

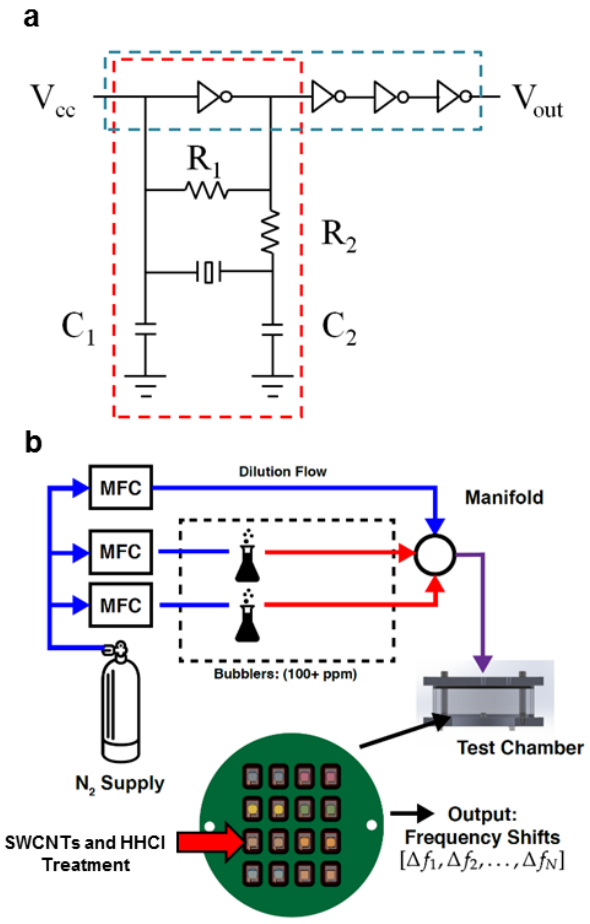

Figure 6. (a) Schematic representation of the Pierce oscillator circuit with the oscillator (outlined by red dashed lines) and a series of inverters (outlined by blue dashed lines). C_1 and C_2 are load capacitors. R_1 is a feedback resistor, and R_2 is an isolation resistor. V_{cc} is the supply voltage, and V_{out} is the output voltage that enters the FPGA frequency counter. (b) Experimental setup utilized to test the sensors exposed to the target gases. The functionalized oscillators were evaluated in a chamber filled with analyte gas from bubblers connected to mass flow controllers and diluted with a stream of nitrogen.

3.3.4 Device Functionalization

SWCNTs were functionalized with HHCl using an inkjet printer in a manner that has been reported previously.[41] In these experiments, 1 μL of the 0.1 mg mL^{-1} SWCNT in tetrahydrofuran (THF) ink was drop cast on to the quartz crystal resonator surface. The devices were left to dry under vacuum ($P \leq 0.4$ Torr) for at least 30 min. Subsequently, 5 nL of a solution of HHCl in methanol (1 mg mL^{-1}) were printed on the resonator surface using a BioFluidix PipeJet P9 piezoelectrically-actuated pipette. After functionalization, the resonator board was stored under vacuum for at least 24 h to remove any residual solvent.

3.3.5 Device Testing

Testing of the devices was performed using the experimental setup shown in Figure 6b. Prior to sensor testing, the resonator board was attached to the instrumentation board, and the 9.5 cm diameter chamber was sealed. The chamber was secured with an in-line flow distribution system to achieve the desired concentrations of the analytes. Nitrogen was connected to a series of mass flow controllers (MFCs) in parallel. Some of the MFCs (MKS 1480A, 40 cm^3 min^{-1}) were connected to bubblers (ChemGlass, AF-0085) with 10 mL of the desired testing analyte. An additional line (MKS 1179A, 500 cm^3 min^{-1}) remained as a pure nitrogen source. The three inlets were connected to a manifold, the output of which was connected directly to the chamber inlet. The chamber was flushed with nitrogen at a flow rate of 500 cm^3 min^{-1} to create an inert environment as the baseline for experimentation. Subsequently, the analyte gases were injected into the chamber to achieve the reported concentrations. Simultaneously, the oscillation frequencies were recorded once per second with a 1 Hz resolution using the myRio FPGA and an in-house LabVIEW program. For all tests, at the beginning of the test, a longer break-in period was used such that the resonators could acclimate to the humidity and temperature of the testing

chamber. This period consisted of a 60-minute pulse of nitrogen at a pressure of 1 atm and a temperature of 25 °C.

3.4 Results and Discussion

SWCNT-based sensor platforms typically require chemical modifications or specific deposition methods to adequately meet sensing metrics. This chemical treatment can be expensive and require multiple chemical steps to provide selectivity and sensitivity among BTX analytes.[42-44] However, when a thin film of SWCNTs was treated with HHCl there was an observed selective response to the BTX analytes. Figure 7a presents the oscillation frequency responses of the SWCNT-coated resonant mass sensors after being treated with 1 mg mL^{-1} HHCl solutions. This surface chemistry allows for the detection of BTX compounds with unique concentration-shift relationships. The average sensitivity of the device to benzene, toluene, and xylene is 136, 35, and 23 ppm Hz^{-1}, respectively.

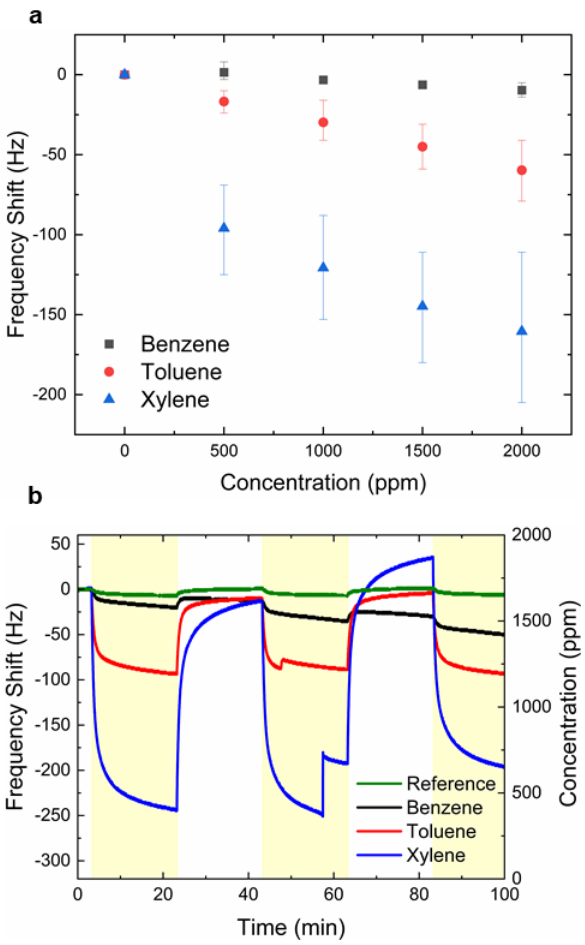

Figure 7. (a) The average shift in oscillation frequency of devices functionalized with SWCNTs and 1 mg mL-1 of HHCl exposed to either benzene, toluene, or xylene, as a function of increasing concentration (500 ppm ≤ C ≤ 2,000 ppm). The error bars represent the maximum and minimum observed shifts across 4 trials. (b) The change in oscillation frequency of a device functionalized with SWCNTs and 1 mg mL^{-1} of HHCl exposed to 2,000 ppm of BTX analytes as a function of time. The response of an unfunctionalized device (reference) exposed to 2,000 ppm of benzene is shown in green for comparison. The yellow bars indicate the concentration of the analyte present and the white bars indicate a nitrogen-only environment.

The sensor shows specific oscillation frequency responses to BTX analytes, and this response only occurs when the treated SWCNTs are present on the resonator (i.e., the reference channel resonators did not show a meaningful response to BTX). The response time and recovery time of the sensor was determined by calculating a time constant (τ), the time it takes the sensor to reach approximately 63.2% of its final value (i.e., either on the fall for the response time or the rise for the recovery time). Here, the average response time of the sensor can be characterized by

a time constant of 31 s ± 15.3 s with an average recovery time constant of 49 s ± 17.2 s. In this work, selectivity is defined as a characteristic response in the magnitude of oscillation frequency shift for individual analytes at a single concentration. Therefore, it is noted that this sensor cannot be used to distinguish between BTX analytes when both are present under testing conditions at the same time (e.g., xylene and benzene both being present in the testing chamber at same time). Moreover, the responses on all the SWCNT-coated oscillators were rapid and reversible, which indicated target analytes were physically adsorbing to the devices. Importantly, the SWCNT-based sensors showed stability over multiple cycles, as the baseline signal of the resonators quickly recovered after desorption of the target analyte (Figure 7b). However, there was an observed jump in oscillation frequency when returning to the baseline value (Figure 7b). These jumps in oscillation frequency are due to an unknown frequency counter glitch. Occasionally, a jump in frequency of a single channel is seen. This is believed to be a control electronics concern exclusively and not an artifact of the functional material or sensor. Additionally, long term stability of the functionalized resonator was determined by testing with five 30-minute pulse cycles of xylene at a concentration of 2,000 ppm (Supporting Information Figure 19). The measured frequency shift from resonators functionalized with SWCNTs and HHCl varies only approximately 10% from the initial pulse. These initial results, though intriguing, did not provide a fundamental understanding of how the sensor was responding to these target analytes.

Exposing the SWCNT thin films to the HHCl solution resulted in a decrease in the concentration of iron impurities present in the carbon nanotubes. Iron is a metal catalyst utilized in the HiPco SWCNT synthesis and, even after purification, can remain in the carbon nanotubes.[45] When chemical modifications occurred on the carbon nanotube surfaces there was typically an observed characteristic change in the Raman spectra,[46] and this was observed in the present work

as well (Figure 8). In particular, the effect of a chemical interaction with the SWCNTs alters the doping levels of SWCNTs, and in turn, alters the carbon nanotube sensing ability.[44] These doping effects can be predicted based on the shifts in the G-band ($\lambda = 1591.4\ cm^{-1}$) in the Raman spectrum. The G-band characteristically describes the sp^2 carbon bond character in these graphitic materials.[47] In the samples that underwent the HHCl treatment, no shifts in this G-band were observed. This indicated that no significant doping effects occurred on the surface of the SWCNTs. However, the D-band ($\lambda = 1308.5\ cm^{-1}$) showed an appreciable decrease as the amount of HHCl added to the films increased. This D-band is associated with the stretching of the sp^3 carbon bond character.[48] This appreciable decrease in the D-band indicated that there was a decrease in the sp^3 C−C bond character. This is likely due to a decrease in iron impurities in the SWCNTs upon exposure to HHCl as these types of impurities can alter the amount of sp^3 C-C bond character in a carbon nanotube by distorting the sp^2 C-C bond character.[46] Additionally, this could also be due to layering effects that can product edge defects in the carbon network.[49,50] When the iron chlorides are formed, they can become layered within the carbon nanotubes. Upon reduction of the iron chlorides with HHCl, there is an observed decrease in the D-band because the layering defects are disrupted. Hence, there is a decrease in the D band region since more sp2 planar type character is expressed after the defects are removed.

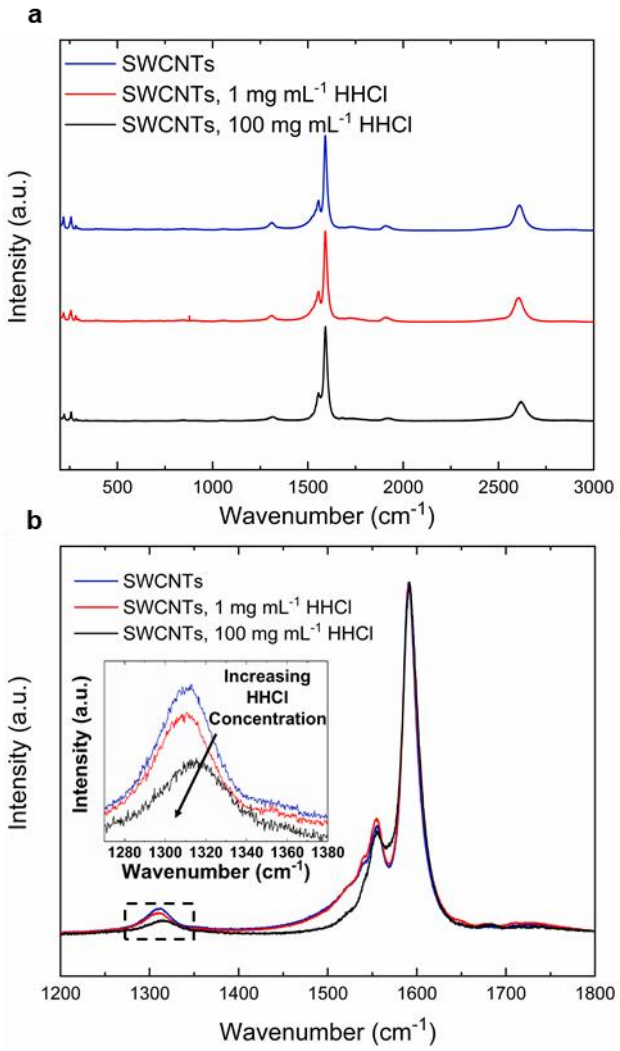

Figure 8. (a) Raman spectra comparison of SWCNTs alone (blue), after 1 mg mL^{-1} HHCl treatment (red), and after 100 mg mL^{-1} HHCl treatment (black). (b) Zoomed overlap view of Raman spectra of the G-band (λ = 1591.4 cm^{-1}) and D-band (λ = 1308.5 cm^{-1}) after the different treatments had been performed.

Moreover, when treating the SWCNTs with HHCl, there was an increase in the nitrogen signature associated with the SWCNTs according to the collected XPS data (Figure 9). From the C1s XPS spectrum, five peaks centered at 284.5 eV, 285.3 eV, 285.7 eV, 286.5 eV, and 288.9 eV are observed, corresponding to C–C sp^2, C–C sp^3, C–N, C–O, and $FeCO_3$ groups, respectively.[51–53] After treatment with the HHCl, the intensities of C–O peaks decrease slightly, which was accompanied by an increase of the nitrogen carbon peak (C–N), revealing that the oxygen-

containing groups were slightly removed or replaced with corresponding nitrogen-containing groups. This increasing C-N character is consistent with previous work describing the reduction of graphene oxide materials using HHCl.[53]

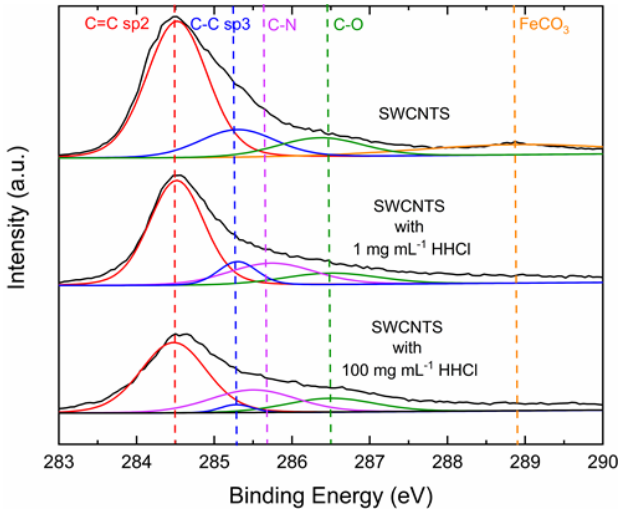

Figure 9. XPS spectra of the C1s level of SWCNTs with increasing concentration of HHCl treatments.

There was a decrease in the C-C sp^2 and sp^3 carbon networks, which could be attributed to the incorporation of a higher concentration of non-carbonaceous materials being present around the carbon nanotubes (i.e., residual HHCl). Additionally, there was a clear loss of a $FeCO_3$ peak at 288.9 eV. This peak reduction most likely correlates to iron carbonates, which are reduced upon exposure to HHCl.[54] Such a trend is consistent with the Raman spectroscopy (*vide supra*) where there was a substantial change in the D band (1308.5 cm^{-1}), as shown in Figure 8b. However, this does indicate the presence of iron in the sample even after purification. In addition to these spectroscopic results, SEM micrograph images show an ordering of the HHCl salts when the SWCNTs are present. That is, SWCNTs cast without the HHCl treatment do not contain any regular nanostructure (Supporting Information Figure 16). Clear nano- and microstructures only appear when the SWCNTs are treated with the HHCl (Supporting Information Figure 17 and

Figure 18). Overall, the observation of increasing C-N bond character in the XPS and decreasing of iron impurities upon HHCl treatment indicates that the iron present had an impact on the sensitivity and selectivity of the device.

The high sensitivity and selectivity among BTX analytes observed in the high-performance sensors described above is likely based on the ability of the HHCl to reduce the iron impurities in the SWCNTs; in turn, this allows for the in-place synthesis of NO_2 functional groups on the surfaces of the carbon nanotubes. This reduction causes an increased formation of C-N type bond character, as observed in the XPS spectra. Residual iron metal in the HiPco SWCNTs, when heated in ambient conditions, can oxidize, and this creates a mixture of iron oxides, consisting of iron(II) and iron(III) oxides. These iron oxides, when exposed to the HCl in the purification process, can be converted into iron chlorides. Then, the SWCNTs containing iron(III) chlorides undergo a redox reaction when they are exposed to the HHCl treatment.[55] This redox reaction produces an NO_2 gas byproduct that can bind to the surface of the SWCNTs and create an electron-poor character in the graphene sheets (Figure 10).[56–59] The change in electron density in the SWCNTs provides the selectivity among BTX analytes. As the electron density in the target analytes increases, there is better sp^2 π-stacking due to the π accepting character in the SWCNTs and the π donor character in the aromatic analytes. Therefore, the treatment of SWCNTs with HHCl provides a reliable and cost-effective selective sensor surface treatment chemistry.

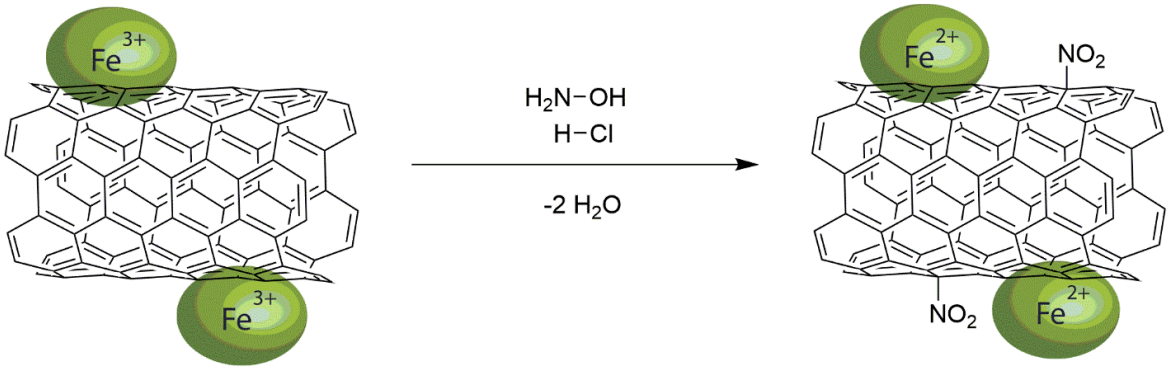

Figure 10. Proposed mechanism for the production of NO_2 functional groups upon treatment with HHCl.

To evaluate this mechanism further, 16 devices were functionalized using combinations of two types of 0.1 mg mL^{-1} SWCNTs in THF (pure and impure) and two types of 1.0 mg mL^{-1} HHCl conditions (with and without treatment). Pure SWCNTs were treated with HCl prior to testing. "HHCl with" or "without" indicates whether the SWCNTs were treated with HHCl prior to testing. A representative response of these four functionalized types of devices and an unfunctionalized device under exposure to 2,000 ppm of xylene is shown in Figure 11. The oscillators functionalized with pure SWCNTs and with HHCl treatment exhibited the largest shift in oscillation frequency to 2,000 ppm xylene of 61.6 Hz. Additionally, these devices had the most consistent device-to-device performance. Therefore, SWCNTs containing iron must have iron(III) chlorides present to produce an adequate response. As shown in Figure 11, without the HCl treatment (impure) there is no formation of iron chlorides, and the device has little to no response to xylene (red and black signals in Figure 11). With the HCl treatment (pure) there is an increase in sp^2 character in the SWCNTs graphene sheets resulting in a more uniform sp^2 hybridized surface and some non-covalent response to xylene. However, it is not until HHCl treatment following the HCl treatment that there is a production of the NO_2 gas to chemically alter the SWCNTs and provide the enhanced response to xylene (magenta line in Figure 11).

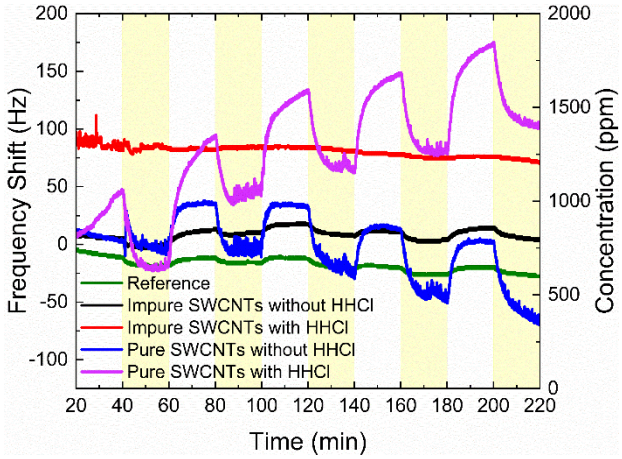

Figure 11. The oscillation frequency of an oscillator functionalized with different combinations of 0.1 mg mL^{-1} SWCNTs and 0.2 mg mL^{-1} HHCl exposed to 2,000 ppm xylene. Impure SWCNTs were not treated with any HCl prior to testing. These combinations consisted of no chemistry added on the device (reference), impure SWCNTs without the HHCl treatment, impure SWCNTs with the HHCl treatment, pure SWCNTs without the HHCl treatment, and pure SWCNTs with the HHCl treatment. The yellow bars indicate the corresponding concentration of xylene in the testing chamber and the white bars indicate a nitrogen-only environment.

To determine if this electron-poor character existed in our SWCNTs, we evaluated other target aromatic analytes (Figure 12). This consisted of electron-rich aromatic compounds (i.e., trimethylbenzene, anisole, and aniline) being evaluated while xylene was used as a reference case analyte. During testing, the electron-rich analytes encounter the electron-poor SWCNTs, and the resonators show an enhanced uptake of the electron-rich analytes relate to the xylene reference. That is, aromatic compounds with high electron densities show a unique frequency response as they interact with the chemically treated SWCNTs. Anisole, xylene, aniline, and trimethylbenzene showed average frequency shifts of 11.7 Hz, 14.7 Hz, 57.7 Hz, and 177.7 Hz, respectively, when fed at a concentration of 750 ppm. This supports the idea that the electron-withdrawing character created in the SWCNTs upon treatment with HHCl is indeed the reason for selectivity among aromatic analytes. The proper calibration of the device to each specific analyte allows for the chemically-selective detection of each compound, which demonstrates the versatility and applicability of this sensing platform.

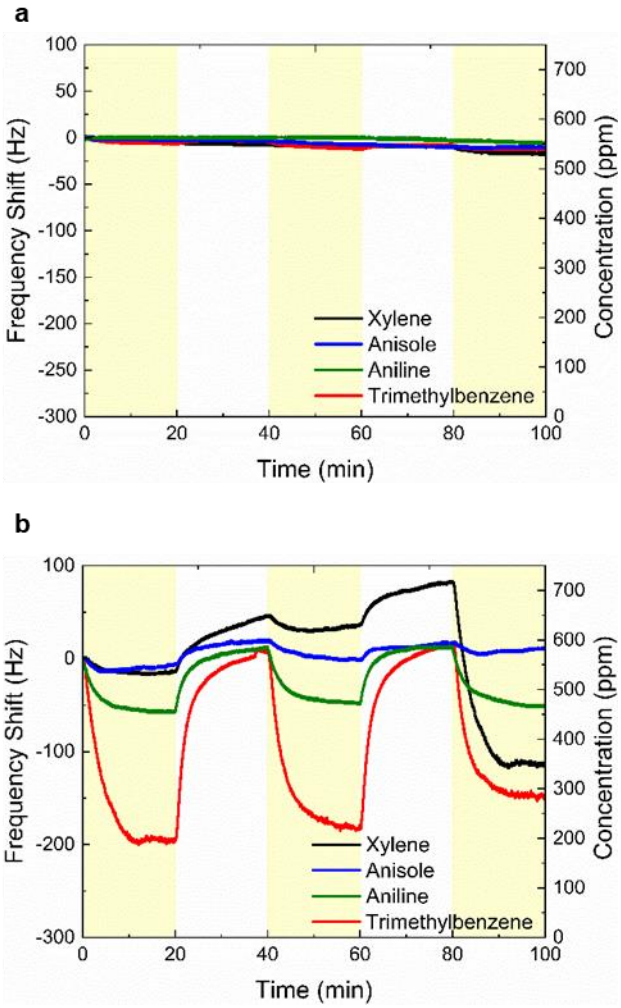

Figure 12. The shift in oscillation frequency of (a) an unfunctionalized oscillator and (b) an oscillator functionalized with 1 mg mL^{-1} HHCl and SWCNTs as referenced from the initial oscillation frequency of devices exposed to 750 ppm of xylene, anisole, aniline, and trimethylbenzene with respect to time. The yellow bars indicate the concentration of the analyte with a background of nitrogen.

The functionalized resonators showed responses to aromatic hydrocarbons in relative humidity environments ranging from 0% to 80% while air was used as the carrier gas. Under these conditions, the SWCNT-based sensors showed meaningful responses to 2,000 ppm of xylene with average frequency shifts of 22.1 Hz ± 1 Hz for the $0\% \leq RH \leq 60\%$ relative humidity levels (Figure 13). The responses remained reliable until the 80% relative humidity level where the average frequency dropped to 16.8 Hz. Once reaching the 80% relative humidity level, there was an

observed downward drift, which we speculate was due to the accumulation of moisture on the surface of the resonator. This moisture accumulation caused a change in the oscillation frequency as a function of time. However, these results do show the applicability and practical performance of the surface functionalization chemistry in combination with this resonant mass sensor platform under conditions that could potentially exist in many indoor air quality monitoring scenarios.

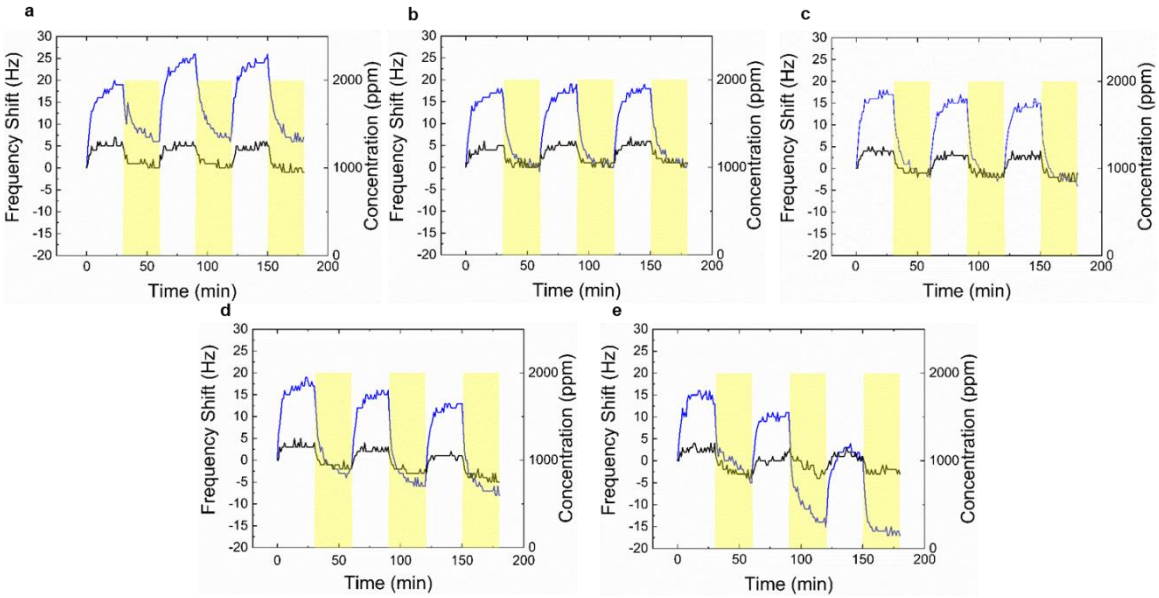

Figure 13. The change in oscillation frequency of a device functionalized with SWCNTs and 1 mg mL^{-1} of HHCl exposed to 2,000 ppm of xylene as a function of time in the presence of increasing relative humidity (RH) levels indicated by the blue line. (a) 0% RH (b) 20% RH (c) 40% RH (d) 60% RH I 80% RH. The response of an unfunctionalized device (reference) under same conditions at same time indicated by the black line. The yellow bars indicate the concentration of the xylene analyte present and the white bars indicate a nitrogen-only environment.

In addition to accounting for relative humidity, practical interior environments could contain interfering volatile organic analytes that could disrupt the response to aromatic analytes. For this reason, pulses of xylene at 2,000 ppm were added to the sensor while pulses of 500 ppm and 1,000 ppm of either ethanol or propane were injected (Figure 14). This allowed us to establish how the response to xylene was impacted in the presence of interfering VOC agents. Figure 8a

shows the response of functionalized and unfunctionalized (i.e., uncoated resonator) devices without any xylene present for comparison. Figure 14b shows the response of a functionalized device with xylene present.

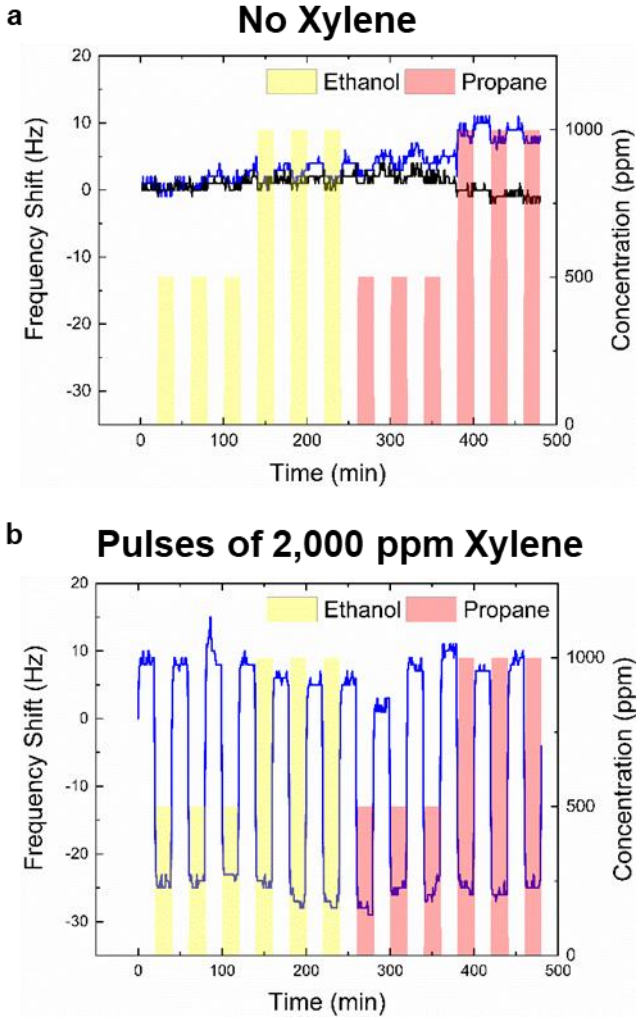

Figure 14. The change in oscillation frequency of a device functionalized with SWCNTs and 1 mg mL^{-1} of HHCl exposed to (a) ethanol and propane pulses as a function of time indicated by the blue line. The response of an unfunctionalized device (reference) under same conditions at same time is indicated by the black line. (b) Ethanol and propane with 2,000 ppm of xylene pulses as a function of time indicated by the blue line.

This sensor only showed responses when xylene was present and showed similar responses in the presence of the interfering gases relative to when the distractant gases were not present

(Figure 14b). That is, this materials combination shows a selectively responsive towards the detection of aromatic gases over other potential gas analyte chemistries. These results demonstrate that this sensor can be utilized in interior locations where interfering gases could potentially be present without disrupting BTX detection.

To determine the limit of detection capability of this platform to a specific aromatic compound, xylene, the device response at 100 ppm of xylene in nitrogen was monitored (Figure 15). The SWCNT-based device was able to show a frequency shift response to xylene at 100 ppm that is greater than the response of the reference channel with a sensitivity of 4 ppm Hz^{-1}. Additionally, this device remained reusable even at this concentration due to the adsorption and desorption pathways occurring when nitrogen gas is purged into the testing chamber. This device offers a feasible and practical surface chemistry that can selectively respond to aromatic compounds at quantitative levels.

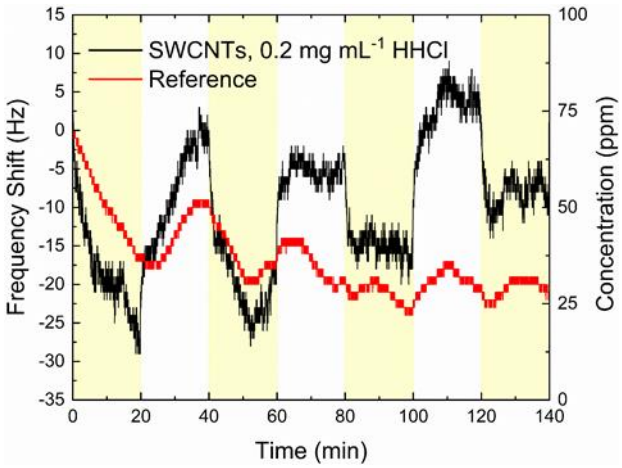

Figure 15. The oscillation frequency of an oscillator functionalized with 0.2 mg mL^{-1} of HHCl and 0.1 mg mL^{-1} SWCNTs exposed to 100 ppm of xylene in nitrogen. The black lines and red lines represent the oscillation frequency of the functionalized and unfunctionalized device (reference) in response to xylene, respectively. The yellow bars indicate the concentration of the analyte present and the white bars indicate a nitrogen-only environment.

3.5 Conclusions

This work leveraged SWCNTs treated with HHCl for enhanced selective BTX sensing when they were incorporated into a mass resonator. The HCl treatment followed by an HHCl treatment on the SWCNTs allowed for an enhanced interaction with aromatic analytes, and thus, yielded a greater response. This carbon nanotube treatment chemistry reduces iron (III) chloride and allows for electron withdrawing-type character in the SWCNTs due to the NO_2 gas released. This surface chemistry and resonant mass sensor combination provides a robust sensor and practical monitoring of BTX compounds, as well as other aromatic compounds. Furthermore, the oscillator-based approach allowed for the detection of xylene at 100 ppm. Additionally, low-cost components and functional materials integrated with additive manufacturing resulted in an efficient, reusable, economical, and feasible BTX sensing platform. This work combined a feasible chemical treatment protocol with the practical implementation of the resonant mass sensors in order to create a robust sensing platform suitable for the detection of aromatic analytes. Therefore, this effort allows for a processable chemistry to be applied in a new manner to detect aromatic

hydrocarbons using advanced nanomaterials. This nanomaterials system, when combined with a straightforward treatment protocol, offers a unique option in the sensors community to improve BTX gas detection using low-cost, high-throughput processing techniques of carbon nanotubes. Importantly, these nanomaterials easily could be incorporated into existing sensor manufacturing efforts to provide efficient and effective indoor air monitoring devices on a relatively rapid timescale.

3.6 Acknowledgments

This work was reprinted with permission from Hodul, J. N.; Murray, A. K.; Carneiro, N. F.; Meseke, J. R.; Morris, J.; He, X.; Zemlyanov, D.; Chiu, G. T.-C.; Braun, J. E.; Rhoads, J. F.; et al. Modifying the Surface Chemistry and Nanostructure of Carbon Nanotubes Facilitates the Detection of Aromatic Hydrocarbon Gases. *ACS Appl. Nano Mater.* **2020**, *3,* 10389 – 10398. This work was funded by the Center for High Performance Buildings at Purdue University (Grant Number: CHPB-44-2019).

3.7 Supporting Information Figures

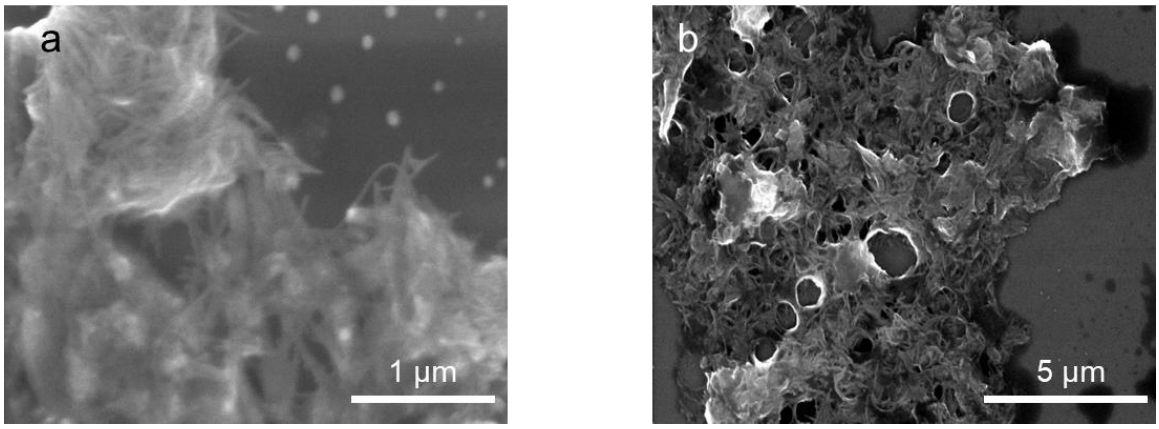

Figure 16. SEM images of SWCNTs after being drop cast onto a glass slide and dried for 12 h under vacuum. The two panels show the same film at two different magnification levels.

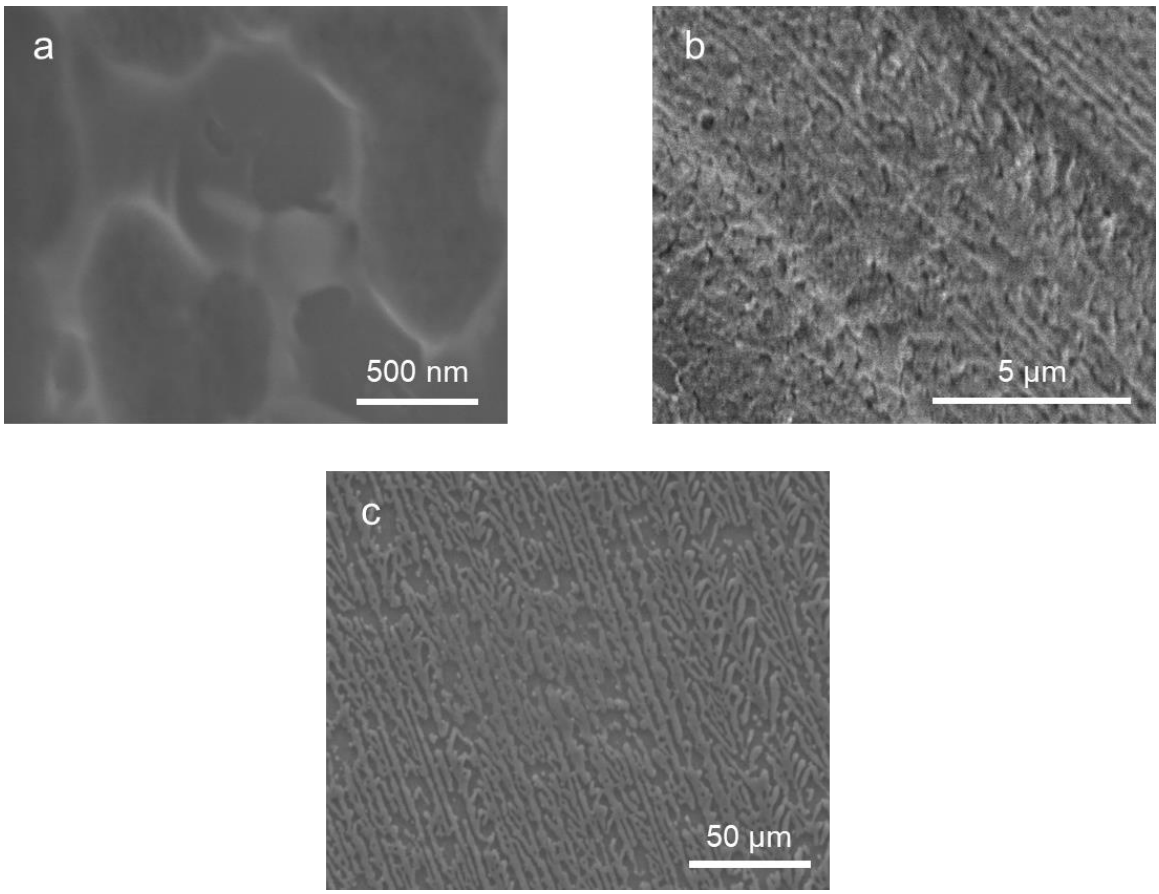

Figure 17. SEM images of SWCNT films after being cast from a 0.1 mg mL-1 SWCNTs in tetrahydrofuran solution, being treated with 1.0 mg mL-1 of HHCl in methanol, being drop cast onto a glass slide, and dried for 24 h under vacuum. The three panels show the same film at three different magnification levels.

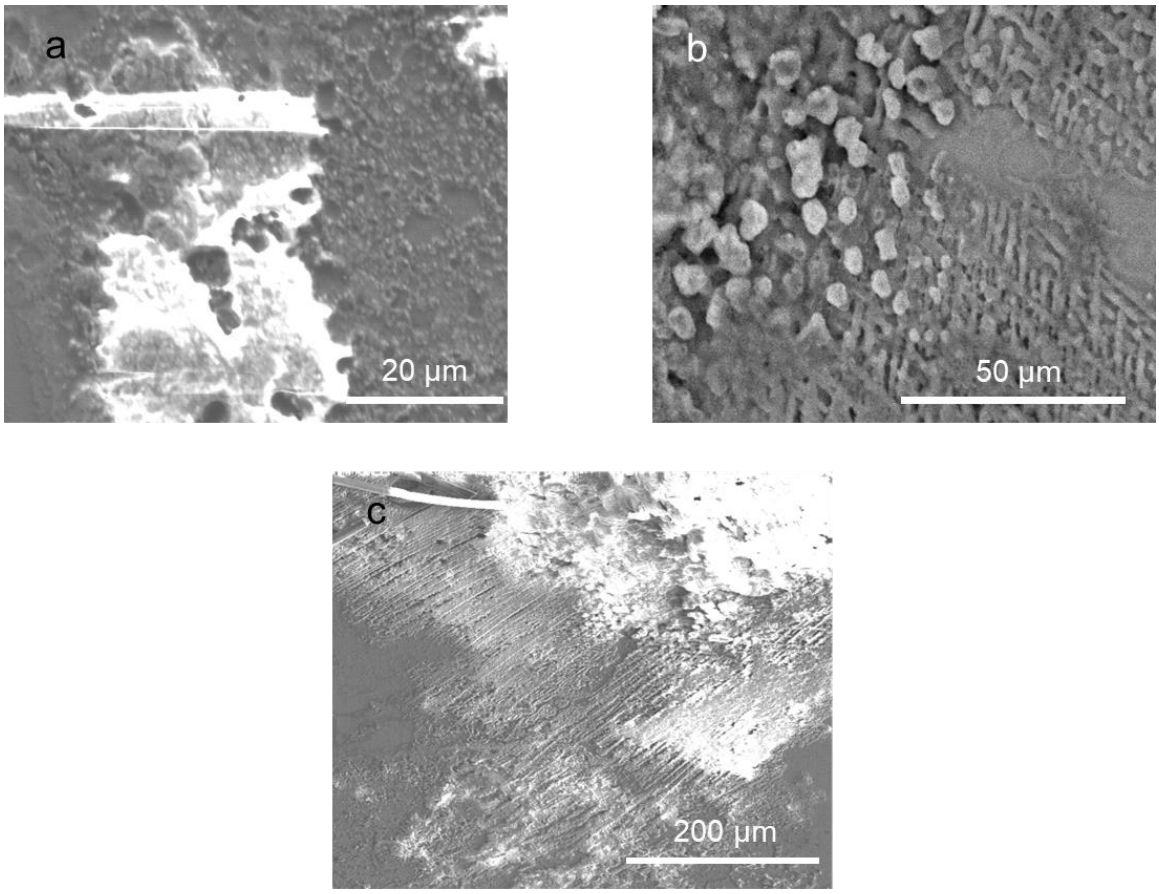

Figure 18. SEM images of SWCNT films after being cast from a 0.1 mg mL-1 SWCNTs in tetrahydrofuran solution, being treated with 100 mg mL-1 of HHCl in methanol, being drop cast onto a glass slide, and dried for 24 h under vacuum. The three panels show the same film at three different magnification levels.

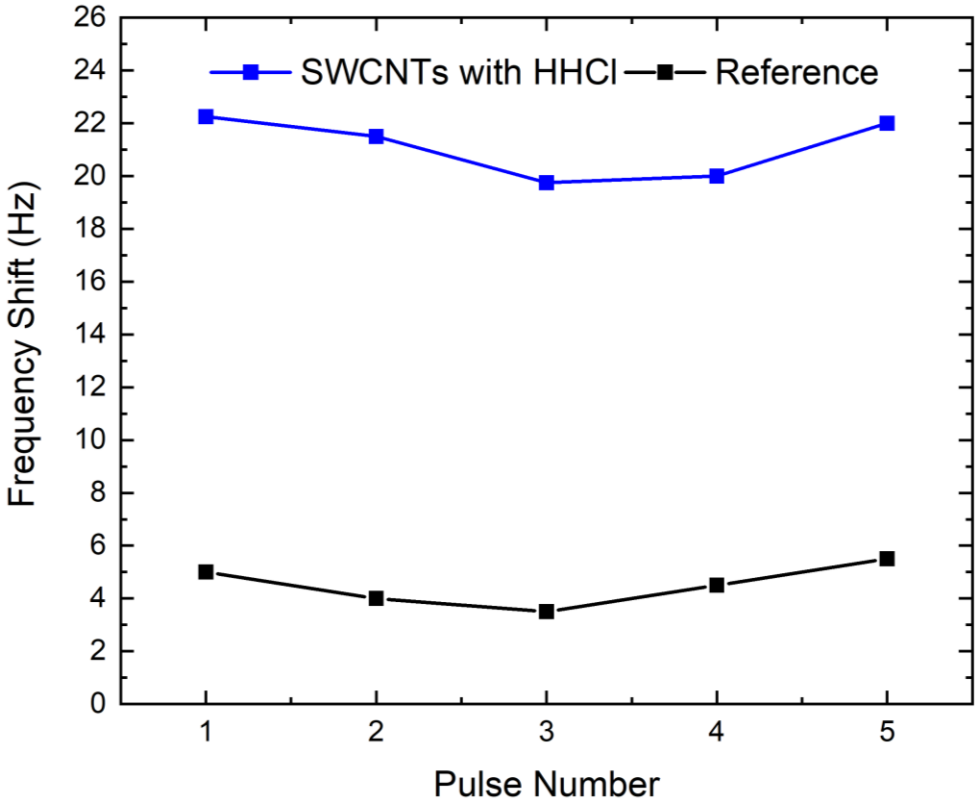

Figure 19. To demonstrate the stability of the sensor, resonators functionalized with SWCNTs and HHCl were tested with five 30-minute pulses of xylene at 2,000 ppm. The average frequency shift of the resonators for their respective pulse number was recorded. As shown in the above plot, the measured frequency shift from resonators functionalized with SWCNTs and HHCl varies only approximately 10% from the initial pulse. The response time of the sensor can be characterized by a time constant of 31 s while the recovery time was 49 s.

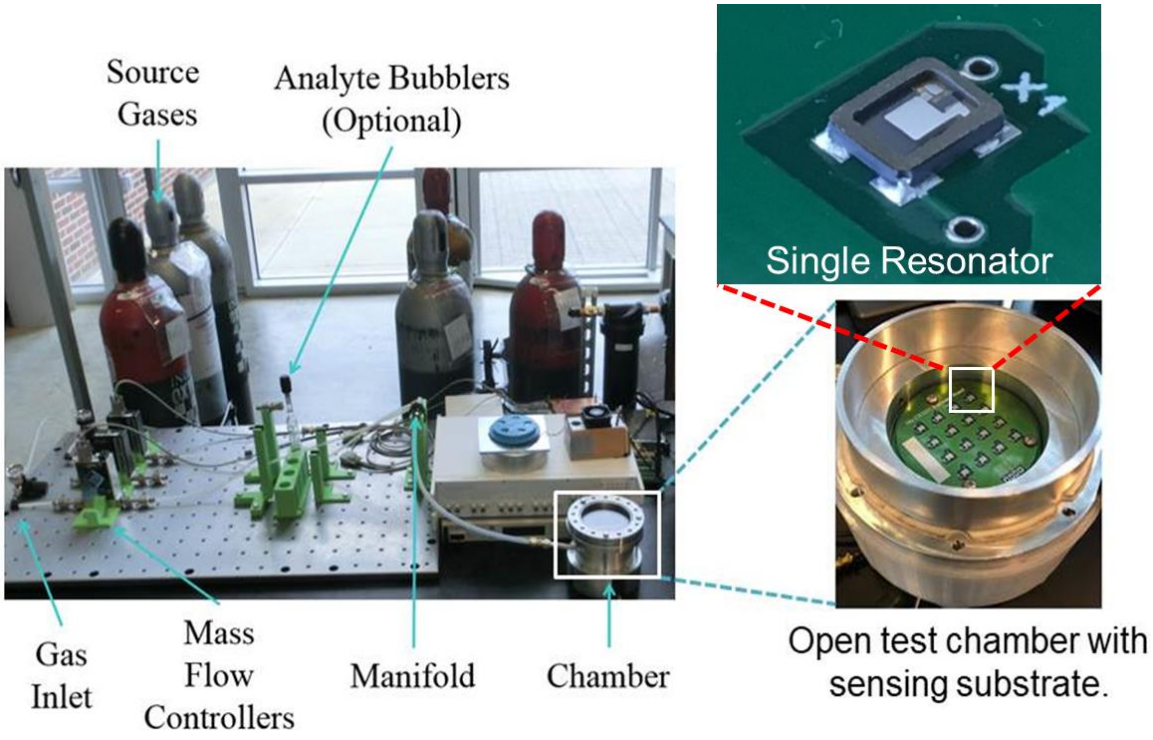

Figure 20. Experimental Testing Set-up with Resonant mass sensor board in testing chamber.

3.8 References

(1) Mirzaei, A.; Kim, J. H.; Kim, H. W.; Kim, S. S. Resistive-Based Gas Sensors for Detection of Benzene, Toluene and Xylene (BTX) Gases: A Review. *J. Mater. Chem. C* **2018**, *6*, 4342–4370.

(2) Ware, J. H.; Spengler, J. D.; Neas, L. M.; Samet, J. M.; Wagner, G. R.; Coultas, D.; Ozkaynak, H.; Schwab, M. Respiratory and Irritant Health Effects of Ambient Volatile Organic Compounds: The Kanawha County Health Study. *Am. J. Epidemiol.* **1993**, *137*, 1287–1301.

(3) Mølhave, L. Volatile Organic Compounds, Indoor Air Quality and Health. *Indoor Air* **1991**, *1*, 357–376.

(4) de Gennaro, G.; Farella, G.; Marzocca, A.; Mazzone, A.; Tutino, M. Indoor and Outdoor Monitoring of Volatile Organic Compounds in School Buildings: Indicators Based on Health Risk Assessment to Single out Critical Issues. *Int. J. Environ. Res. Public Health* **2013**, *10*, 6273–6291.

(5) Holcomb, L. C.; Seabrook, B. S. Review : Indoor Concentrations of Volatile Organic Compounds: Implications for Comfort, Health and Regulation. *Indoor Environ.* **1995**, *4*, 7–26.

(6) Chen, M.; Wang, Z.; Han, D.; Gu, F.; Guo, G. Porous ZnO Polygonal Nanoflakes: Synthesis, Use in High-Sensitivity NO_2 Gas Sensor, and Proposed Mechanism of Gas Sensing. *J. Phys. Chem. C* **2011**, *115*, 12763–12773.

(7) Gist, G. L.; Burg, J. R. Benzene—a Review of the Literature from a Health Effects Perspective. *Toxicol. Ind. Health* **1997**, *13*, 661–714.

(8) Lan, Q.; Zhang, L.; Guilan, L.; Vermeulen, R.; Weinburg, R.S.; Dosemeci, M.; Rappaport, S.M.; Shen, M.; Alter, B. P.; Wu, Y.; Rabkin, C.; Guo, W.; Chanock, S.; Hayes, R. B.; Linet, M.; Kim, S.; Yin, S.; Rothman, N.; Smith, M.T. Hematotoxicity in Workers Exposed to Low Levels of Benzene. *Science* **2004**, *306*, 1774–1776.

(9) McHale, C. M.; Zhang, L.; Smith, M. T. Current Understanding of the Mechanism of Benzene-Induced Leukemia in Humans: Implications for Risk Assessment. *Carcinogenesis* **2012**, *33*, 240–252.

(10) Lin, T.; Lv, X.; Hu, Z.; Xu, A.; Feng, C. Semiconductor Metal Oxides as Chemoresistive Sensors for Detecting Volatile Organic Compounds. *Sensors (Basel).* **2019**, *19*, 233.

(11) Qu, F.; Shang, W.; Wang, D.; Du, S.; Thomas, T.; Ruan, S.; Yang, M. Coordination Polymer-Derived Multishelled Mixed Ni–Co Oxide Microspheres for Robust and Selective Detection of Xylene. *ACS Appl. Mater. Interfaces* **2018**, *10*, 15314–15321.

(12) Kim, B.-Y.; Yoon, J.-W.; Kim, J. K.; Kang, Y. C.; Lee, J.-H. Dual Role of Multiroom-Structured Sn-Doped NiO Microspheres for Ultrasensitive and Highly Selective Detection of Xylene. *ACS Appl. Mater. Interfaces* **2018**, *10*, 16605–16612.

(13) Kim, B.-Y.; Ahn, J. H.; Yoon, J.-W.; Lee, C.-S.; Kang, Y. C.; Abdel-Hady, F.; Wazzan, A. A.; Lee, J.-H. Highly Selective Xylene Sensor Based on $NiO/NiMoO_4$ Nanocomposite Hierarchical Spheres for Indoor Air Monitoring. *ACS Appl. Mater. Interfaces* **2016**, *8*, 34603–34611.

(14) Yoon, J.-W.; Lee, J.-H. Toward Breath Analysis on a Chip for Disease Diagnosis Using Semiconductor-Based Chemiresistors: Recent Progress and Future Perspectives. *Lab Chip* **2017**, *17*, 3537–3557.

(15) Kang, Y.; Kim, K.; Cho, B.; Kwak, Y.; Kim, J. Highly Sensitive Detection of Benzene, Toluene, and Xylene Based on CoPP-Functionalized TiO_2 Nanoparticles with Low-Power Consumption. *ACS Sensors* **2020**, *5*, 754-763.

(16) Kou, D.; Ma, W.; Zhang, S.; Li, R.; Zhang, Y. BTEX Vapor Detection with a Flexible MOF and Functional Polymer by Means of a Composite Photonic Crystal. *ACS Appl. Mater. Interfaces* **2020**, 12, 11955–11964.

(17) Nair, R. V; Vijaya, R. Photonic Crystal Sensors: An Overview. *Prog. Quantum Electron.* **2010**, *34*, 89–134.

(18) Banerjee, M. B.; Pradhan, S.; Roy, R. B.; Tudu, B.; Das, D. K.; Bandyopadhyay, R.; Pramanik, P. Detection of Benzene and Volatile Aromatic Compounds by Molecularly Imprinted Polymer-Coated Quartz Crystal Microbalance Sensor. *IEEE Sens. J.* **2019**, *19*, 885–892.

(19) Rianjanu, A.; Hasanah, S. A.; Nugroho, D. B.; Kusumaatmaja, A.; Roto, R.; Triyana, K. Polyvinyl Acetate Film-Based Quartz Crystal Microbalance for the Detection of Benzene, Toluene, and Xylene Vapors in Air. *Chemosensors* **2019**, *7*, 20.

(20) Pejcic, B.; Myers, M.; Ranwala, N.; Boyd, L.; Baker, M.; Ross, A. Modifying the Response of a Polymer-Based Quartz Crystal Microbalance Hydrocarbon Sensor with Functionalized Carbon Nanotubes. *Talanta* **2011**, *85*, 1648–1657.

(21) Kimura, M.; Liu, Y.; Sakai, R.; Sato, S.; Hirai, T.; Fukawa, T.; Mihara, T. Detection of Volatile Organic Compounds by Analyses of Polymer-Coated Quartz Crystal Microbalance Sensor Arrays. *Sensors Mater.* **2011**, *23*, 359–368.

(22) Nanto, H.; Dougami, N.; Mukai, T.; Habara, M.; Kusano, E.; Kinbara, A.; Ogawa, T.; Oyabu, T. A Smart Gas Sensor Using Polymer-Film-Coated Quartz Resonator Microbalance. *Sensors Actuators B Chem.* **2000**, *66*, 16–18.

(23) Peng, F. M.; Xie, P.; Shi, Y. G.; Wang, J. D.; Liu, W.-Q.; Li, H. Photoionization Detector for Portable Rapid GC. *Chromatographia* **2007**, *65*, 331–336.

(24) Çevik, E.; Dervisevic, M.; Gavba, A.R.; Yanik-Yildirim, K.C.; Abasiyanik, M.F.; and Vardar-Schara, G. Amperometric Monooxygenase Biosensor for the Detection of Aromatic Hydrocarbons. *Sens. Lett.* **2016**, *14*, 234–240.

(25) Kadosaki, M.; Terasawa, T.; Tanino, K.; Tatuyama, C. Exploration of Highly Sensitive Oxide Semiconductor Materials to Indoor-Air Pollutants. *IEEJ Transactions on Sensors and Micromachines*. **1999**, *119*, 383–389.

(26) Liaud, C.; Nguyen, N. T.; Nasreddine, R.; Le Calvé, S. Experimental Performances Study of a Transportable GC-PID and Two Thermo-Desorption Based Methods Coupled to FID and MS Detection to Assess BTEX Exposure at Sub-ppb Level in Air. *Talanta* **2014**, *127*, 33–42.

(27) Kadosaki, M.; Yamazaki, S.; Fujiki, S.; Tanino, K.; Tatsuyama, C. Development of SnO_2-Based Gas Sensors for Detection of Volatile Organic Compounds. *IEEJ Trans. Sensors Micromachines* **2001**, *121*, 395–401.

(28) Nasreddine, R.; Person, V.; Serra, C. A.; Le Calvé, S. Development of a Novel Portable Miniaturized GC for near Real-Time Low Level Detection of BTEX. *Sensors Actuators B Chem.* **2016**, *224*, 159–169.

(29) Lahlou, H.; Vilanova, X.; Correig, X. Gas Phase Micro-Preconcentrators for Benzene Monitoring: A Review. *Sensors Actuators B Chem.* **2013**, *176*, 198–210.

(30) Spinelle, L.; Gerboles, M.; Kok, G.; Persijn, S.; Sauerwald, T. Review of Portable and Low-Cost Sensors for the Ambient Air Monitoring of Benzene and Other Volatile Organic Compounds. *Sensors* **2017**, *17*, 1520.

(31) Rigoni, F.; Tognolini, S.; Borghetti, P.; Drera, G.; Pagliara, S.; Goldoni, A.; Sangaletti, L. Enhancing the Sensitivity of Chemiresistor Gas Sensors Based on Pristine Carbon Nanotubes to Detect Low-ppb Ammonia Concentrations in the Environment. *Analyst* **2013**, *138*, 7392–7399.

(32) Li, J.; Lu, Y.; Ye, Q.; Cinke, M.; Han, J.; Meyyappan, M. Carbon Nanotube Sensors for Gas and Organic Vapor Detection. *Nano Lett.* **2003**, *3*, 929–933.

(33) Yeow, J. T. W.; Wang, Y. A Review of Carbon Nanotubes-Based Gas Sensors. *J. Sensors* **2009**, *2009*, 493904.

(34) Mabrook, M.; Hawkins, P. Benzene Sensing Using Thin Films of Titanium Dioxide Operating at Room Temperature. *Sensors* **2002**, *2*, 374–382.

(35) Janudin, N.; Abdullah, N.; Yunus, W.M.Z.W.; Yasin, M.F.; Yaacob, M.H; Saidi, N.M; Kasim, N.A.M. Effect of Functionalized Carbon Nanotubes in the Detection of Benzene at Room Temperature. *J. Nanotechnol.* **2018**, *2018*, 2107898.

(36) Das, R.; Pattanayak, A. J.; Swain, S. K. 7 – Polymer Nanocomposites for Sensor Devices. In *Woodhead Publishing Series in Composites Science and Engineering*; Jawaid, M., Khan, M. M. B. T.-P. N. for E. and E. A., Eds.; Woodhead Publishing, **2018**, 205–218.

(37) Kerdcharoen, T.; Wongchoosuk, C. 11 – Carbon Nanotube and Metal Oxide Hybrid Materials for Gas Sensing. In *Woodhead Publishing Series in Electronic and Optical Materials*; Jaaniso, R., Tan, O. K. B. T.-S. G. S., Eds.; Woodhead Publishing, **2013**, 386–407.

(38) Ndiaye, A.; Bonnet, P.; Pauly, A.; Dubois, M.; Brunet, J.; Varenne, C.; Guerin, K.; Lauron, B. Noncovalent Functionalization of Single-Wall Carbon Nanotubes for the Elaboration of Gas Sensor Dedicated to BTX Type Gases: The Case of Toluene. *J. Phys. Chem. C* **2013**, *117*, 20217–20228.

(39) Zhang, W.; Sprafke, J. K.; Ma, M.; Tsui, E. Y.; Sydlik, S. A.; Rutledge, G. C.; Swager, T. M. Modular Functionalization of Carbon Nanotubes and Fullerenes. *J. Am. Chem. Soc.* **2009**, *131*, 8446–8454.

(40) Edwards, E. R.; Antunes, E. F.; Botelho, E. C.; Baldan, M. R.; Corat, E. J. Evaluation of Residual Iron in Carbon Nanotubes Purified by Acid Treatments. *Appl. Surf. Sci.* **2011**, *258*, 641–648.

(41) Ishihara, S.; Labuta, J.; Nakanishi, T.; Tanaka, T.; Kataura, H. Amperometric Detection of Sub-ppm Formaldehyde Using Single-Walled Carbon Nanotubes and Hydroxylamines: A Referenced Chemiresistive System. *ACS Sensors* **2017**, *2*, 1405–1409.

(42) Yang, C.-M.; Kanoh, H.; Kaneko, K.; Yudasaka, M.; Iijima, S. Adsorption Behaviors of HiPco Single-Walled Carbon Nanotube Aggregates for Alcohol Vapors. *J. Phys. Chem. B* **2002**, *106*, 8994–8999.

(43) Zhu, Z. An Overview of Carbon Nanotubes and Graphene for Biosensing Applications. *Nano-Micro Lett.* **2017**, *9*, 25.

(44) Schroeder, V.; Savagatrup, S.; He, M.; Lin, S.; Swager, T. M. Carbon Nanotube Chemical Sensors. *Chem. Rev.* **2019**, *119*, 599–663.

(45) Gangoli, V.S.; Godwin, M.A.; Reddy, G.; Bradley, R.K.; Barron, A.R. The State of HiPco Single-Walled Carbon Nanotubes in 2019. *C* **2019**, *5*, 65.

(46) Maultzsch, J.; Reich, S.; Thomsen, C. Raman Scattering in Carbon Nanotubes Revisited. *Phys. Rev. B – Condens. Matter Mater. Phys.* **2002**, *65*, 1–4.

(47) Setaro, A.; Adeli, M.; Glaeske, M.; Przyrembel, D.; Bisswanger, T.; Gordeev, G.; Maschietto, F.; Faghani, A.; Paulus, B.; Weinelt, M.; Arenal, R.; Haag, R.; Reich S. Preserving π-Conjugation in Covalently Functionalized Carbon Nanotubes for Optoelectronic Applications. *Nat. Commun.* **2017**, *8*, 14281.

(48) Saito, R.; Hofmann, M.; Dresselhaus, G.; Jorio, A.; Dresselhaus, M. S. Raman Spectroscopy of Graphene and Carbon Nanotubes. *Adv. Phys.* **2011**, *60*, 413–550.

(49) Smazna, D.; Rodrigues, J.; Shree, S.; Postica, V.; Neubüser, G.; Martins, A. F.; Ben Sedrine, N.; Jena, N. K.; Siebert, L.; Schütt, F.; Lupan, O.; Ahuja, R.; Correia, M.R.; Monteiro, T.; Kienle, L.; Yang, Y.; Adelung, R.; Mishra, Y.K. Buckminsterfullerene Hybridized Zinc Oxide Tetrapods: Defects and Charge Transfer Induced Optical and Electrical Response. *Nanoscale* **2018**, *10*, 10050–10062.

(50) Krätschmer, W.; Lamb, L. D.; Fostiropoulos, K.; Huffman, D. R. Solid C60: A New Form of Carbon. *Nature* **1990**, *347*, 354–358.

(51) Garcia, S.; Rosenbauer, R. J.; Palandri, J.; Maroto-Valer, M. M. Sequestration of Non-Pure Carbon Dioxide Streams in Iron Oxyhydroxide-Containing Saline Repositories. *Int. J. Greenh. Gas Control* **2012**, *7*, 89–97.

(52) Liu, J.; Fu, S.; Yuan, B.; Li, Y.; Deng, Z. Toward a Universal "Adhesive Nanosheet" for the Assembly of Multiple Nanoparticles Based on a Protein-Induced Reduction/Decoration of Graphene Oxide. *J. Am. Chem. Soc.* **2010**, *132*, 7279–7281.

(53) Zhou, X.; Zhang, J.; Wu, H.; Yang, H.; Zhang, J.; Guo, S. Reducing Graphene Oxide via Hydroxylamine: A Simple and Efficient Route to Graphene. *J. Phys. Chem. C* **2011**, *115*, 11957–11961.

(54) Grosvenor, A. P.; Kobe, B. A.; Biesinger, M. C.; McIntyre, N. S. Investigation of Multiplet Splitting of Fe 2p XPS Spectra and Bonding in Iron Compounds. *Surf. Interface Anal.* **2004**, *36*, 1564–1574.

(55) Bengtsson, G.; Fronæus, S.; Bengtsson-Kloo, L. The Kinetics and Mechanism of Oxidation of Hydroxylamine by Iron(III). *J. Chem. Soc. Dalt. Trans.* **2002**, *12*, 2548–2552.

(56) Penza, M.; Rossi, R.; Alvisi, M.; Cassano, G.; Signore, M. A.; Serra, E.; Giorgi, R. Surface Modification of Carbon Nanotube Networked Films with Au Nanoclusters for Enhanced Gas Sensing Applications. *J. Sensors* **2008**, *2008*, 1–8.

(57) Ellison, M. D.; Crotty, M. J.; Koh, D.; Spray, R. L.; Tate, K. E. Adsorption of NH_3 and NO_2 on Single-Walled Carbon Nanotubes. *J. Phys. Chem. B* **2004**, *108*, 7938–7943.

(58) Mercuri, F.; Sgamellotti, A.; Valentini, L.; Armentano, I.; Kenny, J. M. Vacancy-Induced Chemisorption of NO_2 on Carbon Nanotubes: A Combined Theoretical and Experimental Study. *J. Phys. Chem. B* **2005**, *109*, 13175–13179.

(59) Santucci, S.; Picozzi, S.; Di Gregorio, F.; Lozzi, L.; Cantalini, C.; Valentini, L.; Kenny, J. M.; Delley, B. NO_2 and CO Gas Adsorption on Carbon Nanotubes: Experiment and Theory. *J. Chem. Phys.* **2003**, *119*, 10904–10910.

CHAPTER 4. MANIPULATING POLYMER COMPOSITION TO CREATE LOW-COST, HIGH-FIDELITY SENSORS FOR INDOOR CO_2 MONITORING

Content from this chapter has been reprinted with permission from:
Siefker, Z. A.; Hodul, J. N.; Zhao, X.; Bajaj, N.; Brayton, K. M.; Flores-Hansen, C.; Zhao, W.; Chiu, G. T.-C.; Braun, J. E.; Rhoads, J. F.; Boudouris, B.W.
Scientific Reports 2021, *11*, 13237.

4.1 Overview

Carbon dioxide (CO_2) has been linked to many deleterious health effects, and it has also been used as a proxy for building occupancy measurements. These applications have created a need for low-cost and low-power CO_2 sensors that can be seamlessly incorporated into existing buildings. We report a resonant mass sensor coated with a solution-processable polymer blend of poly(ethylene oxide) (PEO) and poly(ethyleneimine) (PEI) for detection of CO_2 across multiple use conditions. Controlling the polymer blend composition and nanostructure enabled better transport of the analyte gas into the sensing layer, which allowed for significantly enhanced CO_2 sensing relative to the state of the art. Moreover, the hydrophilic nature of PEO resulted in water uptake, which provided for higher sensing sensitivity at elevated humidity conditions. Therefore, this key integration of materials and resonant sensor platform could be a potential solution in the future for CO_2 monitoring in smart infrastructures.

4.2 Introduction

It is estimated that the average American and European spends nearly 90%[1–3] of their time indoors, and consequently, CO_2 concentrations in buildings can range from those seen in outdoor environmental conditions (i.e., ~400 ppm) to 3,000 ppm, depending on the occupancy of the

confined space.[4,5] Moreover, CO_2 is regarded as a toxic contaminant with an OSHA time-weighted average (TWA) exposure limit of 5,000 ppm over an 8-hour workday or a short-term exposure limit of 15,000–30,000 ppm over 15 minutes.[6] Importantly, CO_2 exposure at as low of a concentration as 1,000 ppm negatively affects cognitive performance, including decision making and problem resolution.[7–9] Thus, appropriate indoor air quality monitoring and building ventilation systems, equipped with low-cost, high-fidelity CO_2 sensors, are required. However, many current sensing technologies suffer from limitations and drawbacks, such as arduous device fabrication techniques or high-power consumption, which limits their practical and widespread implementation in residential, commercial, and industrial settings. Thus, there is a critical need for a low-cost, low-power CO_2 sensor that is easy to manufacture and can be incorporated into existing buildings to upgrade these structures into "smart buildings" in a seamless manner.

State-of-the-art CO_2 detection methods have relied primarily on gas chromatography and spectroscopy methods, which are typically high-cost and require large instrumentation footprints.[10–13] In particular, there has been a large push to use infrared (IR) spectroscopy to detect CO_2 gas. Typically, CO_2 infrared sensors are nondispersive infrared (NDIR) sensors where a broadband lamp source and an optical filter are used to select a narrow band in the spectral region that overlaps with the absorption region of the gas of interest. However, NDIR detection of CO_2 is limited by spectral interference, a high detection limit, and interference from water vapor.[14] In fact, even many new NDIR CO_2 sensors have readings that deviate from actual CO_2 concentrations by more than 75 ppm[15,16] and potentially even greater error if not regularly calibrated.[17] Additionally, the infrared light inherent to NDIR sensors, often results in bulky instrument size due to the length of the light path (> 1 cm) and high power consumption (> 200 mW), which limits their use in embedded applications, such as internet-of-thing-based (IoT-based) smart buildings.

Recently there has been work in creating a handheld, low-power (i.e., < 1 W), and sensitive (i.e., 50 ppm) CO_2 NDIR sensor capable of performing breath analysis.[18] Though intriguing, this device is not being manufactured for indoor air quality monitoring, and therefore lags in areas of testing and performance typical of indoor environments.[18] Thus, current NDIR CO_2 sensors do not meet the power, size, and selectivity metrics necessary for a practically scalable sensor that can meet the demands of smart building technologies suitable for the indoor monitoring of CO_2.

Conversely, microelectromechanical systems-based (MEMS-based) resonant mass sensors are a promising sensor paradigm for this application space as they exhibit high performance metrics in gas detection due to their compact size, low cost, low power, fast response times, and high sensitivity.[19–23] Importantly, when microresonators are functionalized with specific surface chemistries, target analytes non-covalently bind, or otherwise chemo-mechanically interact, with the sensor. This change in mass on the surface induces a shift in the resonant frequency of the device, which can be readily and precisely quantified. In fact, cantilevered-type resonant mass sensors are sensitive enough to detect bacteria and a single virus in the air.[24,25] Therefore, MEMS-based devices are an ideal platform for smart building integration if they can be functionalized with the appropriate and selective chemistry in a low-cost, high-throughput manner.[26] Given this potential, we fabricated a resonant mass sensor with a solution-processable polymer blend of poly(ethylene oxide) (PEO) and poly(ethyleneimine) (PEI) coated atop the resonant platform. The selection of these two materials was rather straightforward. First, PEI contains multiple amine groups that have been shown to effectively perform reversible acid-base reactions with CO_2.[27–30] However, due to the viscous nature of PEI, diffusion of the CO_2 into the material to perform such reactions is limited. Thus, we employed a hydrophilic, semicrystalline polymer, PEO,[31] in the blend with PEI to enhance the sensitivity and response rate of CO_2 uptake. The PEO has two roles

when being incorporated into the PEI. First, it disrupts intrachain and interchain PEI entanglement at the molecular level and the surface morphology at the nanoscale level. Both of these positive disruptions facilitate increased interactions between accessible amines and CO_2. Second, the hydrophilic nature of PEO attracts water into the blended thin film; in turn, this water converts the reversible acid-base formed carbamates (i.e., the product of CO_2 reacting with primary and secondary amines) into bicarbonates freeing amines to enhance the adsorption and uptake of CO_2. This critical addition of the PEO moiety allows for the macromolecular blend to have selective and significantly enhanced detection of CO_2 relative to previous efforts. This synergetic chemical blending and subsequent polymer processing, in combination with the resonant mass sensor platform, allows for the fabrication of a low-cost and effective CO_2 sensor. In comparison to other CO_2 sensing counterparts, this sensor is compact, with a footprint of < 25 mm^2, and offers high sensitivity (i.e., at a detection limit of CO_2 as low as 5 ppm). Moreover, these sensors detect CO_2 selectively over other polar compounds (e.g., methanol and acetone), as well as non-polar compounds (e.g. xylene and propane). Thus, this sensing platform offers an easily functionalized, low-cost, low-power, multi-channel sensing array capable of quick and reliable detection.

4.3 Experimental Information

4.3.1 Materials

All of the chemicals were purchased from Sigma-Aldrich, and they were used as received unless otherwise noted. The PEI utilized had a reported a weight average molecular weight of 25 kg mol^{-1}. The PEO utilized was purchased from Alfa Aesar, and it had a reported weight average molecular weight of 100 kg mol^{-1}. The methanol utilized to prepare the polymer samples was anhydrous grade and stored under nitrogen. Polished silicon dioxide substrates utilized for imaging were purchased from Silicon Valley Microelectronics.

4.3.2 General Methods

A Veeco Dimension 3100 Atomic Force Microscope (AFM) in tapping mode was utilized for AFM imaging. For these images, the polymer samples were fabricated by depositing 1.0 μL of a 1.0 mg mL^{-1} polymer blend in methanol on a polished silicon dioxide substrate. Then, the sample wafers were dried under vacuum ($P \leq 0.4$ Torr) overnight to remove solvent. The images for the 3:1 PEO:PEI, 1:1 PEO:PEI, PEO-only, and PEI-only films were acquired using this protocol. A Hitachi S-4800 Field Emission scanning electron microscope (SEM) was utilized to image the PEO:PEI. For these images, 1.0 μL of a 1 mg mL^{-1} polymer blend in methanol solution were drop cast on polished silicon dioxide substrates and dried overnight under vacuum. All of the polymer films were then coated with 20 nm of conducting carbon using a SPI carbon sputter coater prior to imaging. The images for the 3:1 PEO:PEI, 1:1 PEO:PEI, PEO-only, and PEI-only films were acquired using this protocol. X-Ray diffraction (XRD) measurements were measured with a Rigaku Cu-Kα source (λ= 1.54056 Å) in parallel beam mode. These samples were acquired while under ambient conditions. The polymer film samples were fabricated using a 240 mg mL^{-1} solution of the polymer blend (by weight ratio) in methanol pipetted into a metal mold and then annealed at 80 °C while being pressed for at least 10 min. After pressing, these films were dried overnight under vacuum ($P \leq 0.4$ Torr) prior to XRD analysis being performed. A Thermo-Nicolet Nexus Fourier Transform Infrared Spectroscopy (FTIR) with a KBr beam splitter with a 800 cm^{-1} – 4500 cm^{-1} spectra range was utilized for FTIR analysis of the PEO:PEI polymer films. The polymer films were fabricated utilizing the same protocol as discussed for XRD analysis. For DMA testing of the polymer films, a TA Instruments DMA Q800 with a film tension clamp was utilized. These experiments were conducted at a temperature ramp of 0.5 °C min^{-1} and at a constant frequency of 1 Hz. The polymer films were fabricated utilizing the same general protocol as discussed for XRD analysis.

4.3.3 Device Testing

The testing protocols utilized in this work are similar to those previously reported.[23,46,56] Testing of the devices was performed using the experimental setup shown in Figure 21a. Gas tanks of nitrogen, air, and carbon dioxide were connected to a series of mass flow controllers (MFC; MKS, 1179C) in parallel. A subset of nitrogen-supplied MFCs was connected to bubblers (ChemGlass, AF-0085) for introducing humidity or select vapor distractants (i.e., acetone, ethanol, toluene, and xylene). The gas lines converged to a mixing manifold, the output of which was connected directly to the test chamber inlet. A 95 mm diameter and 23 mm in height cylindrical aluminum testing chamber was used for evaluating the sensors. A 6.4 mm gas inlet port was centrally-located on the top of the test chamber and two 6.4 mm exhaust ports were located on opposite sides of the test chamber. The small chamber volume allowed for complete gas exchange in less than one minute, facilitating quick sensor responses upon changing MFC flow rates.

Prior to sensor testing, the resonator board was attached to the instrumentation board. The test chamber was flushed with nitrogen or air to create an inert environment as the baseline for experimentation. Subsequently, the analyte gases were injected into the chamber to achieve the reported concentrations. A frequency counter was developed in LabVIEW to monitor the oscillation frequency of each oscillator with a 1 Hz resolution. To facilitate parallel monitoring, the frequency counter was synthesized and executed on an NI myRio Field Programmable Gate Array (FPGA). An FPGA consists of a collection of logic elements between which electrical paths can be created and allows for parallel computing. Thus, each of the 16 frequency counting loops could run simultaneously.

4.3.4 Device Instrumentation

The device instrumentation utilized in this work was previously reported.[23,56] An array of 16 Pierce oscillators was used as the sensing platform. Figure 21 shows the Pierce oscillator circuit, which consisted of an inverter, two load capacitors (C_1 = 22 pF and C_2 = 22 pF), one feedback resistor (R_1 = 2 MΩ), one isolation resistor (R_2 = 510 Ω), and a 16 MHz quartz crystal resonator (Kyocera Corp., CX3225). The crystal oscillator driver (Texas Instruments, SN74LVC1GX04) provided the circuit with the Pierce oscillator inverter as well as three additional inverters, which effectively squared the oscillator output signal. The hardware implementation of the oscillator circuit resulted in two printed circuit boards: (i) a board containing only an array of resonators and (ii) an instrumentation board containing the 16 sets of oscillators with spring pin connectors in place of the resonators (Figure 21e). As such, the resonator boards could be functionalized independent of the rest of the oscillator circuit and easily interchanged without incurring high component costs.

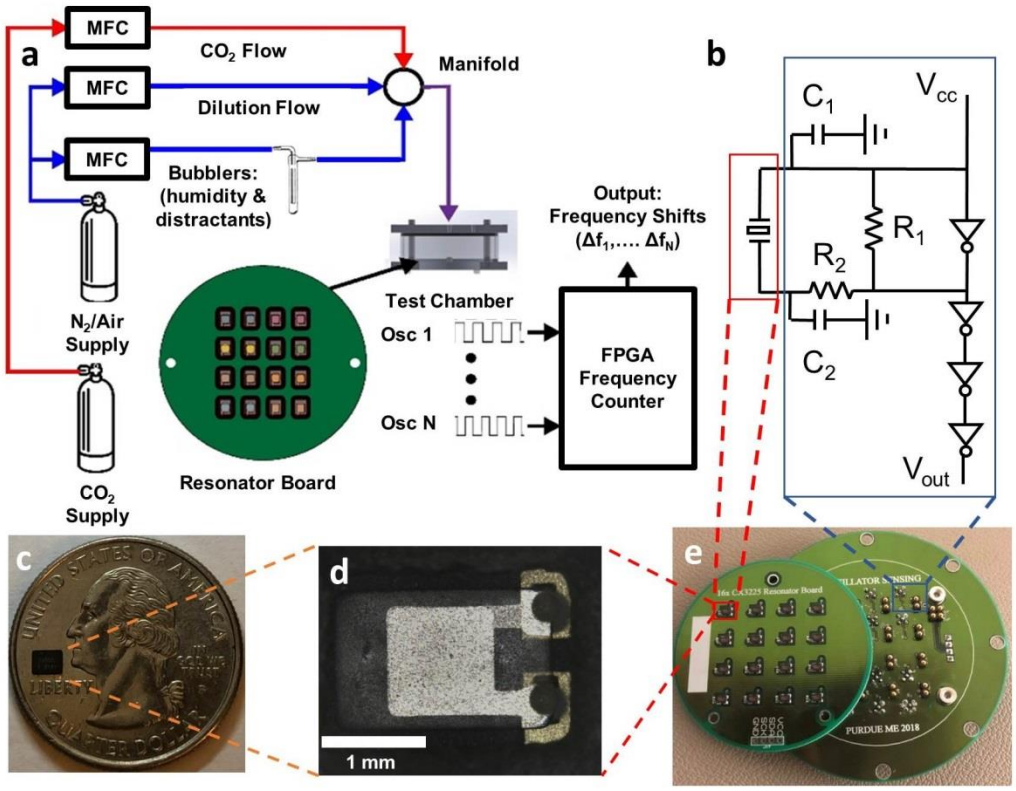

Figure 21. (a) Schematic of the gas distribution system used for sensor testing. Mass flow controllers (MFCs) modulated supply gases to the test chamber containing functionalized oscillators. Bubblers connected to a MFC were used to moderate distractant analytes and humidity levels inside the testing chamber. A frequency counter, executed on a MyRIO FPGA monitored the frequency of each oscillator in parallel. (b) A schematic of the Pierce oscillator used. The resonant element, outlined by the red box, is shown on the left of the circuit diagram. The remainder of the oscillator circuit, which is contained on the instrumentation board, is outlined by the blue box. This portion of the diagram contains two load capacitors (C_1 and C_2), a feedback resistor (R_1), and an isolation resistor (R_2). A series of inverters between the supply voltage (V_{cc}) and the output voltage (Vout) are used to square-off the oscillator output signal to facilitate frequency counting. (c) A single packaged resonant element shown on a US quarter for scale. (d) An exposed quartz crystal resonant element. (e) A resonant mass sensing system with 16 Pierce oscillators. A resonator board (left) containing 16 resonant elements is shown offset from the instrumentation board (right) which completes the Pierce oscillator circuit.

A single crystal resonator has a small footprint (8 mm^2) and low power requirement (< 200 µW) during operation. Figure 21c shows a single packaged crystal resonator on top of a United States quarter, for scale. The small size and low power requirement of a single resonant sensor is particularly promising when considering wireless and distributed sensing in buildings.[53–55] The

resonant element of the Kyocera CX3225 is shown in Figure 21d, after the package cap has been removed. Functional materials were applied directly to this exposed element.

4.3.5 Device Functionalization

PEI and PEO were dissolved in methanol to generate a solution of 0.1% (by volume) of PEI and 0.3% (by volume) of PEO. Then, 1 μL of this solution was deposited onto each resonator. The resonator board was then placed under vacuum at 70 °C for 12 h to remove any residual methanol leaving behind a 3:1 PEO:PEI blend film (by weight). Unless otherwise specified, the devices utilized in the tests were all functionalized with the 3:1 PEO:PEI (by weight). Prior to testing, the resonator board was allowed to equilibrate back to room temperature.

4.4 Results and Discussion

4.4.1 Sensor Response and Dynamic Range

Resonant mass sensors functionalized with a PEI-PEO polymer blend were able to detect CO_2 across an extended range of concentrations relevant to indoor air quality monitoring (Figure 22). Critically, these sensors demonstrated a highly linear response at CO_2 concentrations relevant to the targeted application of buildings. This range is roughly defined by a lower bound of 400 ppm (i.e., the concentration that is typical for air outdoors, located in unoccupied spaces) and an upper bound of 2,000 ppm. A building with well-controlled ventilation will have CO_2 concentrations around 1,100 ppm, which is the central region of interest.[32] Figures 22a-c highlight sensor responses at CO_2 concentrations that are relevant to indoor environments. These data demonstrate sensor performance in a background of nitrogen and a background of air (i.e., ~78% nitrogen, ~21% oxygen, and 0.12% carbon dioxide). In both the nitrogen and air backgrounds, the sensor response was linear and proportional to the increase in CO_2 concentrations above the

background concentrations with an interpolated sensitivity of approximately 0.12 Hz ppm^{-1} CO_2 (Figure 22c). However, these responses were determined for 1-hour pulses of CO_2 which was often not long enough for the functional material to fully saturate with CO_2. This delayed response and recovery time may prove problematic in some applications. In such cases, a thinner film of the functional material may be used such that it saturates with CO_2 in less time. However, this will be done at the expense of increasing the limit of detection which may be interpolated based on a 1 Hz frequency resolution. Thus, optimization of this point will be specific to the end-use application. Further, the desorption of CO_2 occurs at a slower rate than adsorption, resulting in the drifting baseline in the time series data (Figures 22a-b). The time series data (Figures 22a-b) show the resonators decreasing in frequency as CO_2 is adsorbed on top of the resonator. The added CO_2 mass on the resonator decreases its resonant frequency, as described, for example, by the Sauerbrey equation.[33,34] The magnitude of the frequency shift is greater at higher concentrations due to an increased amount of CO_2 adsorbing onto the resonator. Thus, the change in CO_2 concentration induces a clear shift in resonant frequency of the sensor.

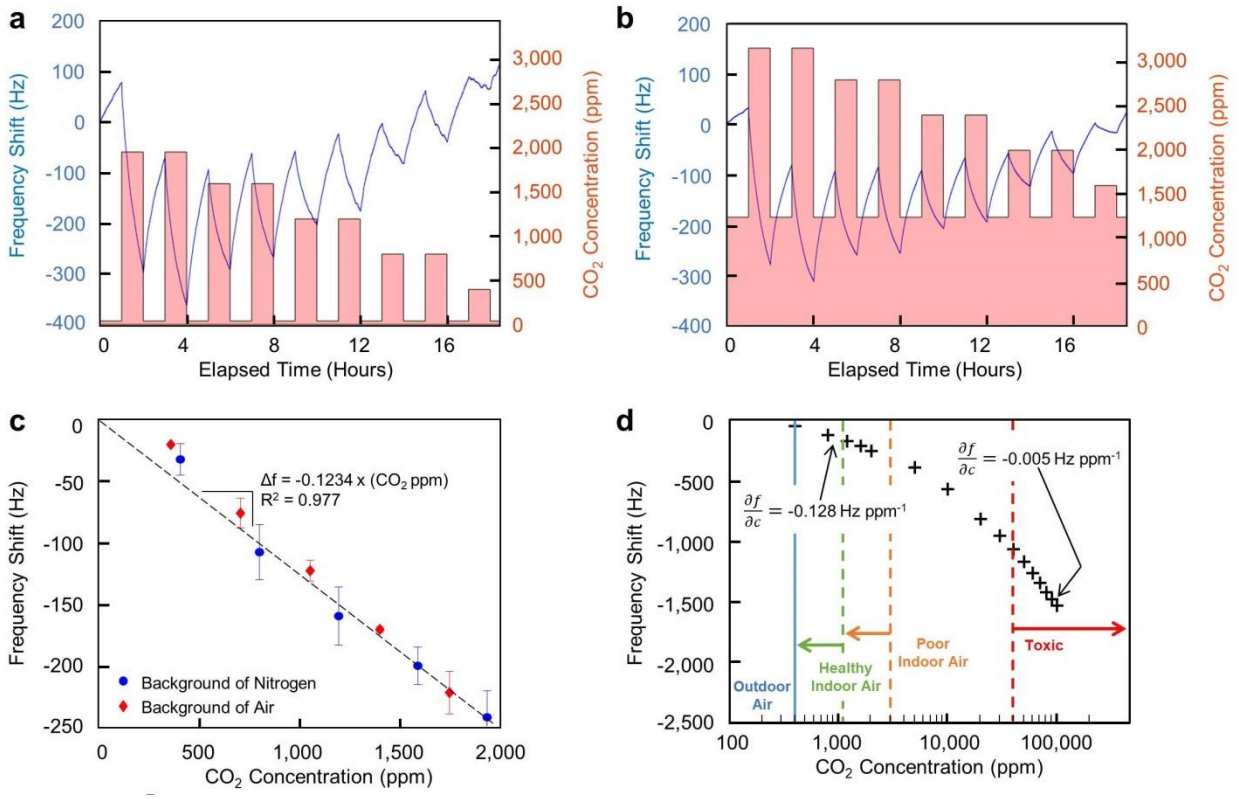

Figure 22. Sensor response to CO_2 shown as a frequency shift of the resonant element. (a) Sensor response to CO_2 over time with a background of nitrogen. The resonant frequency shift response is indicated by the blue line (left vertical axis), and the red bars indicate when CO_2 is present (right vertical axis). (b) Sensor response to CO_2 over time with a background of air. The resonant frequency shift response is indicated by the blue line (left vertical axis), and the red bars indicate when CO_2 is present (right vertical axis). The use of air brought the baseline CO_2 concentration to 1,200 ppm. (c) Total frequency shift of the device after 1 h of CO_2 at specified concentrations. The average of 8 responses is shown with error bars representing one standard deviation. Regardless of the baseline conditions, a similar linear response is obtained by the sensor, as demonstrated by the linear regression fit. (d) The dynamic range of the sensor is shown by plotting the resonant frequency shift in response to 1 h of CO_2 in a background of nitrogen. For comparison, outdoor air CO_2 concentrations[35] are indicated by the solid blue line, healthy indoor air CO_2 levels[32] are indicated by the dashed green line, poor indoor air CO_2 levels[32,36] are indicated by the dashed orange line, and toxic CO_2 levels[37] are indicated by the dashed red line. Additionally, the sensitivity (indicated by the change in frequency per change in CO_2 concentration, $\frac{\partial f}{\partial c}$ is shown at both low and high concentrations.

Moreover, this sensor has a large dynamic range and can detect CO_2 at concentrations well beyond what is relevant to indoor air monitoring (Figure 22d). Unlike the relatively linear response demonstrated below 2,000 ppm CO_2, when the sensor is exposed to larger concentrations, a

nonlinear response is apparent as the frequency shift per ppm of CO_2 decreases asymptotically. This is consistent with a Langmuir sorption model where the rate of adsorption decreases as the available surface binding sites are filled.[38] Nevertheless, this sensor can discriminate CO_2 concentrations well beyond toxic levels for human occupancy.[37]

4.4.2 Performance in Indoor Environments

Even in a relatively well-controlled, indoor environment, air conditions can drastically vary in both temperature and humidity level. Thus, it is important to account for these variables and demonstrate sensor performance across a span of potential environmental conditions. A 'comfort zone', which describes indoor air conditions that most people find comfortable, has been defined by the engineering society ASHRAE.[39] This region is outlined on the psychrometric chart (Figure 23a) based on indoor air temperatures and humidity levels. Using the comfort zone as a guide, a test region was developed spanning approximately 22-26 °C and 0%-80% relative humidity (at a given temperature), and testing was performed near the extremes of this region, as well as near the center.

Previously, PEI has been used to detect and capture CO_2.[27,28,40–42] This is because CO_2 reacts with the primary and secondary amines of PEI readily to form carbamates that can be stabilized by other primary amines or with water and create bicarbonate ions.[29] When PEI is mixed with PEO and supported onto mesoporous oxides, PEI is a powerful adsorbent of CO_2.[43,44] However, few studies have evaluated the adsorption of CO_2 onto blended films of PEO and PEI without a mesoporous substrate for the purpose of measurement under indoor air conditions.[45,46] It must be noted that in these examples of PEO and PEI polymer blend films, that these films were fabricated with graphene-based materials. In our case, without any graphene additives, the PEO-PEI blend enhanced the frequency response and sensitivity of the sensor to CO_2 (Figure 23b,

Supporting Information Table 2). PEO, when blended with PEI enhanced the frequency response and sensitivity of the sensor to CO_2 (Figure 23b). Under dry air conditions (i.e., 0% RH) the frequency response of the polymer blend is more than twice that of PEI alone. Additionally, when increasing the background relative humidity level to 10% and then to 80% at a constant temperature, the frequency shift response to CO_2 is nearly tripled and then quadrupled, respectively, relative to the resonator functionalized with PEI only. Furthermore, the PEO and PEI blends have shown promising performances in both elevated temperature and elevated humidity conditions, simultaneously (Figure 23c and 23d). However, the addition of the hydrophilic PEO chemistry induces an inherent cross-sensitivity to water. Therefore, commercial implementation of this sensing device would require humidity compensation. However, this is a commonly-monitored metric in commercial HVAC systems; thus, only simple circuitry would be required to account for the presence of humidity.

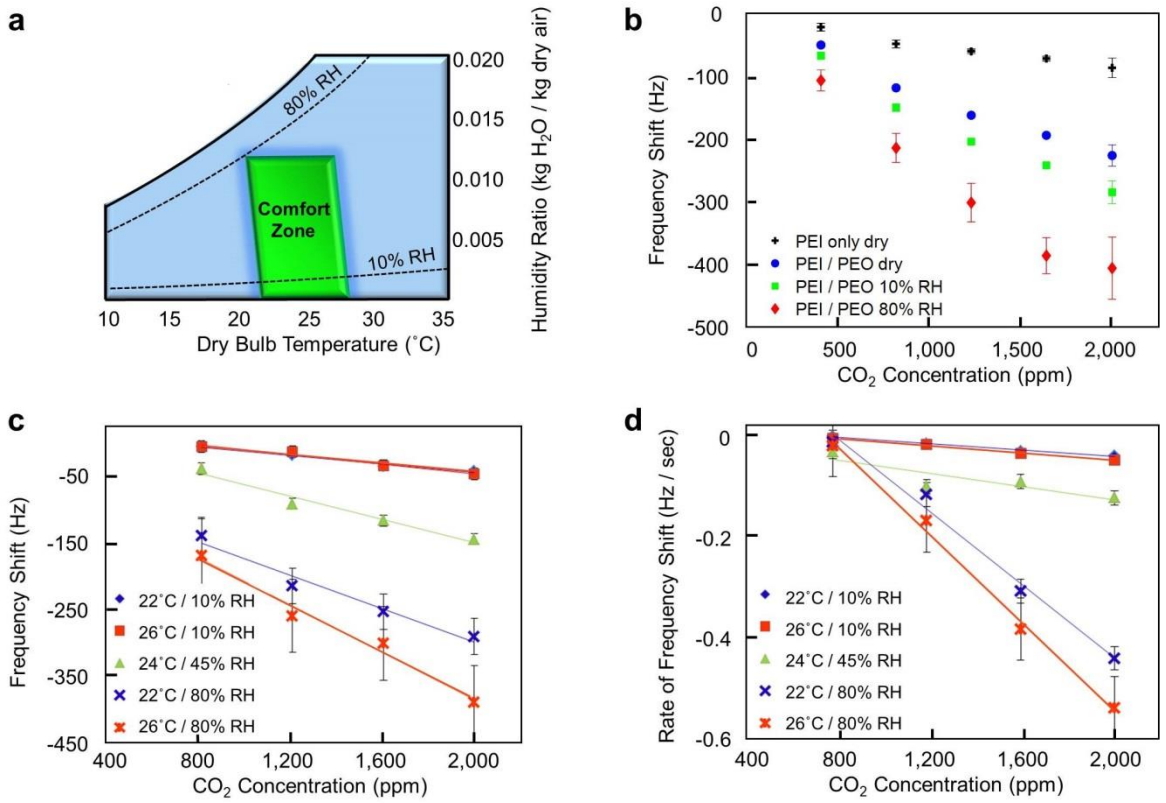

Figure 23. (a) Psychrometric chart defining the 'Comfort Zone' air temperature and humidity range, as defined by the engineering association, ASHRAE. Testing was performed across this region to simulate environmental conditions expected in high performance buildings. (b) Frequency response of devices functionalized with PEI only, and a 3:1 PEO:PEI blend ranging from 0 to 80% relative humidity (RH). Tests were performed holding temperature at 24 °C. The average of 8 responses is shown with error bars representing one standard deviation. (c) Sensor response to CO_2 while varying temperature from 22-26 °C and relative humidity from 10-80% to cover the indoor air comfort zones.[39] The average of 8 responses is shown with error bars representing one standard deviation. A baseline condition of 400 ppm CO_2 in nitrogen was used to simulate outdoor air conditions and a linear response is obtained at each condition, as demonstrated by the linear regression fits. (d) The rate of change in frequency shift after each increase in CO_2 concentration from a background of 400 ppm. The average of 8 responses is shown with error bars representing one standard deviation. A similar linear response is obtained at each condition, as demonstrated by the linear regression fits.

4.4.3 Sensor Selectivity

These sensors showed relative selectivity to CO_2 when interfering gases (i.e., distractant gases) were introduced into the chamber (Figure 24a). Previously, PEI based materials have shown responses to other analytes.[47] Therefore, selectivity testing was performed with analytes that could be present in an interior location. Specifically, these tests were performed with a variety of confounding species including propane, carbon monoxide, acetone, ethanol, toluene, and xylene. Though not an exhaustive list, each of these species were carefully selected to cover a broad range of functional chemical groups (i.e., alkyl hydrocarbons, ketones, alcohols, and aromatic hydrocarbon) typically found in interior locations. Each test alternated between 30 min pulses of analyte gases and a nitrogen purge of the test chamber. CO_2 and the selected interfering gases were each introduced at concentrations of 1,000 ppm for comparison. It should be noted that 1,000 ppm is a common CO_2 level for indoor environments; however, for the distractants considered, this concentration is well above what is considered safe.[36] Thus, these distractant gases tested are on the extreme side of what could potentially confound the sensors under practical operating conditions. Tests were performed to show a CO_2 pulsed alone, the distractant vapor pulsed alone, CO_2 and the distractant pulsed together, and CO_2 pulsed with a background distractant level. Testing in this manner allowed for a direct comparison of sensor response to CO_2 and the distractant, as well as any interacting effects on the sensor when CO_2 and the distractant are presented together. Cross-sensitivity is apparent; however, for all distractants tested, the sensor had a distinguishable response to CO_2 and a lesser response (if any) to the distractant vapor. Acetone, for example, induced an average shift of 128 Hz during a 30-min pulse, whereas, CO_2 induced an average shift of 734 Hz for the same time period (Figure 24b). Thus, the influence of acetone, at a relatively high concentration for indoor environments, was nearly 6 times less than the sensor's response to CO_2 at the same concentration.

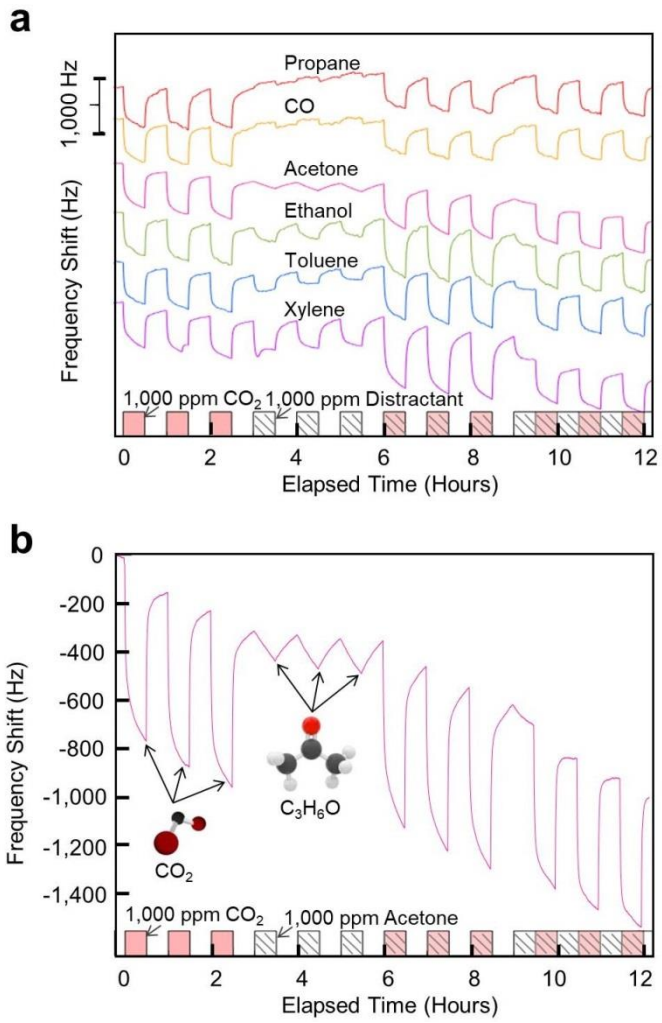

Figure 24. Sensor response to 1,000 ppm pulses of CO_2 and various distractants. (a) Frequency shift responses of a sensor in the presence of various interfering gas analytes. (b) Zoomed frequency shift response of a sensor in response to CO_2 in the presence of acetone. The time series data shows 30 min pulses of CO_2 with a background of nitrogen, followed by pulses of acetone, pulses of CO_2 and acetone together, and finally pulses of CO_2 with a constant background of acetone.

4.4.4 Polymer Film Properties Impact CO_2 Detection

The optimal and reliable detection of CO_2 using a 3:1 PEO:PEI blend film is due to the ability of the semi-crystalline nature of PEO to disrupt the intermolecular interactions of the hyperbranched PEI. PEI, a polymer with many amine branches, ranging from primary to tertiary amines, is an amorphous material that has a relatively low glass transition temperature (i.e., in our hands, it was –50 °C for a PEI molecular weight of 25 kg mol^{-1}). Thus, branched PEI at room

temperature exists as a viscous liquid due to the strong non-covalent interchain amine interactions and polymer entanglements.[48] PEI, when drop cast onto a substrate and dried under vacuum, remains a uniform polymer film with minor surface defects or disruptions (Supporting Information Figure 27a and 27b) on the PEI surface until another material or polymer is introduced into the PEI casting solution. Therefore, a pristine PEI thin film has difficulty detecting CO_2 due to the high viscosity and nanostructural uniformity caused by the hyperbranched amine interchain interactions of a PEI film (Figure 23b), which can hydrogen bond and become highly entangled with each other. These entangled amines, many of which are primary amines, prevent the ready diffusion of CO_2 into the material to interact, which ultimately limits the CO_2 uptake and subsequent sensor response.

When PEO is blended in a 3:1 ratio with PEI, surface features and nanoscale disruptions in the blended polymer film were observed (Figure 25a and 25b). This surface segregation also occurred to a lesser degree in the 1:1 PEO:PEI blend film (Supporting Information Figure 27c-27d). These defects and disruptions in the PEI film are indicative of altering macromolecular interactions when PEO is incorporated into a PEI matrix. This macromolecular rearrangement promotes CO_2 adsorption because CO_2 can now diffuse into the PEI material and interact readily with accessible primary and secondary amines which were not accessible prior to the addition of PEO. Moreover, when incorporating the PEO into the PEI matrix there was an observed crystal structure as seen in X-ray diffraction (XRD) (Figure 25c) with characteristics reflections at $q = 1.3$ $Å^{-1}$ and $q = 1.65$ $Å^{-1}$, which is consistent with the monoclinic crystal structure of PEO.[49,50]

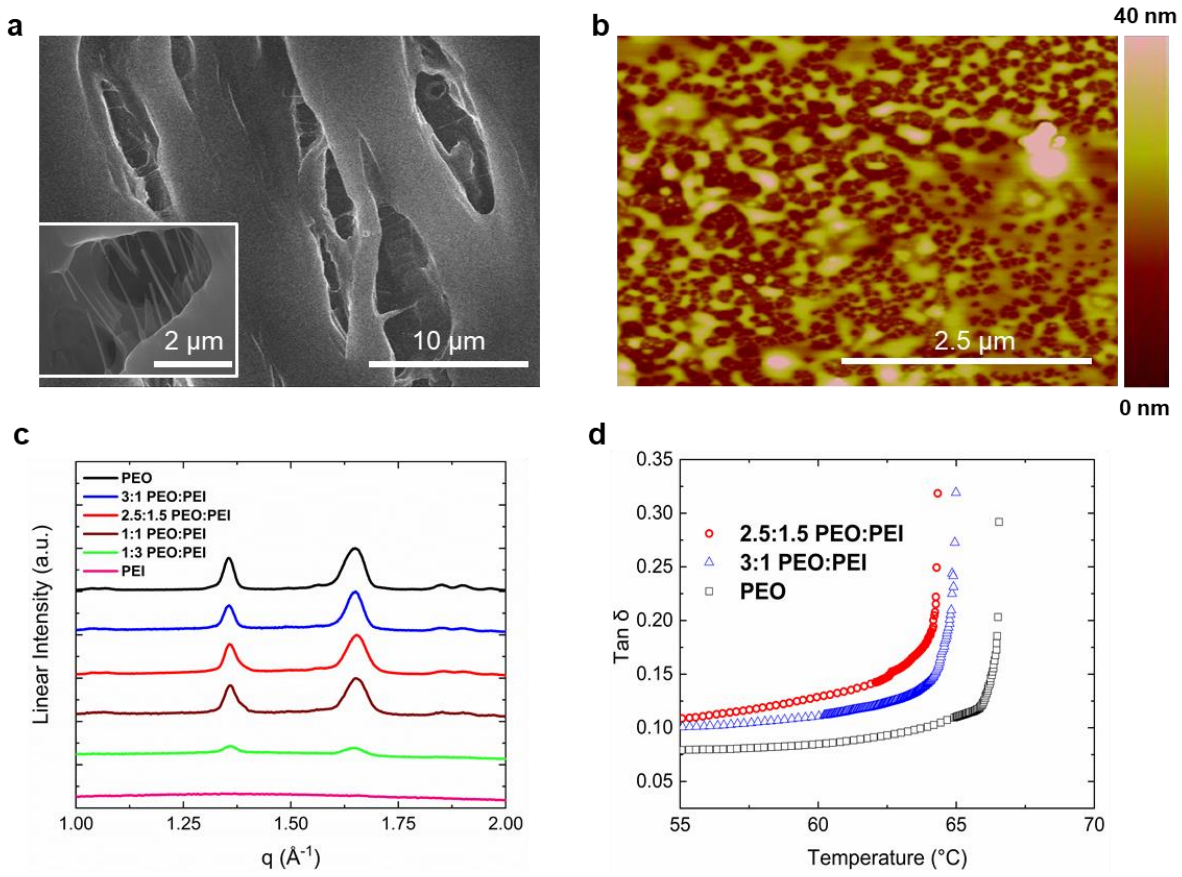

Figure 25. (a) SEM images of a 3:1 PEO:PEI blend film. Both images shown are of the same film but in different sections and locations. (b) AFM images of a 3:1 PEO:PEI blend films. (c) XRD patterns of PEO, 3:1 PEO:PEI blend, 2.5:1.5 PEO:PEI blend, 1:1 PEO:PEI blend, 1:3 PEO:PEI blend, and PEI only films. (d) DMA of a 2.5:1.5 PEO:PEI blend, 3:1 PEO:PEI blend, and PEO-only films.

When PEO is added to the amorphous PEI, PEO tries to maintain order, and this ordering of PEO disrupts the PEI entanglements. In turn, this reduces the side chain amines from interacting with other interchain amines. As a result, there is polymer phase separation and surface morphology alterations in the film. When these alterations occur, CO_2 was transported into the PEI matrix in a more robust manner such that larger uptake occurred. Thus, as seen in a 0% relative humidity environment, the PEO:PEI blended film can interact better with CO_2 than PEI alone (Figure 23b). This surface morphology alteration agrees with previous work with similar blends when the PEO molecules physically shielded the PEI chains from one another to reduce individual

PEI-PEI chain interactions.[43] This PEO-induced physical disruption of interchain PEI amines from one another is in direct agreement that intrachain CO_2 adsorption events (i.e., rather than interchain) are a result of the PEO causing less PEI branched amine interchain interactions resulting in less diffusional limitations and more reactivity between CO_2 and primary and secondary amines.

Furthermore, dynamic mechanical analysis (DMA) showed that a pure PEO film has a decreased tan δ maximum value of 0.28 in comparison to films containing amorphous PEI. This increased storage modulus in PEO reinforces our observations in the XRD data showing that PEO maintains an ordered structure (Figure 25d). Unlike PEI, which behaves as a highly viscous liquid with many entangled amines, PEO has a low tan δ due to a larger storage modulus due to the crystalline order in the material. When PEO is added into the PEI material, at 2.5:1.5 and 3:1 PEO:PEI blend films the tan δ maximum was 0.32. As the ratio of PEO to PEI increases, the tan δ signal decreased due to the physical disruptions of PEO solvating and shielding branched PEI amines as PEO tries to maintain its crystal structure. As a result, this orders the polymer matrix, creates less amine entanglements, and increased the storage modulus in the blended material. This ordering of the PEI by PEO at the 3:1 PEO:PEI ratio produces a tan δ maximum in the material capable of interacting with CO_2. More specifically, this tan δ maximum caused by the PEO allows for less amine entanglements which causes more surface area for CO_2 to adsorb into the material to interact with PEI. Thus, more CO_2 can interact with PEI intrachain amines and yield a better response on the sensor device. Therefore, due to the ability of PEO to provide some structural order to the amorphous PEI there is detection of CO_2 on a 3:1 PEO:PEI blended film.

4.4.5 The Hydrophilic Properties of PEO Further Enhance CO_2 detection

In addition to providing structural changes in the PEI matrix, PEO facilitates water uptake into the polymer matrix, and this allows for more reversible acid-base reactions to occur between

the PEI amines and CO_2. When the 3:1 and 1:1 PEO:PEI blend films were exposed to a humid environment and had their Fourier Transform Infrared Spectroscopy (FTIR) spectra acquired, there was observed water uptake into the blend films (Supporting Information Figure 28). This water uptake in the 3:1 PEO:PEI films is important when detecting CO_2 because these films showed a frequency shift response to CO_2 that was significantly enhanced relative to the resonator functionalized with PEI only (Figures 23b-d). PEI is a highly branched polymer with primary, secondary and tertiary amino groups, and these different chemical environments interact with CO_2 in distinct manners.[51,52] That is, primary and secondary amino groups can directly react with CO_2 to form carbamate groups by a reversible acid-base reaction. More specifically, direct nucleophilic attack on a free CO_2 by a primary or secondary amine forms a zwitterion, which rapidly rearranges to carbamic acid via intramolecular proton transfer. In the presence of another free amine, which now acts as a Brønsted base, the carbamic acid may be converted into a carbamate via intermolecular proton transfer. Thus, these carbamates are stabilized by another amine that becomes protonated to form an ammonium ion. Under dry conditions the reaction stops here; however, the availability of water can further convert the carbamate into stable bicarbonate (Figure 26). As a result, this frees an amine that then can react with more available CO_2 gas. Tertiary amines do not directly react with CO_2 without water. However, there is the possibility that water and CO_2 can form carbonic acid which can be deprotonated by all of the types of substituted amines to form bicarbonate as well. In this alternative route, carbonic acid groups are typically deprotonated at neutral pH by a single amine (i.e., any substitution) instead of multiple amines. Due to a single amine being involved in the deprotonation on the carbonic acid this allows for another amine to be available to attack other carbonic acids that may be present. Regardless of which route is occurring (i.e., direct CO_2 attack or deprotonation of carbonic acid), water does

have a major impact on how the polymer matrix can interact with CO_2. Therefore, PEO in addition to providing order to the PEI and increasing the accessibility of the amines to reversibly react with CO_2 also increases the abundance of water in the polymer matrix when under humid conditions, and this increases the adsorption capacity of CO_2 in the blended film.

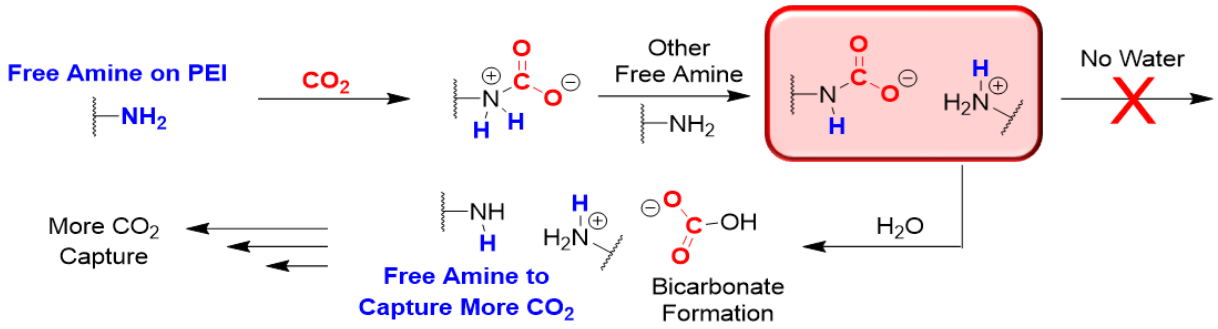

Figure 26. Proposed mechanisms of CO_2 capture by PEI with and without the presence of water. The intermediate step indicated in red is the key step in this reaction process. Without the presence of water the reaction does not proceed and the amine does not become accessible. With the presence of water the reaction can proceed forward due to a free amine which can capture more CO_2.

4.4.6 Conclusions

We have presented a resonant mass sensor treated with a polymer blend of PEO and PEI for the sensitive and selective detection of CO_2. The synergetic blending of PEO and PEI provided an enhanced materials platform for reversible sorption of CO_2. This, combined with a MEMS-based resonant mass sensing platform, created an exceptional sensor for indoor CO_2 monitoring. The small size and low power requirement of these sensors provides the necessary qualifications for wireless and distributed sensing in buildings.[53–55] Further, the readily accessible materials used to manufacture this sensor renders a device that is easy to procure at a low cost. Thus, this unique combination of well-known materials allows for a novel CO_2 sensor that can be seamlessly integrated into smart building environments.

4.4.7 Acknowledgments

This work was reprinted with permission from Siefker, Z. A.; Hodul, J. N.; Zhao, X.; Bajaj, N.; Brayton, K. M.; Flores-Hansen, C.; Zhao, W.; Chiu, G. T.-C.; Braun, J. E.; Rhoads, J. F.; Boudouris, B.W. Sci. Rep. 2021, 11, 13237. Copyright 2021 Scientific Reports, Nature. The information, data, or work presented herein was funded in part by the Advanced Research Projects Agency-Energy (ARPA-E), U.S. Department of Energy, under Award Number DE-AR0000943. The views and opinions of authors expressed herein do not necessarily state or reflect those of the United States Government or any agency thereof.

4.5 Supporting Information Figures

Table 2. A comparison of device performance using PEI and PEO

	PEI dry	*3:1 PEO:PEI dry*	*3:1 PEO:PEI 10% RH*	*3:1 PEO:PEI 80% RH*
Interpolated sensitivity	-0.0502 Hz ppm^{-1} CO_2	-0.1271 Hz ppm^{-1} CO_2	-0.1590 Hz ppm^{-1} CO_2	-0.2349 Hz ppm^{-1} CO_2

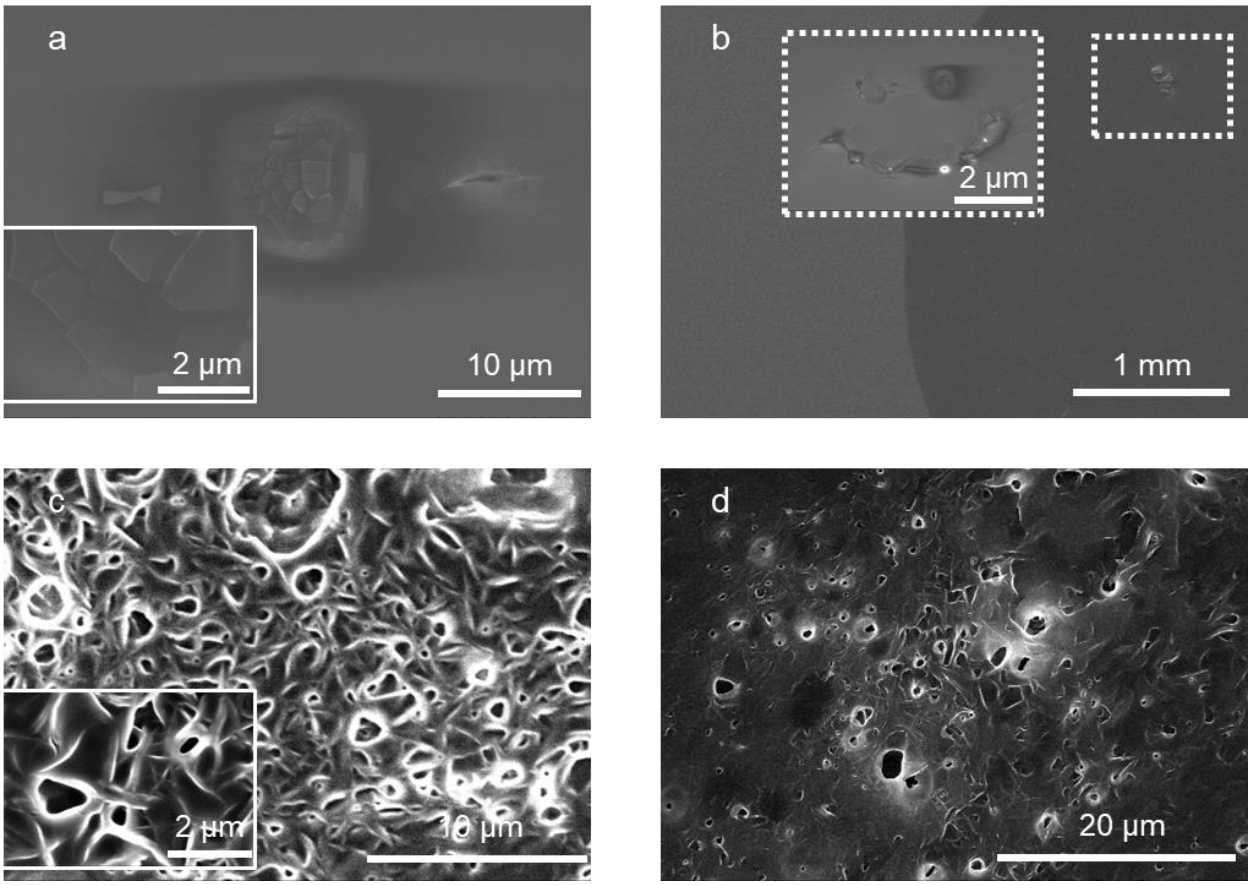

Figure 27. (a) and (b) SEM images of a PEI film after being drop cast onto a silicon wafer and dried for 12 h under vacuum. The two panels show the same film at two different magnification levels. (c) and (d) SEM images of a 1:1 PEO:PEI (by weight) blend film after being drop cast onto a silicon wafer and dried for 12 h under vacuum. The two panels show the same film at two different magnification levels.

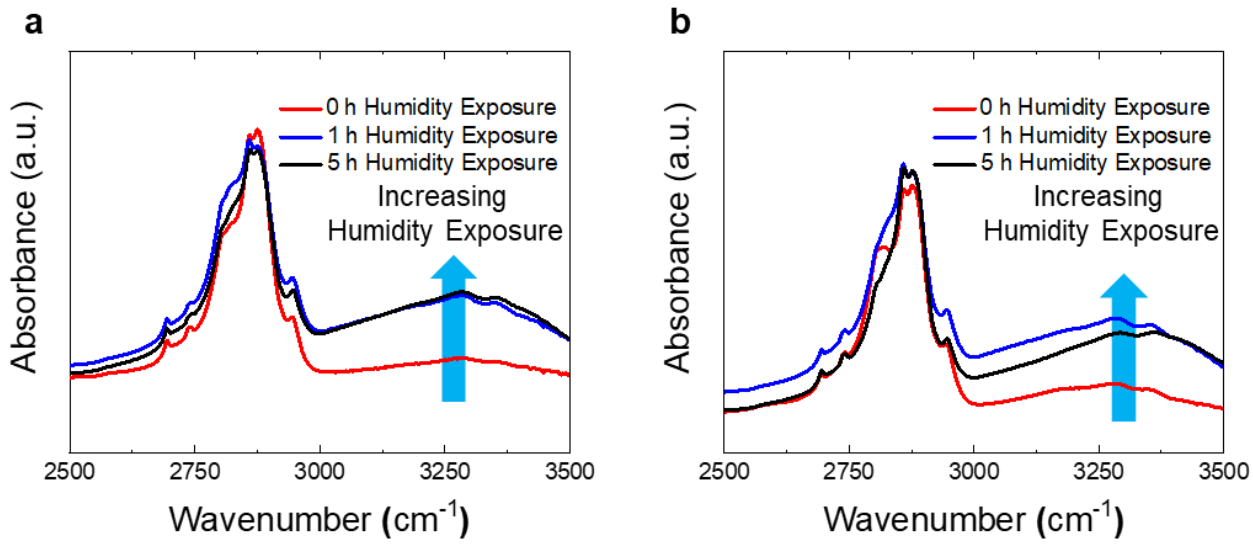

Figure 28. (a) FTIR spectra of a 1:1 PEO:PEI polymer blend film after being annealed and dried under vacuum to remove any excess solvent and exposed to 40% relative humidity at room temperature for up to 5 hours. (b) FTIR spectra of a 3:1 PEO:PEI polymer blend film after being annealed and dried under vacuum to remove any excess solvent and exposed to 40% relative humidity at room temperature for up to 5 hours. The broad OH stretch is observed at 3300 cm^{-1}.

4.6 References

(1) EPA. *Report to Congress on Indoor Air Quality (Vol. 2; Report No. EPA/400/1-89/001C)*; 1989.

(2) European Comission. Indoor Air Pollution: New EU Research Reveals Higher Risks than Previously Thought. *Eur. Com.* **2003**, No. September, IP/03/1278.

(3) Dimosthenis A. Sarigiannis. Combined or Multiple Exposure to Health Stressors in Indoor Built Environments. *World Heal. Organ. Rep. Eur.* **2014**, No. October, 82.

(4) Persily, A.; Gorfain, J. Analysis of Ventilation Data from the U.S. Environmental Protection Agency Building Assessment Survey and Evaluation (BASE) Study. *Environ. Prot.* **2004**.

(5) Shriram, S.; Ramamurthy, K.; Ramakrishnan, S. Effect of Occupant-Induced Indoor CO2 Concentration and Bioeffluents on Human Physiology Using a Spirometric Test. *Build. Environ.* **2019**, *149*, 58–67.

(6) Bhide, A.; Jagannath, B.; Tanak, A.; Willis, R.; Prasad, S. CLIP: Carbon Dioxide Testing Suitable for Low Power Microelectronics and IOT Interfaces Using Room Temperature Ionic Liquid Platform. *Sci. Rep.* **2020**, *10*, 2557.

(7) Azuma, K.; Kagi, N.; Yanagi, U.; Osawa, H. Effects of Low-Level Inhalation Exposure to Carbon Dioxide in Indoor Environments: A Short Review on Human Health and Psychomotor Performance. *Environ. Int.* **2018**, *121*, 51–56.

(8) Satish, U.; Mendell, M. J.; Shekhar, K.; Hotchi, T.; Sullivan, D.; Streufert, S.; Fisk, W. J. Is CO_2 an Indoor Pollutant? Direct Effects of Low-to-Moderate CO_2 Concentrations on Human Decision-Making Performance. *Environ. Health Perspect.* **2012**, *120*, 1671–1677.

(9) Du, B.; Tandoc, M. C.; Mack, M. L.; Siegel, J. A. Indoor CO2 Concentrations and Cognitive Function: A Critical Review. *Indoor Air* **2020**, No. November 2019, 1–16.

(10) Gerlach, G.; Lambrecht, A.; Oelßner, W. Analytical Methods for the Detection of Gaseous CO_2. *Carbon Dioxide Sensing*. April 2019, 45–85.

(11) Murray, J. N.; Doe, J. B. Gas Chromatography Method for Traces of Carbon Dioxide in Air. *Anal. Chem.* **1965**, *37*, 941–942.

(12) Qiao, S.; Qu, Y.; Ma, Y.; He, Y.; Wang, Y.; Hu, Y.; Yu, X.; Zhang, Z.; Tittel, F. K. A Sensitive Carbon Dioxide Sensor Based on Photoacoustic Spectroscopy with a Fixed Wavelength Quantum Cascade Laser. *Sensors* **2019**, *19*, 4187.

(13) Chen, C.; Ren, Q.; Wang, Y.-Z. Review on Multi Gas Detector Using Infrared Spectral Absorption Technology. *Appl. Spectrosc. Rev.* **2019**, *54*, 425–444.

(14) Dinh, T.-V.; Choi, I.-Y.; Son, Y.-S.; Kim, J.-C. A Review on Non-Dispersive Infrared Gas Sensors: Improvement of Sensor Detection Limit and Interference Correction. *Sensors Actuators B Chem.* **2016**, *231*, 529–538.

(15) Fisk, W. J.; Sullivan, D. P.; Faulkner, D.; Eliseeva, E. CO_2 monitoring for demand controlled ventilation in commercial buildings. **2010**, No. 600303000.

(16) Shrestha, S. S. Performance Evaluation of Carbon-Dioxide Sensors Used in Building HVAC Applications. **2009**.

(17) Apte, M. G. A Review of Demand Control Ventilation. **2006**, No. May.

(18) Vincent, T. A.; Gardner, J. W. A Low Cost MEMS Based NDIR System for the Monitoring of Carbon Dioxide in Breath Analysis at Ppm Levels. *Sensors Actuators B Chem.* **2016**, *236*, 954–964.

(19) DeMartini, B. E.; Rhoads, J. F.; Zielke, M. A.; Owen, K. G.; Shaw, S. W.; Turner, K. L. A Single Input-Single Output Coupled Microresonator Array for the Detection and Identification of Multiple Analytes. *Appl. Phys. Lett.* **2008**, *93*, 2006–2009.

(20) Kumar, V.; Boley, J. W.; Yang, Y.; Ekowaluyo, H.; Miller, J. K.; Chiu, G. T. C.; Rhoads, J. F. Bifurcation-Based Mass Sensing Using Piezoelectrically-Actuated Microcantilevers. *Appl. Phys. Lett.* **2011**, *98*, 153510.

(21) Zribi, A.; Knobloch, A.; Tian, W. C.; Goodwin, S. Micromachined Resonant Multiple Gas Sensor. *Sensors Actuators, A Phys.* **2005**, *122* (1 SPEC. ISS.), 31–38.

(22) Adams, J. D.; Parrott, G.; Bauer, C.; Sant, T.; Manning, L.; Jones, M.; Rogers, B.; McCorkle, D.; Ferrell, T. L. Nanowatt Chemical Vapor Detection with a Self-Sensing, Piezoelectric Microcantilever Array. *Appl. Phys. Lett.* **2003**, *83*, 3428–3430.

(23) Siefker, Z. A.; Murray, A. K.; Zhao, X.; Boudouris, B. W.; Bajaj, N.; Chiu, G. T. C.; Rhoads, J. F. A Resonant CO_2 Sensor Functionalized with a Polymerized Ionic Liquid. *Proc. IEEE Sensors* **2019**, *2019-Octob*.

(24) Gupta, A.; Akin, D.; Bashir, R. Detection of Bacterial Cells and Antibodies Using Surface Micromachined Thin Silicon Cantilever Resonators. *J. Vac. Sci. Technol. B Microelectron. Nanom. Struct.* **2004**, *22*, 2785–2791.

(25) Gupta, A.; Akin, D.; Bashir, R. Single Virus Particle Mass Detection Using Microresonators with Nanoscale Thickness. *Appl. Phys. Lett.* **2004**, *84*, 1976–1978.

(26) Swager, T. M. Sensor Technologies Empowered by Materials and Molecular Innovations. *Angew. Chemie Int. Ed.* **2018**, *57*, 4248–4257.

(27) Xie, G. Z.; Kang, T.; Zhou, Y.; Xie, T.; Tai, H. L.; Jiang, Y. D. QCM Sensors Based on PEI Films for CO2 Detection. *J. Electron. Sci. Technol.* **2015**, *13*, 181–187.

(28) Sun, B.; Xie, G.; Jiang, Y.; Li, X. Comparative CO2-Sensing Characteristic Studies of PEI and PEI/Starch Thin Film Sensors. *Energy Procedia* **2011**, *12*, 726–732.

(29) Meth, S.; Goeppert, A.; Prakash, G. K. S.; Olah, G. A. Silica Nanoparticles as Supports for Regenerable CO_2 Sorbents. *Energy & Fuels* **2012**, *26*, 3082–3090.

(30) Hampe, E. M.; Rudkevich, D. M. Exploring Reversible Reactions between CO_2 and Amines. *Tetrahedron* **2003**, *59*, 9619–9625.

(31) Ganji, M.; Docter, M.; Le Grice, S. F. J.; Abbondanzieri, E. A. DNA Binding Proteins Explore Multiple Local Configurations during Docking via Rapid Rebinding. *Nucleic Acids Res.* **2016**, *44*, 8376–8384.

(32) ASHRAE. *ANSI/ASHRAE Standard 62.1-2010 Ventilation for Acceptable Indoor Air Quality*; Atlanta, GA, 2010.

(33) Sauerbrey, G. Verwendung von Schwingquarzen Zur Wagung d ¨ Unner ¨ Schichten Und Zur Mikrowagung. *Zeitschrift fur Phys.* **1959**, *155*, 206–222.

(34) Martin, S. J.; Granstaff, V. E.; Frye; G.C. Characterization of a Quartz Crystal Microbalance with Simultaneous Mass and Liquid Loading. *Anal. Chem.* **1991**, *63*, 2272–2281.

(35) Cui, Y.; Schubert, B. A.; Jahren, A. H. A 23 m.y. Record of Low Atmospheric CO_2. *Geology* **2020**, *48*, 888–892.

(36) Occupational Safety and Health Administration, U. S. D. of L. *Occupational Exposure Limits*; 2019.

(37) Rice, S. A. Human Health Risk Assessment of CO2: Survivors of Acute High-Level Exposure and Population Sensitive to Prolonged Low-Level Exposure. *Third Annu. Conf. Carbon Sequestration* **2004**, No. 056559, 1–9.

(38) Podoll, R. T.; Irwin, K. C. Sorption of Cationic Oligomers on Sediments. *Environ. Toxicol. Chem.* **1988**, *7*, 405–415.

(39) ASHRAE. *ASHRAE/ANSI Standard 55-2010 Thermal Environmental Conditions for Human Occupancy*; Atlanta, GA, 2010.

(40) Wang, D.; Wang, X.; Ma, X.; Fillerup, E.; Song, C. Three-Dimensional Molecular Basket Sorbents for CO_2 Capture: Effects of Pore Structure of Supports and Loading Level of Polyethylenimine. *Catal. Today* **2014**, *233*, 100–107.

(41) Li, K.; Jiang, J.; Yan, F.; Tian, S.; Chen, X. The Influence of Polyethyleneimine Type and Molecular Weight on the CO_2 Capture Performance of PEI-Nano Silica Adsorbents. *Appl. Energy* **2014**, *136*, 750–755.

(42) Zhang, W.; Liu, H.; Sun, C.; Drage, T. C.; Snape, C. E. Capturing CO_2 from Ambient Air Using a Polyethyleneimine–Silica Adsorbent in Fluidized Beds. *Chem. Eng. Sci.* **2014**, *116*, 306–316.

(43) Sakwa-Novak, M. A.; Tan, S.; Jones, C. W. Role of Additives in Composite PEI/Oxide CO2 Adsorbents: Enhancement in the Amine Efficiency of Supported PEI by PEG in CO2 Capture from Simulated Ambient Air. *ACS Appl. Mater. Interfaces* **2015**, *7*, 24748–24759.

(44) Wang, L.; Al-Aufi, M.; Pacheco, C. N.; Xie, L.; Rioux, R. M. Polyethylene Glycol (PEG) Addition to Polyethylenimine (PEI)-Impregnated Silica Increases Amine Accessibility during CO2 Sorption. *ACS Sustain. Chem. Eng.* **2019**, *7*, 14785–14795.

(45) Kobayashi, S.; Shirasaka, H.; Suh, K.-D.; Uyama, H. Viscosity Behaviors and Gel Properties of Linear and Branched Polyethylenimines: Effects of Micro-Structures. *Polym. J.* **1990**, *22*, 442–446.

(46) Takahashi, Y.; Tadokoro, H. Structural Studies of Polyethers, (-(CH2)m-O-)n. X. Crystal Structure of Poly(Ethylene Oxide). *Macromolecules* **1973**, *6*, 672–675.

(47) Yang, S.; Liu, Z.; Liu, Y.; Jiao, Y. Effect of Molecular Weight on Conformational Changes of PEO: An Infrared Spectroscopic Analysis. *J. Mater. Sci.* **2015**, *50*, 1544–1552.

(48) Couchaux, G.; Barth, D.; Jacquin, M.; Faraj, A.; Grandjean, J. Kinetics of Carbon Dioxide with Amines. I. Stopped-Flow Studies in Aqueous Solutions. A Review. *Oil Gas Sci. Technol.* **2014**, *69*, 865–884.

(49) Kortunov, P. V; Siskin, M.; Paccagnini, M.; Thomann, H. CO2 Reaction Mechanisms with Hindered Alkanolamines: Control and Promotion of Reaction Pathways. *Energy & Fuels* **2016**, *30*, 1223–1236.

(50) Oikonomou, P.; Botsialas, A.; Olziersky, A.; Kazas, I.; Stratakos, I.; Katsikas, S.; Dimas, D.; Mermikli, K.; Sotiropoulos, G.; Goustouridis, D.; et al. A Wireless Sensing System for Monitoring the Workplace Environment of an Industrial Installation. *Sensors Actuators, B Chem.* **2016**, *224*, 266–274.

(51) Sutton, F.; Forno, R. Da; Gschwend, D.; Gsell, T.; Lim, R.; Beutel, J.; Thiele, L. The Design of a Responsive and Energy-Efficient Event-Triggered Wireless Sensing System. *Proc. 14th Int. Conf. Embed. Wirel. Syst. Networks (EWSN 2017)* **2017**, 144–155.

(52) Gunay, B.; Shen, W. Connected and Distributed Sensing in Buildings: Improving Operation and Maintenance. *IEEE Syst. Man, Cybern. Mag.* **2017**, *3*, 27–34.

CHAPTER 5. SORPTION KINETICS OF POLY(ETHYLENEIMINE)-POLY(ETHYLENE OXIDE) BLENDS AND THE IMPLICATION FOR LOW-COST, SMALL-SCALE CO_2 SENSORS

Content from this chapter has been submitted for publication and is currently under review.

5.1 Overview

Public health depends on reliable, low-cost methods of measuring indoor air quality (IAQ), and carbon dioxide (CO_2) is often used as a surrogate measure for IAQ. There is an increasing interest in the development of low-cost CO_2 sensors that can be seamlessly integrated into existing ventilation systems for smart and connected healthy buildings. To this aim, microelectromechanical systems-based (MEMS-based) resonant mass sensors functionalized with specific surface chemistries are a promising sensing platform due to their compact size, low-cost, and fast response times. Further, poly(ethyleneimine)-based (PEI-based) materials have been shown to capture CO_2 selectively and reversibly. Here, we report the temperature dependencies of a polymer blend composed of PEI and poly(ethylene oxide) (PEO), as this synergetically blended materials platform is useful as a low-cost, small-scale CO_2 sensing system when coated atop a MEMS-based resonant mass sensor. Importantly, we report how temperature can impact polymer characteristics, which ultimately dictate sensor performance. To achieve this aim, adsorption rate constants and thermodynamic parameters were calculated using a Langmuir model for a series of polymer blends with different compositions. Throughout a range of temperatures relevant to indoor sensing systems, these polymer blends adsorbed less and desorbed more CO_2 with increasing temperature. This was due, in part, to the melting of the polymer materials and a decrease in the availability of PEI amines to capture CO_2. Ultimately, these data provide a deeper understanding of the selection criteria and boundaries to consider when using polymer-based

selective recognition layers in indoor environments and inform the development of low-cost and small-scale IAQ sensors.

5.2 Introduction

It has been estimated that people spend about 90% of their time in indoor locations in modern society, even prior to the start of the current global pandemic.[1] This time inside involves private and public indoor environments, such as homes, gyms, schools, and workplaces. However, these interior locations can contain elevated concentrations of deleterious gas analytes, especially when they are poorly ventilated, which can impact the indoor air quality (IAQ) of these locations.[2] Carbon dioxide (CO_2) is a deleterious gas analyte that, in poorly ventilated spaces, can exist at concentrations of upwards of several thousand parts per million (ppm).[3] At these concentrations, CO_2 can have substantial effects on human cognitive performance with statistically significant and meaningful reductions in decision-making performance.[4–6] However, even at significantly lower concentrations, CO_2 is a useful IAQ metric, because it serves as a proxy measure for human occupancy and the proportional impacts on IAQ.[7,8] Thus, there is an increasing interest in developing low-cost IAQ sensors for smart and connected buildings to monitor the concentration of CO_2 while being seamlessly integrated with existing ventilation systems. Among the potential gas sensing technologies available, microelectromechanical systems (MEMS) gas sensors (i.e., electrochemical, acoustic, and optical sensors) are a promising avenue for low-cost and small-scale gas sensing applications.[9–13] In particular, adsorption-based electrochemical and electromechanical gas sensors have demonstrated potentials for carbon dioxide (CO_2) monitoring in buildings,[14–19] which is a market that has historically been dominated by optical non-dispersive infrared (NDIR) sensors.[20–24] In principle, in electrochemical and electromechanical gas sensor devices, the adsorption of a target gas analyte onto a chemically selective recognition layer induces

a physical property change in the material, which is then transduced into a signal by the gas sensor. This physical property change can be a change in conductivity (i.e., electrochemical devices) or a change in mechanical behavior (i.e., resonance frequency). Thus, the careful selection of a chemical selective recognition layer allows for a selective gas sensor for CO_2 that is compatible with modern IAQ monitoring needs (e.g., low cost and low power devices).

Among the potential chemically selective materials for CO_2 sensing, poly(ethyleneimine) (PEI) is an intriguing polymer as PEI can capture, and even store, CO_2.[25–32] This viability, in part, is because PEI contains primary and secondary amines that reversibly interact with CO_2 via acid-base redox reactions.[33–35] The ability of PEI to reversibly adsorb CO_2 makes it an attractive candidate for sensing applications.[15,36–44] Further, the blending of additives into a PEI matrix can enhance the uptake of CO_2 in the materials system.[42,44–47] This is thought to occur because the additives disrupt intrachain and interchain amine entanglements in the PEI matrix, which increases the available number of PEI surface sites that interact with CO_2 molecules. For example, PEI combined with starch is more effective than PEI alone for developing CO_2 sensors.[42,44] Additionally, PEI and poly(ethylene oxide) (PEO) blends have enhanced CO_2 uptake relative to pristine PEI thin films.[14] These results are important as they provide performance metrics relevant to CO_2 monitoring for a conditioned indoor environment. However, the sensing of CO_2 with a PEI-PEO polymer blend is still limited for IAQ monitoring because the materials system was only evaluated across a limited temperature range of 4° C, whereas a much larger temperature range is appropriate for indoor applications. Furthermore, data across a larger temperature range is desirable for determining temperature-related sensor dependencies and optimizing sensing material performance. Thus, characterizing the temperature-dependent adsorption kinetics of CO_2

for this polymer platform provides critical information for this polymer system in terms of a promising end-use application.

Here, we evaluate the role of temperature on the sorption kinetics of CO_2 into PEI-PEO blends that have been deposited on a small-scale electromechanical resonant mass sensor to determine the underlying environmental factors that impact the practical application of the sensor. To achieve this aim, measurements were made across an extended temperature range, to better understand and characterize the polymer blend response. Using these data, the temperature-dependent kinetics of the resonant mass sensor functionalized with a PEI-based material were determined in a manner similar to other quartz crystal microbalance-based (QCM-based) adsorption kinetic studies.[48–51] In this way, this study establishes the robust performance of PEI-based polymer blends, quantifies key sorption characteristics, and provides a means by which to further develop low-cost and small-scale CO_2 sensors for indoor environments.

5.3 Experimental Information

5.3.1 Materials

All of the chemicals use in this study were purchased from Sigma-Aldrich, and they were used as received unless otherwise noted. The hyperbranched PEI utilized has a reported a weight-average molecular weight of 25 kg mol^{-1}. The PEO utilized was purchased from Alfa Aesar, and the weight-average molecular weight of the PEO was 100 kg mol^{-1}. The methanol utilized to prepare the polymer samples was anhydrous grade and stored under nitrogen.

5.3.2 General Methods

A Hitachi S-4800 Field Emission scanning electron microscope (SEM) was utilized to image the polymer samples. For these images, 1.0 μL of a 1 mg mL^{-1} polymer blend in methanol

solution were drop-cast on polished silicon dioxide substrates and dried overnight under vacuum. The films were then coated with 20 nm of carbon prior to imaging using a SPI carbon sputter coater to prevent charging during image acquisition. For the samples that were heated, the polymer films were heated to greater than 343.15 K (max 423.15 K) and held to isotherm for 15 min. The samples were then immediately sputter coated with 20 nm of carbon prior to imaging. Attenuated total internal reflectance-Fourier transform infrared (ATR-FTIR) spectroscopy was performed using a diamond substrate of a Thermo-Nicolet Nexus FTIR, using a deuterated triglycine sulfate KBr detector with a KBr beam splitter. Under a dry nitrogen purge, 100 scans were acquired over a range of $800\ cm^{-1} \leq \nu \leq 4500\ cm^{-1}$ for each sample. X-ray diffraction (XRD) measurements were measured with a Rigaku Cu-Kα source ($\lambda = 1.54056$ Å) in parallel beam mode. These samples were acquired while under ambient conditions. The polymer film samples were fabricated using a 240 mg mL^{-1} solution of the polymer blend (by weight ratio) in methanol pipetted into a metal mold and then annealed at 353.15 K while being pressed for at least 10 min. After pressing, these films were dried overnight under vacuum ($P \leq 0.4$ Torr) prior to XRD analysis being performed. A TA Instruments Q20 Series differential scanning calorimeter (DSC) was used for thermal transition analysis. The samples were sealed in Tzero hermetic pans, were first annealed at 348.15 K under a nitrogen gas purge, and then cooled to 213.15 K, before the trace that started at 213.15 K and ended at 348.15 K (at a scan rate of 1.0983 K min^{-1}) was collected.

5.3.3 Experimental Adsorption Apparatus and Procedure

The testing protocols utilized in this work are similar to those previously reported.[14] Experiments were performed using the setup shown in Figure 35. Gas tanks of nitrogen and 1% CO_2 and 99% nitrogen were connected to a series of mass flow controllers (MFC; MKS, 1179C) in parallel. The polymer blend-based resonant mass sensors were enclosed in a test chamber with

an approximate volume of 163 cm^3. A recirculating chiller (Thermo Fisher; Polar Series Accel 500 LT) and custom thermal blanket were utilized for temperature control of the test chamber. The recirculating chiller provides a working temperature range of 248.15 to 353.15 K. Prior to data collection at each test condition, the test chamber was flushed with nitrogen for 3 h at each reported temperature to allow the chamber to reach a steady-state baseline condition. Then, CO_2 gas was injected into the chamber to achieve the reported concentrations. A frequency counter was developed in LabVIEW to monitor the oscillation frequency of each oscillator with a 1 Hz resolution.

5.3.4 Device Fabrication

The device instrumentation utilized in this work was previously reported.[14] This included a small-scale resonator (Kyocera Corp., CX3225) and a crystal oscillator driver (Texas Instruments, SN74LVC1GX04) implemented in a Pierce oscillator circuit. Upon construction of the oscillator circuit, the cap on the resonator packaging was removed to expose the resonant element for functionalization. To coat a pristine PEI thin film, a solution of 0.1% (by volume) of PEI in methanol was created. For creating the 3:1 PEO:PEI thin films, PEI and PEO were dissolved in methanol to generate a solution of 0.1% (by volume) of PEI and 0.3% (by volume) of PEO. Then, 1 μL of each solution was deposited onto each respective resonator. The resonators were then placed under vacuum at 343.15 K for 24 hr to remove any residual methanol leaving behind PEI and the 3:1 PEO:PEI blend, on each respective substrate.

5.3.5 Adsorbed Mass and Resonance Frequency Correlation

Resonance frequency measurements of the small-scale resonators were employed to monitor the CO_2 sorption process. As CO_2 adsorbs on the resonator (increasing the total mass) the

oscillation frequency of the resonator decreases, allowing real-time monitoring of the sorption kinetics. The observed frequency shift is correlated to the deposited mass by[52,53]

$$\Delta m = \frac{1}{S_m}\frac{\Delta f}{f_0} \quad (1)$$

where Δm is the change in mass, S_m is the mass sensitivity of the sensor, f_0 is the resonance frequency of the unloaded resonator, and Δf is the change in resonance frequency. Thus, an increase in the mass of CO_2 adsorbed would result in a proportional decrease in resonance frequency.

5.4 Results and Discussion

5.4.1 Characterization of Polymer Blend

As shown previously, a 3:1 PEO:PEI polymer blend, when drop cast and dried on a resonant mass sensor, yields a nanoscale structure that affords high-performing, robust, and reliable CO_2 gas detection sensors.[14] This detection is possible due to the crystalline features of PEO which can induce pores into a PEI matrix by disrupting the strong intermolecular amine interactions that can limit the interaction of CO_2 with the polymer matrix. When the amines are disrupted, the CO_2 gas can then better interact with primary and secondary amines in PEI and transduce a response to the resonator. This pore formation, occurring at ambient temperatures, is observed via SEM imaging (Figure 29a). However, it is important to note that this detection of CO_2 gas is reliant on PEO maintaining its crystalline structure and keeping the interchain and intrachain amines accessible to interact with CO_2. At elevated temperatures (i.e., T > 343 K), there is a loss of the porous features in the polymer film as observed in SEM imaging (Figure 29b). This implies that the polymer film at elevated temperature conditions is entering a melt state in which there is a disappearance of PEO crystalline features and the reformation of strong amine intermolecular forces in the polymer

matrix. Thus, it is important to maintain an operation temperature in which the polymer is not melted, and the porous structure is maintained as it allows for CO_2 to diffuse into the polymer matrix and interact with free amine moieties.

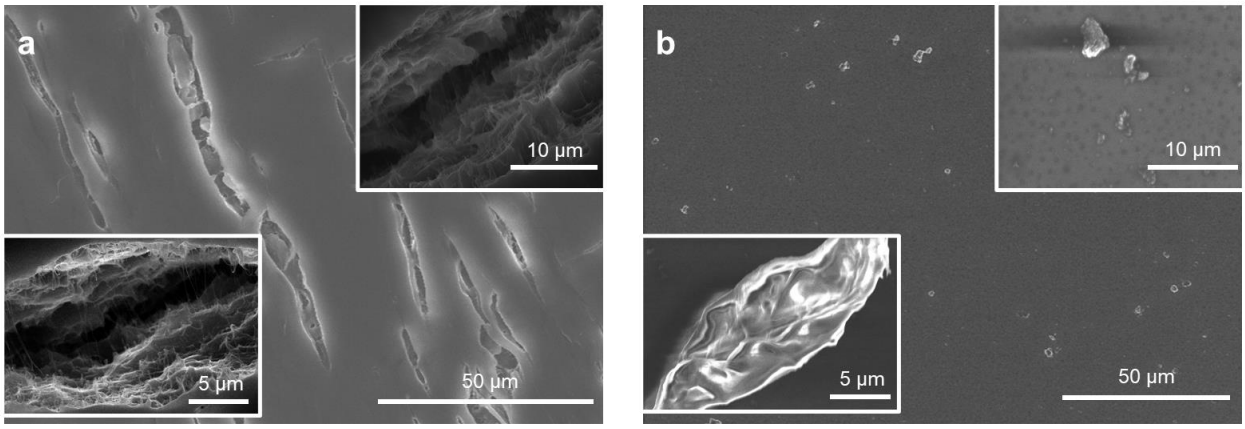

Figure 29. SEM images of a 3:1 PEO:PEI blend film. (a) Room temperature image of the polymer film. These images are highlighting the micron-sized pores formed in the polymer matrix. All of the images shown are of the same film but in different sections and locations. (b) A polymer film exposed to a > 343.15 K (max 423.15 K), isotherm for 15 min, and then imaged. These images are highlighting the melting of the polymer film and the loss of porous structure. All of the images shown are of the same film but in different sections and locations.

FTIR analysis showed that there were distinct features of both PEI and PEO expressed in the 3:1 PEO:PEI polymer film (Figure 30a). PEI N-H stretching (3270 cm^{-1}), PEO C-H stretching (2880 cm^{-1}), PEI N-H bending (1580 cm^{-1}), PEO C-C stretching (1475 cm^{-1}), PEO O-H bending (1380 cm^{-1}), PEO CH_2 waging (1310 cm^{-1}), and PEO C-O-C stretching (1090 cm^{-1}) were observed. These spectra peak locations are consistent with previous FTIR analysis studies of PEO and PEI.[54–57] The combination of PEO and PEI features expressed in the 3:1 PEO:PEI film without any shifts or alterations in peak locations implied that there were no chemical bond formations occurring in the polymer blend; rather, this was a miscible polymer blend. XRD analysis showed that a 3:1 PEO:PEI film expressed the monoclinic crystal structure of PEO.[58,59] These characteristics occurred at $q = 1.3$ $Å^{-1}$ and $q = 1.65$ $Å^{-1}$ (Figure 30b). There were no crystalline features observed

in the PEI because the branched PEI was an amorphous polymer. Notably, the DSC traces of the materials showed features which correspond to the melting and crystalline properties of PEO and the 3:1 PEO:PEI polymer blend (Figure 30c). DSC heating traces of the polymer films showed that PEO has a melting point (T_m) of 338.15 K and 3:1 PEO:PEI has a T_m of 331.15 K. PEI, a hyperbranched polymer, when incorporated into PEO did not allow for PEO to pack its polymer chains as efficiently and thus this lowered the packing density and the melting point in the 3:1 PEO:PEI polymer blend. This is interesting as it corresponded to the SEM image (Figure 29b), which showed melting features as the 3:1 polymer film was heated past 333.15 K and lost its porosity in the polymer film. Additionally, in the DSC cooling trace, PEO had a crystallization temperature (T_c) of 317.15 K while a 3:1 PEO:PEI film had a T_c of 310.15 K owing again to the hyperbranched nature of PEI being incorporated into the polymer blend. This hyperbranched structure of PEI did not allow for PEO to maintain its packing of polymer chains and thus it formed its crystalline structure at a lower temperature (Figure 30c). Upon integration of these heating and cooling traces, the 3:1 PEO:PEI showed an integration value of 70% of the intensity of PEO in both the heating and cooling traces, individually. Overall, a 3:1 PEO:PEI polymer blend showed chemical and structural features of both PEO and PEI. These features play a critical role in the performance of detecting and interacting with CO_2. Additionally, it is important to note that a 3:1 PEO:PEI polymer blend offers optimal performance under conditions that are likely to be encountered in an interior location.

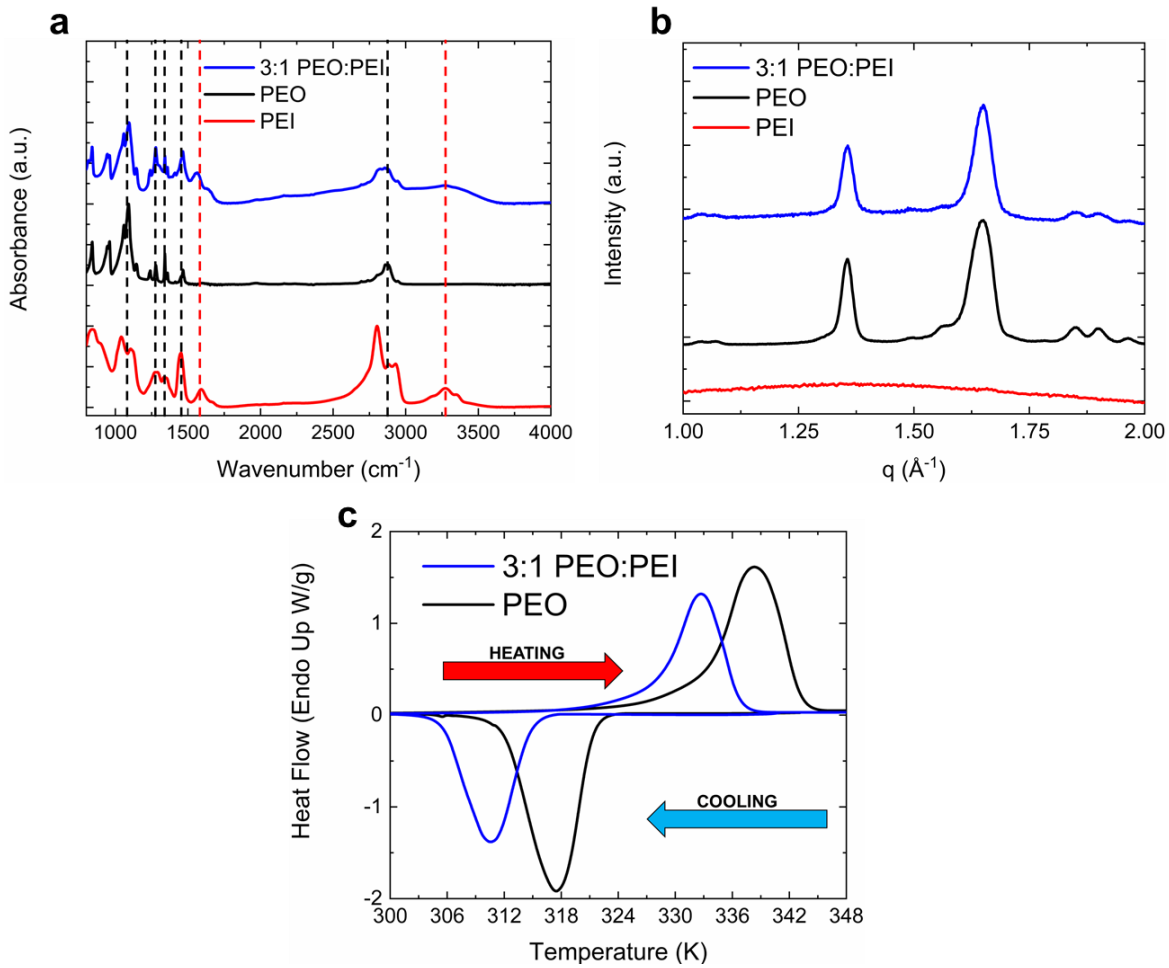

Figure 30. (a) FTIR spectra of PEI, PEO, and 3:1 PEO:PEI polymer films. Dashed lines highlight the spectrum peaks at 3270 cm^{-1}, 2880 cm^{-1}, 1580 cm^{-1}, 1475 cm^{-1}, 1380 cm^{-1}, 1310 cm^{-1}, and 1090 cm^{-1} which occur in the 3:1 PEO:PEI polymer sample corresponding to the peaks in PEO and PEI. (b) XRD patterns of PEI, PEO, 3:1 PEO:PEI blend films. Highlighting the crystal structure of PEO expressed in the 3:1 PEO:PEI polymer film. (c) DSC heating and cooling traces of PEO and 3:1 PEO:PEI polymer films. Highlighting that PEO has a T_m of 338.15 K and T_c of 317.15 K while a 3:1 PEO:PEI film has a T_m of 331.15 K and a T_c of 310.15 K. Upon integration, 3:1 PEO:PEI heating and cooling peaks were 70% of the PEO peaks area, respectively.

5.4.2 CO_2 Adsorption-Desorption Profiles

To determine if these structural characteristics were impacting the sensor performance, the CO_2 adsorption-desorption performance was measured across CO_2 concentrations between 0% and 1% for both pristine PEI thin films and the 3:1 PEO:PEI blend thin films. A sample time-series depiction of the frequency data (Figure 31) shows the sorption characteristics of the device and

that it is a reversible process. The addition of CO_2 results in a rapid decrease in the resonance frequency of the device as CO_2 interacts with the PEI and increases the total mass of the resonator. Upon removal of CO_2, immediate desorption occurs, and the resonance frequency of the device increases, due to a decrease in total mass.

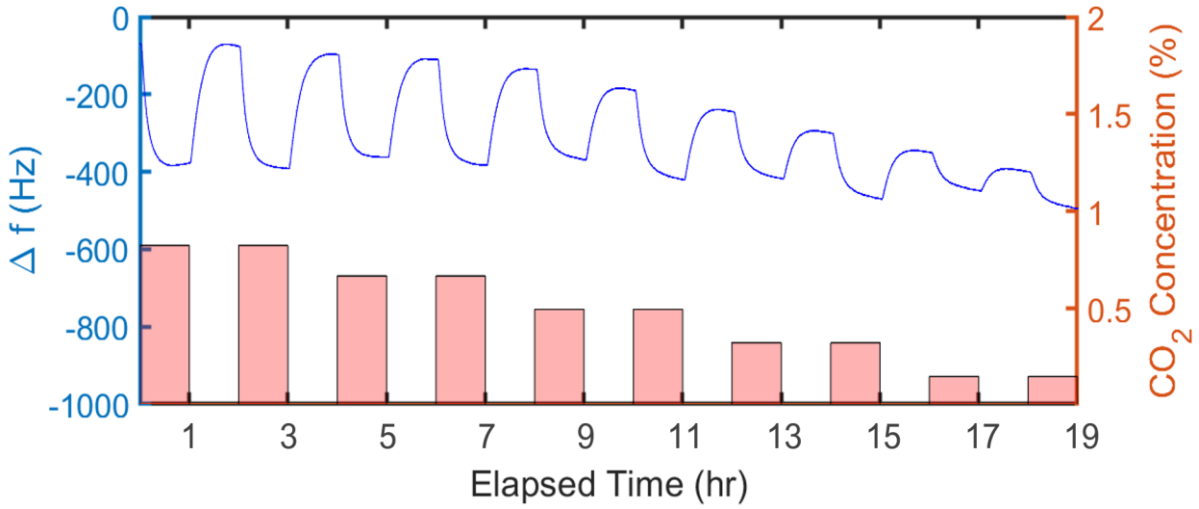

Figure 31. Representative time-series data showing the response of 3:1 PEO:PEI functionalized resonator to concentrations of CO2 between 0% and 0.8 % in a 325 K environment.

Figure 32a and Supporting Information Figure 36a show the adsorption-desorption profiles of a 3:1 PEO:PEI blend film and of pristine PEI film, respectively, for 4 consecutive 1-hr cycles across a range of temperatures relevant to indoor CO_2 monitoring. A clear trend of increasing temperature causing a decrease in the net amount of CO_2 adsorbed, relative to the available PEI, is seen. Further, during the four consecutive adsorption-desorption cycles, there was no sign of deteriorating sorbent behavior. This stability is consistent with other studies on PEI-functionalized solid sorbents where materials persisted after numerous adsorption-desorption cycles.[32,60,61] As shown in Figure 32b and Supporting Information Figure 36b, this trend continued

across a range of CO_2 concentrations for each temperature condition, as indicated by the small error bars (representing one standard deviation from the average).

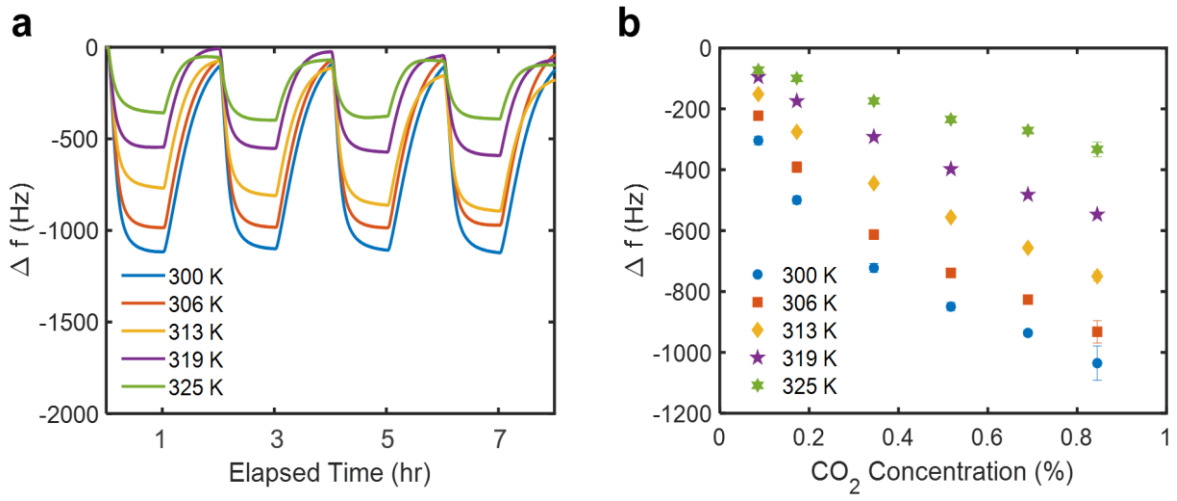

Figure 32. (a) CO_2 adsorption-desorption cycles at various temperatures for a 3:1 PEO:PEI functionalized resonator in response to 1-hr on/off pulses of CO_2 at a concentration of 0.84 %. (b) The mean resonance frequency shift after 1-hr of CO_2 exposure at various concentrations for a 3:1 PEO:PEI functionalized resonator. The error bars represent one standard deviation of the data.

Notably, the resonator coated with a 3:1 PEO:PEI blend (Figure 32) is more sensitive to both changes in CO_2 concentration and changes in temperature, as compared to the resonator coated with pristine PEI (Figure 36). The CO_2 concentration sensitivity is due, in part, to PEO disrupting intrachain and interchain PEI amine entanglement (Figure 29a). This disruption allows for more accessible amines to interact with CO_2, resulting in increased sensitivity to available CO_2. Further, the temperature dependence can be corroborated with a starker decrease in accessible amines with increasing temperature.[46] As temperature increases in the system, the polymers begin to melt with an onset melting point as low as 322 K in a 3:1 PEO:PEI polymer blend (Figure 30c). This melting causes the porous structure in the polymer film to disappear (Figure 29b). Hence, the disruption PEO induced into the PEI polymer matrix no longer occurs because PEO has lost its crystalline texture (Figure 30c). This higher temperature sensitivity of the 3:1 PEO:PEI polymer

blend compared to PEI alone indicates that the system may be thermodynamically controlled and kinetic effects play less of a role in a PEI-dilute system.

5.4.3 Analysis of CO_2 Sorption Kinetics

As shown in Figures 31 and 32a, a 3:1 PEO:PEI coated resonator responds in a reversible manner with respect to changing CO_2 concentration (i.e., a certain partial pressure). The surface coverage of PEI-based materials is governed by a balance of the adsorption and desorption of CO_2, and fit well with a Langmuir model.[62,63] Thus, the change of surface coverage θ of the molecules can be described by a Langmuir equation,

$$\frac{d\theta}{dt} = k_a(1-\theta)C - k_d\theta, \tag{2}$$

where k_a and k_d are the adsorption and desorption rate constants (respectively) and C is the concentration of CO_2. Integrating Equation 2 we have

$$\theta(t) = \frac{C}{C + \frac{k_d}{k_a}}\left(1 - e^{-(k_aC + k_d)t}\right), \tag{3}$$

which illustrate the time dependence of the surface coverage after the concentration change, as a new equilibrium value is approached. In Eq. 3, setting

$$k_{obs} = k_aC + k_d \tag{4}$$

and

$$k_q = \frac{C}{C + \frac{k_d}{k_a}}, \tag{5}$$

results in

$$\theta(t) = k_q(1 - e^{-k_{obs}t}). \tag{6}$$

Equation 6 shows that the surface coverage approaches the equilibrium value exponentially, which matches the time-series data shown in Figures 31 and 32a. As shown in Equation 1, the frequency shift of the resonator is proportional to the mass of adsorbed CO_2, and thus, may be assumed to be proportional to the change in fractional coverage on the polymer surface. Therefore, if the fractional surface coverage θ is measured as a function of time t, k_{obs} and k_q can be determined by

fitting the (negative) frequency shift of the resonator to Equation 6 (Figure 33a). Further, considering Equation 4, a plot of k_{obs} vs. C (Figure 33b) yields a line with slope k_a and intercept of k_d.

By definition, the equilibrium constant K_{eq} for this process is

$$K_{eq} = \frac{k_a}{k_d}. \tag{7}$$

Thus, the free energy of adsorption ΔG_{ads} at a given temperature can be found directly from the equilibrium constant

$$\Delta G_{ads} = -RTlnK_{eq}. \tag{8}$$

Figure 33d shows the calculated free energy of adsorption for both a PEI functionalized resoantor and a 3:1 PEO:PEI functionalized resonator. Because

$$\Delta G_{ads} = \Delta H_{ads} - T\Delta S_{ads}, \tag{9}$$

both ΔH_{ads} and ΔS_{ads} can be determined by carrying out this analysis over a range of temperatures and plotting ΔG_{ads} vs. T (Figure 33d). The negative values for ΔG_{ads} and ΔH_{ads} denote that the reaction occurs spontaneously and is exothermic; which is consistent with other CO_2-PEI adsorption studies.[64–66]

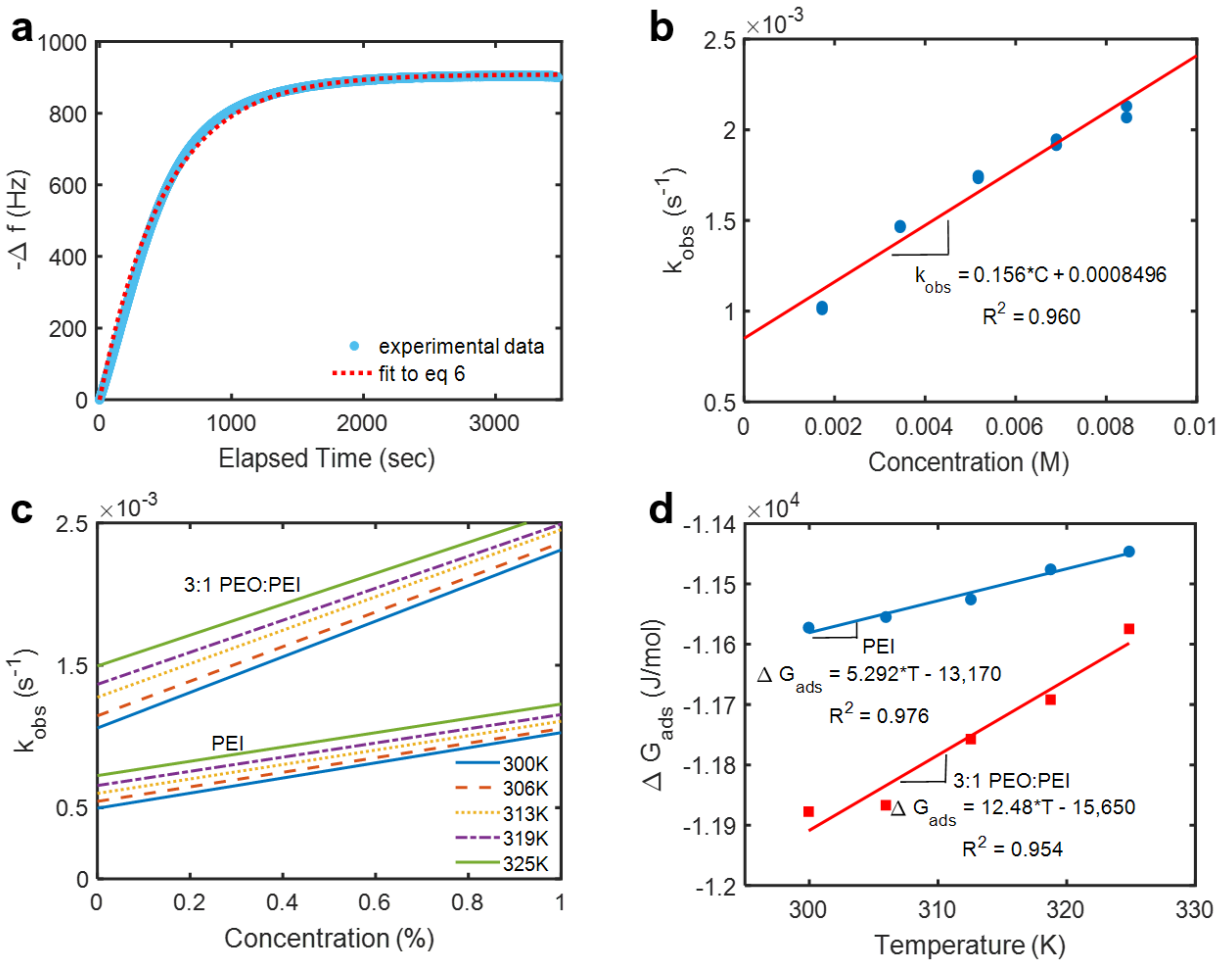

Figure 33. (a) A fit of the Langmuir adsorption isotherm (Equation 6) to frequency data of a 3:1 PEO:PEI functionalized resonator at a concentration of 0.84 % CO_2 and in a 300 K environment. (b) Fit to calculated k_{obs} for a 3:1 PEO:PEI functionalized resonator in a 300 K environment. (c) Fitted relationship between k_{obs} and CO_2 concentration for pristine PEI and a 3:1 PEO:PEI blend for temperatures ranging from 300 K to 325 K. (d) Calculated Gibbs free energy at each temperature condition for pristine PEI and a 3:1 PEO:PEI blend.

Figure 34 shows Arrhenius plots for the adsorption and desorption constants (k_a and k_d) that were obtained from the data in Figures 33b and 33c. Notably, across the measured temperatures, k_a is relatively constant while k_d increases with increasing temperature. This suggests that the decrease in sensor response is due, in part, to a faster desorption rate at higher temperatures. Further, the rate constants for the PEI and 3:1 PEO:PEI blend functionalized resonators showed similar trends with respect to temperature. However, the trends are slightly shifted owing to the

shorter time response of the 3:1 PEO:PEI functionalized resonator relative to the resonator functionalized with only PEI. This is, in part, due to PEO disruption of the intermolecular chains of PEI, which makes the free amines more readily available to interact with CO_2.

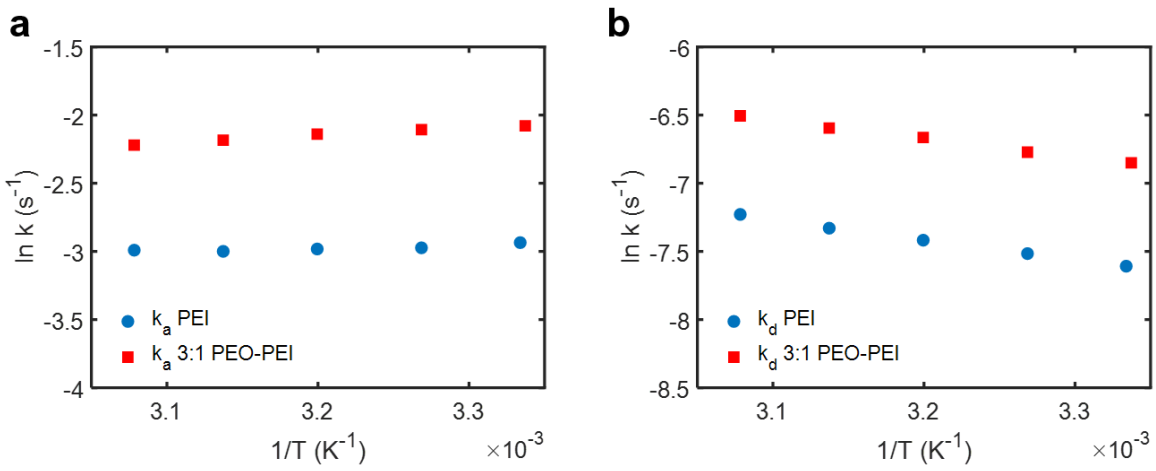

Figure 34. Arrhenius plot showing (a) k_a and (b) k_d for PEI alone and a 3:1 PEO:PEI functionalized resonator. Notably, k_a is relatively constant while k_d increases with increasing temperature. Thus, the decrease in response can partly be attributed to a faster desorption rate at higher temperatures.

5.5 Conclusions

Adsorption of CO_2 into PEI and 3:1 PEO:PEI polymer thin films coated atop resonant mass sensors was investigated over a range of conditions relevant to indoor sensing environments. Sensor performance was measured across an extended temperature range to better understand the capabilities and boundaries of resonant mass sensors functionalized with a PEI-based polymer system. A Langmuir model was fit to the data, from which adsorption rate constants and basic thermodynamic parameters were calculated to describe the sorption of CO_2 on the sensor. Throughout a range of temperatures relevant to indoor sensing systems, these polymer materials adsorbed less and desorbed more CO_2 with increasing temperature. This was due, in part, to the melting of the polymer materials. Specifically, in a 3:1 PEO:PEI polymer blend, such melting decreases the crystalline features of PEO in the PEI matrix and ultimately causes a loss of porosity

in the polymer films. Further, the 3:1 PEO:PEI blended material adsorbed more CO_2, at a faster rate, than PEI alone due to the crystalline features of PEO disrupting strong interchain and intrachain amine interactions which limit the interaction of CO_2 gas into the polymer matrix. Thus, the 3:1 PEO:PEI blended polymer system provides higher sensitivity and faster response times for indoor sensing applications over PEI alone and will perform well until the PEO moiety melts.

5.6 Acknowledgements

The information, data, or work presented herein was funded in part by the Advanced Research Projects Agency-Energy (ARPA-E), U.S. Department of Energy, under Award Number DE-AR0000943. The views and opinions of authors expressed herein do not necessarily state or reflect those of the United States Government or any agency thereof.

5.7 Supporting Information Figures

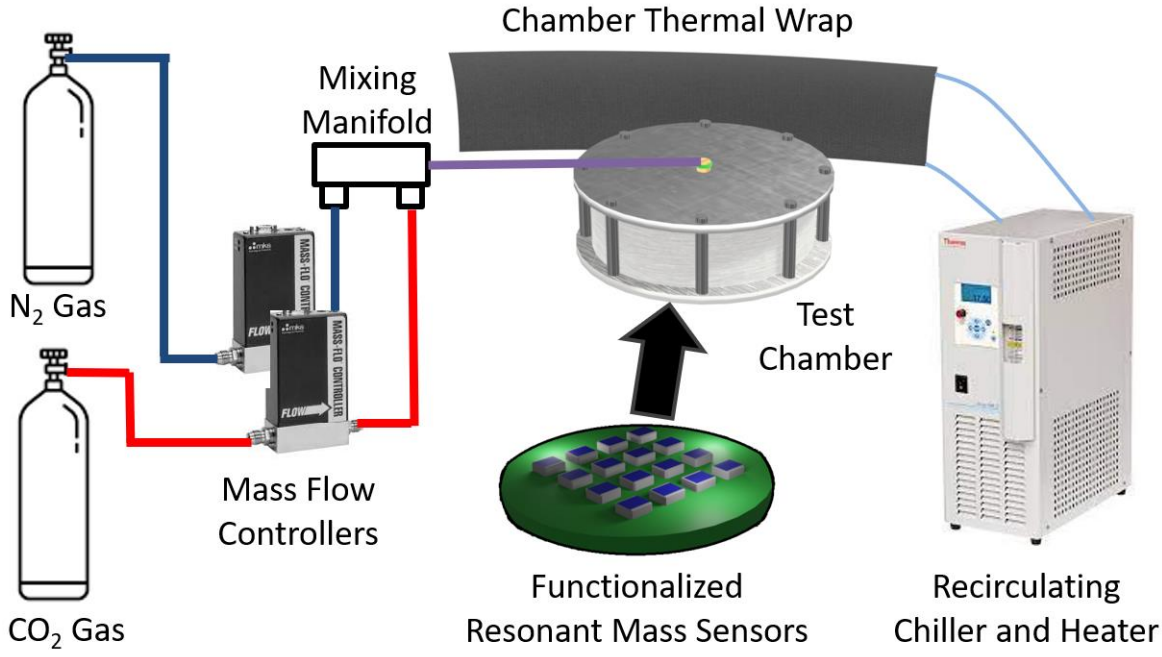

Figure 35. Schematic of the experimental setup used for sensor characterization. The mass flow controllers (MFCs) modulated supply gases to the test chamber containing functionalized quartz crystal resonators. A recirculating heater/chiller and a thermal wrap were used to regulate the temperature of the test chamber at the reported conditions.

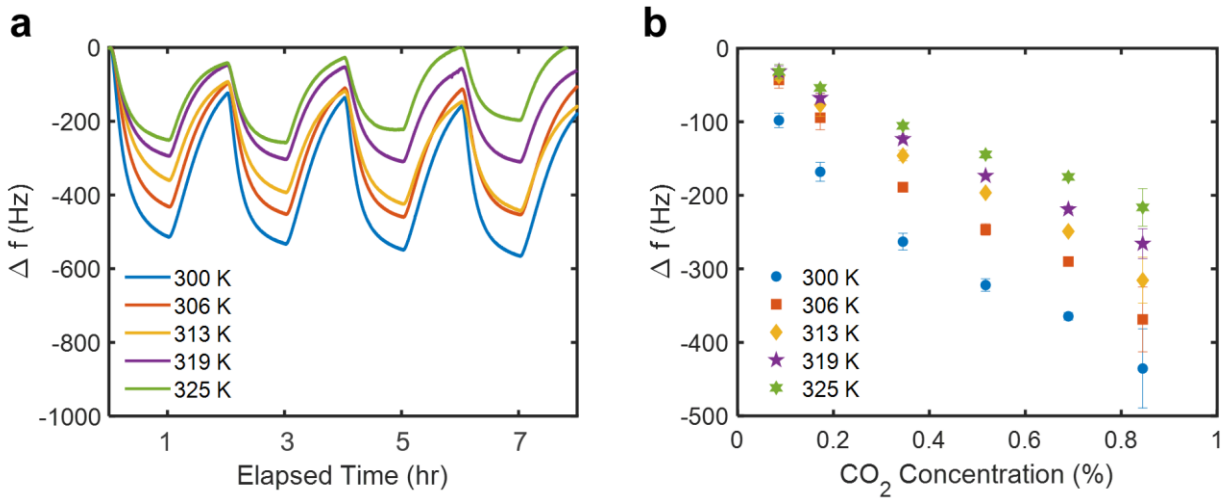

Figure 36. (a) CO_2 adsorption-desorption cycles at various temperatures for a PEI functionalized resonator in response to 1-hr on/off pulses of CO_2 at a concentration of 0.84 %. (b) The mean resonance frequency shift after 1-hr of CO_2 exposure at various concentrations for a PEI functionalized resonator. The error bars represent one standard deviation of the data.

5.8 References

(1) Mannan, M.; Al-Ghamdi, S. G. Indoor air quality in buildings: A comprehensive review on the factors influencing air pollution in residential and commercial structure. *Int. J. Environ. Res. Public Health* **2021**, *18*, 3276.

(2) Cincinelli, A.; Martellini, T. Indoor air quality and health. *Int. J. Environ. Res. Public Health* **2017**, *14*, 1286.

(3) The Occupational Safety and Health Administration. *Occupational Health Guideline for Carbon Dioxide.* (2020).

(4) Persily, A.; Gorfain, J. Analysis of ventilation data from the U.S. Environmental Protection Agency building assessment survey and evaluation (BASE) study. *NIST Interagency/Internal Report (NSITIR) 7145.* **2004**.

(5) Satish, U.; Mendell, M. J.; Shekhar, K.; Hotchi, T.; Sullivan, D.; Streufert, S.; Fisk, W. J. Is CO_2 an indoor pollutant? Direct effects of low-to-moderate CO_2 concentrations on human decision-making performance. *Environ. Health Perspect.* **2012**, *120*, 1671–1677.

(6) Scully, R. R.; Basner, M.; Nasrini, J.; Lam, C.-W.; Hermosillo, E.; Gur, R. C.; Moore, T.; Alexander, D. J.; Satish, U.; Ryder, V. E. Effects of acute exposures to carbon dioxide on decision making and cognition in astronaut-like subjects. *NPJ microgravity* **2019**, *5*, 17.

(7) Sayers, J. A.; Smith, R. E.; Holland, R. L.; Keatinge, W. R. Effects of carbon dioxide on mental performance. *J. Appl. Physiol.* **1987**, *63*, 25–30.

(8) Collier-Oxandale, A.; Thorson, J.; Halliday, H.; Milford, J.; Hannigan, M. Understanding the ability of low-cost MOx sensors to quantify ambient VOCs. *Atmos. Meas. Tech. Discuss.* **2018**, 1–29.

(9) Hodul, J. N.; Murray, A. K.; Carneiro, N. F.; Meseke, J. R.; Morris, J.; He, X.; Zemlyanov, D.; Chiu, G. T. C.; Braun, J. E.; Rhoads, J. F.; Boudouris, B. W. Modifying the surface chemistry and nanostructure of carbon nanotubes facilitates the detection of aromatic hydrocarbon gases. *ACS Appl. Nano Mater.* **2020**, *3*, 10389–10398.

(10) Siefker, Z. A.; Murray, A. K.; Zhao, X.; Boudouris, B. W.; Bajaj, N.; Chiu, G. T. C.; Rhoads, J. F. A resonant CO_2 sensor functionalized with a polymerized ionic liquid. *Proc. IEEE Sensors* **2019**, *2019-Octob*, 1-4.

(11) Lewis, A. C.; Lee, J. D.; Edwards, P. M.; Shaw, M. D.; Evans, M. J.; Moller, S. J.; Smith, K. R.; Buckley, J. W.; Ellis, M.; Gillot, S. R.; White, A. Evaluating the performance of low cost chemical sensors for air pollution research. *Faraday Discuss.* **2016**, *189*, 85–103.

(12) Asri, M. I. A.; Hasan, M. N.; Fuaad, M. R. A.; Yunos, Y. M.; Ali, M. S. M. MEMS gas sensors: A review. *IEEE Sens. J.* **2021**, *21*, 18381–18397.

(13) Siefker, Z. A.; Hodul, J. N.; Zhao, X.; Bajaj, N.; Brayton, K. M.; Flores-Hansen, C.; Zhao, W.; Chiu, G. T. C.; Braun, J. E.; Rhoads, J. F.; Boudouris, B. W. Manipulating polymer composition to create low-cost, high-fidelity sensors for indoor CO_2 monitoring. *Sci. Rep.* **2021**, *11*, 1–10.

(14) Siefker, Z. A.; Boyina, A.; Braun, J. E.; Zhao, X.; Boudouris, B. W.; Bajaj, N.; Chiu, G. T. C.; Rhoads, J. F. A chemiresistive CO_2 sensor based on CNT-functional polymer composite films. *Proc. IEEE Sensors* **2020**, *2020-Octob*, 1–4.

(15) Herberger, S.; Herold, M.; Ulmer, H.; Burdack-Freitag, A.; Mayer, F. Detection of human effluents by a MOS gas sensor in correlation to VOC quantification by GC/MS. *Build. Environ.* **2010**, *45*, 2430–2439.

(16) Lin, Y.; Fan, Z. Compositing strategies to enhance the performance of chemiresistive CO_2 gas sensors. *Mater. Sci. Semicond. Process.* **2020**, *107*, 104820.

(17) Molina, A.; Escobar-Barrios, V.; Oliva, J. A review on hybrid and flexible CO_2 gas sensors. *Synth. Met.* **2020**, *270*, 116602.

(18) Fanget, S.; Hentz, S.; Puget, P.; Arcamone, J.; Matheron, M.; Colinet, E.; Andreucci, P.; Duraffourg, L.; Myers, E.; Roukes, M. L. Gas sensors based on gravimetric detection—A review. *Sensors Actuators B Chem.* **2011**, *160*, 804–821.

(19) Shrestha, S. S. Performance evaluation of carbon-dioxide sensors used in building HVAC applications, Ph.D Dissertation, Iowa State University, **2005**.

(20) J. Petersen, J. Kristensen, H. Elarga, R. Andersen, and A. M. Accuracy and air temperature dependency of commercial low-cost NDIR CO_2 sensors: An experimental investigation. In *4th International Conference On Building Energy, Environment*, **2018**, 203–207.

(21) Emmerich, S. J.; Persily, A. K. State-of-the-art review of CO_2 demand controlled ventilation technology and application state-of-the-art review of CO_2 demand controlled ventilation technology and application. *NIST Interagency/Internal Report (NSITIR) 6729.* **2001.**

(22) Dinh, T.-V.; Choi, I.-Y.; Son, Y.-S.; Kim, J.-C. A Review on non-dispersive infrared gas sensors: Improvement of sensor detection limit and interference correction. *Sensors Actuators B Chem.* **2016**, *231*, 529–538.

(23) Dervieux, E.; Théron, M.; Uhring, W. Carbon dioxide sensing-biomedical applications to human subjects. *Sensors*. **2022**, *22*, 188.

(24) Li, K.; Jiang, J.; Tian, S.; Yan, F.; Chen, X. Polyethyleneimine-nano silica composites: A low-cost and promising adsorbent for CO_2 capture. *J. Mater. Chem. A* **2015**, *3*, 2166–2175.

(25) Li, K.; Jiang, J.; Yan, F.; Tian, S.; Chen, X. The influence of polyethyleneimine type and molecular weight on the CO_2 capture performance of PEI-nano silica adsorbents. *Appl. Energy* **2014**, *136*, 750–755.

(26) Choi, W.; Min, K.; Kim, C.; Ko, Y. S.; Jeon, J. W.; Seo, H.; Park, Y. K.; Choi, M. Epoxide-functionalization of polyethyleneimine for synthesis of stable carbon dioxide adsorbent in temperature swing adsorption. *Nat. Commun.* **2016**, *7*, 1–8.

(27) Wang, J.; Chen, H.; Zhou, H.; Liu, X.; Qiao, W.; Long, D.; Ling, L. Carbon dioxide capture using polyethylenimine-loaded mesoporous carbons. *J. Environ. Sci. (China)* **2013**, *25*, 124–132.

(28) Heydari-Gorji, A.; Sayari, A. CO_2 capture on polyethylenimine-impregnated hydrophobic mesoporous silica: Experimental and kinetic modeling. *Chem. Eng. J.* **2011**, *173*, 72–79.

(29) Zhang, W.; Liu, H.; Sun, C.; Drage, T. C.; Snape, C. E. Capturing CO_2 from ambient air using a polyethyleneimine-silica adsorbent in fluidized beds. *Chem. Eng. Sci.* **2014**, *116*, 306–316.

(30) Monazam, E. R.; Spenik, J.; Shadle, L. J. CO_2 desorption kinetics for immobilized polyethylenimine (PEI). *Energy and Fuels* **2014**, *28*, 650–656.

(31) Al-Marri, M. J.; Khader, M. M.; Tawfik, M.; Qi, G.; Giannelis, E. P. CO_2 sorption kinetics of scaled-up polyethylenimine-functionalized mesoporous silica sorbent. *Langmuir* **2015**, *31*, 3569–3576.

(32) Xie, G. Z.; Kang, T.; Zhou, Y.; Xie, T.; Tai, H. L.; Jiang, Y. D. QCM sensors based on PEI films for CO_2 detection. *J. Electron. Sci. Technol.* **2015**, *13*, 181–187.

(33) Meth, S.; Goeppert, A.; Prakash, G. K. S.; Olah, G. A. Silica nanoparticles as supports for regenerable CO_2 sorbents. *Energy and Fuels* **2012**, *26*, 3082–3090.

(34) Hampe, E. M.; Rudkevich, D. M. Exploring reversible reactions between CO_2 and amines. *Tetrahedron* **2003**, *59*, 9619–9625.

(35) Ma, W.; Wang, R.; Rong, Q.; Shao, Z.; Zhang, W.; Guo, T.; Wang, J.; Qiao, X. CO_2 gas sensing using optical fiber Fabry-Perot interferometer based on polyethyleneimine/poly(vinyl alcohol) coating. *IEEE Photonics J.* **2017**, *9*, 1–8.

(36) Chiang, C. J.; Tsai, K. T.; Lee, Y. H.; Lin, H. W.; Yang, Y. L.; Shih, C. C.; Lin, C. Y.; Jeng, H. A.; Weng, Y. H.; Cheng, Y. Y.; Ho, K. C.; Dai, C. A. In situ fabrication of conducting polymer composite film as a chemical resistive CO_2 gas sensor. *Microelectron. Eng.* **2013**, *111*, 409–415.

(37) Wang, H.; Wu, H.; Hasan, D.; He, T.; Shi, Q.; Lee, C. Self-powered dual-mode amenity sensor based on the water-air triboelectric nanogenerator. *ACS Nano* **2017**, *11*, 10337–10346.

(38) Srinives, S.; Sarkar, T.; Hernandez, R.; Mulchandani, A. A miniature chemiresistor sensor for carbon dioxide. *Anal. Chim. Acta* **2015**, *874*, 54–58.

(39) Lu, W.; Xiao, P.; Gu, J.; Zhang, J.; Huang, Y.; Huang, Q.; Chen, T. Aggregation-induced emission of tetraphenylethylene-modified polyethyleneimine for highly selective CO_2 detection. *Sensors Actuators, B Chem.* **2016**, *228*, 551–556.

(40) Doan, T. C. D.; Baggerman, J.; Ramaneti, R.; Tong, H. D.; Marcelis, A. T. M.; Van Rijn, C. J. M. Carbon dioxide detection with polyethylenimine blended with polyelectrolytes. *Sensors Actuators, B Chem.* **2014**, *201*, 452–459.

(41) Sun, B.; Xie, G.; Jiang, Y.; Li, X. Comparative CO_2-sensing characteristic studies of PEI and PEI/starch thin film sensors. *Energy Procedia* **2011**, *12*, 726–732.

(42) Bag, S.; Pal, K. A PCB based chemiresistive carbon dioxide sensor operating at room temperature under different relative humidity. *IEEE Trans. Nanotechnol.* **2019**, *18*, 1119–1128.

(43) Star, A.; Han, T. R.; Joshi, V.; Gabriel, J. C. P.; Grüner, G. Nanoelectronic carbon dioxide sensors. *Adv. Mater.* **2004**, *16*, 2049–2052.

(44) Wang, L.; Al-Aufi, M.; Pacheco, C. N.; Xie, L.; Rioux, R. M. Polyethylene glycol (PEG) addition to polyethylenimine (PEI)-impregnated silica increases amine accessibility during CO_2 sorption. *ACS Sustain. Chem. Eng.* **2019**, *7*, 14785–14795.

(45) Sakwa-Novak, M. A.; Tan, S.; Jones, C. W. Role of additives in composite PEI/oxide CO_2 adsorbents: Enhancement in the amine efficiency of supported PEI by PEG in CO_2 capture from simulated ambient air. *ACS Appl. Mater. Interfaces* **2015**, *7*, 24748–24759.

(46) Son, M.; Pak, Y.; Chee, S. S.; Auxilia, F. M.; Kim, K.; Lee, B. K.; Lee, S.; Kang, S. K.; Lee, C.; Lee, J. S.; Kim, K. K.; Jang, Y. H.; Lee, B. H.; Jung, G. Y.; Ham, M. H. Charge transfer in graphene/polymer interfaces for CO_2 detection. *Nano Res.* **2018**, *11*, 3529–3536.

(47) Karpovich, D. S.; Blanchard, G. J. Direct measurement of the adsorption kinetics of alkanethiolate self-assembled monolayers on a microcrystalline gold surface. *Langmuir* **1994**, *10*, 3315–3322.

(48) Yoshimoto, M.; Matsunaga, T.; Tanaka, M.; Kurosawa, S. Determination of thermodynamic parameters for enolization reaction of malonic and metylmalonic acids by using quartz crystal microbalance. *Anal. Chem. Res.* **2016**, *8*, 9–15.

(49) Wu, B.; Wu, K.; Wang, P.; Zhu, D. M. Adsorption kinetics and adsorption isotherm of poly(N-isopropylacrylamide) on gold surfaces studied using QCM-D. *J. Phys. Chem. C* **2007**, *111*, 1131–1135.

(50) Stavila, V.; Volponi, J.; Katzenmeyer, A. M.; Dixon, M. C.; Allendorf, M. D. Kinetics and mechanism of metal-organic framework thin film growth: Systematic investigation of HKUST-1 deposition on QCM electrodes. *Chem. Sci.* **2012**, *3*, 1531–1540.

(51) Thundat, T.; Oden, P. I.; Warmack, R. J. Microcantilever sensors. *Microscale Thermophys. Eng.* **1997**, *1*, 185–199.

(52) Bajaj, N.; Rhoads, J. F.; Chiu, G. T. C. Characterizing the spatially dependent sensitivity of resonant mass sensors using inkjet deposition. *J. Dyn. Syst. Meas. Control. Trans. ASME* **2017**, *139*, 1–6.

(53) Su, Y.; Wang, J.; Liu, H. FTIR spectroscopic study on effects of temperature and polymer composition on the structural properties of PEO−PPO−PEO block copolymer micelles. *Langmuir* **2002**, *18*, 5370–5374.

(54) Pucić, I.; Jurkin, T. FTIR assessment of poly(ethylene oxide) irradiated in solid state, melt and aqeuous solution. *Radiat. Phys. Chem.* **2012**, *81*, 1426–1429.

(55) Wang, F.; Liu, P.; Nie, T.; Wei, H.; Cui, Z. Characterization of a polyamine microsphere and its adsorption for protein. *International Journal of Molecular Sciences*. **2013**, *14*, 17–29**.**

(56) Arabi, S.; Akbari Javar, H.; Khoobi, M. Preparation and characterization of modified polyethyleneimine magnetic nanoparticles for cancer drug delivery. *J. Nanomater.* **2016**, 2806407.

(57) Takahashi, Y.; Tadokoro, H. Structural studies of polyethers, $(-(CH2)m-O-)_n$. X. crystal structure of poly(ethylene oxide). *Macromolecules* **1973**, *6*, 672–675.

(58) Yang, S.; Liu, Z.; Liu, Y.; Jiao, Y. Effect of molecular weight on conformational changes of PEO: An infrared spectroscopic analysis. *J. Mater. Sci.* **2015**, *50*, 1544–1552.

(59) Qi, G.; Wang, Y.; Estevez, L.; Duan, X.; Anako, N.; Park, A. H. A.; Li, W.; Jones, C. W.; Giannelis, E. P. High efficiency nanocomposite sorbents for CO_2 capture based on amine-functionalized mesoporous capsules. *Energy Environ. Sci.* **2011**, *4*, 444–452.

(60) Qi, G.; Fu, L.; Choi, B. H.; Giannelis, E. P. Efficient CO_2 sorbents based on silica foam with ultra-large mesopores. *Energy Environ. Sci.* **2012**, *5*, 7368–7375.

(61) Al-Marri, M.J.; Al-Saad, K.A.; Sadd, M.A.; Cortes, D.J.; Khader, M.M. Thermodynamics of CO_2 adsorption on polyethyleneimine mesoporous silica and activated carbon. *J. Phys. Chem. Biophys.* **2017**, *7*, 1–5.

(62) Jung, W.; Park, J.; Lee, K. S. Kinetic modeling of CO_2 adsorption on an amine-functionalized solid sorbent. *Chem. Eng. Sci.* **2018**, *177*, 122–131.

(63) Satyapal, S.; Filburn, T.; Trela, J.; Strange, J. Performance and properties of a solid amine sorbent for carbon dioxide removal in space life support applications. *Energy and Fuels* **2001**, *15*, 250–255.

(64) Liu, F.; Chen, S.; Gao, Y. Synthesis of porous polymer based solid amine adsorbent: Effect of pore size and amine loading on CO_2 adsorption. *J. Colloid Interface Sci.* **2017**, *506*, 236–244.

(65) Yan, W.; Tang, J.; Bian, Z.; Hu, J.; Liu, H. Carbon dioxide capture by amine-impregnated mesocellular- foam-containing template. *Ind. Eng. Chem. Res.* **2012**, 51, 3653–3662.

CHAPTER 6. INVESTIGATING POLY (5-CARBOXYINDOLE) BETA-CYCLODEXTRIN NANOCOMPOSITE FOR THE ENHANCED INDOOR DETECTION OF FORMALDEHYDE GAS

Content from this chapter has been submitted for publication and is currently under review.

6.1 Overview

Formaldehyde, a compound commonly employed in many construction materials, paints, and plastics, has been linked to deleterious health effects. Thus, monitoring the presence of formaldehyde in interior locations is increasingly important when it comes to public health. Currently, there is a crucial need for a low-cost, small-scale, selective, and sensitive indoor sensor capable of real-time formaldehyde detection. To meet these performance metrics, materials need to be incorporated onto existing gas sensor platforms to act as chemically selective recognition layers. A main challenge when addressing this issue is creating a material that can remain easily processable, can be easily synthesized, and can operate in practical environments (i.e., at common temperatures, humidity values, and in the presence of distractant analytes). Here, we show the unique properties of poly(5-carboxyindole) (P5C), a facile one-pot synthesized polymer, for practical indoor air monitoring of formaldehyde gas at concentrations as low as 25 ppm with rapid response and recovery times characterized by time constants of 27 s and 16 s, respectively. Importantly, we show that β-cyclodextrin (BCD), when blended into P5C to create a poly(5-carboxyindole) with β-cyclodextrin nanocomposite (P5C-BCD), offers distinct properties that enhance the response to formaldehyde gas in common operational conditions. More specifically, BCD adds features into the P5C such as its ability to form strong host-guest interactions with formaldehyde, its ability to buffer P5C protonation states to allow for more protonated carboxylic acid moieties on P5C which can hydrogen bond more effectively with formaldehyde, as well as

creating a cylindrical morphology with the polymer film to assist the diffusion of formaldehyde into the polymer matrix. Additionally, these materials provide for chemically selective adsorption to formaldehyde gas in environments where interfering analytes could exist. Due to the practical advantages these materials offer, these materials can unlock new avenues for future formaldehyde sensor materials.

6.2 Introduction

Volatile organic compounds (VOCs) are widely found in the manufacturing of indoor household materials.[1] These materials include structural building elements, carpeting, wood, adhesives, coatings, paints, and plastic products.[2–5] However, many of these indoor household materials can emit VOCs over time, thus affecting the quality of indoor air. Indoor air quality can be a major health concern due to the many health risk factors that have been associated with VOCs.[6,7] For instance, formaldehyde is a VOC that is primarily released from the aforementioned materials over time,[8] and exposure to formaldehyde can cause irritation of the eyes, skin, and the respiratory and nervous systems in the short term.[9–12] Additionally, long-term exposure to formaldehyde has been linked to acute myeloid leukemia and Hodgkin's disease.[13–16] Thus, the World Health Organization (WHO) has set a 30 min exposure limit of 0.08 ppm for formaldehyde, while the US National Institute for Occupational Safety and Health (NIOSH) has established a maximum long-term exposure limit of 0.016 ppm for formaldehyde (TWA).[17,18] Due to these low exposure limits, there is a compelling need for an energy-efficient, low-cost, and reliable sensing platform that is designed to detect formaldehyde with high sensitivity, while also sufficing in terms of formfactor such that it can be implemented in interior spaces.

Various types of sensor platforms have been utilized for monitoring formaldehyde gas. These techniques include spectrophotometry, gas chromatography, high-performance liquid

chromatography, ion chromatography, polarography, fluorescence spectroscopy, and ultraviolet-visible (UV-Vis) light spectroscopy.[19–23] These approaches, though effective at detecting formaldehyde, are not realistic to implement in common indoor air quality monitoring end-use cases due to their bulky instrumentation, and they are largely unable to detect formaldehyde in a real-time manner. This has created a market for lower-cost and smaller-scale sensors that operate mainly through electrochemical or electromechanical mechanisms that use a selective chemical recognition layer.[1,24–29] These sensors have shown great success with respect to their small sizes, their ability to be portable, and their detection of formaldehyde gas (i.e., as low as 1 ppm).[30–34] However, electrochemical-based sensors are limited by their surface chemistry, which typically requires metal or graphene additives to provide a conductive media to measure conductivity changes on the device. This can make fabrication difficult and create selectivity issues when trying to detect the target analyte in the presence of interfering gases.[35] One sub-category of electrochemical sensors, metal oxide sensors, utilize electron donors or electron acceptors in the gas phase, which can adsorb onto a metal oxide-based material. In most cases, this adsorption requires high temperatures (i.e., > 150 °C) or UV light during operation, which allows the adsorbed species to exchange electrons with the metal oxide. Unfortunately, this heating and photochemical processes require high energy input.[36–39] There are metal oxide sensors that operate at room temperature, but these require additives and/or extensive processing techniques to acquire a reliable response.[39–41] Electromechanical sensors, such as gravimetric sensors, offer the advantage of not requiring the sensing material to be conductive, which broadens the range of useable sensing materials. These sensors have shown much promise in the area of formaldehyde detection, detecting formaldehyde in the ppb concentration range. [42–44] However, these materials suffer from many of the same disadvantages of electrochemical materials, such as extensive processing or

fabrication techniques or lack of sensing performance under practical conditions (i.e., humidity). Therefore, it is of great importance to create a sensor material that can assist a sensor device to remain compact, practical, low-cost, and offer selective and real-time response at low operating temperatures. Furthermore, it is paramount to fabricate a surface chemistry that is solution processable, will meet the required sensing metrics relative to the state of the art, and does not require additional preparation processes or components to yield a response to formaldehyde.

Utilizing polymeric materials in sensing applications allows devices to remain compact with facile fabrication protocols while maintaining high performance. Polymer thin films composed of macromolecules such as poly(3-hexylithiophene) (P3HT), poly(ethyleneimine) (PEI), polypyrrole (PPy), and biodegradable polysaccharides have shown promise in the detection of formaldehyde.[45–50] Additionally, inks composed of these polymeric materials offer solution processability and require little to no additives to detect formaldehyde. Some of these sensors utilize microheaters and NiO thin films to detect formaldehyde at concentrations as low as 1.2 ppm.[28,51] Yet, finding a non-chemiresistive sensor device platform that can utilize these polymer thin films while remaining at a small scale and low cost remains challenging. As such, there is much promise in combining polymers with resonant mass sensors. Resonant mass sensors, a form of gravimetric sensors, are inexpensive to manufacture, require low energy input to operate, and facilitate a robust sampling rate. In this effort, this is accomplished by utilizing an array of Pierce oscillators and a frequency counting algorithm that allows for simultaneously monitoring of 16 sensors that have a temporal resolution of 1 s and frequency resolution of 1 Hz. This rapid and real-time detection approach offers surface chemistries a reliable sensor platform to monitor surface interactions with a target analyte. Recently, resonant mass sensors, when combined with a modified materials surface chemistry, have shown rapid and selective responses in the detection

of aromatic VOC compounds.[52] Combining the robust, inexpensive, small-scale, and low-energy properties of a resonant mass sensor platform with the processable and chemically selective properties of polymer materials could enable the development of practical formaldehyde sensors for buildings.

Here, a resonant mass sensor was coated with poly (5-carboxyindole) (P5C). P5C has been used previously in electrochemical sensors for the detection of saturated ethanol, toluene, methanol, ether, and acetone vapors.[53,54] However, P5C has not been previously utilized for the detection of formaldehyde, and it has not been used to achieve lower gas detection limits (i.e., < 100 ppm of analyte). Additionally, when 50% (by weight) of β-cyclodextrin was blended with the P5C (P5C-BCD), the sensor showed improved performance. Furthermore, by using the resonant mass sensor platform and this chemical functionalization protocol, formaldehyde was detected with rapid response and recovery times characterized by time constants of 27 s and 16 s, respectively. In comparison to other polymer-based sensing counterparts, this sensor offers straightforward implementation due to its high sensitivity, low operating temperature, and cyclability. Moreover, these sensors detect formaldehyde gas through physisorption, which allows for repeated use. The apparent adsorption of formaldehyde gas is related to the non-covalent interactions between P5C and formaldehyde. Importantly, this interaction can be enhanced using β-cyclodextrin. This surface chemistry allows for feasible solution processing and does not require any additional device manipulations to suffice sensing ability. Thus, this sensing material could offer an easily functionalized and cheap alternative capable of quick and reliable detection of formaldehyde gas.

6.3 Experimental Information

6.3.1 Materials

All of the chemicals utilized in this study were purchased from Sigma-Aldrich, and they were used as received unless otherwise noted. P5C was synthesized utilizing previously reported procedures.[55,56] The reaction was performed in a scintillation vial at room temperature (~25 °C). A 1:2 molar ratio of monomer to oxidizing agent was utilized for this polymerization. To begin the polymerization, 100 mg of 5-carboxyindole monomer (0.031 M) was dissolved in 1.5 mL of ethanol. To this monomer solution, a pre-prepared oxidizing agent solution of 0.062 M ammonium peroxodisulphate in 0.1 M H_2SO_4 (aq.) was added dropwise while maintaining constant stirring. As the reaction proceeded, a gradual darkening of solution occurred, which indicated that the polymerization reaction had occurred. The resulting solution was left to continuously stir overnight. After 24 h, the black precipitate solids were collected by centrifugation followed by washing with excess ethanol and water. The remaining polymer solids were then dried under vacuum (i.e., < 1 Torr). P5C inks were prepared by dispersing P5C in an ethanol solution at a loading of 1.0 mg mL^{-1}. The P5C-BCD ink preparation followed the same protocol as P5C. However, in the P5C-BCD synthesis, prior to adding the ammonium peroxodisulphate in the 0.1 M H_2SO_4 solution, β-cycloclodextrin was added in a 1:2 mass ratio relative to the 5-carboxindole monomer.

6.3.2 General Methods

A Hitachi S-4800 Field Emission scanning electron microscope (SEM) was utilized to image the P5C and P5C-BCD polymer films. For each of these images, 1 μL of the P5C or P5C-BCD at a concentration of 1.0 mg mL^{-1} polymer solution was printed on a silicon dioxide substrate and dried under vacuum overnight. The films were then coated with 20 nm of carbon prior to

imaging using a SPI carbon sputter coater to prevent charging during image acquisition. Attenuated total internal reflectance-Fourier transform infrared (ATR-FTIR) spectroscopy was performed using dried samples. The samples were placed on a diamond substrate of a Thermo-Nicolet Nexus FTIR using a deuterated triglycine sulfate KBr detector with a KBr beam splitter. Under a dry nitrogen purge, 100 scans were acquired over a range of 800 $cm^{-1} \leq \nu \leq 4500\ cm^{-1}$ for each sample. A TA SDT Q600 instrument was used for thermal gravimetric analysis of the samples. The samples were loaded into an alumina ceramic crucible and kept under ambient conditions, and then they were heated from room temperature, at a rate of 10 °C min^{-1}, to a final temperature of 800 °C. A TA Instruments Q20 Series differential scanning calorimeter (DSC) was used for thermal transition analysis. The samples were sealed in Tzero hermetic pans, then annealed at 220 °C under a nitrogen gas purge, and then cooled to −50 °C, before the trace that started at −50 °C and ended at 220 °C (at a scan rate of 10 °C min^{-1}) was collected. A Kratos Axis Ultra DLD imaging X-ray photoelectron spectrometer with a monochromatic Al Kα (E = 1486.6 eV) was utilized for X-ray photoelectron spectroscopy (XPS) measurements, and these data were acquired while the sample was under high vacuum (P ~ 10^{-9} Torr). CasaXPS software was utilized for all of the XPS data analyses.

6.3.3 Device Functionalization

In the following experiments, small-scale quartz crystal resonators were functionalized by casting 1 μL of a 1 mg mL^{-1} solution of P5C or P5C-BCD onto the resonator surface. The devices were left to dry for at least 30 min under vacuum (P ≤ 0.4 Torr) to remove any residual solvent.

6.3.4 Device Instrumentation

The device instrumentation utilized in this work was previously reported.[48] An array of Pierce oscillators was used to evaluate the response of the devices to target analytes. Each oscillator consisted of a quartz crystal resonator (Kyocera Corp., CX3225) that had a capacitance of C_L = 12 pF, an isolation resistor (R_2 = 510 Ω), one feedback resistor (R_1 = 2 MΩ), two load capacitors (C_1 = 22 pF and C_2 = 22 pF), and an inverter. The Pierce oscillator inverter and three additional inverters were provided by a crystal oscillator driver in order to convert the output signal to a square wave. These oscillators were then assembled as an array of 16 devices (Supplementary Information Figure 37a). To track oscillation frequency, a Field Programmable Gate Array (FPGA) was used as a frequency counter, which was also able to track all of the oscillators in parallel. With all of these components, a frequency resolution of 1 Hz was achieved for all 16 devices. For testing purposes, the 16 resonators were decoupled from the rest of the circuit but still connected to an instrumentation board. The instrumentation board contained the remaining elements of the circuit mentioned previously. By decoupling the circuit, functionalized resonators could be added and removed more efficiently.

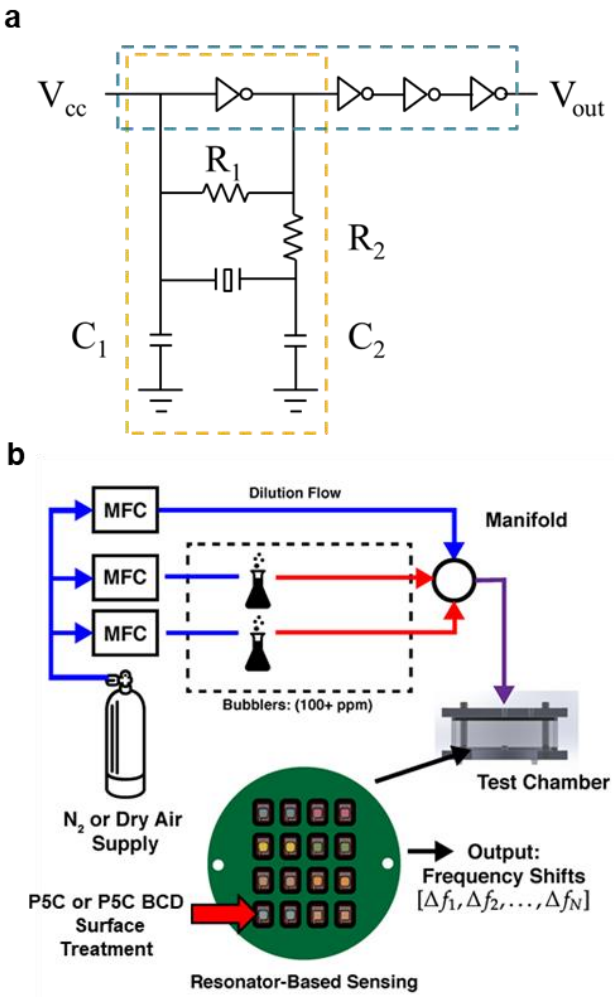

Figure 37. (a) A schematic representation of the Pierce oscillator circuit with the oscillator (outlined by orange dashed lines) and a series of inverters (outlined by blue dashed lines). C1 and C2 are load capacitors. R1 is a feedback resistor, and R2 is an isolation resistor. V_{cc} is the supply voltage, and V_{out} is the output voltage that enters the FPGA frequency counter. (b) The experimental setup utilized to test target analyte gases. The functionalized oscillators were evaluated in a chamber filled with analyte gas from bubblers connected to mass flow controllers and diluted with a stream of pure nitrogen or dry air.

6.3.5 Device Testing

The testing protocols utilized in this work were reported previously.[48] The experimental setup shown in Supplementary Information Figure 37b was used to test the devices. A board with 16 resonators was first secured to an instrumentation board that was attached to the inside of a 9.5 cm diameter chamber. The chamber remained at room temperature (~22.5 °C) and was sealed

during testing. An in-line flow distribution system, which was connected to the chamber, controlled the concentrations of the target analytes. To control the concentration of analytes, air or nitrogen was passed through a series of mass flow controllers (MFC) in parallel. One MFC (MKS 1179A, 500 cm^3 min^{-1}) would lead directly into the chamber while the other set of MFCs (MKS 1480A, 40 cm^3 min^{-1}) would pass through a bubbler (Chemglass, AF-0085), which contained 10 mL of the target analyte. It should be noted that the target analytes were in aqueous solutions before they were introduced into the chamber in gaseous form. These lines would reconnect at a manifold and flow into the chamber. Before and after the target analyte was introduced into the chamber, nitrogen or air was used to flush the chamber at a flow rate of 500 cm^3 min^{-1} so that the environment could remain inert. During experimentation, the frequency of each device was recorded using the FPGA and LabVIEW.

6.4 Results and Discussion

6.4.1 Material Characterization

Upon drop casting and drying of the polymer films, a surface morphology unique to each film was observed under SEM imaging (Figure 38). When drop-cast, P5C formed spherical sub-micron sized particles with some particles showing nanoscale features when they were not agglomerated (Figure 38a). The individual P5C nanoparticles had a spherical morphology. This spherical morphology is consistent with the polyindole class of polymers.[57] However, these particles were also observed to be agglomerated in patches as large as 5 μm in diameter (Figure 38a).

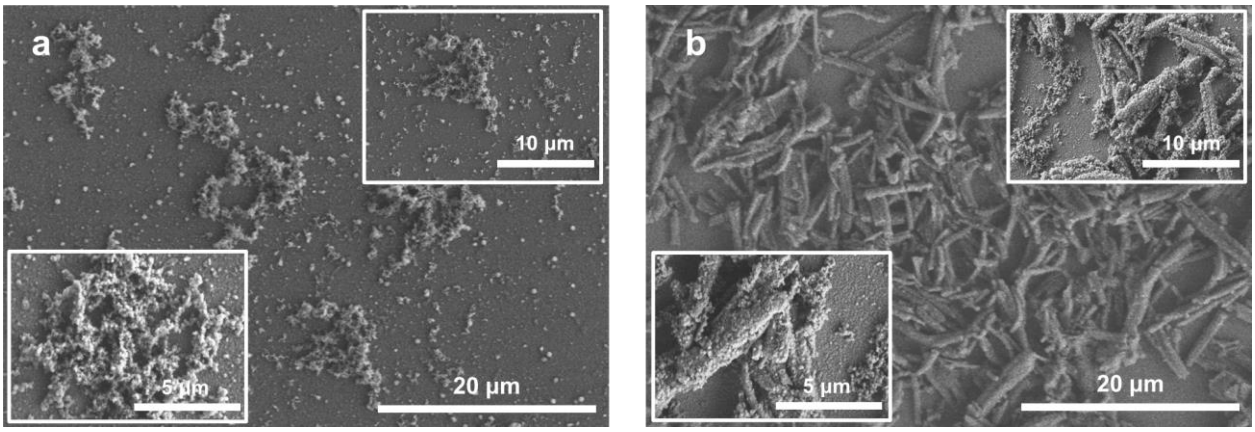

Figure 38. SEM images of (a) the P5C polymer and (b) P5C-BCD polymer after being dissolved in ethanol (1 mg mL^{-1}), drop cast onto a silicon wafer, dried for 12 h under vacuum, and coated with carbon. The three panels show the same film at three different magnification levels.

Additionally, these 5 µm patches of agglomerated particles did not reside uniformly across the surface. On the other hand, when P5C-BCD was drop-cast, it formed agglomerated micron-sized patches that uniformly coated the surface (Figure 38b). However, the individual particles that constituted these micron-sized patches had a cylindrical or tubular surface morphology. This cylindrical surface morphology, which was uniformly coated over the surface substrate, allowed for an increased lateral surface area of the surface chemistry. Thus, we believe that the combination of these features (i.e., better surface coating and larger surface area) in the P5C-BCD composites allowed for better interactions with formaldehyde gas because more of the surface chemistry contacted formaldehyde as it was present (*vide infra*).

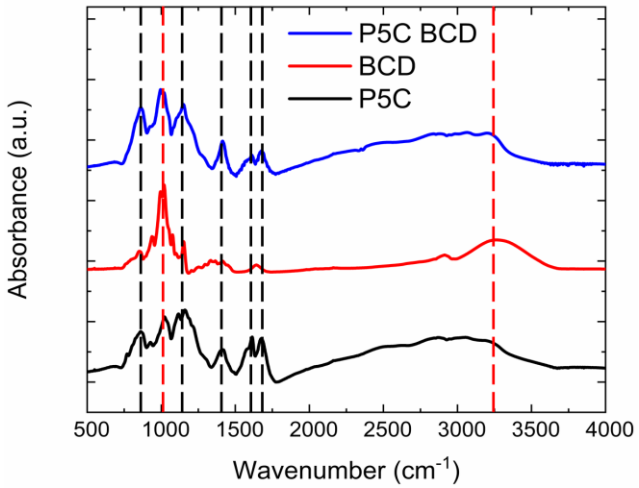

Figure 39. Attenuated total internal reflectance-Fourier transform infrared (ATR-FTIR) spectrum of the P5C, P5C-BCD, and BCD samples. This spectrum highlights the sharp P5C peaks at 1690 cm^{-1}, 1534 cm^{-1}, 1450 cm^{-1}, 1220 cm^{-1}, and 760 cm^{-1} and broad (3250 cm^{-1}) and sharp (1077 cm^{-1}) BCD peaks, which appeared in the P5C-BCD nanocomposite.

The P5C-BCD nanocomposite structure expressed features of both P5C and BCD, as confirmed via FTIR spectroscopy (Figure 39). As previously reported, the vibrational peaks of P5C include sharp C=O stretching (1690 cm^{-1}), sharp N-H bending (1534 cm^{-1}), sharp C=C alkene stretching (1450 cm^{-1}), sharp C-N aromatic stretching (1220 cm^{-1}), and sharp C-H bending 760 cm^{-1} spectra peaks.[58] These peaks are associated with the carboxylic acid, amine, and aromatic conjugated structural features of P5C. Having these chemical functionalities is important as carboxylic acid functionalities have been shown to non-covalently interact with formaldehyde in related polymeric materials.[59] BCD expressed broad O-H stretching at 3250 cm^{-1} and sharp C-O-C stretching (1077 cm^{-1}) spectral signals, which were in agreement with previous BCD studies.[60] The lack of chemical shifts of the P5C-BCD composite relative to the pristine P5C and BCD materials suggests that no chemical bonds were formed between BCD and P5C during the nanocomposite formulation, consistent with our expectations. Rather the functional groups for P5C and BCD remained intact and coexist in the nanocomposite material. Overall, this characterization

shows the synthesis of P5C-BCD with the proper chemical functionalities to potentially interact with formaldehyde.

Upon heating, P5C-BCD expressed a higher melting point (T_m = 211 °C) relative to P5C (T_m = 199 °C), as shown in Figure 40a. This increase in T_m is likely due to the strong intermolecular forces between the BCD and P5C. Additionally, P5C-BCD showed a glass transition temperature (T_g) of 154 °C while P5C showed a T_g of 156 °C. Moreover, P5C degraded (i.e., passing 10% weight loss) after 225 °C while P5C-BCD showed degradation (i.e., passing 10% weight loss) after 300 °C (Figure 40b). The initial approximate 10% in weight loss in P5C and P5C-BCD and 14% weight loss in BCD is attributed to the loss of water entrained within the materials. BCD then showed a degradation (i.e., passing 14% weight loss) at 310 °C, which is characteristic of previous BCD TGA studies.[60]

The improved thermal stability of the P5C-BCD nanocomposites is attributed to some possible points. First, BCD has a higher degradation temperature and when loading the P5C with BCD at a higher loading, this increased the degradation temperature. Because P5C-BCD has a higher loading of BCD, this then expressed more degradation characteristics of the BCD instead of the P5C. Second, BCD reduced the mobility of the P5C polymer chains due to the presence of strong intermolecular forces or partial non-covalent inclusion complexes between the BCD and P5C, and this in turn, caused increased thermal stability.[61] This reduction in mobility is common in systems where nanoparticles are added to a polymer.[62] Essentially, the thermal degradation of polymers starts with free radical formations at weak bonds or at chain ends, followed by their transfer to adjacent chains via interchain reactions.[62,63] However, when BCD is present, it suppressed the free radical transfer of the interchain reactions upon thermal ionization and as a result suppressed the degradation temperature and rate. Overall, these thermal characterization

studies show that the P5C-BCD nanocomposite did not go through any thermal transitions, and it did not degrade anywhere near room temperature. These thermal properties are reassuring that this material can be utilized in an interior environment, where temperature might fluctuate (i.e., 20-30 °C), and maintain temperature stability as chemical recognition layer on a sensor.

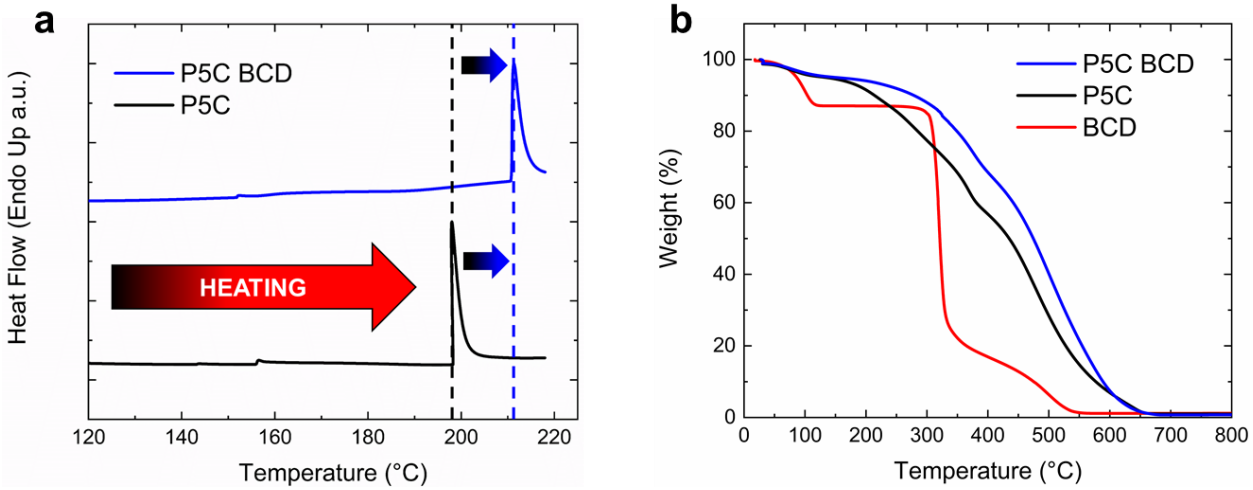

Figure 40. (a) DSC heating trace of P5C and P5C-BCD highlighting that P5C has approximately a T_g of 156 °C and a T_m of 199 °C while P5C has approximately a T_g of 155 °C and a T_m of 211 °C. Note, P5C-BCD showed a 12 °C increase in melting point. (b) Thermogravimetric analysis (TGA) of P5C, P5C-BCD, and BCD under ambient air conditions. This TGA study highlights P5C degradation (i.e., passing 10% weight loss) after 225 °C, P5C-BCD degradation (i.e., passing 10% weight loss) after 300 °C, and BCD degradation (i.e., passing 14% weight loss) at 310 °C.

The C 1s, N 1s, and O 1s binding energy regions were observed in the XPS spectra of both P5C and P5C-BCD upon the initial survey scans (Figure 41a). Focusing on the C 1s region (Figure 41b) for both P5C and P5C-BCD, there was primarily an sp^2 C=C peak observed at 284.8 eV, which is associated with the conjugated aromatic structure of P5C. P5C also showed a peak at 285.8 eV, which was characteristic peak of the C-N bond, resultant from the nitrogen heteroatom in the conjugated indole ring.[64] P5C-BCD did not show any C-N character likely due to the low intensity of the peak as there is a low concentration of nitrogen in the material once BCD is added. However, P5C-BCD did show a peak at 286.6 eV, which is in good agreement with C-O binding

energy characteristics.[65] This C-O peak is due to the C-O binding that occurs on BCD as it is a cyclic oligosaccharide consisting of seven glucose units that all contain C-O bonds.

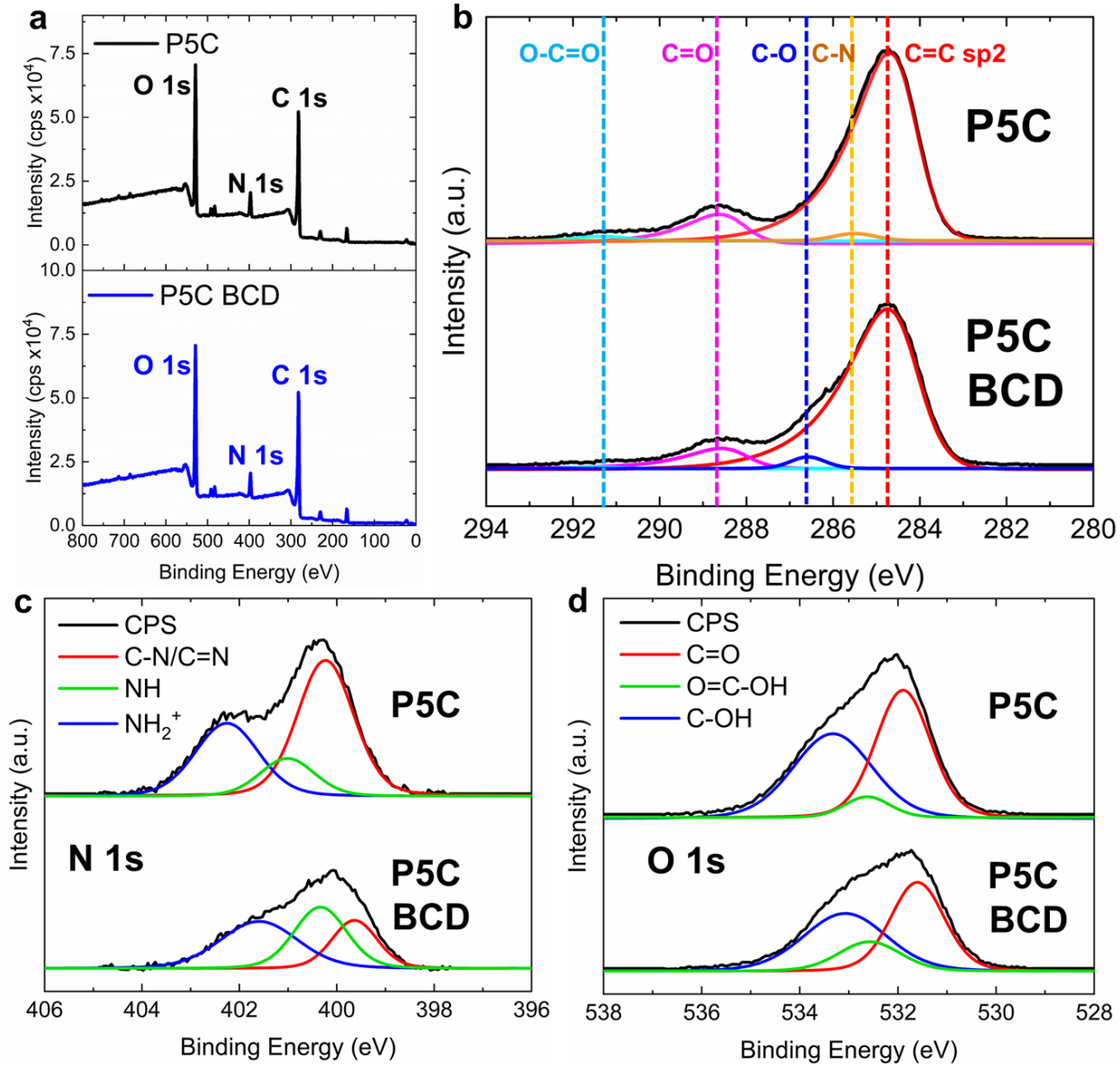

Figure 41. X-ray photoelectron spectroscopy analysis of P5C and P5C samples. (a) XPS survey spectra highlighting C 1s, N 1s, and O 1s in both the P5C and P5C-BCD samples. (b) P5C and P5C-BCD C 1s region of the XPS spectra. Dashed lines in this region are highlighting carbon sp2, C-N, C-O, C=O, and O=C-O regions in the XPS spectra. (c) P5C and P5C-BCD N 1s region of the XPS spectra. This region is highlighting the different protonation states of the nitrogen in the P5C polymer. (d) P5C and P5C-BCD O 1s region of the XPS spectra. This region is highlighting the carboxylic acid groups in P5C as well as the C-OH character increase in P5C-BCD.

There was no observation of C-O binding character in P5C alone; again, this is likely due to the low concentration of this type of bond. P5C and P5C-BCD did show a C=O binding energy at 288.6 eV and a small O-C=O binding energy at 291.1 eV due to the carboxylic acid functional

group in the P5C structure.[65] Focusing on the N 1s region (Figure 41c), there were 3 characteristic binding peaks shown for P5C and P5C-BCD which correspond to the C-N/C=N, NH, and NH_2^+ bonds. C-N/C=N is expressed prevalently in both samples due to the nitrogen being in a conjugated indole structure in which carbon-nitrogen bonds can exist in a mixture of single and double bonded states. Importantly, P5C and P5C-BCD also showed varying levels of NH and NH_2^+ bonds in their N 1s regions as well. There has been previous XPS studies on conjugated polymers containing nitrogen which show that nitrogen binding energies can change based on their relative protonation state.[66,67] In P5C, there was a higher amount of nitrogen atoms in a more protonated state compared to the P5C-BCD samples (NH_2^+ > NH bonds). In P5C, upon synthesis in solution, the solution remained under low pH conditions due to the carboxylic acid groups present in the system. This prompted the nucleophilic nitrogen to enter proton exchange mechanisms with the carboxylic acid groups and thus the nitrogen existed in a more protonated state where NH_2^+ > NH bonds (Figure 42). This indicates that there is also more unprotonated carboxylic acid groups present in the P5C as well. However, in P5C-BCD there is a greater amount of NH bonding character expressed in comparison to the NH_2^+, which is due to the pendant alcohol moieties on the BCD neutralized the unstable NH_2^+ and drove the proton exchange equilibrium to favor the neutral carboxylic acid and amine structure during synthesis in solution (NH). This is likely critical in terms of formaldehyde sensing as carboxylic acid groups can hydrogen bond more effectively with formaldehyde than their unprotonated carboxylate (COO^-) counterparts. Focusing on the O 1s binding region (Figure 41d), there was observed C=O, O-C-OH, and C-OH character which is expressed in both P5C and BCD due to the carboxylic acid and alcohol groups in P5C and BCD. BCD, due to the high concentration of pendant alcohols in its structure, created a high intensity of C-OH binding region which masks the majority of the carboxylic acid region. This, in turn, did not allow for relative

comparison of carboxylic acid groups between the P5C and P5C-BCD, but rather just showed the appearance of both groups. Overall, P5C was observed to have indole features with carboxylic acid functional group which can alter protonation states based on the appearance or disappearance of BCD.

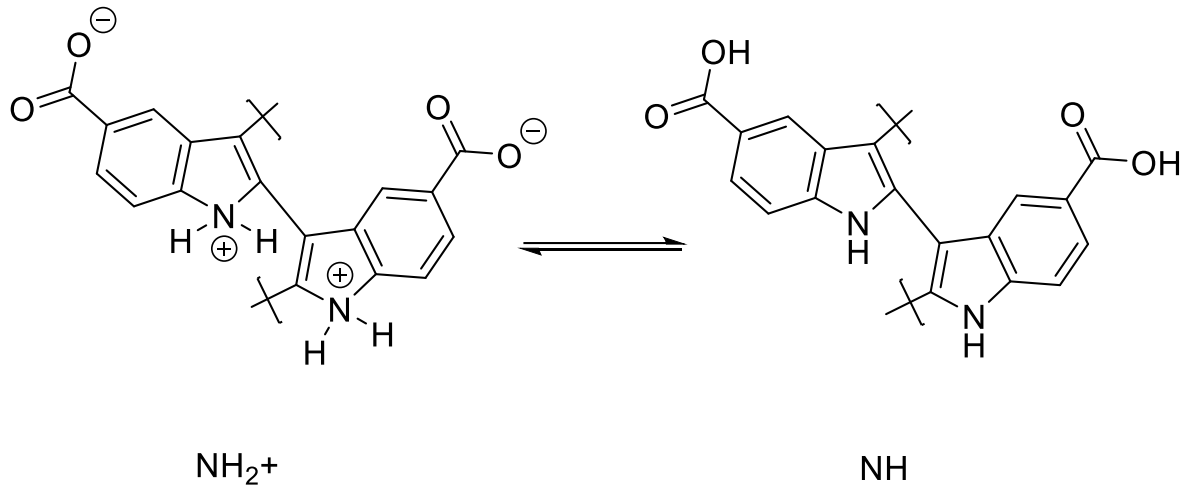

Figure 42. Structure of P5C highlighting the proton exchange mechanism of P5C. Nitrogen protonation and carboxylic acid deprotonation showing the existence of NH and NH_2^+ states.

6.4.2 Sensor Performance

In a background of nitrogen, resonators functionalized with P5C and P5C-BCD produced oscillation frequency shifts when exposed to formaldehyde at various concentrations ranging from 25 ppm to 100 ppm (Figure 43a). To begin testing, a board of resonators was functionalized with 1 μL of a 1 mg mL^{-1} P5C solution or 1 μL of a 1 mg mL^{-1} P5C-BCD solution (i.e., each resonator was functionalized with only one type of chemistry, either P5C or P5C-BCD). After evaporation of the residual solvent, approximately 1 μg of functionalization chemistry remained on each resonator. The board was placed in the test chamber and the oscillation frequency of each resonator was recorded over time. Formaldehyde was introduced into the chamber in 20 min intervals at

concentrations of 25, 50, and 100 ppm with a background of nitrogen. Twenty-minute intervals of nitrogen were used to purge the chamber between intervals of formaldehyde.

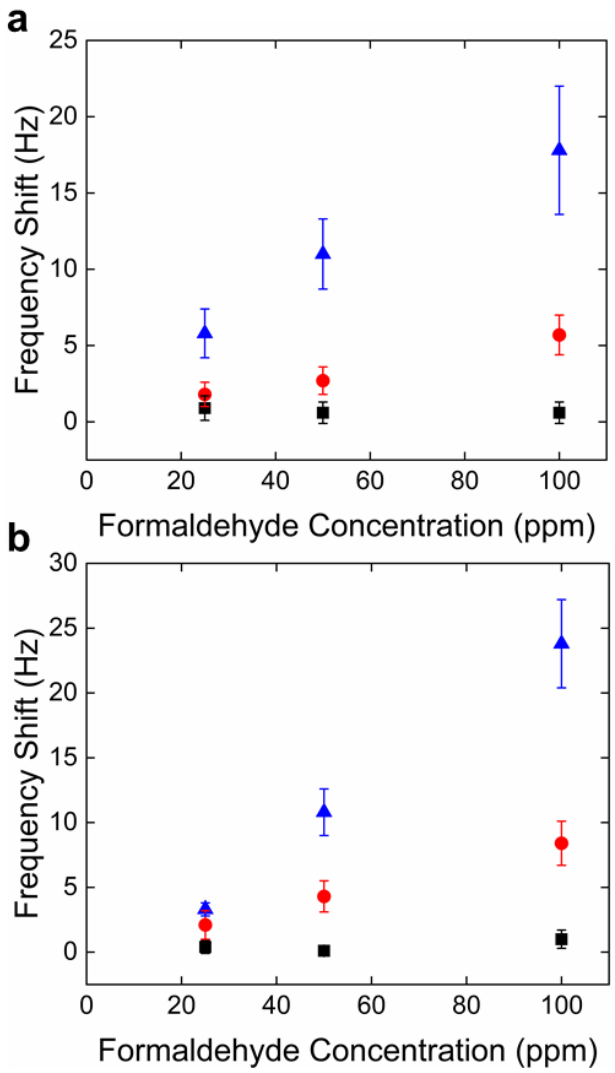

Figure 43. The average oscillation frequency shifts after 20 min plotted against different formaldehyde concentrations as recovered in a (a) background of nitrogen and (b) background of air. The blue triangles, red circles, and black squares represent the average oscillation frequency shifts of P5C-BCD, P5C, and unfunctionalized (i.e., reference) chemistries, respectively. Error bars represent one standard deviation from the average.

The concentration of formaldehyde was directly proportional to the frequency shifts from the oscillator board (Supporting Information Figure 47). This test confirmed the detection of the

formaldehyde gas at a concentration as low as 25 ppm in a background of nitrogen. Moreover, P5C-BCD yielded larger frequency shifts when exposed to formaldehyde under nitrogen background conditions relative to P5C (Figure 43a). When evaluated at concentrations lower than 25 ppm, P5C and P5C-BCD produced negligible frequency shifts compared to those observed from reference channels. The average sensitivity for the sensor in this environment was 13.7 ppm Hz^{-1} and 4.3 ppm Hz^{-1} for P5C and P5C-BCD, respectively. Frequency shifts from the reference channels can be attributed to small fluctuations in temperature and humidity within the testing chamber. This enhanced performance agreed with previous work suggesting that cyclodextrin-based materials enhanced the uptake of formaldehyde.[68–73]

The functionalized resonators also produced significant oscillation frequency shifts when exposed to formaldehyde in a background of air (Supporting Information Figure 47). Additionally, the average frequency shifts were approximately the same as the responses yielded from the test with a background gas of nitrogen (Figure 43b). A linear relationship between oscillation frequency and formaldehyde concentration was found even when the background gas was changed from nitrogen to air. The average sensitivity for the sensor in this environment was 11.9 ppm Hz^{-1} and 7.7 ppm Hz^{-1} for P5C and P5C-BCD, respectively. Again, in this case, P5C-functionalized devices demonstrated less of a response with an air background relative to P5C-BCD functionalized sensors. It has been noted that residual moisture, temperature, or interfering gases being present in an air background can alter the adsorption properties of β-cyclodextrin.[74] Thus, we believe that the better performance of P5C-BCD over P5C in this case was caused by one of these variables.

To test the practicality of the materials chemistry, the sensors were tested in the presence of interfering analytes. The sensors functionalized with P5C or P5C-BCD detected formaldehyde

in the presence of xylene, acetone, and methanol, which were introduced intentionally to serve as interfering gases. Each interfering analyte was added into the chamber at 500 ppm and 1,000 ppm for 20 min intervals with a background of nitrogen. For comparison, formaldehyde at 1,000 ppm was tested separately (Supplementary Information Figure 48). When each analyte was tested separately without any formaldehyde present, most of the interfering analytes showed minimal response (Figure 44a). Xylene at a concentration of 1,000 ppm was the only analyte to generate a significant response from our surface chemistry without formaldehyde present. This is likely because xylene condensed on the surface over time due to its relatively low vapor pressure, which caused the observed response at higher gas concentrations. Moreover, as depicted in Figure 44b, the sensors produced significant oscillation frequency shifts in response to formaldehyde when interfering gases were present with the formaldehyde. These responses to formaldehyde were significant with both the P5C and P5C-BCD functional chemistries. As shown in Table 3, the average frequency shift for resonators exposed to formaldehyde at all of the concentrations was 11.2 Hz, while the interfering gases had a maximum frequency shift of 5.9 Hz from xylene at 1,000 ppm after accounting for frequency shifts from reference channels. While resonators functionalized with P5C and P5C-BCD produced frequency shifts when exposed to xylene, these shifts were markedly smaller than the frequency shifts relative to when exposed to formaldehyde alone. Additionally, almost no response was observed when the resonators were exposed to acetone or methanol (Table 3). However, there was an observed frequency shift having an average magnitude of 7.1 Hz larger when formaldehyde is present, indicating that formaldehyde could still be detected in the presence of other interfering analytes. Thus, formaldehyde could effectively be detected with these materials in the presence of interfering gases that could exist in interior locations.

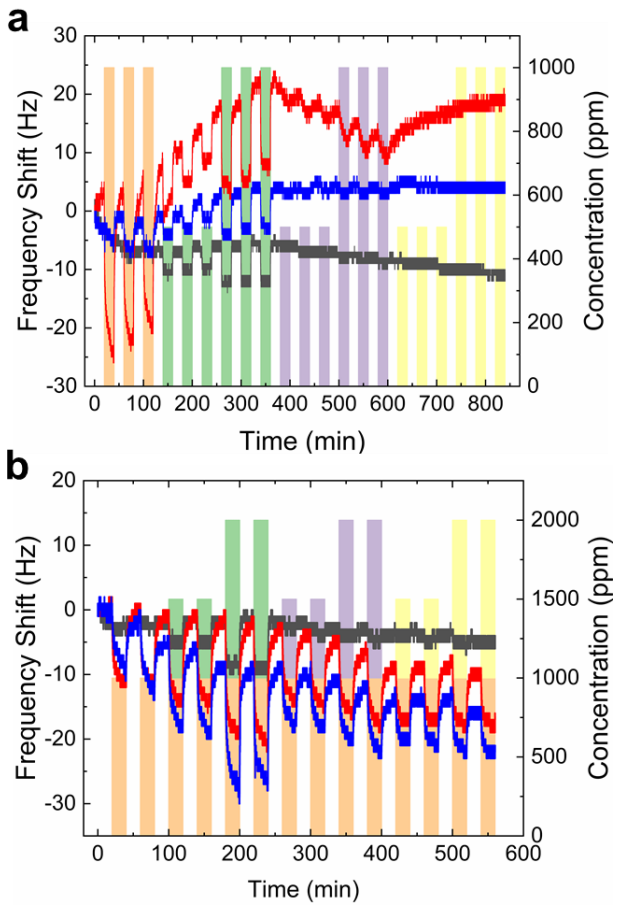

Figure 44. (a) Resonators exposed to 20 min pulses of formaldehyde, methanol, acetone, and xylene separately at concentrations of 500 ppm and 1,000 ppm with a background of nitrogen. (b) Resonators exposed to 20 min pulses of methanol, acetone, and xylene at concentrations of 500 and 1,000 ppm in the presence of 1,000 ppm formaldehyde with a background of nitrogen. The red and blue lines refer to the oscillation frequency shift of resonators functionalized with 1 μL of P5C solution and 1 μL of P5C-BCD solution, respectively, with respect to time. The black line represents the oscillation frequency shift of a reference resonator. Yellow, blue, green, and orange bars indicate the concentration of methanol, acetone, xylene, and formaldehyde, respectively.

Table 3. The average frequency shift of resonators functionalized with 1 μL of P5C solution, 1 μL of P5C-BCD solution, or left unfunctionalized (i.e., reference). Resonators were exposed to 20 min pulse of xylene, acetone, and methanol. The resonators were then run again in similar conditions, except that the resonators were tested in the presence of formaldehyde at 1000 ppm in each 20 min pulse at the same time as the other analytes.

Analyte Concentration	Functionalization Chemistry without Exposure to Formaldehyde			Functionalization Chemistry with Exposure to Formaldehyde at 1000 ppm		
	Reference	P5C	P5C-BCD	Reference	P5C	P5C-BCD
Xylene 500 ppm	2.7 Hz	3.9 Hz	2.6 Hz	3.3 Hz	12.3 Hz	14.0 Hz
Xylene 1000 ppm	5.4 Hz	11.3 Hz	6.1 Hz	7.1 Hz	17.0 Hz	17.7 Hz
Acetone 500 ppm	0.9 Hz	1.4 Hz	1.1 Hz	1.8 Hz	6.6 Hz	11.3 Hz
Acetone 1000 ppm	0.7 Hz	3.9 Hz	1.2 Hz	1.0 Hz	7.8 Hz	11.3 Hz
Methanol 500 ppm	0.6 Hz	0.8 Hz	0.2 Hz	0.9 Hz	5.6 Hz	8.5 Hz
Methanol 1000 ppm	0.7 Hz	1.1 Hz	0.2 Hz	1.1 Hz	5.9 Hz	9.5 Hz

While the relative humidity of the testing environment altered the response of the sensor, significant oscillation frequency shifts were still generated in response to formaldehyde. To understand the effect of humidity on device sensitivity, a board with resonators functionalized with either P5C or P5C-BCD was placed in a chamber with varying humidity levels (Figure 45). The relative humidity in the chamber ranged from 0% to 80% in increments of 20% while formaldehyde was introduced in 30 min intervals. After formaldehyde, pure nitrogen was introduced in 30 min intervals between formaldehyde pulses to purge the chamber of formaldehyde between pulses. When conducting these experiments, the functionalized resonators provided responses to formaldehyde up to 80% relative humidity. There was an increase in frequency shift as the relative humidity was increased, and this is likely due to the hydrophilic nature of the P5C and P5C-BCD. However, as the testing continued, there was an overall downward drift in oscillation frequency as shown clearly in Figure 45d and 45e. We speculate that this downward

drift (Figure 45) was due to the accumulation of moisture on the surface of the resonator. This test indicates that formaldehyde can be detected at different levels of relative humidity with two different chemistries up to 60% relative humidity levels. Resonators functionalized with P5C-BCD had greater overall frequency responses during the duration of the test even at higher relative humidity levels.

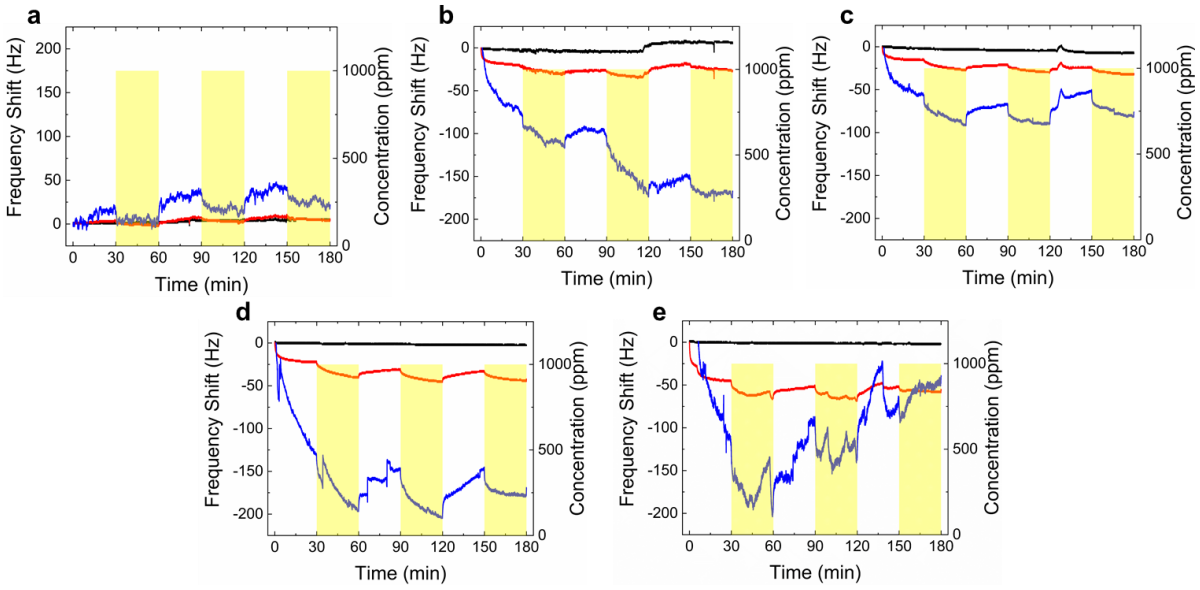

Figure 45. Resonators were exposed to 30 min pulse of formaldehyde at concentrations of 1,000 ppm with a background of nitrogen and different relative levels of humidity: (a) 0% relative humidity, (b) 20% relative humidity, (c) 40% relative humidity, (d) 60% relative humidity, and (e) 80% relative humidity. Relative humidity values were measured at a dry bulb temperature of 22.5 °C. The red and blue lines refer to the oscillation frequency shift with respect to time of resonators functionalized with 1 μL of P5C solution and 1 μL of P5C-BCD solution, respectively. The black lines represent the oscillation frequency shift of an unfunctionalized resonator (i.e., reference). Yellow bars indicate the presence of formaldehyde.

As the relative humidity levels increased, the P5C-BCD produced greater responses to formaldehyde for a variety of reasons. First, formaldehyde could be better adsorbed into the BCD hydrophobic cavity. Due to the hydrophobic cavity and hydrophilic exterior of the β-cyclodextrin, this creates an ideal host-guest interaction with formaldehyde, even as the relative humidity levels

increase. On the other hand, when β-cyclodextrin was present at lower relative humidity levels, there were also better responses to formaldehyde. Thus, we also put forward that β-cyclodextrin can not only act as a robust host for formaldehyde, but it can also act as a spacer in the P5C. It was observed upon the drop casting and drying of the polymer films that there was a surface texture unique to each film. When drop cast, P5C forms a more uniform film with spherical morphologies (Figure 38). However, when P5C-BCD is cast, it forms a more rigid textured and disrupted surface with cylindrical or tubular morphologies (Figure 38). At lower relative humidity levels, the P5C-BCD, due to the formed cylindrical rigid surface, allowed for more lateral surface area. This, in turn, allowed better diffusion of formaldehyde gas into the material and allowed formaldehyde to better interact with the surface chemistry. In this case, the host-guest interactions in the P5C-BCD thin films are not utilized because there is a low abundance of water. In turn, more surface interactions are a product of better diffusion of the gas into the material. Third, BCD allows for more carboxylic acid groups to remain protonated on the P5C polymer chain. As shown in the XPS N 1s region (Figure 41c), in P5C-BCD there was a higher amount of NH bonds over NH_2^+ bonds present in the sample in comparison to P5C. Due to the pendant alcohol moieties in the BCD this, in turn buffers the system, allowing for the proton exchange equilibrium to favor the NH state (Figure 42). The NH state allows for a higher amount of carboxylic acid groups to be present which can hydrogen bond more effectively with formaldehyde and thus produce greater sensors responses. We believe the synergy of these three plausible sensing mechanisms allows for a robust formaldehyde sensing chemistry capable of detecting formaldehyde down to 25 ppm concentration levels in a variety of practical indoor environments.

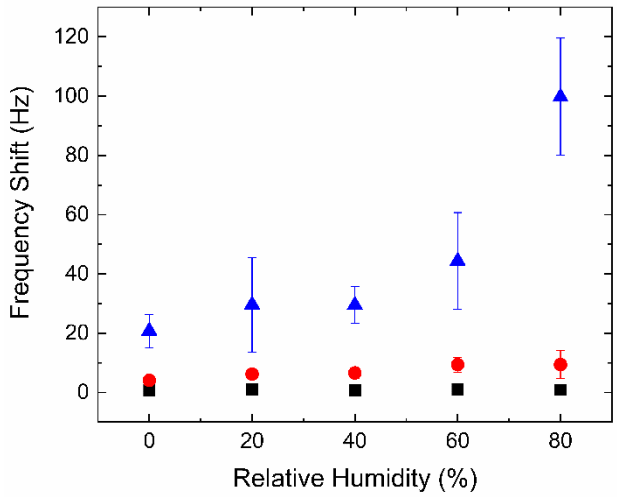

Figure 46. The red circles and blue triangles refer to the average oscillation frequency shift of resonators functionalized with 1 µL of P5C solution and 1 µL of P5C-BCD solution, respectively, with respect to each relative humidity level. The black squares represent the average oscillation frequency shift of an unfunctionalized resonator (i.e., reference). Resonators were exposed to 30 min pulses of formaldehyde at 1000 ppm at different levels of relative humidity. Error bars represent one standard deviation from the average.

6.5 Conclusions

A resonant mass sensor coated with P5C or P5C-BCD was utilized for enhanced formaldehyde sensing. P5C enabled enhanced adsorption of formaldehyde on the resonant mass sensor to 25 ppm levels. Moreover, the response of P5C to formaldehyde can be further enhanced by blending P5C with BCD, which allows for better diffusion of formaldehyde gas into the material, a hydrophobic cavity suitable for capturing formaldehyde, and more carboxylic acid moieties to promote better formaldehyde adsorption in a humid environment. This work implemented a feasible chemical treatment protocol combined with the practical utilization of resonant mass sensors to create a robust sensing platform suitable for the detection of formaldehyde. We anticipate that these materials will be utilized further in future formaldehyde sensing studies to reach lower concentration detection limits while leveraging the materials properties of P5C and BCD in a useful manner. Overall, this formaldehyde sensor materials

chemistry offers an inexpensive, facile to synthesize, and processable material which makes it a practical commercial contender for the interior monitoring of formaldehyde

6.6 Acknowledgments

This work was funded by the Center for High Performance Buildings at Purdue University (Grant number CHPB-44-2019).

6.7 Supporting Information Figures

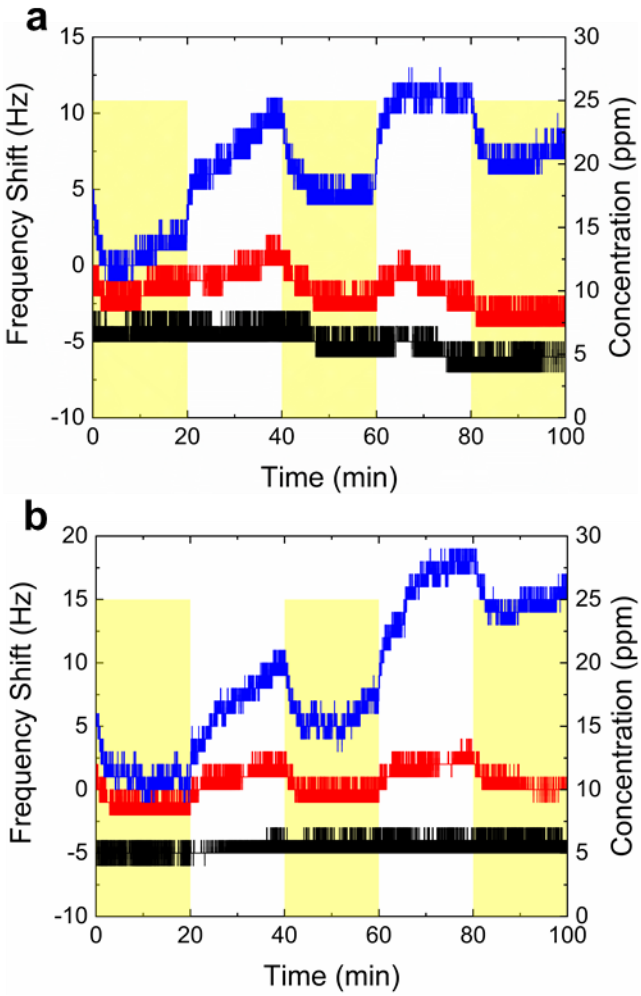

Figure 47. Real-time data of resonator frequency when exposed to 20 min pulses of formaldehyde at a concentration of 25 ppm with a background of (a) nitrogen and (b) air. The red and blue lines refer to the oscillation frequency shift with respect to time of resonators functionalized with 1 μL of P5C solution and 1 μL of P5C-BCD solution, respectively. The black line represents the oscillation frequency shift of an unfunctionalized resonator (i.e., reference). Yellow bars indicate when the formaldehyde analyte was injected into the testing chamber.

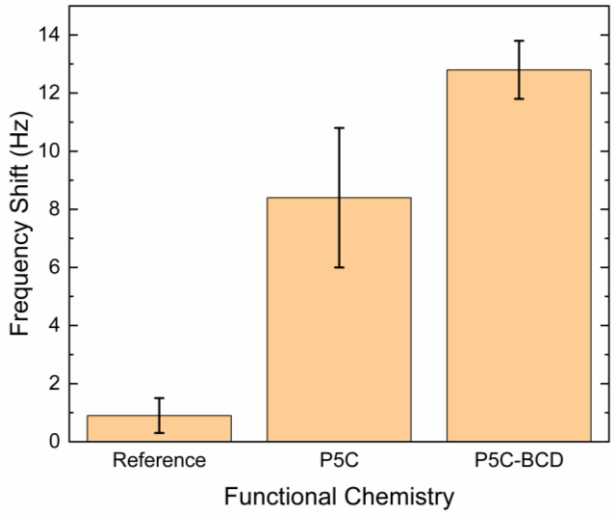

Figure 48. The average oscillation frequency shift of resonators functionalized with 1 µg of P5C and 1 µg of P5C-BCD with respect to 20-min pulses of formaldehyde at a concentration of 1,000 ppm. Error bars represent one standard deviation from the average value that is plotted.

6.8 References

(1) Chung, P. R.; Tzeng, C. T.; Ke, M. T.; Lee, C. Y. Formaldehyde Gas Sensors: A Review. *Sensors (Switzerland)* **2013**, *13*, 4468–4484.

(2) Castro-Hurtado, I.; Mandayo, G. G.; Castaño, E. Conductometric Formaldehyde Gas Sensors. A Review: From Conventional Films to Nanostructured Materials. *Thin Solid Films* **2013**, *548*, 665–676.

(3) Flueckiger, J.; Ko, F.; Cheung, K. Microfabricated Formaldehyde Gas Sensors. *Sensors* **2009**, *9*, 9196–9215.

(4) Chan, W. H.; Xie, T. Y. Determination of Sub-Ppbv Levels of Formaldehyde in Ambient Air Using Girard's Reagent T-Coated Glass Fiber Filters and Adsorption Voltammetry. *Anal. Chim. Acta* **1997**, *349*, 349–357.

(5) Emery, J. A. Formaldehyde Release from Wood Panel Products Bonded with Phenol Formaldehyde Adhesives. In *Formaldehyde Release from Wood Products*; ACS Symposium Series; American Chemical Society, 1986; Vol. 316, 3–26.

(6) Cincinelli, A.; Martellini, T. Indoor Air Quality and Health. *Int. J. Environ. Res. Public Health* **2017**, *14*, 1286.

(7) Kawamura, K.; Kerman, K.; Fujihara, M.; Nagatani, N.; Hashiba, T.; Tamiya, E. Development of a Novel Hand-Held Formaldehyde Gas Sensor for the Rapid Detection of Sick Building Syndrome. *Sensors Actuators B Chem.* **2005**, *105*, 495–501.

(8) Sekine, Y.; Nishimura, A. Removal of Formaldehyde from Indoor Air by Passive Type Air-Cleaning Materials. *Atmos. Environ.* **2001**, *35*, 2001–2007.

(9) Hu, J.; Wu, X.; Zeng, W. Formaldehyde Sensor Based on Polypyrrole/ β -Cyclodextrin. *J. Control. Release* **2011**, *152*, 211–213.

(10) Partanen, T.; Kauppinen, T.; Hernberg, S.; Nickels, J.; Luukkonen, R.; Hakulinen, T.; Pukkala, E. Formaldehyde Exposure and Respiratory Cancer among Woodworkers--an Update. *Scand. J. Work. Environ. Health* **1990**, No. 6, 394–400.

(11) Gupta, K. C.; Ulsamer, A. G.; Preuss, P. W. Formaldehyde in Indoor Air: Sources and Toxicity. *Environ. Int.* **1982**, *8*, 349–358.

(12) Kim, W. J.; Terada, N.; Nomura, T.; Takahashi, R.; Lee, S. D.; Park, J. H.; Konno, A. Effect of Formaldehyde on the Expression of Adhesion Molecules in Nasal Microvascular Endothelial Cells: The Role of Formaldehyde in the Pathogenesis of Sick Building Syndrome. *Clin. Exp. Allergy* **2002**, *32*, 287–295.

(13) Hauptmann, M. Mortality From Lymphohematopoietic Malignancies Among Workers in Formaldehyde Industries. *CancerSpectrum Knowl. Environ.* **2003**, *95*, 1615–1623.

(14) Pinkerton, L. E.; Hein, M. J.; Stayner, L. T. Mortality among a Cohort of Garment Workers Exposed to Formaldehyde: An Update. *Occup. Environ. Med.* **2004**, *61*, 193–200.

(15) Zhang, L.; Steinmaus, C.; Eastmond, D. A.; Xin, X. K.; Smith, M. T. Formaldehyde Exposure and Leukemia: A New Meta-Analysis and Potential Mechanisms. *Mutat. Res. Mutat. Res.* **2009**, *681*, 150–168.

(16) Wang, R.; Zhang, Y.; Lan, Q.; Holford, T. R.; Leaderer, B.; Zahm, S. H.; Boyle, P.; Dosemeci, M.; Rothman, N.; Zhu, Y.; et al. Occupational Exposure to Solvents and Risk of Non-Hodgkin Lymphoma in Connecticut Women. *Am. J. Epidemiol.* **2009**, *169*, 176–185.

(17) *Air Quality Guidelines, 2nd Ed.; WHO Regional Office for Europe: Copenhagen, Denmark,* **2001***, 15.*

(18) *Occupational Safety and Health Guideline for Formaldehyde Potential Human Carcinogen; U.S. Department of Health and Human Services: Washington, DC, USA,* **1988**, *16.*

(19) Chen, D.; Yuan, Y. J. Thin-Film Sensors for Detection of Formaldehyde: A Review. *IEEE Sens. J.* **2015**, *15*, 6749–6760.

(20) Dojahn, J. G.; Wentworth, W. E.; Stearns, S. D. Characterization of Formaldehyde by Gas Chromatography Using Multiple Pulsed-Discharge Photoionization Detectors and a Flame Ionization Detector. *J. Chromatogr. Sci.* **2001**, *39*, 54–58.

(21) Davenport, J. J.; Hodgkinson, J.; Saffell, J. R.; Tatam, R. P. Formaldehyde Sensor Using Non-Dispersive UV Spectroscopy at 340nm. In *Proc.SPIE*; **2014**, *9141*, Optical Sensing and Detection III, 91410K.

(22) Septon, J. C.; Ku, J. C. Workplace Air Sampling and Polarographic Determination of Formaldehyde. *Am. Ind. Hyg. Assoc. J.* **1982**, *43*, 845–852.

(23) Möhlmann, G. R. Formaldehyde Detection in Air by Laser-Induced Fluorescence. *Appl. Spectrosc.* **1985**, *39*, 98–101.

(24) van den Broek, J.; Klein Cerrejon, D.; Pratsinis, S. E.; Güntner, A. T. Selective Formaldehyde Detection at Ppb in Indoor Air with a Portable Sensor. *J. Hazard. Mater.* **2020**, *399*, 123052.

(25) Tian, H.; Fan, H.; Li, M.; Ma, L. Zeolitic Imidazolate Framework Coated ZnO Nanorods as Molecular Sieving to Improve Selectivity of Formaldehyde Gas Sensor. *ACS Sensors* **2016**, *1*, 243–250.

(26) Wang, Z.; Hou, C.; De, Q.; Gu, F.; Han, D. One-Step Synthesis of Co-Doped In_2O_3 Nanorods for High Response of Formaldehyde Sensor at Low Temperature. *ACS Sensors* 1**2018**, *3*, 468–475.

(27) Ishihara, S.; Labuta, J.; Nakanishi, T.; Tanaka, T.; Kataura, H. Amperometric Detection of Sub-Ppm Formaldehyde Using Single-Walled Carbon Nanotubes and Hydroxylamines: A Referenced Chemiresistive System. *ACS Sensors* **2017**, *2*, 1405–1409.

(28) Wang, Y. H.; Lee, C. Y.; Lin, C. H.; Fu, L. M. Enhanced Sensing Characteristics in MEMS-Based Formaldehyde Gas Sensors. *Microsyst. Technol.* **2008**, *14*, 995–1000.

(29) Asri, M. I. A.; Hasan, M. N.; Fuaad, M. R. A.; Yunos, Y. M.; Ali, M. S. M. MEMS Gas Sensors: A Review. *IEEE Sens. J.* **2021**, *21*, 18381–18397.

(30) Zhou, Z.-L.; Kang, T.-F.; Zhang, Y.; Cheng, S.-Y. Electrochemical Sensor for Formaldehyde Based on Pt–Pd Nanoparticles and a Nafion-Modified Glassy Carbon Electrode. *Microchim. Acta* **2009**, *164*, 133–138.

(31) Chen, T.; Liu, Q. J.; Zhou, Z. L.; Wang, Y. D. The Fabrication and Gas-Sensing Characteristics of the Formaldehyde Gas Sensors with High Sensitivity. *Sensors Actuators B Chem.* **2008**, *131*, 301–305.

(32) Dirksen, J. A.; Duval, K.; Ring, T. A. NiO Thin-Film Formaldehyde Gas Sensor. *Sensors Actuators B Chem.* **2001**, *80*, 106–115.

(33) Knake, R.; Jacquinot, P.; Hodgson, A. W. E.; Hauser, P. C. Amperometric Sensing in the Gas-Phase. *Anal. Chim. Acta* **2005**, *549*, 1–9.

(34) Wang, H.; Chi, Y.; Gao, X.; Lv, S.; Chu, X.; Wang, C.; Zhou, L.; Yang, X. Amperometric Formaldehyde Sensor Based on a Pd Nanocrystal Modified C/Co_2P Electrode. *J. Chem.* **2017**, *2017*, 2346895.

(35) McGinn, C. K.; Lamport, Z. A.; Kymissis, I. Review of Gravimetric Sensing of Volatile Organic Compounds. *ACS Sensors* **2020**, *5*, 1514–1534.

(36) Flueckiger, J.; Ko, F. K.; Cheung, K. C. Microfabricated Formaldehyde Gas Sensors. *Sensors (Basel).* **2009**, *9*, 9196–9215.

(37) Choi, N.-J.; Lee, H.-K.; Moon, S. E.; Kim, J.; Yang, W. S. Ultrafast Response Sensor to Formaldehyde Gas Based on Metal Oxide. *J. Nanosci. Nanotechnol.* **2014**, *14*, 5807–5810.

(38) Zhou, W.; Wu, Y.-P.; Zhao, J.; Dong, W.-W.; Qiao, X.-Q.; Hou, D.-F.; Bu, X.; Li, D.-S. Efficient Gas-Sensing for Formaldehyde with 3D Hierarchical Co_3O_4 Derived from Co5-Based MOF Microcrystals. *Inorg. Chem.* **2017**, *56*, 14111–14117.

(39) Bouchikhi, B.; Chludziński, T.; Saidi, T.; Smulko, J.; Bari, N. El; Wen, H.; Ionescu, R. Formaldehyde Detection with Chemical Gas Sensors Based on WO_3 Nanowires Decorated with Metal Nanoparticles under Dark Conditions and UV Light Irradiation. *Sensors Actuators B Chem.* **2020**, *320*, 128331.

(40) Zhang, D.; Liu, J.; Jiang, C.; Liu, A.; Xia, B. Quantitative Detection of Formaldehyde and Ammonia Gas via Metal Oxide-Modified Graphene-Based Sensor Array Combining with Neural Network Model. *Sensors Actuators B Chem.* **2017**, *240*, 55–65.

(41) Zaki, M.; Hashim, U.; Arshad, M. K. M.; Nasir, M.; Ruslinda, A. R. Sensitivity and Selectivity of Metal Oxides Based Sensor towards Detection of Formaldehyde. In *2016 IEEE International Conference on Semiconductor Electronics (ICSE)*; 2016; 312–315.

(42) Diltemiz, S. E.; Ecevit, K. High-Performance Formaldehyde Adsorption on CuO/ZnO Composite Nanofiber Coated QCM Sensors. *J. Alloys Compd.* **2019**, *783*, 608–616.

(43) Hussain, M.; Kotova, K.; Lieberzeit, P. A. Molecularly Imprinted Polymer Nanoparticles for Formaldehyde Sensing with QCM. *Sensors* **2016**, *16*, 1011.

(44) Feng, L.; Feng, L.; Li, Q.; Cui, J.; Guo, J. Sensitive Formaldehyde Detection with QCM Sensor Based on PAAm/MWCNTs and PVAm/MWCNTs. *ACS Omega* **2021**, *6*, 14004–14014.

(45) Tai, H.; Jiang, Y.; Duan, C.; Dan, W.; Li, X. Development of a Novel Formaldehyde OTFT Sensor Based on P3HT/Fe2O3 Nanocomposite Thin Film. *Integr. Ferroelectr.* **2013**, *144*, 15–21.

(46) Tang, X.; Raskin, J.-P.; Lahem, D.; Krumpmann, A.; Decroly, A.; Debliquy, M. A Formaldehyde Sensor Based on Molecularly-Imprinted Polymer on a TiO_2 Nanotube Array. *Sensors (Basel).* **2017**, *17*, 675.

(47) Rovina, K.; Vonnie, J. M.; Shaeera, S. N.; Yi, S. X.; Halid, N. F. A. Development of Biodegradable Hybrid Polymer Film for Detection of Formaldehyde in Seafood Products. *Sens. Bio-Sensing Res.* **2020**, *27*, 100310.

(48) Zhang, D.; Zhang, M.; Ding, F.; Liu, W.; Zhang, L.; Cui, L. Efficient Removal of Formaldehyde by Polyethyleneimine Modified Activated Carbon in a Fixed Bed. *Environ. Sci. Pollut. Res.* **2020**, *27*, 18109–18116.

(49) Tai, H.; Bao, X.; He, Y.; Du, X.; Xie, G.; Jiang, Y. Enhanced Formaldehyde-Sensing Performances of Mixed Polyethyleneimine-Multiwalled Carbon Nanotubes Composite Films on Quartz Crystal Microbalance. *IEEE Sens. J.* **2015**, *15*, 6904–6911.

(50) Ariyageadsakul, P.; Vchirawongkwin, V.; Kritayakornupong, C. Role and Impact of Differently Charged Polypyrrole on Formaldehyde Sensing Behavior. *Synth. Met.* **2017**, *230*, 27–38.

(51) Lee, C. Y.; Hsieh, P. R.; Lin, C. H.; Chou, P. C.; Fu, L. M.; Chiang, C. M. MEMS-Based Formaldehyde Gas Sensor Integrated with a Micro-Hotplate. In *Microsystem Technologies*; 2006, *12*, 893–898.

(52) Hodul, J. N.; Murray, A. K.; Carneiro, N. F.; Meseke, J. R.; Morris, J.; He, X.; Zemlyanov, D.; Chiu, G. T.-C.; Braun, J. E.; Rhoads, J. F.; et al. Modifying the Surface Chemistry and Nanostructure of Carbon Nanotubes Facilitates the Detection of Aromatic Hydrocarbon Gases. *ACS Appl. Nano Mater.* **2020**, *3*, 10389–10398.

(53) Bartlett, P. N.; Ling-Chung, S. K. Conducting Polymer Gas Sensors Part III: Results for Four Different Polymers and Five Different Vapours. *Sensors and Actuators* **1989**, *20*, 287–292.

(54) Bartlett, P. N.; Archer, P. B. M.; Ling-Chung, S. K. Conducting Polymer Gas Sensors Part I: Fabrication and Characterization. *Sensors and Actuators* **1989**, *19*, 125–140.

(55) Joshi, L.; Gupta, B.; Prakash, R. Chemical Synthesis of Poly(5-Carboxyindole) and Poly(5-Carboxyindole)/ Carboxylated Multiwall Carbon Nanotube Nanocomposite. *Thin Solid Films* **2010**, *519*, 218–222.

(56) Gupta, B.; Chauhan, D. S.; Prakash, R. Controlled Morphology of Conducting Polymers: Formation of Nanorods and Microspheres of Polyindole. *Mater. Chem. Phys.* **2010**, *120*, 625–630.

(57) Joshi, L.; Prakash, R. Synthesis of Conducting Poly(5-Carboxyindole)/Au Nanocomposite: Investigation of Structural and Nanoscale Electrical Properties. *Thin Solid Films* **2013**, *534*, 120–125.

(58) Abarca, R. L.; Rodríguez, F. J.; Guarda, A.; Galotto, M. J.; Bruna, J. E. Characterization of Beta-Cyclodextrin Inclusion Complexes Containing an Essential Oil Component. *Food Chem.* **2016**, *196*, 968–975.

(59) Thurein, S. M.; Lertsuphotvanit, N.; Phaechamud, T. Physicochemical Properties of β-Cyclodextrin Solutions and Precipitates Prepared from Injectable Vehicles. *Asian J. Pharm. Sci.* **2018**, *13*, 438–449.

(60) Joshi, L.; Gupta, B.; Prakash, R. Chemical Synthesis of Poly(5-Carboxyindole) and Poly(5-Carboxyindole)/Carboxylated Multiwall Carbon Nanotube Nanocomposite. *Thin Solid Films* **2010**, *519*, 218–222.

(61) Afzal, A. B.; Akhtar, M. J.; Nadeem, M.; Hassan, M. M. Investigation of Structural and Electrical Properties of Polyaniline/Gold Nanocomposites. *J. Phys. Chem. C* **2009**, *113*, 17560–17565.

(62) Mbhele, Z. H.; Salemane, M. G.; van Sittert, C. G. C. E.; Nedeljković, J. M.; Djoković, V.; Luyt, A. S. Fabrication and Characterization of Silver−Polyvinyl Alcohol Nanocomposites. *Chem. Mater.* **2003**, *15*, 5019–5024.

(63) Yan, X.; Xu, T.; Chen, G.; Yang, S.; Liu, H.; Xue, Q. Preparation and Characterization of Electrochemically Deposited Carbon Nitride Films on Silicon Substrate. *J. Phys. D. Appl. Phys.* **2004**, *37*, 907–913.

(64) Chen, X.; Wang, X.; Fang, D. A Review on C1s XPS-Spectra for Some Kinds of Carbon Materials. *Fullerenes, Nanotub. Carbon Nanostructures* **2020**, *28*, 1048–1058.

(65) Neoh, K. G.; Kang, E. T.; Tan, K. L. Protonation and Deprotonation Behaviour of Amine Units in Polyaniline. *Polymer (Guildf).* **1993**, *34*, 1630–1636.

(66) Tong, Z.; Yang, Y.; Wang, J.; Zhao, J.; Su, B.-L.; Li, Y. Layered Polyaniline/Graphene Film from Sandwich-Structured Polyaniline/Graphene/Polyaniline Nanosheets for High-Performance Pseudosupercapacitors. *J. Mater. Chem. A* **2014**, *2*, 4642–4651.

(67) Wang, L.; Liang, X.-Y.; Chang, Z.-Y.; Ding, L.-S.; Zhang, S.; Li, B.-J. Effective Formaldehyde Capture by Green Cyclodextrin-Based Metal–Organic Framework. *ACS Appl. Mater. Interfaces* **2018**, *10*, 42–46.

(68) Yang, Z.; Miao, H.; Rui, Z.; Ji, H. Enhanced Formaldehyde Removal from Air Using Fully Biodegradable Chitosan Grafted β-Cyclodextrin Adsorbent with Weak Chemical Interaction. *Polymers (Basel).* **2019**, *11*, 276.

(69) Noreña-Caro, D.; Álvarez-Láinez, M. Functionalization of Polyacrylonitrile Nanofibers with β-Cyclodextrin for the Capture of Formaldehyde. *Mater. Des.* **2016**, *95*, 632–640.

(70) Kadam, V.; Kyratzis, I. L.; Truong, Y. B.; Wang, L.; Padhye, R. Air Filter Media Functionalized with β-Cyclodextrin for Efficient Adsorption of Volatile Organic Compounds. *J. Appl. Polym. Sci.* **2020**, *137*, 49228.

(71) Liu, Z.; Yan, A.; Miao, R. Removal of Indoor Pollutants by Nano TiO2/Beta-Cyclodextrin Coated Paper under UV Irradiation. In *2010 4th International Conference on Bioinformatics and Biomedical Engineering*; **2010**; 1–4.

(72) Yu, X.; Qi, H.; Huang, Z.; Zhang, B.; Liu, S. Preparation and Characterization of Spherical β-Cyclodextrin/Urea–Formaldehyde Microcapsules Modified by Nano-Titanium Oxide. *RSC Adv.* **2017**, *7*, 7857–7863.

(73) Zhao, W.; Shi, B.; Hu, C. Adsorption Properties of B-Cyclodextrin for Adsorbing Aromatic Hydrocarbons from the Gas Phase and Water. *J. Macromol. Sci. Part B* **2007**, *47*, 211–216.

CHAPTER 7. FUTURE WORK

7.1 Overview

The main challenges associated with resonant mass MEMS indoor gas sensors are primarily sensitivity and selectivity performance issues. In other words, the performance of a gravimetric gas sensor device is limited by the ability of the sensor to detect the gas analyte at lower concentrations (i.e., sensitivity), as well as distinguishing the target analyte from other analytes that are simultaneously present (i.e., selectivity). Moreover, investigating or synthesizing a novel high-performing chemical recognition layer for each target analyte is difficult as this requires extensive chemical intuition, time, and cost. This section hopes to offer plausible future work to address these issues through three main ideas. First, through the utilization of gas micro pre-concentrators incorporated into the resonant mass sensor system. The gas pre-concentrator allows for an increase in sensitivity (i.e., limit of detection) to target analytes present at lower concentrations. Second, the utilization of different material processing techniques. Utilizing enhanced processing of the chemical recognition layers on the devices can allow for less agglomeration of material chemistry causing an enhanced interaction with target analytes and an increase in sensitivity of the devices. Third, utilization of a pre-chemical recognition layer to act as a barrier to limit interfering analytes that can contact the surface chemistry on the device. This, in theory will allow for more selectivity on the devices as only target analyte molecules can interact with the chemical recognition layer. Overall, the synergy of materials chemistry and engineering barriers implemented into the resonant mass sensor devices will allow for better performance of these MEMS resonant mass sensor devices.

7.2 Introduction of Gas Sensor Pre-concentrators and Pre-concentrator Integration

Scenarios where the exposure limit of a target analyte is particularly at a low concentration (i.e., ≤ 1 ppm) can create a challenge in designing a robust surface chemistry on the device that can interact with the target analyte and allow the sensor to detect at these low concentration limits. Thus, recent efforts in MEMS gas sensor devices have looked to utilizing a pre-concentrator integrated into the sensor device.[1] A pre-concentrator is a device that contains a micro heater coated with a highly gas absorbing material that over-time can accumulate target gas analyte molecules.[2] Once the gas molecules have absorbed into the absorbent material, the material can be heated to allow for thermal desorption of the gas molecules. These desorbed gas molecules can then contact the chemical recognition layers on the resonators and transduce a response. Because there is an accumulation of gas molecules over time, the concentration of the desorbed gas analyte contacting the chemical recognition layer is at a higher concentration and in the capable working concentration detection range of that surface chemistry. In this report, formaldehyde had a reported exposure limit of 0.016 ppm in an 8-h timeframe. However, our P5C-BCD nanocomposites were only capable of detecting formaldehyde at 25 ppm concentration levels. Thus, if there was a way to incorporate a micro pre-concentrator into the resonator device setup, this would allow for an accumulation of formaldehyde over time and when thermally desorbed the detection would be in the working detection limit of the P5C-BCD surface chemistry.

There are many considerations associated with adding a pre-concentrator such as accounting for dead volume, breakthrough volume, thermal desorption temperatures of analytes, type of absorbent material, and additional costs of these components.[3] The term “dead volume” is often used to refer to the fixed volume surrounding the sensor, which includes the chamber volumes surrounding the devices, as well as the adjacent volumes introduced by interconnect tubing and valves due to interfacing with an external gas flow system.[3-8] Dead volume needs to be accounted

for as it dilutes the concentration of the target analyte as it thermally desorbs from the pre-concentrator absorbent material. Thus, having a multi-component system that is connected by long tubing or tubing with large diameters is not feasible. Rather, it is recommended that the micro-pre-concentrator be directly located in or directly attached to the same chamber as the resonant mass sensor board so that the dead volume can be minimized. Another consideration is breakthrough volume. Breakthrough volume refers to the volume of analyte-loaded gas at a fixed concentration that passes or "breaks through" the pre-concentrator once the pre-concentrator absorbent material has reached saturation.[3,9,10] In other words, the point at which the analyte begins to elute into the chamber without being absorbed by the absorbent material. Breakthrough volume needs to be accounted for in a fixed volume system. If there is high breakthrough volume this can create a buildup of pressure and make it difficult for gas molecules coming from the pre-concentrator after thermal desorption to reach the chemical selective layers on the resonators. This breakthrough volume can be accounted for by utilizing highly absorbent materials with high breakthrough capacity values. Additionally, using materials with high partition coefficients or high specific surface area that have a high capacity for the target analyte is another solution. Next, the thermal desorption temperature of the target analytes needs to be accounted for as well. Various gas-phase species desorb at different temperatures from a given absorbent material based on the vapor pressure and boiling point of the compounds and interaction between the analyte and absorbent.[11,12] Thus, it is important to understand the specific target analyte of interest and how it desorbs from the absorbent material in use. Reaching the optimal thermal desorption temperature for the target analyte quickly minimizes the time it takes to heat the material, thus minimizing the energy usage of the micro heater. Additionally, knowing the target analyte's boiling point in comparison to other analytes that are simultaneously present can add a coarse selectivity to the

system since only a few analytes are likely to desorb in the same temperature region as the target species. The additional costs and materials are also a crucial consideration for proper device function. When adding a pre-concentrator there are additional components such as a micro-heater and additional materials necessary for high absorption of the target gas molecules. These components add an additional cost and energy usage to the device and need to be considered if implementing into resonant mass sensor devices. Typically, micro heaters require alternating currents of 5–10 A at relatively high voltages of 20–50 V to heat a pre-concentrator.[13] The heating rate, operation time, and maximum temperatures achieved depend on the size and shape of the absorbent material used in the pre-concentrator. Previous studies have utilized metal organic frameworks (MOFs), ceramic, polymeric, or graphene-based materials (i.e., carbon nanotubes and activated charcoal) as their highly absorbent pre-concentrating material.[14-19] Choosing the correct material, as previously mentioned, to use in the pre-concentrator is the most critical consideration mainly because it must be a highly absorbent material for your target gas analyte, have high break through capacity, but also capable of withstanding temperatures up to 300 °C upon thermal desorption. Thus, there remains an ongoing challenge in developing novel pre-concentrating materials just as well as developing novel chemical recognition layers on MEMS sensor devices. Overall, when incorporating a pre-concentrator into the resonant mass sensor devices due to the above considerations it is recommended to utilize a previously established absorbent material which can later be optimized in this current sensor system.

Integrating and designing the pre-concentrator that can fit into our resonant mass sensor platform must account for the previously mentioned considerations to perform optimally. Implementing the pre-concentrator into our resonant mass sensor gas sensing system would take place at the interface of the manifold tubing and the testing chamber. This proposed

implementation is outlined in Figure 49. It is recommended to have the pre-concentrator be directly attached to the testing chamber and the tubing from the manifold to be as short as possible to eliminate dead volume. Moreover, the concentration of gas analyte can still be controlled in the same manner using the manifold already installed in our current testing process. If dead volume is too large the volume in the chamber can be decreased to eliminate the space between the pre-concentrator and the resonant mass sensors. The pre-concentrator shown in Figure 49 and Figure 50 have an array of 3 micro heaters coated with the absorbent material. This is a proposed but not a fixed layout. Studies have shown that further optimization of the absorbent material layout and morphology of the absorbent material can further decrease dead volume, increase break through capacity, and decrease thermal desorption times.[3,20-23] Thus, it is important to understand that the location of the pre-concentrator and the configuration of the absorbent material in the pre-concentrator in the current testing system needs to be accounted for to ameliorate the performance of the pre-concentrator device.

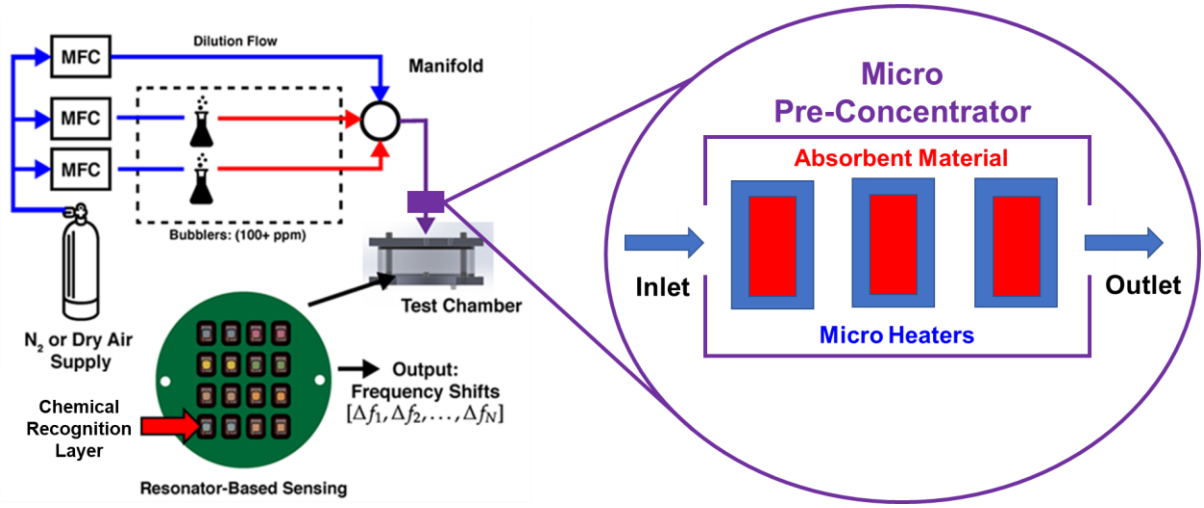

Figure 49. Proposed configuration of current sensing testing setup with added micro pre-concentrator component. This component shown in purple will be added at the interface of the manifold tubing (inlet) from manifold and the chamber entrance (outlet) to resonators.

The size of the pre-concentrator (i.e., length, width, and height) is another critical consideration. The size can vary based on the diameter of the attached tubing and the amount of absorbent material necessary to eliminate dead volume, increase break through capacity, and optimize thermal desorption. Previous studies have utilized an absorbent material thickness on the scale of 1 to several hundred μm.[1,24-26] There is not a set thickness when designing these devices. However, the higher the thickness of the absorbent material, the better absorption of gases and better break through capacity and lower dead volume. On the other hand, more material thickness means it will take longer to thermally desorb the target analyte as heat will take longer to dissipate through the material. Therefore, there will need to be some optimization on the absorbent material thickness in the pre-concentrator to find the ideal performance. The surface area of the absorbent material can range from 1-1000 mm^2 (i.e., ranging 1 mm x 1 mm to 100 mm x 100 mm) depending on the specific surface area of the absorbent material and the size of the pre-concentrator device. This surface area again has the same optimization requirements as thickness as it relates directly to the performance of the pre-concentrator. With these considerations in mind, a schematic of the pre-concentrator is outlined in Figure 50. Overall, adding a pre-concentrator into the resonant mass sensor platform is feasible and offers and excellent solution to reaching lower concentration detection limits on the resonant mass sensor devices. However, to gain the enhanced sensitivity these considerations must be accounted for when incorporating a pre-concentrator into resonant mass sensor devices.

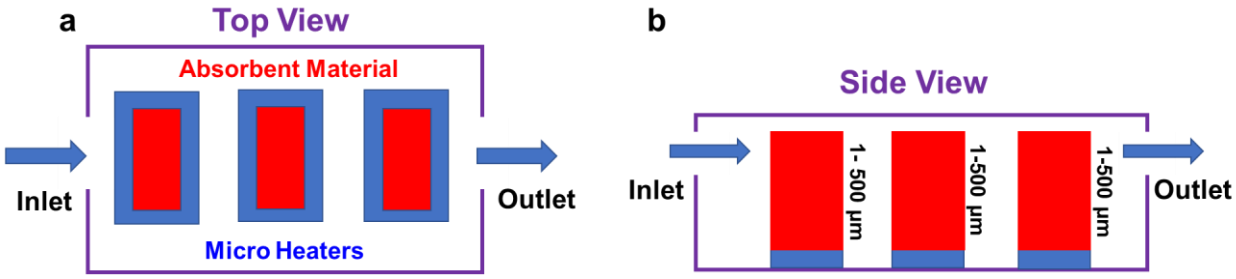

Figure 50. Proposed pre-concentrator schematic. Blue boxes indicating the micro heaters underneath the material. Red boxes indicating the absorbent material on top of the micro heaters. (a) Indicating the top view of the proposed pre-concentrator. (b) Indicating the side view of the proposed pre-concentrator. The thickness of the absorbent material recommends being in the range of 1-500 µm thickness with a surface area ranging from 1-1000 mm^2 to maintain low dead volume and high breakthrough capacity depending on the absorbent material. The length of the pre-concentrator and amount of absorbent material can be altered to optimize pressure and thermal desorption conditions.

7.3 Optimizing The Processing of Materials onto Sensor Devices

Soft materials, as shown in this report, possess a combination of remarkable properties that make them promising candidates for chemical recognition layers in MEMS gas sensors. Moreover, these properties are their high specific surface area, mechanical flexibility, processability, and relatively low fabrication cost. However, one main challenge when using soft materials on MEMS sensors is that the dispersed particles (i.e., nanoparticles and microparticles) utilized in chemical recognition layer inks, like the particles expressed in this report, agglomerate when drop-cast onto the devices. Agglomeration can occur in metal oxides, graphene materials, polymers, and nanocomposite inks. Agglomeration occurs in situations when particles are loosely held together by physical and chemical forces. In many cases, these particles consist of the same chemical composition and share an affinity for each other causing the particles to stick or clump together. When the particles agglomerate this causes a reduction in surface area and a decrease in diffusion of the target gas analyte into the chemical recognition layer. Due to these limiting effects, agglomeration of particles can lower the sensitivity of the gas sensor. These effects were observed in this report for P5C-BCD nanocomposites for formaldehyde detection in Figure 38 (25 ppm detection limit) and carbon nanotubes for BTX detection in Figure 16 and Figure 17 (100 ppm detection limit). Thus, there remains a need to investigate different methods of processing the surface chemistries expressed in this report onto the resonant mass sensor devices. Different processing methods would seek to prevent agglomeration from occurring, increasing the uniformity of the chemical recognition layer, and enhancing the sensor sensitivity to target analytes and lower current detection limits. Electro-spinning, spin coating, and chemical vapor deposition are all methods of optimizing the processing of our soft materials onto gas sensor devices to prevent agglomeration and increase uniformity.

7.3.1 Electro-Spinning

Electro-spinning is a relatively simple and low-cost method that creates strands of polymer or nanocomposite fibers using electric force.[27] These fibers can have diameters on the order of hundreds of nanometers to micrometer in size. Moreover, electrospinning is a type of electrospray process which uses an electrostatic field to form and accelerate liquid jets from the tip of a needle.[28,29] Electrospinning applies a high voltage by a power supply to a liquid droplet as it leaves a syringe needle, thus charging the body of the liquid, and electrostatic repulsion counteracts the surface tension in the droplet, allowing it to be stretched. Due to this counteraction of surface tension by the electric field, at some critical point the surface of a hemispherical liquid drop suspended in equilibrium will be distorted into a conical shape.[30] In the case of more viscous liquids (i.e., polymers or nanocomposite ink solutions) that were utilized in this report, the ejected liquid from the syringe (jet liquid) would not break up into small droplets, but rather it would travel to the grounded substrate.[31] As the jet liquid dries in flight, the jet liquid is elongated by a whipping process caused by electrostatic repulsion initiated at the charged small bends in the fiber, until it is finally deposited on the grounded substrate.[32] The elongation and thinning of the fiber resulting from this bending electrostatic repulsion leads to the formation of uniform fibers with sub-micron scale diameters. The electrospinning process is outlined in Figure 51 (*vide infra*). Due to the uniformity and small scale of the electrospinning process this would allow for an increase in surface area of the chemical recognition layers containing polymers and carbon nanotubes.[33] This increase in surface area to volume ratio would allow for enhanced sensitivity due to the enhanced diffusion and interaction of the target analyte with the chemical recognition layer.

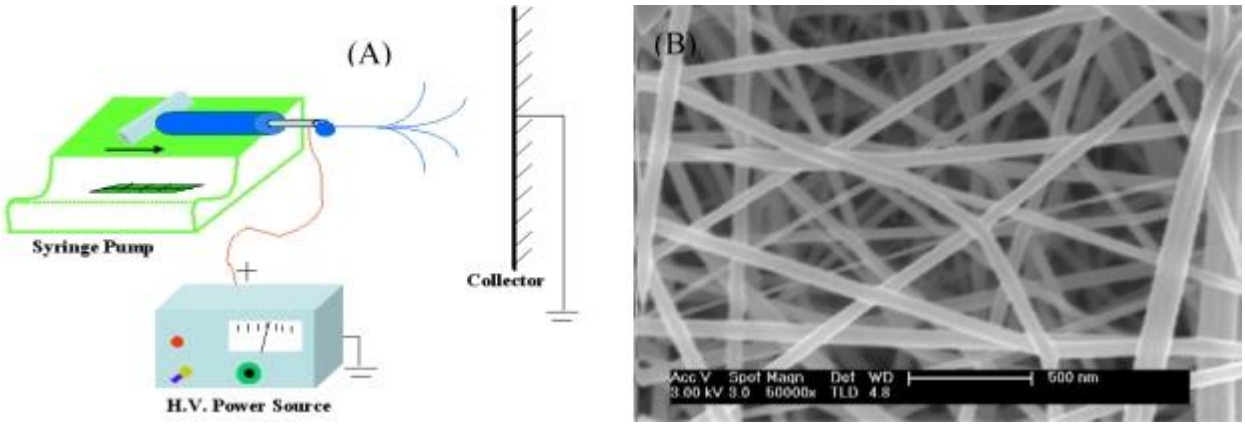

Figure 51. (a) Schematic of an electrospinning set-up consisting of a syringe pump, syringe, and a power supply. (b) SEM image of electrospun polymer fibers consisting on the nano scale in diameter. This image was reproduced from Figure 1 in Reference 27.

7.3.2 Spin Coating

In addition to electrospinning, spin coating, also known as spin casting, offers another alternative processing technique to overcome the agglomeration that was observed in this report. Spin coating is a low-cost and relatively facile procedure used to deposit uniform thin films onto flat substrates. In this case, a small amount of material ink is applied on the center of the substrate. The chemistry can be applied when either spinning at low speed or not spinning at all. The substrate is then rotated at speed up to 10,000 rpm to spread the coating material by centripetal force.[34] When the centripetal force, controlled by the spin rate (rpm), is optimized this can keep the surface chemistry from agglomerating when drying on the devices.[35] An instrument used for spin coating is called a spin coater and is shown in Figure 52a. Moreover, the film thickness of the chemical recognition layer can be modified and predicted based on the amount of material deposited and the spin rate.[36,37] For spin coater, gas sensor applications a film thickness of 1 μm or less is recommended to maintain a high surface area for the target gas analyte to interact with the surface chemistry. For our current resonator board, consisting of 16 individual resonators, this board might

require a large chuck (spinning substrate that holds the board) on the spin coater with vacuum applied to keep the resonant board from falling off (Figure 52b). However, different board configurations consisting of less resonators per board might allow for a surface substrate that could fit current spin coater instruments. Additionally, to perform optimal coating the printed circuit board substrate around the resonators should be masked with masking tape to eliminate the chemical ink from leaching onto the board while spinning. Therefore, due to the simplicity of this technique and low-costs necessary to implement this processing technique into our surface chemistries expressed in this report it would be worth pursuing in future work.

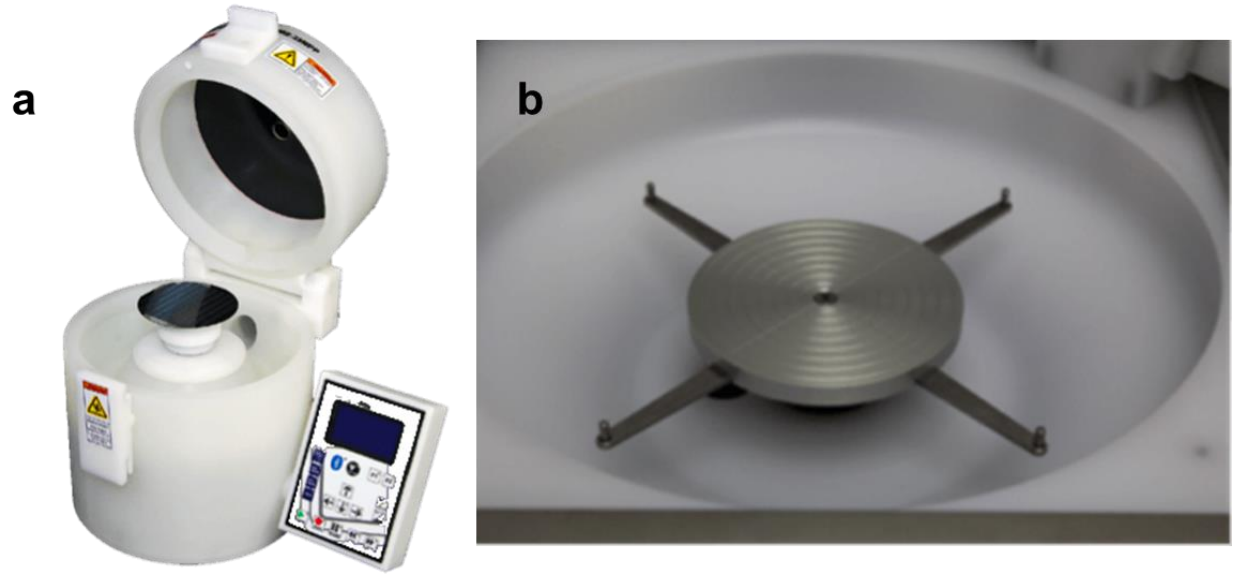

Figure 52. (a) A spin coater instrument from Elve Flow. (b) An adaptable chuck substrate from Elve Flow. These images were reproduced from the Elve Flow manufacture's website.

7.3.3 Chemical Vapor Deposition

Chemical vapor deposition (CVD) offers another alternative processing technique for depositing our materials uniformly onto the resonators. CVD describes any process in which vapor phase precursors chemically react at a surface substrate to generate a thin solid uniform film.[38]

During this process, volatile or gas precursors are fed into a heated reduced pressure chamber and react or decompose on a temperature controlled surface substrate to produce a desired deposited film.[39] In this way, the film properties are easily controlled and tunable by altering the composition of the feed gas and temperature parameters without the need for solvent. This results in coatings that are uniform and defect free over large areas while also conformal on the nanoscale. CVD is mainly applied to inorganic materials. However, different forms of the CVD process exist, such as catalytic CVD, initiated CVD, oxidative CVD, and more which can apply to the materials expressed in this report.[40-42] These methods each use a slightly alternative process where a catalyst, initiator, or oxidative agent can be pumped into the chamber via a feed gas or heated to sublimation to react with a monomer or starting material. This monomer or starting material will eventually deposit on the substrate as a polymer or grown material (i.e., carbon nanotubes or graphene). With these alternative processes, this allows for researchers to capitalize on all of the excellent features CVD process has to offer and expand to other classes of materials such as polymers and carbon nanotubes.

For polymeric materials, oxidative CVD (oCVD) has had much success with common conducting polymers such as poly(3,4-ethylenedioxythiophene) (PEDOT), poly(pyrrole) (PPy), and poly(aniline) (PANI).[38,43-45] These conjugated conductive polymers are comparable to the poly (5-carboxyindole) (P5C) expressed in this report and are a good comparison when implementing oCVD into our materials. In the oCVD process, a solid-state oxidant (i.e., Ferric Chloride or Vanadium OxyTrichloride) is loaded as a powder into a crucible placed inside the reaction chamber with the substrate suspended overhead. The monomer then flows into the reaction chamber from a side port and spontaneously reacts with the oxidant to polymerize. This oxidation step-growth polymerization then occurs on the substrate surface. This process is outlined in Figure

53. This would be a recommended setup when implementing oCVD for P5C onto the resonant mass sensors. Implementing the oCVD process on P5C could potentially allow for more uniform coatings on the resonator surface which in turn would allow for an enhanced interaction when targeting formaldehyde gas. Ideally, if P5C were able to be processed onto the resonators without agglomeration this would allow for enhanced surface area of the P5C to interact with formaldehyde and a lower detection limit than what is currently reached with this material (< 25 ppm).

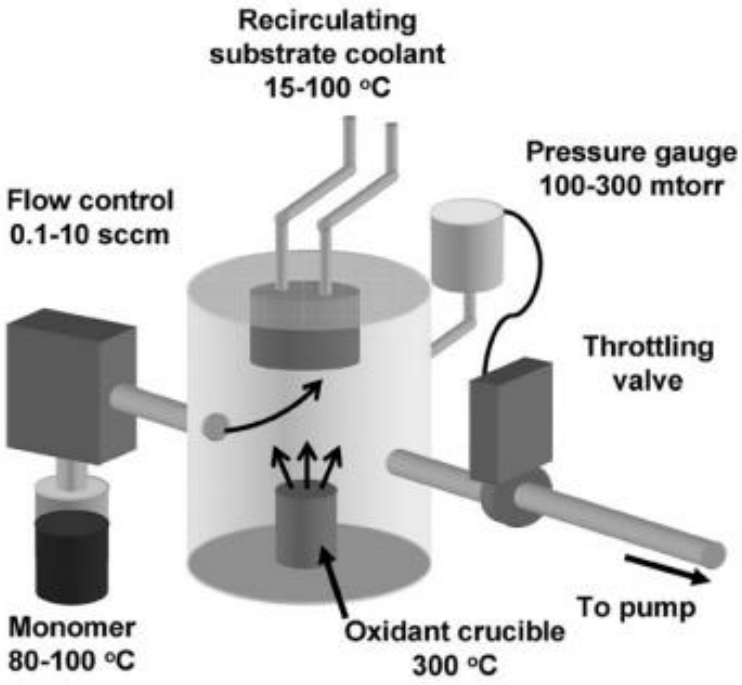

Figure 53. Schematic of the oCVD process outlining the location and operating temperatures of each component. This Figure has been reproduced from Figure 3 in Reference 38.

Catalytic chemical vapor deposition (CCVD) process has shown much promise for graphene and carbon nanotube (CNT) materials for depositing uniform films with limited agglomeration on surface substrates.[46-48] Moreover, utilizing the CCVD process allows for the reliable, highly pure, controlled growth of CNTs on surface substrates which makes this process ideal for depositing our single walled CNTs on our resonators. In this CCVD process, a catalyst is

deposited on surface exposed substrate and then nucleation of the catalyst is completed via chemical etching or thermal annealing.[47] This process is outlined in Figure 54. The type of catalyst used is based on the type of surface substrate material (conductive vs non-conductive) and the target dimensions of the CNTs (i.e., tube diameter and tube length).[48] The substrate is then put into a heated reaction chamber for the CNTs growth process. After the chamber is heated to the sufficient reaction temperature (600–1200 °C), a mixture of hydrocarbon gas (ethylene, methane, acetylene etc.) and a process gas (nitrogen, hydrogen, argon) is made to react in a reaction chamber over the surface of metal catalysts for a fixed amount of time (15–60 min).[47] Once the hydrocarbon gas decomposes and interact with the surface catalyst, CNTs begin to grow on the catalyst in the reactor which are collected on the substrate surface as the substrate cools.

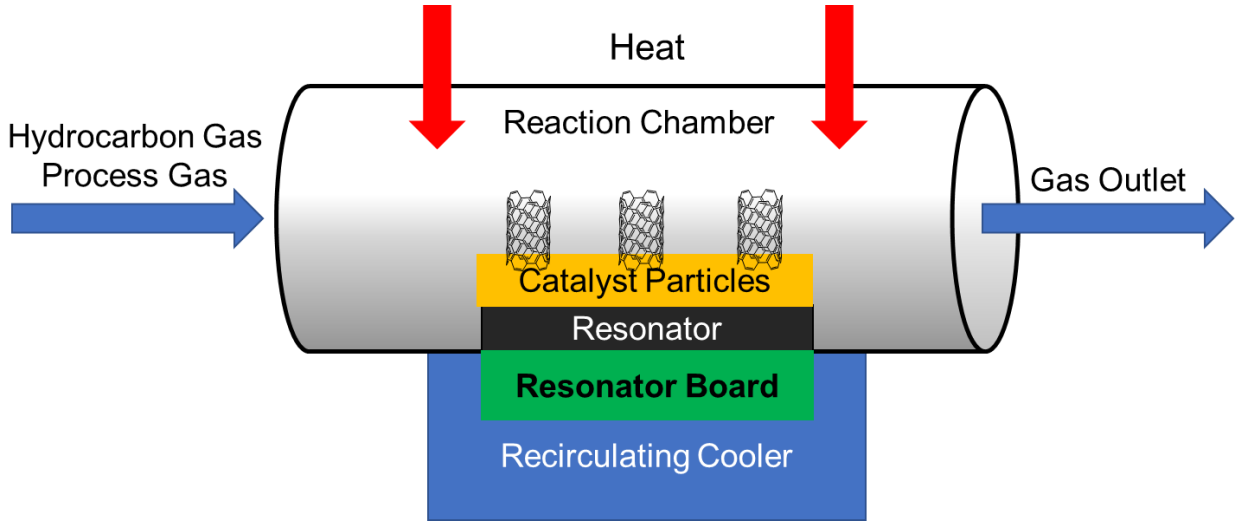

Figure 54. Proposed schematic of the CCVD process outlining the growth of CNTs on the catalytic particles on the resonators.

When performing any CVD process, it is important to consider the temperature of substrate, flow rate of the precursors, pressure in the chamber, and heating rate as these are all are critical parameters that can impact the film properties on the surface substrate. Specifically, for our

resonant mass sensor boards, the boards should not exceed a temperature of 70 °C to limit damage to the board. However, the quartz resonators should be able to withstand the CVD process temperatures. Thus, the recirculating cooler would be necessary to keep the board under the resonators below 70 °C. Additionally, it is important to mask any part of the board with masking tape and thermal insulation tape so that no chemistry gets on the board and the heat from the reactor does not melt the board. This will ensure that only the surface of the mass resonators will be coated with the chemical recognition layer. With these considerations in mind, CVD offers another alternative process for P5C and our SWCNTs in this report to decrease agglomeration and increase uniformity on the resonators.

7.3.4 Additional Processing Step Consideration

Overall, it is important to consider when optimizing materials processing onto MEMS devices to seek improved performance that this adds an additional step. This additional step can add costs in the fabrication of low-cost MEMS gas sensor devices and should not be used unless necessary. The goal with MEMS devices is keeping them low-cost which allows the devices to be easily incorporated into existing building infrastructures. However, in the case of these processing techniques allowing for improved device performance outweighing the costs, especially in cases where low detection limits (i.e., formaldehyde 0.016 ppm) could be achieved, then these techniques could provide substantial value.

7.4 Pre-Selective Recognition Layers for Resonant Mass Sensor Devices

Increasing selectivity and specificity on gas sensor devices remains an ongoing challenge even with the incorporation of novel chemical recognition layers. In this report, P5C-BCD which was utilized for detection of the target analyte formaldehyde still responded to interfering analytes

at the same concentration as the target when in the chamber at different times (target analyte not in chamber when interfering analyte is present) but observed less magnitude in frequency shift response on the device. Thus, P5C-BCD chemical recognition layer is more selective to formaldehyde, but not specific to formaldehyde alone. In addition to P5C-BCD for formaldehyde detection, a PEO and PEI polymer blend utilized for CO_2 detection observed similar results as this polymer blend responded to interfering analytes at the same concentration as CO_2 when in the chamber at different times, again observing lower magnitude of frequency shifts. This subtle response to interfering analytes existing at the same or higher concentration as the target analyte could remain a problem if the interfering analyte is simultaneously in the chamber with the target analyte. Simultaneously coexisting target and interfering analytes could reduce the frequency shift response as the chemical recognition layer could not interact with the target analyte as the interfering analyte blocks the target analyte from accessing the surface of the chemical recognition layer. On the other hand, this situation could enhance the frequency shift response, as observed in this report, as both analytes are adding mass to the resonator. This mostly occurred in situations where each analyte was at lower concentration levels and more surface sites in the chemical recognition layers were available to interact with both analytes. In both these cases, this would generate an inaccurate concentration reading on the sensor device because the magnitude of the frequency shift would not reflect the true added mass of the target analyte alone. Therefore, if there was a way to limit the interfering analytes from contacting the chemical recognition layer this would provide an added level of selectivity and possibly provide specificity to the target analyte when other analytes are present. This limitation would also ensure that the responses on the sensor device are accurately reading the concentration of target analyte present in the chamber.

To address this ongoing challenge, molecularly imprinted technology (MIT) such as molecularly imprinted polymers (MIPs) or molecularly imprinted membranes (MIMs) could be utilized as pre-selective gas layers on top of current chemical recognition layers to optimize the selectivity to the target analyte by limiting the passage of interfering analytes contacting the surface chemistry. MIPs grown over chemical recognition layers have shown much success previously for gravimetric sensors for the highly selective detection of formaldehyde gas where a poly(pyrrole) (PPy) MIP was grown over a TiO_2 nanotube array to allow for detection limits to < 1 ppm levels.[49] MIPs use a polymer which is grown around a template molecule to create molecular recognition sites capable of separating out a target analyte from other surrounding chemistries.[50] More specifically, MIPs use a mixture of a template (in this case a target VOC analyte liquid), functional monomer, cross-linker, initiator, and solvent which is activated typically by heating past the initiation temperature or applying UV light. The mixture can then polymerize and cross-link with the template inside the material matrix. After cross-linking, the template can be removed from the polymeric matrix, which leaves behind some pores in the material. These pores are complementary to the template molecules in size, shape, and functionality.[51] Thus, only the target analyte can proceed through the pores on the MIP since it has the exact structure necessary to fit into the pores. This process is outlined in Figure 55. Moreover, MIP materials due to their cross-linked structure are not affected by heat or moisture which makes them practical in interior locations.

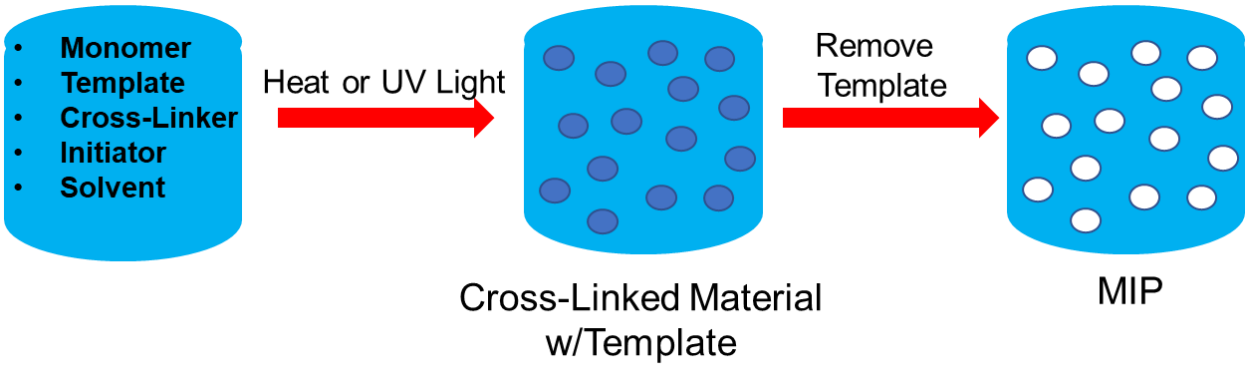

Figure 55. Schematic of MIP fabrication process. A mixture of monomer, template, cross-linker, initiator, and solvent (if necessary) is activated using heat or UV light which creates a cross-linked polymer network. The template in the cross-linked polymer matrix can then be removed by washing with solvent to generate a MIP.

Integration of the MIPs onto our resonant mass sensor devices will still utilize the materials preparation and chemical processing techniques in this report. However, the MIP will be added above the chemical recognition layer after processing the chemical recognition layer on the resonators. This addition process of the MIP onto the current resonators is depicted in Figure 56. After the chemical recognition layer is processed onto the devices a mixture of the monomer, template, initiator, cross-linker, and solvent can be drop-cast in 1 μL quantities on each of the resonators above the previously processed chemical recognition layer. This quantity of liquid can be adjusted if necessary to optimize the MIP thickness. The resonator board will then be heated to 70 °C or have UV light applied for at least 24 hr to ensure a cross-linked polymer network. The resonator board will then be submerged in a solvent bath (type of solvent depending on template molecule) to dissolve the template out of the templated material matrix. The resonator board can then be dried in vacuum to remove any residual liquid prior to testing the material. If this process is completed successfully, it will ensure an extra layer of selectivity to the chemical recognition layer by only allowing target analytes to move through the MIP to reach the chemical recognition layer.

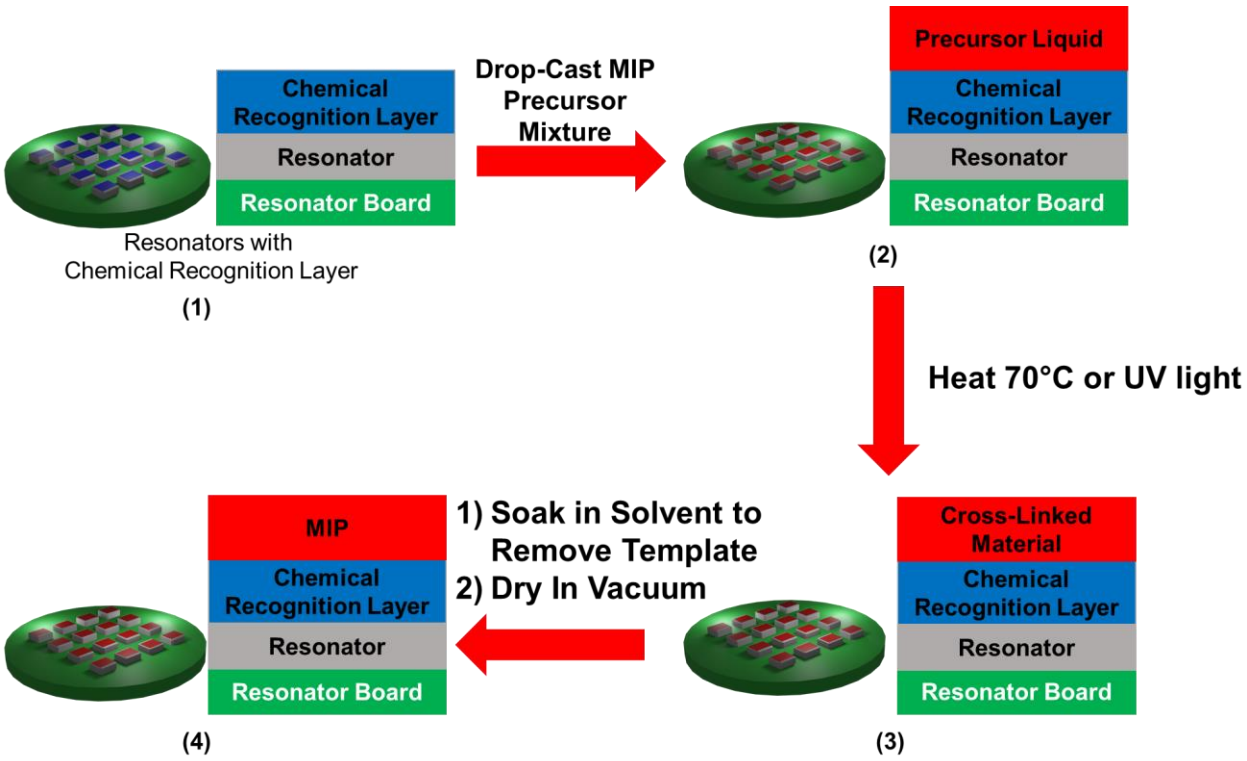

Figure 56. MIP incorporation process onto the chemically functionalized resonators.

MIMs offer another alternative MIT process that could offer a potential solution to the selectivity issues associated with current gas sensors. MIMs are prepared using a similar protocol to molecularly imprinted polymers (MIPs) (Figure 57) which use a template molecule (in this case a target VOC analyte liquid), functional monomer, cross-linker, initiator, and solvent. However, in a MIM the functional monomers are polymerized and cross-linked in-situ on a prefabricated polymer membrane (i.e., PVDF membrane or PET membrane in most cases) with sub-nanometer pore sizes using an initiator in the presence of the template molecules.[52-54] The use of a prefabricated membrane with a fixed pore size and distribution allows for the MIP grown in-situ on the prefabricated membrane to retain a uniform pore distribution which could increase the permeability of the pre-selective layer.[55] This additional step could be important in cases where the permeability of the MIP is too low causing the target gas analyte limited diffusion through the MIP to be detected in real-time. After cross-linking, the templates can again be removed from the

polymeric matrix, which leaves behind some pores in the material. Thus, only allowing the target analyte to proceed through the pores on the MIM since it has the exact structure necessary to fit into the pores. Moreover, this process is low-cost and creates a robust membrane that is not altered by elevated humidity and temperature conditions making MIMS ideal for MEMS interior sensor applications. Thus, MIPS can be utilized with the resonant mass sensors to increase the selectivity of the chemical recognition layers.

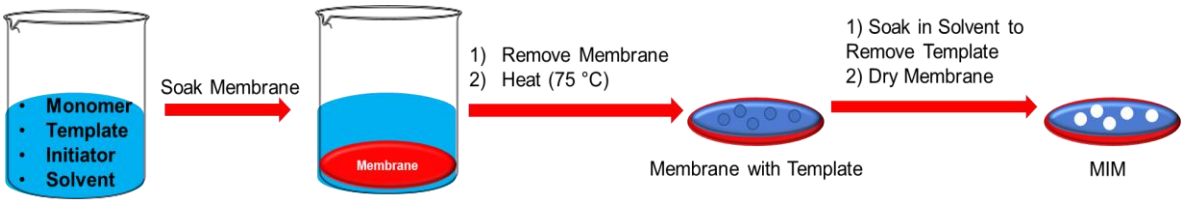

Figure 57. Fabrication process of MIMs. A prefabricated membrane is soaked in template monomer solution. The membrane is then removed and heated to activate the radical initiator and cross-link the polymer around the template on the membrane surface. The membrane is then soaked in a solvent to remove the template in the cross-linked polymer matrix. After soaking the membrane is dried and ready for processing onto resonators.

Similar to MIPS, integration of the MIMS onto our resonant mass sensor devices will still utilize the materials preparation and chemical processing techniques in this report and will be added on top of the current chemical recognition layers on the resonators. This additional process of adding the MIM onto the current resonators is depicted in Figure 58. Since the MIM is fabricated prior to being added onto the resonators (Figure 57), the resonator board does not need to be soaked in solvent or go through an additional drying process after putting the membrane over the chemical recognition layer. This MIM will be cut to 1 mm x 1 mm in size to cover the surface of the resonator. The thicknesses of the membrane will have to be 100 nm or less so that the gas can permeate and interact with the chemical recognition layer. In this situation, having a MIM with a thickness too large will either not allow the target analyte to interact with the chemical recognition layer and

will add too much mass to the resonators causing them to damp out their oscillation. Thus, optimizing the MIM thickness could lead to better device performance. Overall, MIMS offer another alternative solution as a pre-selective layer on top of chemical recognition layers and a low-cost and robust additional step that could enhance our current surface chemistries.

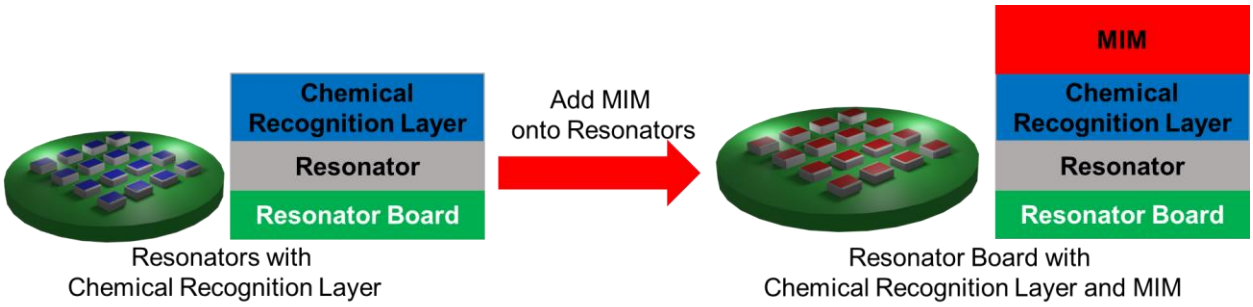

Figure 58. Addition process of the MIM onto the mass resonator devices. The MIM will be added above the chemical recognition layer to act as a barrier to minimize the diffusion of interfering analytes and only allowing the target analyte to actively diffuse onto the surface chemistry.

7.5 References

(1) James, F.; Breuil, P.; Pijolat, C.; Camara, M.; Briand, D.; Bart, A.; Cozic, R. Development of a MEMS Preconcentrator for Micro-Gas Chromatography Analyses. *Procedia Eng.* **2014**, *87*, 500–503.

(2) Leidinger, M.; Sauerwald, T.; Schütze, A.; Alépée, C.; Rieger, M. Integrated Pre-Concentrator Gas Sensor System for Improved Trace Gas Sensing Performance. In *2016 IEEE SENSORS*; **2016** 1–3.

(3) Carron, C. J. Development of MEMS-Based Chemical Pre-Concentrators with Integrated Sensing Units for Analysis of Gas-Phase Volatile Organic Compounds (Georgia Institute of Technology); **2015,** Thesis.

(4) Kim, S. K.; Burris, D. R.; Chang, H.; Bryant-Genevier, J.; Zellers, E. T. Microfabricated Gas Chromatograph for On-Site Determination of Trichloroethylene in Indoor Air Arising from Vapor Intrusion. 1. Field Evaluation. *Environ. Sci. Technol.* **2012**, *46*, 6065–6072.

(5) Wong, M.-Y.; Cheng, W.-R.; Liu, M.-H.; Tian, W.-C.; Lu, C.-J. A Preconcentrator Chip Employing μ-SPME Array Coated with in-Situ-Synthesized Carbon Adsorbent Film for VOCs Analysis. *Talanta* **2012**, *101*, 307–313.

(6) Sukaew, T.; Chang, H.; Serrano, G.; Zellers, E. T. Multi-Stage Preconcentrator/Focuser Module Designed to Enable Trace Level Determinations of Trichloroethylene in Indoor Air with a Microfabricated Gas Chromatograph. *Analyst* **2011**, *136*, 1664–1674.

(7) Tian, W.-C.; Chan, H. K. L.; Lu, C.-J.; Pang, S. W.; Zellers, E. T. Multiple-Stage Microfabricated Preconcentrator-Focuser for Micro Gas Chromatography System. *J. Microelectromechanical Syst.* **2005**, *14*, 498–507.

(8) Alfeeli, B.; Zareian-Jahromi, M. A.; Agah, M. Selective Micro Preconcentration of Propofol for Anesthetic Depth Monitoring by Using Seedless Electroplated Gold as Adsorbent. In *2009 Annual International Conference of the IEEE Engineering in Medicine and Biology Society*; **2009**; 2763–2766.

(9) Zellers, E. T.; Reidy, S.; Veeneman, R. A.; Gordenker, R.; Steinecker, W. H.; Lambertus, G. R.; Kim, H.; Potkay, J. A.; Rowe, M. P.; Zhong, Q.; et al. An Integrated Micro-Analytical System for Complex Vapor Mixtures. In *TRANSDUCERS 2007 - International Solid-State Sensors, Actuators and Microsystems Conference*; **2007**;1491–1496.

(10) Hoover, A. M. W & M ScholarWorks Evaluation of Micro-Preconcentrators and Solid Phase Microextraction Fibers for MEMS-Based Gas Chromatography Systems. **2011**.

(11) Duran, C.; Vilanova, X.; Brezmes, J.; Llobet, E.; Correig, X. Thermal Desorption Pre-Concentrator Based System to Assess Carbon Dioxide Contamination by Benzene. *Sensors Actuators B Chem.* **2008**, *131*, 85–92.

(12) Huang, X.; Bauder, T.; Do, T.; Suen, H.; Boss, C.; Kwon, P.; Yeom, J. A Binder Jet Printed, Stainless Steel Preconcentrator as an In-Line Injector of Volatile Organic Compounds. *Sensors* **2019**, *19*, 2748.

(13) Cook, K. A.; Sastry, A. M. Influence of Scaling Effects on Designing for Power Efficiency of a Micropreconcentrator. *J. Vac. Sci. Technol. B Microelectron. Nanom. Struct. Process. Meas. Phenom.* **2005**, *23*, 599–611.

(14) Alfeeli, B.; Cho, D.; Ashraf-Khorassani, M.; Taylor, L. T.; Agah, M. MEMS-Based Multi-Inlet/Outlet Preconcentrator Coated by Inkjet Printing of Polymer Adsorbents. *Sensors Actuators B Chem.* **2008**, *133*, 24–32.

(15) Leidinger, M.; Rieger, M.; Sauerwald, T.; Alépée, C.; Schütze, A. Integrated Pre-Concentrator Gas Sensor Microsystem for Ppb Level Benzene Detection. *Sensors Actuators B Chem.* **2016**, *236*, 988–996.

(16) Zaidi, N. A.; Tahir, M. W.; Vellekoop, M. J.; Lang, W. Design of Novel Ceramic Preconcentrator and Integration in Gas Chromatographic System for Detection of Ethylene Gas from Ripening Bananas. *Sensors* **2018**, *18*, 2589.

(17) Pijolat, C.; Camara, M.; Courbat, J.; Viricelle, J.-P.; Briand, D.; de Rooij, N. F. Application of Carbon Nano-Powders for a Gas Micro-Preconcentrator. *Sensors Actuators B Chem.* **2007**, *127*, 179–185.

(18) Lahlou, H.; Leghrib, R.; Llobet, E.; Vilanova, X.; Correig, X. Development of a Gas Pre-Concentrator Based on Carbon Nanotubes for Benzene Detection. *Procedia Eng.* **2011**, *25*, 239–242.

(19) Yeom, J. Micro-Preconcentrator Technology for Portable Gas Chromatography System. *Encycl. Nanotechnol.* **2020**.

(20) Camara, E. H. M.; Breuil, P.; Briand, D.; Guillot, L.; Pijolat, C.; de Rooij, N. F. Micro Gas Preconcentrator in Porous Silicon Filled with a Carbon Absorbent. *Sensors Actuators B Chem.* **2010**, *148*, 610–619.

(21) McCartney, M. M.; Zrodnikov, Y.; Fung, A. G.; LeVasseur, M. K.; Pedersen, J. M.; Zamuruyev, K. O.; Aksenov, A. A.; Kenyon, N. J.; Davis, C. E. An Easy to Manufacture Micro Gas Preconcentrator for Chemical Sensing Applications. *ACS sensors* **2017**, *2*, 1167–1174.

(22) Seo, J. H.; Kurabayashi, K. Thermal Desorption/Injection Characterization of a Microfabricated Passive Preconcentrator/Injector for Micro Gas Chromatography. In *13th InterSociety Conference on Thermal and Thermomechanical Phenomena in Electronic Systems*; **2012**; 923–927.

(23) Winter, W.; Day, C.; Prestage, J.; Hutter, T. Temporally Resolved Thermal Desorption of Volatile Organics from Nanoporous Silica Preconcentrator. *Analyst* **2021**, *146*, 109–117.

(24) Ivanov, P.; Gracia, I.; Sabate, N.; Fonseca, L.; Figueras, E.; Cane, C.; Blanco, F.; Vergara, A.; Vilanova, X.; Correig, X. Spiral μ-Preconcentrator for Gas Sensor Detection in the Ppb Range. In *SENSORS, 2007 IEEE*; **2007**; 151–154.

(25) Qin, Y.; Gianchandani, Y. B. A Fully Electronic Microfabricated Gas Chromatograph with Complementary Capacitive Detectors for Indoor Pollutants . *Microsystems Nanoeng.* **2016**, *2*, 15049.

(26) Pederson, J.D.; Davis, C. E.; Horsley, D. A. Glass Micro Preconcentrators for Point of Care Diagnostics : Low Cost Fabrication Techniques and Evaluation Methods (San Francisco State University) **2012** Thesis.

(27) Ding, B.; Wang, M.; Yu, J.; Sun, G. Gas Sensors Based on Electrospun Nanofibers. *Sensors (Basel).* **2009**, *9*, 1609–1624.

(28) Reneker, D. H.; Yarin, A. L.; Fong, H.; Koombhongse, S. Bending Instability of Electrically Charged Liquid Jets of Polymer Solutions in Electrospinning. *J. Appl. Phys.* **2000**, *87*, 4531–4547.

(29) Shin, Y. M. H. MM; Brenner, MP; Rutiedge, GC," Experimental Characterization of Electrospinning: The Electrically Forced Jet and Instabilities,". *Polymer (Guildf).* **2001**, *42*, 9955–9967.

(30) Deitzel, J. M.; Kleinmeyer, J.; Harris, D. E. A.; Tan, N. C. B. The Effect of Processing Variables on the Morphology of Electrospun Nanofibers and Textiles. *Polymer (Guildf).* **2001**, *42*, 261–272.

(31) Doshi, J.; Reneker, D. H. Electrospinning Process and Applications of Electrospun Fibers. *J. Electrostat.* **1995**, *35*, 151–160.

(32) Li, D.; Xia, Y. Electrospinning of Nanofibers: Reinventing the Wheel? *Adv. Mater.* **2004**, *16*, 1151–1170.

(33) Miao, F.; Shao, C.; Li, X.; Wang, K.; Lu, N.; Liu, Y. Electrospun Carbon Nanofibers/Carbon Nanotubes/Polyaniline Ternary Composites with Enhanced Electrochemical Performance for Flexible Solid-State Supercapacitors. *ACS Sustain. Chem. Eng.* **2016**, *4*, 1689–1696.

(34) Cohen, E.; Lightfoot, E. J. Coating Processes. *Kirk-Othmer Encyclopedia of Chemical Technology* **2011**, 1–68.

(35) Nguyen, A. N.; Solard, J.; Nong, H. T.; Ben Osman, C.; Gomez, A.; Bockelée, V.; Tencé-Girault, S.; Schoenstein, F.; Simón-Sorbed, M.; Carrillo, A. E.; et al. Spin Coating and Micro-Patterning Optimization of Composite Thin Films Based on PVDF. *Materials* . 2020.

(36) Wilson, S.K.; Hunt, R.; Duffy, B.R. The Rate of Spreading in Spin Coating. *J. Fluid Mech.* **2000**, *413*, 65–88.

(37) Danglad-Flores, J.; Eickelmann, S.; Riegler, H. Deposition of Polymer Films by Spin Casting: A Quantitative Analysis. *Chem. Eng. Sci.* **2018**, *179*, 257–264.

(38) Baxamusa, S. H.; Im, S. G.; Gleason, K. K. Initiated and Oxidative Chemical Vapor Deposition: A Scalable Method for Conformal and Functional Polymer Films on Real Substrates. *Phys. Chem. Chem. Phys.* **2009**, *11*, 5227–5240.

(39) Hamzan, N. binti; Bin Ng, C. Y.; Sadri, R.; Lee, M. K.; Chang, L.-J.; Tripathi, M.; Dalton, A.; Goh, B. T. Controlled Physical Properties and Growth Mechanism of Manganese Silicide Nanorods. *J. Alloys Compd.* **2021**, *851*, 156693.

(40) Lee, C. H.; Xie, M.; Kayastha, V.; Wang, J.; Yap, Y. K. Patterned Growth of Boron Nitride Nanotubes by Catalytic Chemical Vapor Deposition. *Chem. Mater.* **2010**, *22*, 1782–1787.

(41) Gupta, M.; Kapur, V.; Pinkerton, N. M.; Gleason, K. K. Initiated Chemical Vapor Deposition (ICVD) of Conformal Polymeric Nanocoatings for the Surface Modification of High-Aspect-Ratio Pores. *Chem. Mater.* **2008**, *20*, 1646–1651.

(42) Lock, J. P.; Im, S. G.; Gleason, K. K. Oxidative Chemical Vapor Deposition of Electrically Conducting Poly(3,4-Ethylenedioxythiophene) Films. *Macromolecules* **2006**, *39*, 5326–5329.

(43) Drewelow, G.; Wook Song, H.; Jiang, Z.-T.; Lee, S. Factors Controlling Conductivity of PEDOT Deposited Using Oxidative Chemical Vapor Deposition. *Appl. Surf. Sci.* **2020**, *501*, 144105.

(44) Smolin, Y. Y.; Soroush, M.; Lau, K. K. S. Oxidative Chemical Vapor Deposition of Polyaniline Thin Films. *Beilstein J. Nanotechnol.* **2017**, *8*, 1266–1276.

(45) Lee, J. E.; Lee, Y.; Ahn, K.-J.; Huh, J.; Shim, H. W.; Sampath, G.; Im, W. Bin; Huh, Y.; Yoon, H. Role of Co-Vapors in Vapor Deposition Polymerization. *Sci. Rep.* **2015**, *5*, 8420.

(46) Wang, X.-D. Synthesis of Carbon Nanotubes by Catalytic Chemical Vapor Deposition; Vinodgopal, K., Ed.; IntechOpen: Rijeka, **2019**; p Ch. 2.

(47) Shah, K. A.; Tali, B. A. Synthesis of Carbon Nanotubes by Catalytic Chemical Vapour Deposition: A Review on Carbon Sources, Catalysts and Substrates. *Mater. Sci. Semicond. Process.* **2016**, *41*, 67–82.

(48) Li, Y.; Li, Z.; Lei, L.; Lan, T.; Li, Y.; Li, P.; Lin, X.; Liu, R.; Huang, Z.; Fen, X.; et al. Chemical Vapor Deposition-Grown Carbon Nanotubes/Graphene Hybrids for Electrochemical Energy Storage and Conversion. *FlatChem* **2019**, *15*, 100091.

(49) Tang, X.; Raskin, J.-P.; Lahem, D.; Krumpmann, A.; Decroly, A.; Debliquy, M. A Formaldehyde Sensor Based on Molecularly-Imprinted Polymer on a TiO_2 Nanotube Array. *Sensors (Basel).* **2017**, *17*, 675.

(50) Zhang, Y.; Zhang, J.; Liu, Q. Gas Sensors Based on Molecular Imprinting Technology. *Sensors (Basel).* **2017**, *17*, 1567.

(51) Lowdon, J. W.; Diliën, H.; Singla, P.; Peeters, M.; Cleij, T. J.; van Grinsven, B.; Eersels, K. MIPs for Commercial Application in Low-Cost Sensors and Assays – An Overview of the Current Status Quo. *Sensors Actuators B Chem.* **2020**, *325*, 128973.

(52) Trotta, F.; Biasizzo, M.; Caldera, F. Molecularly Imprinted Membranes. *Membranes*. **2012**, *3*, 440–477.

(53) Raza, A.; Yousaf, M. F.; Farrukh, S.; Hussain, A. Thickness Effect on Permeance of CO_2/CH_4 Gases in CA Coated PVDF Composite Membranes. *Trans. Indian Ceram. Soc.* **2021**, *80*, 89–95.

(54) Zhao, X.; Cheng, Y.; Xu, H.; Hao, Y.; Lv, Y.; Li, X. Design and Preparation of Molecularly Imprinted Membranes for Selective Separation of Acteoside . *Frontiers in Chemistry* **2020**, *8*, 2296–2646.

(55) Yoshikawa, M.; Tharpa, K.; Dima, Ş.-O. Molecularly Imprinted Membranes: Past, Present, and Future. *Chem. Rev.* **2016**, *116*, 11500–11528.

LIST OF PUBLICATIONS

(1) Hodul, J. N.; Murray, A. K.; Carneiro, N. F.; Meseke, J. R.; Morris, J.; He, X.; Zemlyanov, D.; Chiu, G. T.-C.; Braun, J. E.; Rhoads, J. F.; et al. Modifying the Surface Chemistry and Nanostructure of Carbon Nanotubes Facilitates the Detection of Aromatic Hydrocarbon Gases. *ACS Appl. Nano Mater.* **2020**, *3*, 10389 – 10398.

(2) Siefker, Z. A.; Hodul, J. N.; Zhao, X.; Bajaj, N.; Brayton, K. M.; Flores-Hansen, C.; Zhao, W.; Chiu, G. T.-C.; Braun, J. E.; Rhoads, J. F.; et al. Manipulating Polymer Composition to Create Low-Cost, High-Fidelity Sensors for Indoor CO_2 Monitoring. *Scientific Reports* **2021**, *11*, 13237.

VITA

John Nicholas Hodul was born in Berwyn, IL. USA. His family moved to Orland Park, IL. where he attended Carl Sandburg High School prior to his undergraduate studies. He completed his B.S. in Chemistry in May 2017 from Lewis University in Romeoville, IL. Following graduation, John entered the Department of Chemistry Graduate School at Purdue University in August 2017.